UNIVERSITY OF LIVERPOOL

IRIS PIGMENTED EPITHELIAL STEM CELLS AS A STRATEGY TO TREAT AGE-RELATED MACULAR DEGENERATION

Thesis submitted in accordance with the requirements of the University of Liverpool for the degree of Doctor of Philosophy

By

Valentin Georges Andre Pied

2023

Abstract

The existence of iris pigmented epithelial stem cells has been hypothesised in the end of the 90s when ophthalmologists and scientists started to compare the iris pigmented epithelium (IPE) and the retinal pigmented epithelium (RPE). Early investigations demonstrated functional similarities between both tissues in various models, in which IPE cells were able to integrate the RPE without subsequent issues and proved RPE rescue effect. Over investigations, IPE cells demonstrated a certain phenotypic plasticity as neurons and photoreceptors were also generated *in vitro*. These early works brought the possibility that IPE cells could replace RPE cells in non-exudative age-related macular degeneration (AMD), a progressive and permanent loss of vision without therapeutic options until our days. However, no IPE stem cells were identified so far and their existence remain hypothetic until today.

Stem cells therapies aim to replace degraded tissues with cell grafts developed *in vitro*. Intense research is dedicated to develop RPE grafts with some clinical trials already completed, which demonstrated abilities to stabilise the vision. Therefore, the identification of IPE stem cells is of interest in a clinical perspective as it is biologically close to the RPE, so potential development would not have prohibitive cost while a therapy could be developed in a personalised manner, so the patient would provides its own stem cells to treat its affection.

Histological investigations defined some native features of the porcine IPE. Smooth muscle proteins composed the anterior layer, conjugated with a global flexible cytoskeleton. The basal lamina surrounds the porcine IPE, its composition varying according to the cell functions. Finally, cell proliferation occurs mainly in and near the ciliary body-IPE junction, where proteins associated with multipotency were observed.

IPE cells were then processed *in vitro* as neurospheres. Spheres obtained were resulting from cell aggregation and not clonal proliferation. Specific neuronal proteins were observed in some aggregates. Follow-up investigations revealed the upregulation of cell transformation-associated pathways and the downregulation of RPE development-associated ones after the switch from generic FBS & adherent-based conditions to a specific neurosphere culture environment. Neuronal cell culture using B27 supplement was then used. Four subsequent cell types were commonly observed: epithelial-like cells/fibroblasts-like, neurons-like and a third undefined group. Small epithelial-like cells morphologically close to induced-pluripotent stem cells (iPSC) were observed in medium supplemented with 2X B27. However, lab constraints did not allow to characterise them more.

Collectively, these data confirmed that the porcine IPE tissue conducts smooth muscular functions *in vivo*. The tissue seems to preserve its homeostasis by maintaining proliferation in its periphery, where cells express neuronal multipotent-associated proteins. The ability to transform into other cells was then observed *in vitro*. No stem cells were identified but further investigations shall follow this work as the small epithelial-like may be IPE stem cells.

Acknowledgements

At first, I would like to say a massive thank you to my supervisors Victoria Kearns, Hannah Levis and Rachel Williams for giving me the opportunity to do this PhD abroad. You gave me the opportunity to learn a new language in a completely different environment and that experience changed me. Professionally, you have let me built the plans, the experiments and the analysis. I have made mistakes that I have learnt from and I have shaped my spirit as a scientist. As time passes, I realise the chance I had to handle a research project by my own. It is not an exaggeration to say that this PhD made me grow up. So, thank you for this changing-life experience!

A big thank you to Kevin Hamill who kept his door and its Teams® opened over all circumstances. Your mentoring was crucial, your advices precious and your book fundamental in this PhD. It was a real pleasure to learn about Science from you. A big thanks to the histological team as well, Gemma Charleston, Andrew Ainsworth and Catherine Sperinck, for their help and dedication over the different parts of this PhD. Finally, a big thanks to Andy Houghton for his support in lab maintenance.

Thank you to everyone in the labs who helped me along the lab time, especially Jessica Eyre and Lee Throughton for their advices, mentoring, help and support. You showed me many precious things in the lab. A big thanks to Catarina Castanheira for her help about PCRs processes and analysis. Things would have been much more difficult without your lights. A big thanks to Xiaochen Fan for her help in many fields over this PhD. Your advices and experiences have been essential many times. Finally, a very special thanks to Gaia Lugano, Kubra Bilir, Lina Zaripova, Barbara Clemencon, Neil Saptarshi, Conor Sugden, Ufuk Ersoy, Aibek Smagul, Daniel Green and Eloic Lafouine for the irrational number of tragedies and comedies that happened with them. We will meet again.

Finally, a massive thanks to Mum & Dad for having hosted me over the writing. Things would have been much harder if you had not been there, so from the bottom of the heart, thank you. A big thanks to my little brothers, this thesis may have been completed earlier if you had not used me as a guinea pig for your physiological exercises. Last but not least, thank you to the French Ladies and Guys from Rouen and Angers. You kept me healthy in body and spirit over all circumstances over the last years abroad and here and I could not dream about better friends.

"*The PhD is a long run, a marathon.*" Umar Sharif

Strengh and honour to the next one!

Table of Contents

Abstract II

Acknowledgements III

Table of Content V

Index of figures XII

Index of tables XV

Index of abbreviations XVI

1 **Chapter 1: Introduction** 1

1.1 **Anatomy of the eye** 1

1.1.1 Sagittal plan of the mammalian eye 2

1.1.2 The light path 7

1.1.2.1 From the cornea to the retina 7

1.1.2.2 Optic paths toward the occipital lobes 8

1.1.2.3 Differences between the human and the porcine eye 11

1.2 **The IPE, functions, development & potential** 13

1.2.1 Anatomy and functions of the IPE in vivo 13

1.2.2 IPE development 16

1.2.2.1 The human neural development, starting at the gastrulation 16

1.2.2.2 From the Prosencephalon arises the eye 19

1.3 **Age-related Macular Degeneration** 24

1.3.1 Physiopathology 24

1.3.1.1 RPE and retina 24

1.3.1.2 AMD in its wet and dry forms 26

1.3.2 Classification and techniques of diagnosis of AMD 30

1.3.3 Few words about the therapeutic arsenal against AMD 31

1.3.4 Stem cells-based therapies against AMD 33

1.3.4.1 Prior to stem cells, cell lines-based cellular grafts 33

1.3.4.2 Stem cells in clinic 33

1.3.5 The IPE's plasticity and its potential to replace the RPE 37

1.3.6 *In vitro* 2D versus 3D cell culture 39

1.4 **In summary** 40
1.5 **Aim & objectives of the thesis** 41
1.5.1 Aim 41
1.5.2 Objectives 41
2 **Chapter 2: materials and methods** 43
2.1 **Materials** 43
2.2 **Methods** 45
2.2.1 Porcine eye dissection: from their reception to the eye opening 45
2.2.2 Histology & immunohistochemistry 47
2.2.2.1 Porcine eye dissection 47
2.2.2.2 H&E staining 48
2.2.2.3 Fluorescent/immunohistochemistry 48
2.2.3 Western-Blot – samples preparation 50
2.2.3.1 Cell lysis 50
2.2.3.2 Protein quantification 51
2.2.4 Western-Blot - process 51
2.2.4.1 Electrophoresis - gel preparation 52
2.2.4.2 Electrophoresis run 53
2.2.4.3 Protein transfer 53
2.2.4.4 Immunodetection 55
2.2.4.5 Stripping 56
2.2.5 Cell culture 56
2.2.5.1 Primary IPE cell extraction – early protocol 56
2.2.5.2 Primary IPE cell extraction – late protocol 57
2.2.5.3 Adherent and suspended cultures used in Chapter 4 58
2.2.5.4 Adherent cell culture used in Chapter 5 58
2.2.6 Reverse transcription-quantitative real time PCR 59
2.2.6.1 Transcript design 59
2.2.6.2 RNA extraction 59
2.2.6.3 Reverse transcription 60
2.2.6.4 Quantitative real-time PCR 60
2.2.6.5 DNA electrophoresis 63
2.2.6.6 Analysis by computer 63
2.2.6.7 Statistics 63
2.2.7 Adherent IPE cell staining on 13 mm glass slides 64

2.2.7.1 Cell extraction and culture 64
2.2.7.2 Staining and imaging 64
2.2.8 Adherent IPE cell staining on 24 well plates 65
2.2.8.1 Cell extraction and culture 65
2.2.8.2 Staining and imaging 65
2.2.9 IPE aggregates staining 65
2.2.9.1 Cell culture 65
2.2.9.2 Staining and imaging 66
2.2.9.3 CFSE and DiD-/DiI Vybrant staining and imaging 66
2.2.10 Resazurin-based metabolic assessment 67
2.2.11 Statistics 68
3 **Chapter 3: Characterisation of the porcine IPE tissue** 70
3.1 **Overview** 70
3.2 **Aim & objectives of the chapter** 70
3.3 **Depigmentation of the porcine IPE** 71
3.3.1 H_2O_2-based depigmentation runs well into a haematoxylin and eosin staining protocol 71
3.3.2 H_2O_2-based depigmentation requires optimisation to run into fluorescent immunohistochemistry 73
3.3.3 Desmin was labelled on depigmented section with an appropriate fixation of the original tissue 75
3.3.4 Investigation of the chemicals, the time of the process and the pH 77
3.4 **Porcine IPE cytoskeleton assessment** 82
3.4.1 Intermediate filaments 82
3.4.1.1 Vimentin is present in human and porcine irises 82
3.4.1.2 Cytokeratins type I and II are absent 86
3.4.1.3 Nestin is present in the ciliary bodies – IPE junction 91
3.4.2 Micro-filaments are linked to smooth muscle activities 93
3.5 **Porcine IPE basal lamina assessment** 95
3.5.1 Collagen type IV 95
3.5.2 Laminins 98
3.5.2.1 Porcine ocular sections did not react to the pan-laminin antibody 98
3.5.2.2 Laminin α4 was marked on human sections only 100
3.5.2.3 Laminin-β1 & laminin-β2 103
3.6 **Cell-cell junctions in the IPE** 103

3.6.1 Cadherins 103
3.6.1.1 N-cadherin was the major cadherin used in the IPE 103
3.6.1.2 E-cadherin investigation demonstrated unclear/irrelevant distributions 105
3.6.2 Tight junctions 106
3.7 **Proliferation in the IPE** 109
3.7.1 PCNA labelled few cell cycle S-phase only 109
3.7.2 Ki67 marked differentially the IPE depending the location 111
3.8 **No IPE cells expressed the stem cell marker ΔN-p63 *in vivo*** 114
3.9 **Developmental markers in the IPE** 115
3.9.1 PAX6 is present in the IPE and the iris 115
3.9.2 SOX2 is present in the IPE cell cytoplasm 117
3.10 **Discussion** 117
3.10.1 Depigmentation, a process to deepen 117
3.10.1.1 Initially, depigmentation produced the desired result 118
3.10.1.2 Initial desmin FIHC being negative, adjustments were required 119
3.10.2 Features of the IPE tissue 120
3.10.2.1 IPE has a mesenchymal cytoskeleton 121
3.10.2.2 Basal lamina contains collagen type IV and laminin-α4 122
3.10.2.3 N-cadherin was the adherent junction protein detected 123
3.10.3 So, the IPE exhibits the features of a smooth muscle 123
3.10.4 Proliferation could occur at/near the ciliary body–IPE junction 126
3.10.5 Developmental markers: PAX6 present, SOX2 absent? 127
3.10.5.1 PAX6 distributed over the IPE length, for what purpose? 127
3.10.5.2 Further investigations are required for SOX2 128
3.11 **In conclusion** 129
4 **Chapter 4: Porcine IPE cells in neurogenic conditions develop specific neuronal proteins** 130
4.1 **Overview** 130
4.2 **Aim & objectives of the chapter** 130
4.3 **Development of cell culture processes** 130
4.3.1 IPE contamination was resolved by an increased antibiotic concentration in the cell culture medium 131

4.3.2 IPE-derived aggregates formed and remained suspended only on Nunclon sphere plates 134

4.4 **IPE spheres result from the aggregation of original cells** 136

4.4.1 CFSE-labelled spheres demonstrated heterogeneous cell proliferation over eight days 137

4.4.2 DiD and DiI were mixed in spheres demonstrating an aggregation process rather than a proliferation one 140

4.5 **Epithelial and muscular features found in the tissue are conserved in the spheres** 142

4.5.1 A-smooth actin is ubiquitously expressed by adherent cells and remained at the aggregate surface 142

4.5.2 Desmin was observed in both adherent cells and spheres at a lower rate 144

4.5.3 Vimentin and nestin are major cytoskeletal proteins in both IPE adherent cells and IPE aggregates 145

4.6 **Do IPE spheres revert their phenotype in culture?** 147

4.6.1 IPE aggregates reduced over time the expression of the transcripts of interest 147

4.6.1.1 TBP expression is the most stable of the reference transcripts 149

4.6.1.2 WNT2B expression decreases while β-catenin increases, then decreases 149

4.6.1.3 C-Myc and GNL3 followed β-catenin 150

4.6.1.4 Nestin increased, SOX2 decreased 150

4.6.1.5 PAX6 rises then falls, MITF drops off, OTX1 stabilises then falls 151

4.6.2 IPE cells and aggregates demonstrated presence of developmental markers and neural-associated ones 152

4.6.2.1 GNL3 present in both adherent cells and aggregates, in both cytoplasms and nuclei 154

4.6.2.2 PAX6 demonstrated a similar distribution to GNL3 154

4.6.2.3 SOX2 was labelled, in adherent cells and in spheres 155

4.6.2.4 BIII-tubulin appeared in spheres 155

4.6.3 IPE aggregates conserve markers in suspension found in adherent ones 156

4.6.3.1 N-cadherin was used by adherent cells and aggregates 158

4.6.3.2 Tyrosinase clustered in adherent cells and distributed everywhere in aggregates 158

4.6.3.3 SNAIL and SLUG were present in all cultures 159

4.7 **Discussion** 159

4.7.1 The origin of the contamination remained unknown 160
4.7.2 IPE cells in suspension generated aggregates 160
4.7.3 IPE aggregates conserve their original cytoskeleton, plus nestin 161
4.7.4 In IPE aggregates, a neurogenic transformation occurred on the side of a potential epithelial one 163
4.7.4.1 The main use of B-catenin could be the reformation of AJs 163
4.7.4.2 C-Myc and GNL3 played with chromatin 165
4.7.4.3 WNT2B, MITF and OTX1 were the last priority 165
4.7.4.4 PAX6 and SOX2 demonstrated opposite evolutions 167
4.8 **In conclusion** 168
5 **Chapter 5: Identifying IPE-based neuronal progenitor cells** 169
5.1 **Background** 169
5.2 **Aim & objectives of the chapter** 169
5.3 **Result** 170
5.3.1 Diverse cells in a single IPE were observed in both FBS and B27 conditions 170
5.3.2 B27 reduced metabolic activity compared to FBS in IPE cells 173
5.3.3 B27 favoured more epithelial-associated genes transcription than the neuronal one 174
5.3.4 FICC demonstrated the absence of proper neuronal- and epithelial-like cells 176
5.3.5 WB demonstrated mostly no protein content 179
5.4 **Discussion** 181
5.4.1 B27 favoured the epithelial-like cell and the neuronal-like one over the others 181
5.4.2 B27 composition was optimised for neuronal cell long-term metabolism, not their proliferation 183
5.4.3 Small pro-epithelial cells in 2X B27 with iPSC-like morphology 188
5.5 **In conclusion** 188
6 **Chapter 5: General discussion & conclusion** 189
6.1 **IPE stem cell existence remains to be proved, potentially by cultivating them in medium supplemented with B27** 189
6.2 **Future plans** 193

6.2.1 Short term plan: small epithelial-like cell characterisation & cell culture developments 193
6.2.2 Long-term plan: RPE differentiation & AMD treatment 196
6.3 **General conclusion** 198
6.4 **Summary of findings** 199
7 **Appendices** 200
7.1 Appendix 1: adjustement of the H_2O_2 depigmentation 200
7.2 Appendix 2: Adjustement of the H2O2 solution 201
7.3 Appendix 3: Laminin β1 and β2 in the human IPE 202
7.4 Appendix 4: positive control for ΔN-p63. 203
7.5 Appendix 5: SOX2 in porcine cornea and iris sections 204
7.6 Appendix 6: Cytokeratins in IPE cells and aggregates 205
References 206

Index of figures

Figure 1.1: Representative sagittal plan of the mammalian eye. 5
Figure 1.2: Image of the mammal pigmented epithelia from the IPE to the RPE. 6
Figure 1.3: Representative plan of the light path from the cornea to the fovea of the retina in an intense light stimulation. 8
Figure 1.4: Representation of the human optic path from the eye to the brain occipital cortex. 11
Figure 1.5: Representation of two mammalian IPE cells in vivo in the in-between iris area. 14
Figure 1.6: Representative H&E-processed sections of the mammalian iris from the pupil on its junction with the ciliary body in its periphery. 15
Figure 1.7: Human embryogenesis from day 16 to day 22. 18
Figure 1.8: Representation of the three neural vesicles during the fourth week of the human development. 19
Figure 1.9: Human optic cup development: the lens development. 22
Figure 1.10: Representation of the human ciliary margin zone and its evolution from day 33 to the 13th week of development. 24
Figure 1.11: Representation of the human RPE and retina from a physiological situation to a late AMD one. 29
Figure 2.1: Diagram of the porcine eye generic dissection. 46
Figure 3.1: H&E analysis of porcine ocular pigmented epithelial sections depigmented by a 10% H_2O_2-based solution. 72
Figure 3.2: Representative pictures of desmin in porcine iris sections depigmented by a 10% H_2O_2 solution. 75
Figure 3.3: Representative pictures of the experiment 76
Figure 3.4: Porcine iris sections depigmented by 3% H_2O_2 at 60^{o}C for 20 min. 79
Figure 3.5: Porcine iris sections depigmented by 3% H_2O_2 at pH 9. 81
Figure 3.6: Representative pictures of vimentin in human and porcine iris sections. 84
Figure 3.7: Representative pictures of vimentin in human iris section and on porcine ocular protein extract. 86
Figure 3.8: Representative images of C-11 2931-labelled porcine iris sections. 88
Figure 3.9: Representative images of MNF-116-labelled porcine iris sections. 89
Figure 3.10: Second assessment of MNF-116-labelled porcine cornea and iris sections. 90

Figure 3.11: Representative images of nestin-labelled porcine iris sections and nestin-labelled porcine ocular protein samples. 93
Figure 3.12: Representative images of α-SMA-labelled porcine iris sections. 94
Figure 3.13: Representative images of collagen type IV-labelled human and porcine ocular sections. 97
Figure 3.14: Representative images of pan-laminin-labelled porcine sections. 99
Figure 3.15: Representative images of laminin-α4--labelled human sections. 101
Figure 3.16: Representative images of laminin-4-labelled porcine sections. 103
Figure 3.17: Representative images of N-cadherin-labelled porcine ocular sections. ... 104
Figure 3.18: Representative images of E-cadherin-labelled porcine ocular sections. 106
Figure 3.19: Representative images of porcine IPE-labelled for ZO-1. 108
Figure 3.20: Representative images of PCNA-labelled porcine ocular anterior chamber. 111
Figure 3.21: Representative images of Ki67-labelled porcine ocular anterior chamber. 113
Figure 3.22: Representative pictures of porcine ocular sections labelled for ΔN-p63. .. 115
Figure 3.23: Representative images of PAX6-labelled human and porcine iris sections. 117
Figure 3.24: Balance of the depigmentation technical investigation. 120
Figure 4.1: Representative images of primary porcine IPE cells in culture after extraction. 133
Figure 4.2: Plates efficiencies to generate aggregates from porcine IPE cells. 136
Figure 4.3: Representative scheme of CFSE and Di-dies used. 137
Figure 4.4: Representative images of CFSE-labelled porcine IPE spheres grown for eight days. 140
Figure 4.5: Fluorescent images of IPE aggregates labelled with anti-PCNA and anti-Ki67 antibodies. 140
Figure 4.6: Representative images of DiD- and DiI-labelled porcine IPE spheres grown for 8 days. 141
Figure 4.7: Representative images of α-smooth actin-labelled aRPE-19 cells, adherent IPE cells and IPE aggregates. 143
Figure 4.8: Representative images of desmin in aRPE19 cells, adherent IPE ones and IPE aggregates. 145
Figure 4.9: Representative images of nestin & vimentin-labelled IPE cells and IPE aggregates. 146

Figure 4.10: qPCR analysis of the various transcripts of interest in IPE cells and spheres. 149
Figure 4.11: Representative images of IPE adherent cells and aggregates labelled for GNL3, PAX6, SOX2, vimentin, βIII-tubulin & nestin. 154
Figure 4.12: Representative images of IPE adherent cells and aggregates labelled for N-cadherin, tyrosinase, SNAIL/Slug and vimentin. 158
Figure 5.1: Schematic representation of the cell culture process undertaken in the chapter 4. 170
Figure 5.2: Representative pictures of IPE cells grown FBS and B27 conditions over 14 days. 173
Figure 5.3: Resazurin-assessed metabolic activity of cells exposed to FBS or B27 measured from day 10 to day 14. 174
Figure 5.4: Gene expression and metabolic activities among IPE cells cultivated in FBS, B27 1X or 2X. 176
Figure 5.5: Representative pictures of IPE adherent cells labelled for Nestin, SOX2, PAX6 and tyrosinase. 179
Figure 5.6: WB analysis on IPE samples and ocular tissues assessed for SOX2, SNAIL/SLUG and PAX6. 181
Figure 7.1: Representative pictures of porcine tissue sections depigmented in 10% H_2O_2 at 60^{o}C. 200
Figure 7.2: Representative pictures of porcine section depigmented in 10% H_2O_2 1% Na_2. 201
Figure 7.3: Representative pictures of Laminin B1 and laminin B2 in the human eye... 203
Figure 7.4: Representative pictures of human corneal sections labelled for DN-p63.... 203
Figure 7.5: Representative pictures of SOX2-labelled cornea and iris sections. 204
Figure 7.6: Representative pictures of aPRE19 cells, IPE cells and IPE aggregates labelled with a C-2931 pan-cytokeratin antibody. 205

Index of tables

Table 1-1: Structural dimensions in porcine and human eyes 12
Table 1-2: Summary of AMD-associated risk factors[74] 29
Table 1-3: Antibodies-based anti-exudative AMD drugs summary[116, 117, 118, 119] 32
Table 1-4: Classification of stem cell according to their plasticity 34
Table 2-1: Human samples from the Liverpool Royal Eye Bank 45
Table 2-2: Cornea embedding program 47
Table 2-3: Antibody list 49
Table 2-4: Blocking and antibody buffers 55
Table 2-5: qPCR features 61
Table 2-6: Porcine transcripts 61
Table 2-7: Summary of dyes used 67
Table 3-1: Scheme of optimisation 75
Table 3-2: Hydrogen peroxide solutions 77
Table 3-3: Summary of short and long depigmentations with different H_2O_2 solutions 78
Table 3-4: Summary of pH-based depigmentation 80
Table 3-5: Pan-cytokeratin antibodies targets 87
Table 4-1: Summary of changes included 131
Table 4-2: Summary of IPE spheres-based protein samples 147
Table 5-1: Controls from porcine tissues used 180
Table 5-2: Composition of B27 supplement[398] 183

List of abbreviations

AAV → Adenovirus-associated vector

AF → Alexa fluor

AMD → Age-related macular degeneration

ANOVA → Analysis of variance

A-SMA/α-SMA → Alpha-smooth actin

APS → Ammonium persulfate

ATCC → American type culture collection

BMP → Bone morphogenic protein

BSA → Bovine serum albumin

cDNA → Complementary deoxyribonucleic acid

CB → Ciliary body

CBE → Ciliary body epithelia

CBPE → Ciliary body pigmented epithelia

CBNPE → Ciliary body non-pigmented epithelia

CRALBP → Cellular retinaldehyde-binding protein

CNV → Choroidal neovascularisation

DAB → 3,3'-Diaminobenzidine

DAPI → 4', 6-Diamidino-2-phenylindole dihydrochloride

DMEM-F12 → Dulbecco's modified eagle's medium F-12 ham

DNA → Deoxyribonucleic acid

ΔN-P63 → Delta N – p63

ECM → Extracellular matrix

EGF → Epithelium growth factor

ESC → Embryonic stem cells

FBS → Foetal bovine serum

FDA → Food & drug administration

FFPE → Formalin-fixed paraffin-embedded

bFGF/FGF2 → Basic fibroblast growth factor/Fibroblast growth factor 2

FICC → Fluorescent immunocytochemistry

FIHC → Fluorescent immunohistochemistry

GAPDH → Glyceraldehyde 3-phosphate dehydrogenase

GFAP → Glial fibrillary protein

GFP → Green fluorescent protein

GNL3 → G-protein nucleolar 3

H_2O_2 → Hydrogen peroxide

HCl → Chlorhydric acid

H&E → Haematoxylin and eosin

HRP → Horseradish peroxidase

IHC → Immunohistochemistry

Ig → Immunoglobuline

IgG → Immunoglobuline type G

IPE → Iris pigmented epithelium

iPSC → Induced-pluripotent stem cells

$KMnO_4$ → Potassium permanganate

Lam a/b → Laminin alpha/beta

LEAD → Laser intervention in Early AMD study

LSM → Laser scanning microscope

MAB → Membrane attack complex

mAbs → Monoclonal antibody

MEF → Mouse embryonic fibroblasts

MITF → Microphthalmia-associated transcription factor

NaCl → Sodium chloride

NaOH → Sodium hydroxide

Na_2PO_4 → Disodium phosphate

NBF → Neutral buffer formalin

PAX → Paired-box protein

PBS → Phosphate buffer saline

PCNA → Proliferating cell nuclear antigen

PEDF → Pigmented epithelial growth factor

PET → Polyethylene Terephthalate

PLCL → Poly(L-lactide-co-ε-caprolactone)

PLGA → Poly(lactic-co-glycolic acid)

POS → Photoreceptor outer segment

P/S/F → Penicillin/streptavidin/fungicide

RIPA → Radio-immunoprecipitation assay buffer

RNA → Ribonucleic acid

RPE → Retinal pigmented epithelium

RT-qPCR → Reverse transcription real=time polymerase chain reaction

SB → Scale bars

SDS → Sodium dodecyl sulfate

SOX → Sex determining region Y box

TAC → Transient amplifying cells

TEMED → Tetramethylethylenediamine

TFEC → Transcription factor EC

TGF-β → Transforming-growth factor β

UV → Ultra-violet

VEGF → Vascular endothelial growth factor

VIP → Vasoactive intestinal peptide

WB → Western-Blot

WNT → Wnt signaling pathway

ZO1 → Zona occluding 1

1 Chapter 1: Introduction

Over the last two decades, fundamental research on the IPE has led researchers to believe that a subpopulation within this tissue has a certain potential to integrate other ocular tissues and generate other ocular cell types with a certain degree of specification thanks to the use of generic or specific *in vivo* and *in vitro* conditions. This led to the idea that IPE cells might serve as a cell therapy to treat some ocular diseases.

Among the various ocular pathologies is age-related macular degeneration (AMD), a chronic condition progressively reducing central then peripheral vision until total blindness. Affecting mainly people over 60 years[1], its prevalence increases in Europe as European population ages[2]. Various therapeutic options exist with various degrees of success depending the form AMD takes. What happens at the pathophysiological level requires attention as the tissue of concerns, the RPE, closely relates to the IPE from a development perspective while *in vitro* cell characterisation demonstrated similarities between them. In AMD, the loss of vision results from the disrupted architecture of the retina, itself a consequence of the RPE degression. Consequently, a cell therapy aiming to cure AMD requires to focus the RPE first to then support the retina.

In this project, porcine IPE stem cells (IPE) were hypothesised to exist to then be able to generate RPE cells *in vitro* that would be functional and efficient for a cell therapy dedicated to AMD. Limited information exists on the IPE and many gaps exist relating to their fundamental features. However, their ability to replace the retinal pigmented epithelium (RPE) without secondary affects has been demonstrated in several animal models and in human patients.

Thus, this thesis aimed to gain a broader understanding of the IPE in its native state; then to identify potential IPE stem cells *in vitro*; finally, to differentiate them into RPE cells *in vitro* by a defined pathway.

1.1 Anatomy of the eye

As an organ, the eye could be compared with a ping-pong ball with a small protrusion on its anterior surface representing a sixth of its surface[3]. It localises at the front of the face

where it transforms the photons into chemical signals sent to the occipital lobe, the most posterior brain lobe[4].

1.1.1 Sagittal plan of the mammalian eye

The eye envelope is composed of the cornea at the forefront of the eye and the sclera for the rest of it[3] (see **Figure 1.1 – Cor. & Scl.**). The cornea is a transparent, convergent and non-vascularised tissue while the sclera is a dense conjunctive tissue. The first one favours light entering into the eye while the second brings the mechanical stability, *skleros* in Greek, meaning hard[3]. On the back of the eye, the sclera has a hole, the optic disc, by which the optic nerve emerges from the eye[3] (see **Figure 1.1 – Opt.**). Being exposed to the external environment, the cornea is circled by the limbus at the corneo-scleral junction[5]. Limbii are localised at the external side of the sclera and are specifically dedicated to regenerate the corneal epithelium. Moreover, in absence of vascularisation, the cornea is considered as immunologically privileged with a network of resident immune cells[6].

The internal structure of the eye can be divided into the anterior chamber and the posterior one (see **Figure 1.1 – Ant.** & **Post.**). The anterior chamber is a liquid space between the cornea and the iris. It contains the aqueous humour, which replaces the blood vascularisation by supplying corneal cells with nutrients, metabolites and electrolytes. It also maintains a certain pressure into the anterior chamber, which maintains the corneal convergence to allow an optimal light entering[7]. Unbalanced pressures often lead to pathological situations, such as glaucoma where an increased intraocular pressure favours retinal fibers degeneration[8, 9]. Further at the iris – sclera junction lie the trabecular meshworks (see **Figure 1.1 – T.M.**), a sieve-like structure evacuating the aqueous humour toward (see **Figure 1.1 – S.C.**). Finally, the Schlemm's canal distributes the aqueous humour into the intra-scleral venous plexuses, which redistributes it into the episcleral veins[3], localising on the scleral surface.

Closing the anterior chamber, the iris is a loose-to-dense stromal conjunctive tissue (see **Figure 1.1 – Iris** & **Figure *1.2***) circling in its centre the pupil (see **Figure 1.1 – Pup.**), a diaphragm by which rays of lights pass toward the posterior chamber. Other rays of lights are blocked in the iris stroma by the high content of resident melanocytes and by the iris pigmented epithelium covering the back of the iris stroma (**Figure 1.1 – IPE**). The opening

or closing of the pupil is dictated by two muscles: **1**. the peripheral dilator muscle characterised by radial fibres and innerved by the parasympathic system, its contraction opens the pupil; **2**. the central sphincter muscle circling the pupil and innervated by the sympathic nervous system, its contraction closes the pupil[4]. Both the parasympathic and sympathic systems are parts of the autonomous nervous system, which regulate the cardiac muscle and the smooth muscle among other functions[4].

To note, all iris have a similar colour after birth due to the presence of a single pigment. The coloration observed later results from its increase due to the exposure to various wavelengths to which the iris is exposed, plus genetic factors[10, 11]. A low amount will make the iris blue, green or grey, a greater amount will make it brown.

The posterior chamber starts on the back of the iris (see **Figure 1.1**). Connected to it on its periphery, the ciliary body forms a muscle ring responsible for the contraction or relaxation of the lens (see **Figure 1.1 – C.B. & Lens**). The lens is a biconvex transparent and avascular structure placed in a central position, after the pupil. It is held to the ciliary bodies by a set of tendons called the ciliary zonules (see **Figure 1.1 – Zon.**). Another function of the ciliary body is to secrete the aqueous humour by the ciliary processes, a multifolded area right after the IPE[3]. These processes contain a high content of blood vessels with leaky endothelial walls allowing a large supply of nutrients and oxygen[3] (see **Figure 1.2**). There, the aqueous humour formation is a dynamic process, with three distinguished steps: **1**. delivery of water, proteins and nutrients by blood vessels; **2**. filtration and diffusion into the ciliary body stroma with fluids being driven thanks to the osmotic pressure; **3**. transport of into the basolateral spaces between the non-pigmented epithelial cells[12]. This production depends on the blood supply, the blood oxygen content and the secretory or inhibitory environment[12]. Finally, the ciliary body contains a strongly pigmented epithelium below its non-pigmented epithelium (see **Figure 1.2-A** & **-B**). This pigmented epithelium is in continuity with the IPE to complete the light absorption[3].

The multifolded region of the ciliary body is also named the pars placita and represents a third of the total surface of the ciliary body[3]. The two other thirds are named the pars plana as they form a relatively straight area[3] (see **Figure 1.2-B**). The ciliary body finishes at the ora serrata, the junction between the ciliary epithelia, the retinal pigmented epithelium and the retina (see **Figure 1.2-B**). The RPE covers most of the posterior chamber surface (see **Figure 1.1 – RPE.**). It supports on its front the retina, the neuronal layer in charge of the photonic-chemical conversion (see **Figure 1.1 – Ret.**). Generally, the

mammal retina is distinguished in five layers, described here from the most peripheral to the most internal: **1**. the photoreceptor layer; **2**. the outer nuclear layer; **3**. The outer plexiform layer; **4**. The inner nuclear layer; **5**. The inner plexiform layer[3, 4] (see **Figure 1.2-C**). Further elements are distinguished by specialists such as the ganglion cell layer followed by the nerve fiber layer on the top of the inner plexiform layer[13, 14]. The optic nerve results from the assembling of projections from the ganglion cell layer at the inner side of the disc of the optic nerve where they form the optic nerve[3] (see **Figure 1.1**). Nearby is the macular region, which is responsible of the central vision (see section **1.1.2.1**). Inside this specific region is the fovea, a small depression into the retina (see **Figure 1.1 – Fov.**). The rational is that most of retinal cells are placed on the side of it, except the photoreceptors. That results in an improved visual acuity.

To hold the retina in line with the RPE, the posterior chamber is filled by a transparent gel called the vitreous (see **Figure 1.1**). It is composed of 98% water, which explains its transparency, other molecules being collagen fibrils and hyaluronans giving it its jelly-based consistency. Finally, it contains a high content of ascorbate, which is believed to regulate the intraocular oxygen tension[15]. The high metabolic activity required to process these elements together is supported by the choroid, from the greek *khorion* meaning membrane. It is a highly vascularised envelope surrounding the RPE on its back and limited to the optic disc. It stops at the junction of the RPE with the ciliary body and also contains a certain amount of pigment.

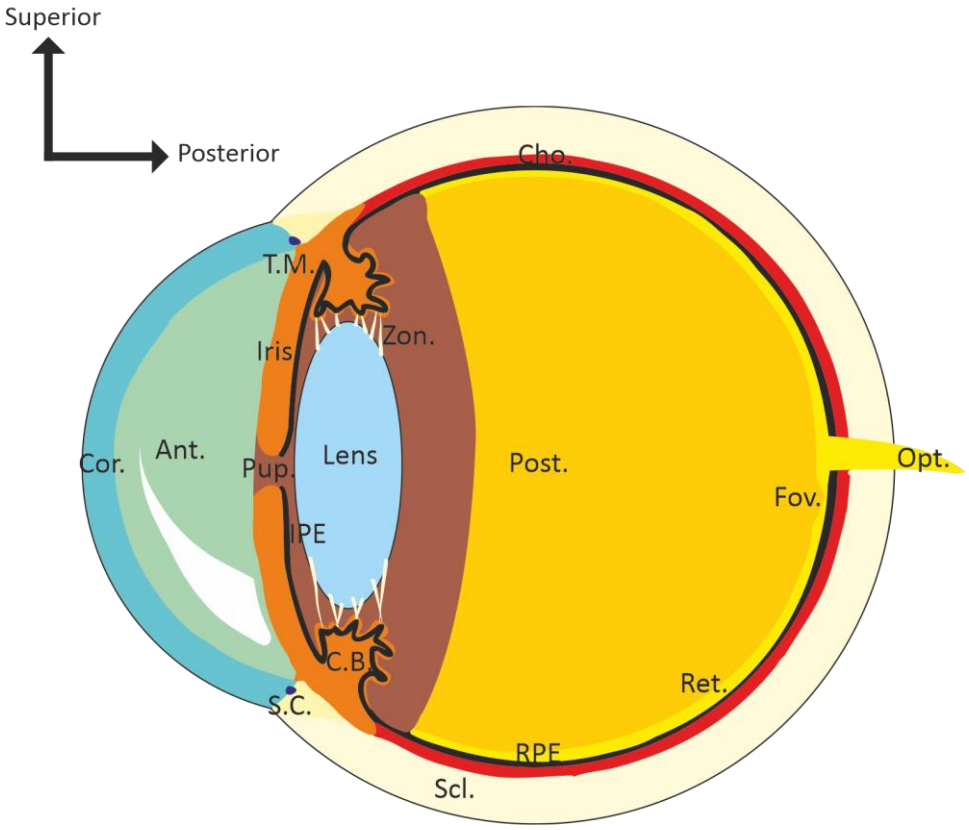

Figure 1.1: Representative sagittal plan of the mammalian eye. Arrows in the superior left angle indicate the orientations of the plan. Cor. = cornea; Ant. = anterior chamber; T.M. = trabecular meshwork; Pup. = pupil; S.C. = Schlemm's channel; C.B. = ciliary bodies; Scl. = sclera; Zon. = ciliary zonules; Post. = posterior chamber; Cho. = choroid; Ret. = retina; Fov. = fovea; Opt. = optic nerve.

A. Sagittal/transverse view of the mammalian peripheral iris & ciliary body

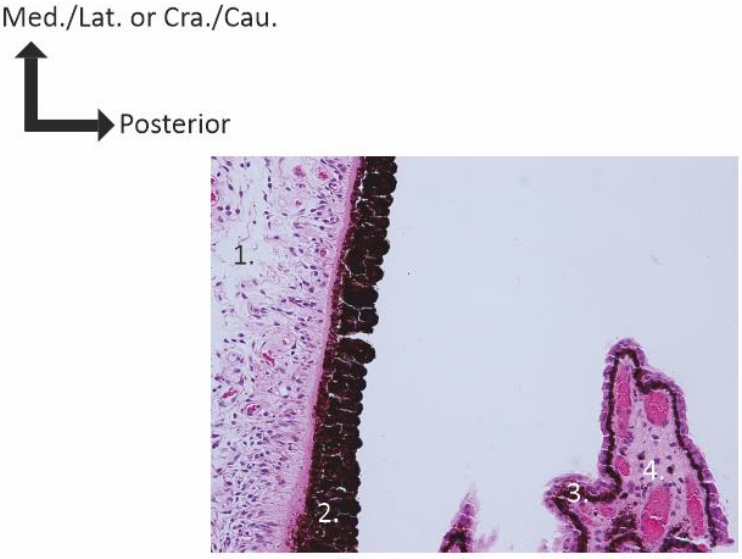

1. Iris
2. IPE
3. Ciliary body epithelia
4. Ciliary body stroma

B. Sagittal/transverse view of the mammalian ciliary body, pars placita, pars plana, retina & RPE

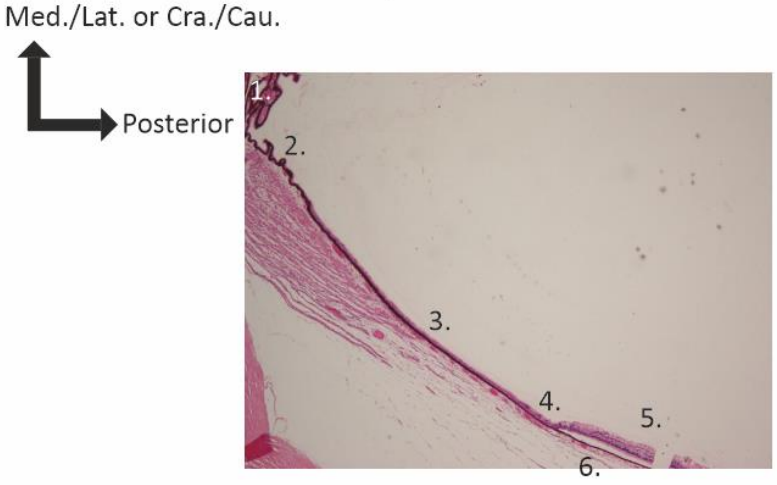

1. Ciliary body
2. Pars plicata
3. Pars plana
4. Ora serrata
5. Retina
6. RPE

C. Cross-section of the mammalian retina & RPE

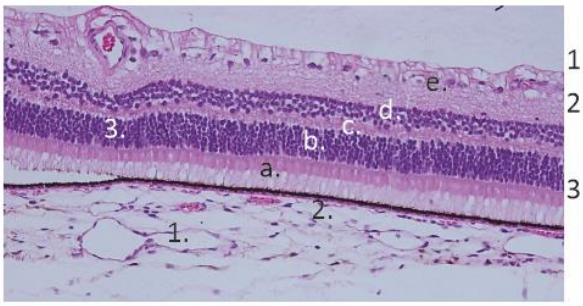

1. Sclera
2. RPE & choroid
3. Retina

a. Photoreceptor layer b. Outer nuclear layer c. Outer plexiform layer
d. Inner nuclear layer e. Inner plexiform layer

Figure 1.2: Image of the mammal pigmented epithelia from the IPE to the RPE. A. Sagittal or transverse view of the mammalian peripheral iris and ciliary body. **B.** Sagittal or transverse view of the mammalian cilicary body, pars placita, pars plana, retina and RPE. For both A. & B., Black arrows on the left indicate the picture orientation. As the pictures

were furnished without orientations, all potential directions are represented. Med. = medial; Lat. = lateral; Cra. = cranial; Cau. = caudal. Numbers on the picture are indications of tissues named on the right of the picture. **C.** Cross-section of the mammalian retina and RPE. Numbers indicate tissues named on the right of the picture. Letters indicate retinal layers named below the picture. All pictures were furnished without indications of magnifications or resolutions. Pictures were obtained from the Moran Core open-source data: https://morancore.utah.edu/section-04-ophthalmic-pathology/uvea; 2023-08).

1.1.2 The light path

1.1.2.1 From the cornea to the retina

The eye is a sensitive organ dedicated to inform the organism about its environment by converting photons into pictures (see **Figure *1.3*-A**). To note, the International Unit System has used the sensitivity of the human eye to define the Candela, the unit of the light intensity[16]. Photons are the basic units, particles of the light[17]. They have an energy but no mass, which explains their high speed, 299 792 458 m/s in an environment free of any bodies[18].

The way the eye processes photons is the same as a camera. First in contact, the cornea catches and converges the photons toward the pupil[4] (see **Figure *1.3* – L., 1. & 2.**). The pupil opening is then conditioned by the light intensity: mydriasis for a maximal opening at low light intensity; myosis for the opposite situation[3, 4]. In synchrony with the pupil, the lens size is adjusted to catch the photons which pass (see **Figure *1.3*– L. & 3.**). Then, it reverses and focuses them toward the macular region (see **Figure *1.3* – L. & 4.**) with a varied spread. With a low number of candela, the spread gets larger, while in the opposite situation, it targets mostly the fovea (see **Figure *1.3***).

In accordance with this, the retina has an organised distribution of its photoreceptors[3, 4]. Two types of photoreceptors exist in mammals: the cones processing photons in an intense light exposure, mostly during the day, and the rods doing the same for low light exposure[4]. The firsts localise mainly in the macular region and the fovea. They are the main effectors of the central vision. The seconds compose the rest of the retina and work for the peripheral vision mainly[4]. This is why the visual acuity is better in the day than at night[4]. Stimuli generated by the photoreceptors are then analysed and processed through the retina to be finally transmitted to the optic nerve[3, 4] (**see Figure *1.3* – L. & 5.**).

Protons which passed through the cornea but were not aligned enough with the pupil are blocked by the iris and can not pass into the posterior chamber (see **Figure *1.3* – l. & 6.**)

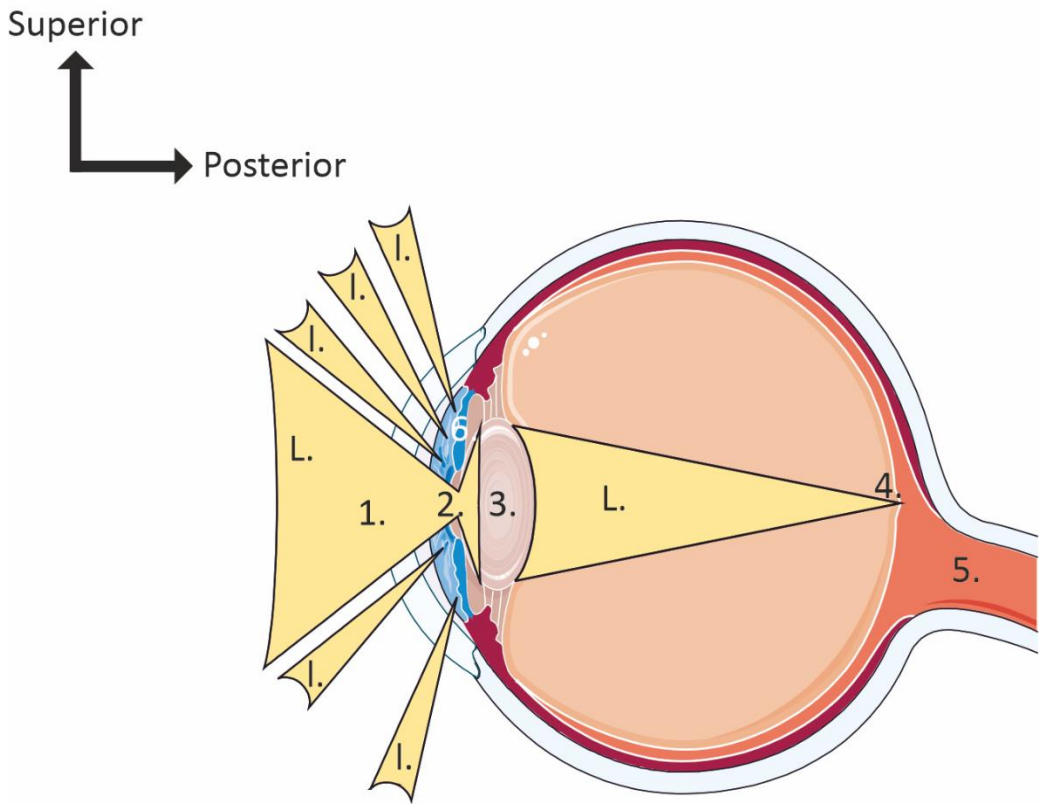

Figure 1.3: Representative plan of the light path from the cornea to the fovea of the retina in an intense light stimulation. Arrows in the superior left angle indicate the orientations of the plan. L. = Light passing through : the cornea (= 1), then the pupil (= 2) prior to be redirected by the lens (= 3) toward the fovea (= 4). The optic nerve (= 5) then leaves the eye. l = light passing through the cornea but being blocked by the iris (= 6). The representation is based on original draws from the open source Smart Servier Medical art (cf. https://smart.servier.com; 2023-08).

1.1.2.2 Optic paths toward the occipital lobes

The optic nerve, also called nerve II, results from the prolongation of the fibres from the most internal retinal layer[3, 4] (see **Figure 1.2-C**). Starting from the back of the eye, it passes through the orbit in the middle of the rectii, the extraocular muscles involved in the eye movements (see **Figure 1.4-A – Med., Inf. & Sup.**). It then passes through the common tendinous ring, also named the annulus of Zinn[3, 4] (see **Figure 1.4-A – Com.**), to finally penetrate into the brain by the optic canal, a hole in the lesser wing of the sphenoid bone[3, 4] (see **Figure 1.4-B – *Sph.* & 1.**).

Once on the posterior side of the sphenoid, into the pituitary fossa, the two optic nerves fuse in a structure called the optic chiasm[3, 4] (see **Figure 1.4-C – 3.**). There, human retinal fibres redistribute depending their region of origin in the eye: the medial retinal projections cross each other and continue into the opposite optic tracts while the external retinal projections do not. Other said, all retinal projections from the left side of both eyes localise on the left cerebral hemisphere on the posterior side of the optic chiasm while their right counterparts mimick them on the right cerebral hemisphere (see **Figure 1.4-C**). This is called the decussation[4].

The main body of fibres connect with the optic radiations at the thalamus lateral geniculated nuclei[4] (see **Figure 1.4-C – 4.**). Those fibres relay the signals toward the occipital lobes (see **Figure 1.4-C – 5.**), which process and transform them into the sight.

Between the optic chiasm and the thalamus lateral geniculated nuclei (see **Figure 1.4-C**), some projections diverge inward and connect to the pretectal nuclei and the superior colliculi[4]. Those centres are respectively responsible for the eye movements in the ocular cavity and the photomotor reflex of the pupil to light stimuli[4]. There, among other molecules, specifically localises the melanopsin, also named the circadian pigment, responsible of the circadian rhythm[4].

A. Sagittal view of the human right eye and some of its extraocular muscles

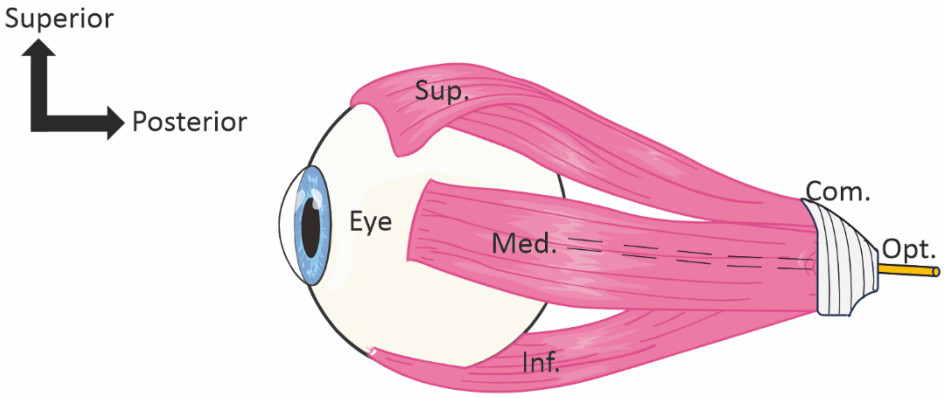

B. Frontal view of the human right orbit

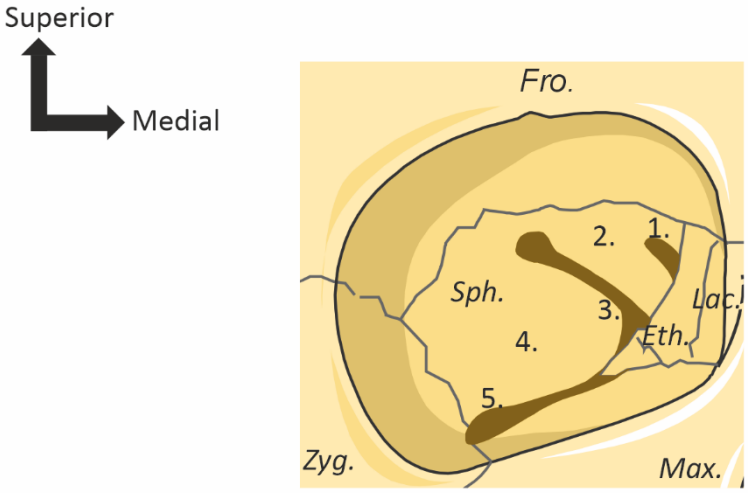

C. Inferior view of the human optic verve in the brain

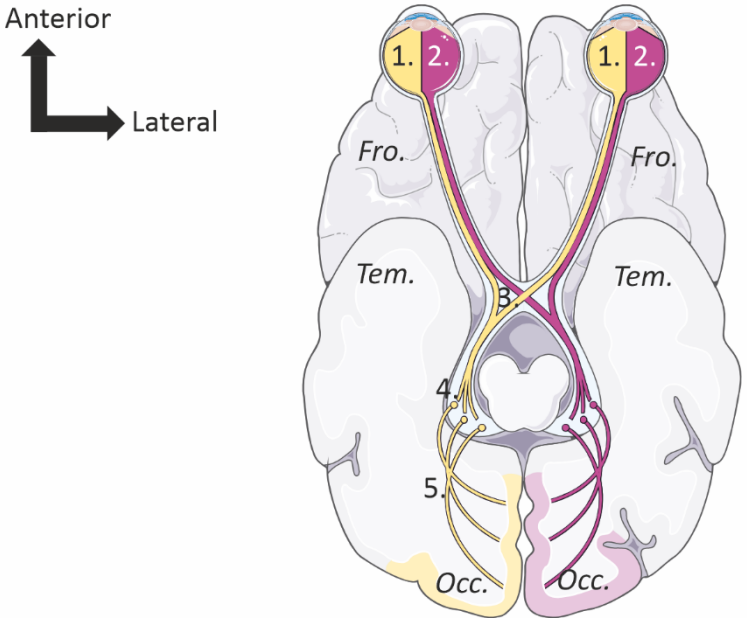

Figure 1.4: Representation of the human optic path from the eye to the brain occipital cortex. Arrows in the superior left angle indicate the orientations of the plans. **A.** Medial view of the human right eye with its recti and the optic nerve. Black lines represent the optic nerve path on the back of the rectus medialis muscle (= Med.). Other muscles represented include the rectus superior (= Sup.) and the rectus inferior (= Inf.). All take their origin from the common tendinous ring (= Com.). The optic nerve (= Opt.) emerges from the common tendinous ring on its posterior side. **B.** Frontal view of the human right orbit. Bone's names are represented in italic: Fro. = frontal bone; Zyg. = zygomatic bone; Max. = maxillary; Eth. = ethmoid bone; Lac. = lachrymal bone; Sph. = sphenoid bone. Elements associated with the sphenoid bone are labelled by numbers: 1. the optic canal; 2. the lesser wing of the sphenoid; 3. the superior orbital fissure; 4. the greater wing of the sphenoid; 5. the inferior orbital fissure. **C.** Inferior view of the human brain and optic paths from the eyes to the occipital lobes. Brain lobe's names are represented in italic: Fro. = frontal lob; Tem. = temporal lob; Occ. = occipital lob. Numbers indicate the optic paths from the eyes to the occipital lobes: 1. left optic fibers prior and after the decussation, they are colored in yellow; 2. Right optic fibers prior and after the decussation, they are colored in purple; 3. the optic chiasm where the decussation happens; 4. The thalamus lateral geniculate nuclei; 5. the optic radiations with those originating from the left optic fibers colored in yellow and those originating from the right optic fibers colored in purple. The representations are based on original draws from the open source Smart Servier Medical art (cf. https://smart.servier.com; 2023-08).

1.1.2.3 Differences between the human and the porcine eye

Despite having direct access to human organs provided by the Liverpool Research Eye Biobank, their cost was consequent. Thus, the porcine eye was used instead, thanks to an easy purchase from the Tam House Family farm abattoir in the Liverpool region. That had two very convenient advantages:

- That allowed to get fresh eyes on a weekly basis at low cost
- Results from porcine-based investigations could be transposable to the human physiology due to the close similarity between the two respective eyes.

Indeed, both human and porcine eyes are structured in a very close manner[19, 20]. The porcine eye is divided into the anterior and the posterior chambers, each of them being delimited by the iris. The anterior chamber is contained by the cornea at its forefront, the iris and the pupil on its backward and the trabecular meshwork at the corneal – scleral junction. Passed the pupil comes the lens, held by the ciliary zonules anchored into the ciliary bodies. The posterior chamber is covered by continuous pigmented epithelia from the iris to the disc of the optic nerve. Retina covers most of the surface of the posterior chamber. As in humans, it is hold in place by a transparent jelly vitreous. On the other side of the epithelia lies the choroid, which ensures the nutrient supply. The integrity of the

porcine system is guaranteed by the conjunctival sclera, nearly equivalent to the human one in thickness[14]. Still, despite being structurally quite close, porcine and human eyes also demonstrate several differences about their respective dimensions (see **Table 1-1**).

Table 1-1: Structural dimensions in porcine and human eyes

Features	Porcine	Human	References
anteroposterior axis (mm)	23.9 ±0.08	24.4 ± 0.93	[22, 23]
Globe weight (g)	/	6.7 – 7.5	[20]
Globe volume (ml)	6.5	6.5	[20]
Central pachymetry* (µm)	1,009	523	[20]
Peripheral pachymetry (µm)	1,340	564	[24]
Anterior chamber depth (mm)	1.77	3.11	[24]
Anterior chamber angle (°)	28.83 ±4.16	38.1 ±12.3	[24, 25]
Sclera thickness (mm):			[21, 26]
at the corneoscleral ring	0.31 – 0.91	0.53	
at the ora serata	0.56 – 0.86	0.39	
at the disc of the optic nerve	0.78 - 1.00	0.9 – 1.00	
Sclera surface (cm^2)	7.78 – 11.92	14.5 – 18.1	[21]
Average iris thickness (µm)	550.0	310.6	[27, 28]
Pupil size at mydriasis (mm)	/	2.9 – 3.1	[29]
Lens diameter (mm)	/	8.9 – 9.5	[30]

**Measure of the corneal thickness*.

1.2 The IPE, functions, development & potential

1.2.1 Anatomy and functions of the IPE in vivo

Located on the back of the iris (see **Figure 1.1**, **Figure 1.2** & **Figure 1.6**), the IPE is a bilayered epithelium starting from the iris roots, in continuity with the ciliary body pigmented epithelium and finishing at the pupillary ruff. It has three known functions in mammals: its pigments protect the posterior chamber from overexposure to light from the anterior chamber; its muscular fibres form the dilator muscle dedicated to open the pupil; its intercellular junctions form an impermeable barrier between the iris stromal compartment and the posterior chamber[31, 32].

Early microscopic studies observed that the two layers are polarised as follows: the anterior myoepithelial layer has its basal side in touch with the iris stroma, while the posterior one has its own basal side facing the posterior chamber[32] (see **Figure 1.5**). This results with the two layers having their apical side facing each other. The anterior layer is itself highly polarised due to its muscular activities, with all melanosomes and nuclei being in the apical side of the cell, while the muscle fibres and the majority of the mitochondrial content constitute the majority of the basal side[32]. To prevent the simultaneous activation of the sphincter muscle in the iris stroma and the dilator muscle in the anterior IPE layer, the muscles are innervated by the sympathetic and the parasympathetic nervous system respectively[3, 4]. To optimise the contraction of the dilator, muscle fibres are organised radially starting from the IPE roots and ending near the pupil ruff[3, 32]. Consequently, dilator contractions ensure a homogeneous pupil dilatation.

The IPE posterior layer (see **Figure 1.5**) is organised in a striped manner paralleling the pupil to absorb the mechanical forces generated during the dilator's contraction[32]. The posterior layer by itself varies in shape depending the iris state passing from a "flat-like" form for pupil contraction to a columnar one during pupil dilatation. In consequence, nuclei are closer from the basal side. Packed melanosomes type III and IV are taller in size than melanosomes from the iris stromal melanocytes[32]. The posterior cells also contain a mitochondrial content lower than the anterior layer ones. The endoplasmic reticulum and the Golgi apparatus follow the same trend[32]. Finally, the posterior basal surface shows a significant number of microvilli, covered by a continuous thin basal lamina[32].

Past investigations in the monkey demonstrated that the IPE presents a certain number of junctions over its length and its width[33]. At that time, such structural organisation was generally believed to play for the blood-ocular barrier[34]. Tight junctions are the main junctions involved in the barrier function as they connect the plasma membranes of adjacent cells. For these reasons, they were mostly found in the basolateral side of cells. Desmosomes linking cytoskeletons of adjacent cells were found on both lateral and apical sides. Finally, gap junctions allowing cytoplasmic exchanges between adjacent cells were found from the basolateral sides to the apical ones.

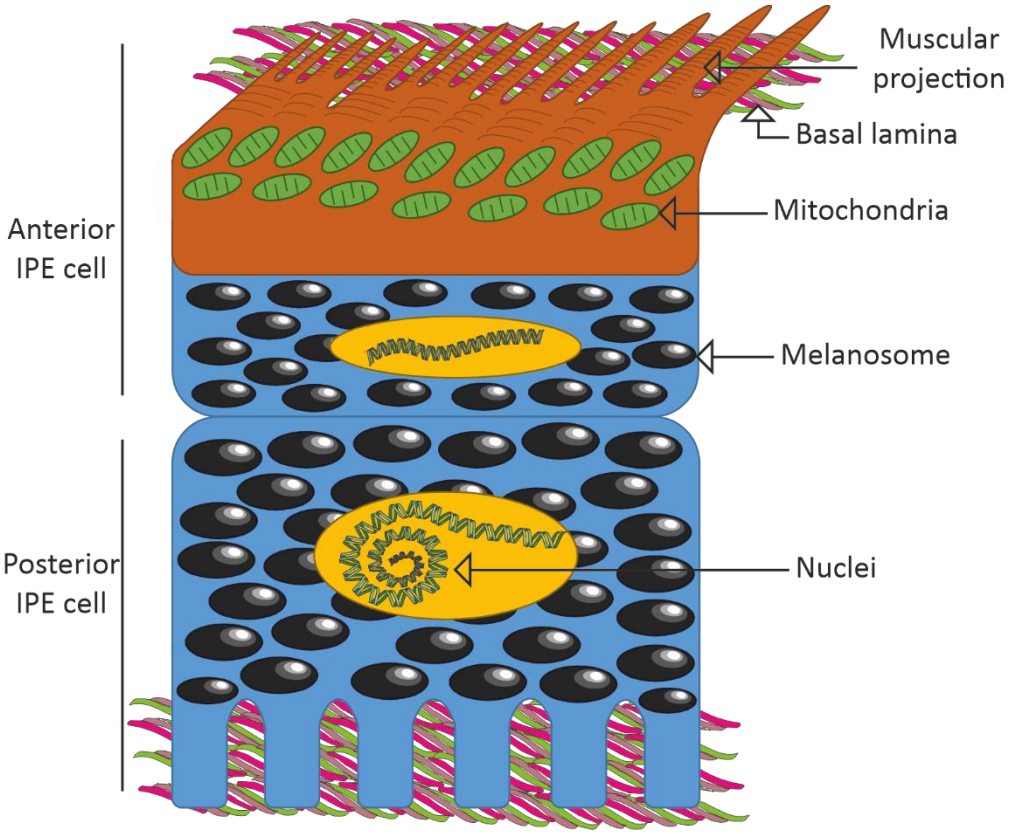

Figure 1.5: Representation of two mammalian IPE cells in vivo in the in-between iris area. The is a bilayer epithelium with an anterior one being dedicated for most of it to smooth muscles activities. The involvement of cells from the anterior layer of the IPE constitutes the dilator muscle. The rest of the IPE anterior layer contains melanosomes and other cell structures such as the nucleus. The IPE posterior layer is dedicated to the pigmentation of the epithelium. Both anterior and posterior layers have their apex facing each other, making their basal surface turned externally where stands their basal lamina. Anterior and posterior layers are indicated on the figure left. Cell structures are indicated by the arrows and labelled on the right.

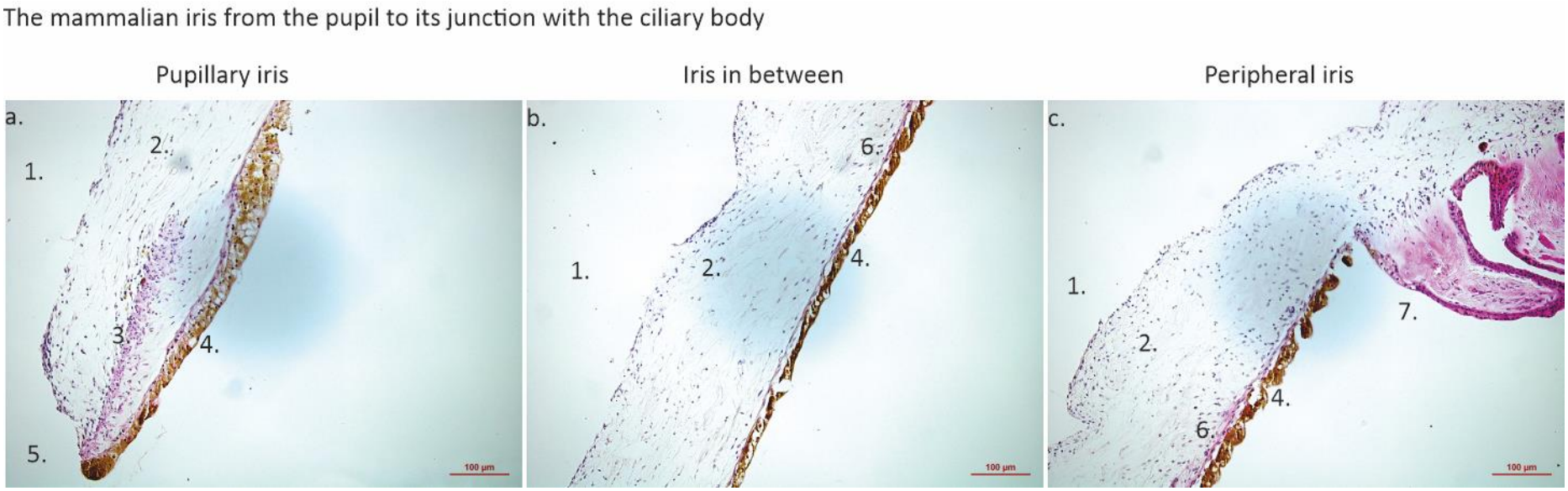

Figure 1.6: Representative H&E-processed sections of the mammalian iris from the pupil on its junction with the ciliary body in its periphery. Tissues have been processed for H&E after having being depigmented as indicated in the conclusion of section 3.3.4.4, Chapter 3. **a.** The pupillary iris. **b.** The iris in-between the pupillary iris and the peripheral iris. **c.** The peripheral iris where it connects with the ciliary body. Numbers indicate tissue structures: 1. The anterior chamber at the front of the iris; 2. The iris stroma constitutes the main body of the iris; 3. The sphincter muscle circles the pupil; its spread is limited to this area: 4. The IPE entirely covers the iris stroma on its posterior side; 5. The pupil; 6. The dilator muscle is a thin smooth muscle between the IPE and the iris stroma spreading in a radial manner over most of the iris posterior side, with the exception of the area associated with the sphincter muscle: 7. The ciliary body. Scale bars = 100 µm.

1.2.2 IPE development

In line with the anatomy, the IPE, the RPE, the ciliary body epithelia and the retina share a common origin. This section is a summary of the development of these tissues.

1.2.2.1 The human neural development, starting at the gastrulation

During the third week of human development, the embryo takes on an ovoid shape and develops as a three-layered tissue, composed of the ectoderm, the mesoderm and the endoderm[3, 4, 35] (see **Figure 1.7-A 1., 2.** & **3.**).

At days 16 - 17, the ectoderm thickens around a medial line called the primitive streak going along a cranial-caudal axis[3, 35] (see **Figure 1.7-A 5.**). This is the result of local ectoblastic cell proliferation and migration of other ectoblastic cells toward this area. On the end of the primitive streak localises the primitive node, also called the Hensen node (see **Figure 1.7-A 4.**). Three ectoblastic cell-based movements have been distinguished so far: **1**. one passes through the primitive streak, the original ectoblastic cells move toward the endoderm and colonise it[35]; **2**. another one passes through the primitive node to give rise to the notochord[35] (see **Figure 1.7-B 7.**), which support the axial development[4]; **3**. the last one moves between the ectoderm and the endoderm to transform into the mesoderm.

Over human development, the mesoderm, from which emerges the somites (see **Figure 1.7-D 9.**) is in charge of the conjunctive tissues, such as the myo-skeletal system and the dermis[4]. The endoderm differentiates into the digestive system and participates in the development of the thyroid and parathyroid glands, and the thymus by providing them their epithelia[4]. Finally, the ectoderm gives rise to the epidermis and its appendices such as the hair, the nail and the tooth[4].

Under the influence of the mesoderm and paralleling the development of the notochord[35], at days 18 – 19, the neurectoderm differentiates from the ectoderm and forms the neural plate (see **Figure 1.7-B 6.**). This tissue is the origin of the central and peripheral nervous system[36]. Soon, the neural plate invaginates, forming the neural groove (see **Figure 1.7-C 8.**). The invagination continues to run with the closure of the neural groove in the cranial area, forming the neural tube (see **Figure 1.7-D 10.**). The neural tube cranial end, also called the anterior neuropore, closes at day 29, while its caudal counterpart does so at day 30[35]. The neuroepithelium transits from a prismatic

unistatified epithelium to a pluristratified one[35]. During the closure of the neural tube, some cells from the lateral sides of the tube migrate above it and form the neural crests[4, 35] (see **Figure 1.7-D 11.**). Finally, the ectoderm recovers the neural tube as soon the closure of the second is completed[35].

While the neural tube is forming and prior to the closure of the anterior neuropore, at day 25, the neuroectoderm forms three vesicles on the cranial-caudal axis: **1**. The prosencephalon; **2**. The mesencephalon; **3**. The rhombencephalon[4, 35] (see **Figure 1.8**). At the same time, the embryo inclines toward its developing digestive system.

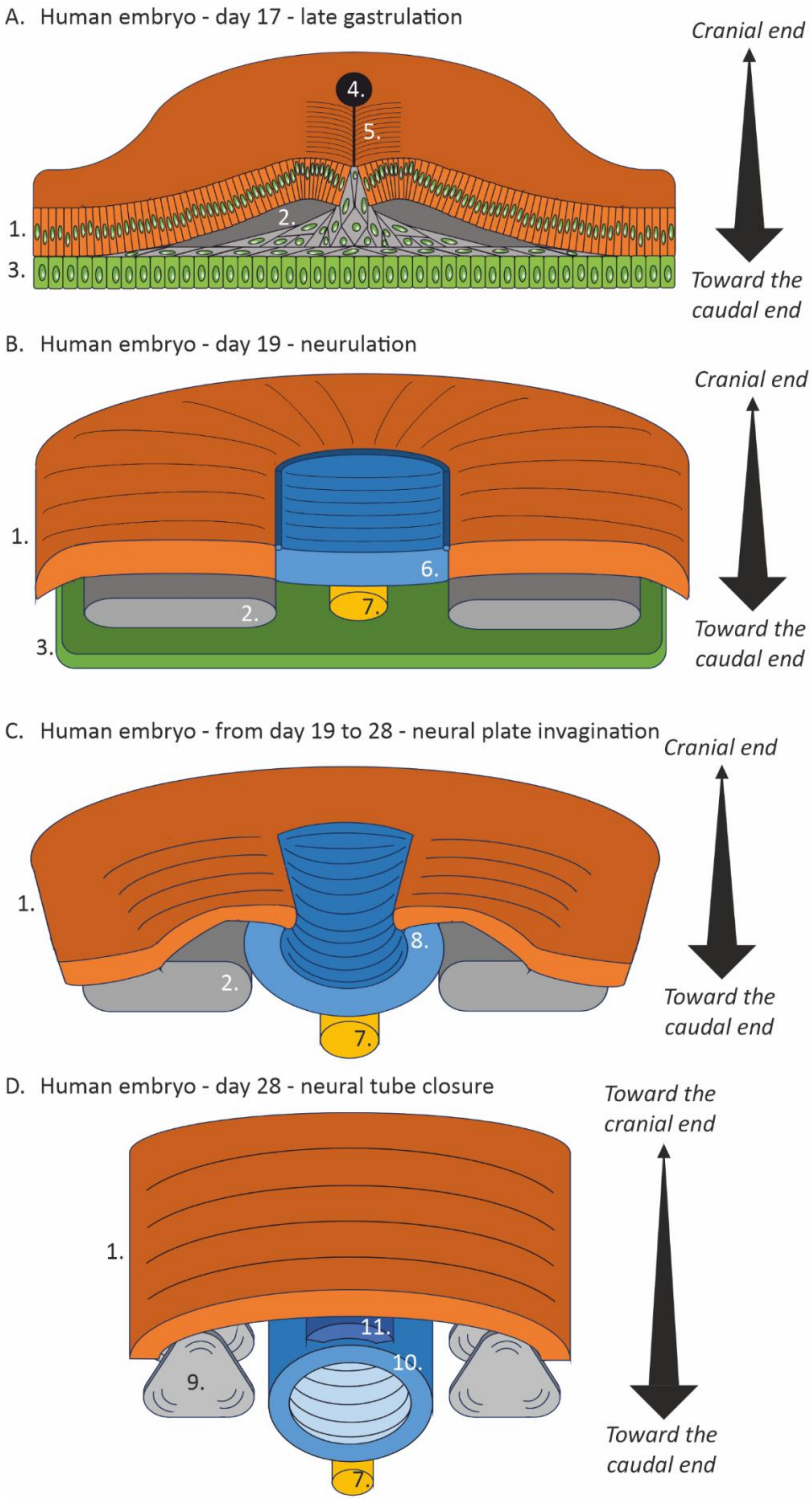

Figure 1.7: Human embryogenesis from day 16 to day 22. A. Human embryo at day 16, or late-stage gastrula. The three germ layers, the ectoderm (= 1.), the mesoderm (= 2.) and the endoderm (= 3.), are differentiated and expand. The primitive node (= 4.) is a depression localising on the cranial end and prolonged by the primitive streak (= 5.), giving to the embryo its bilateral symetry[4]. **B.** At day 18, the neural plate (= 6.) differentiates from the ectoderm, where stood the primitive streak, while the notochord (= 7.), the first axial support of the embryo[4], appears under the neural plate. **C.** At day 18, the invagination of the neural plate is visible, forming the neural groove (= 8.). **D.** At day 22, mesoderm-based somites (= 9.) have formed. The medial part of a human embryo neural

groove is closed and so, forms the neural tube (= 10.). This closure will progress toward both ends until total closure of the tube. Between the neural tube and the ectoderm have arised the neural crest (= 11.), from ectoderm origin. Their will give rise to several cell types, including the melanocytes. Black arrows on the right indicate the ends of the embryo.

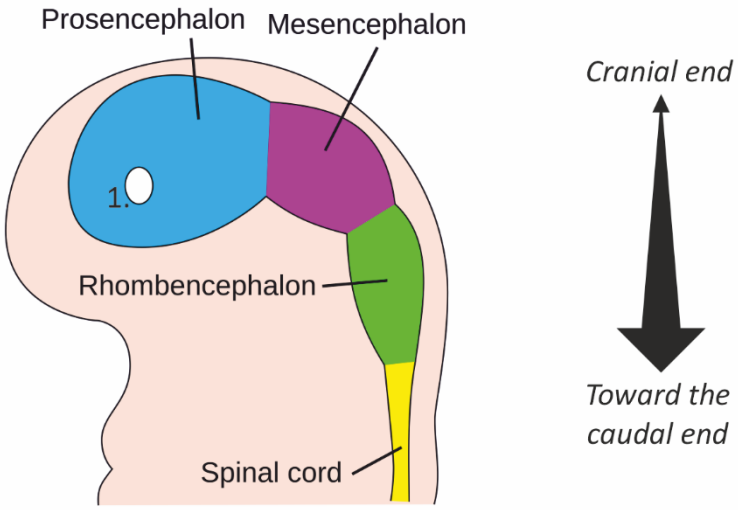

Figure 1.8: Representation of the three neural vesicles during the fourth week of the human development. Each neural vesicle is labelled. The optic vesicles (= 1.) starts to be appear at this stage. Black arrows on the right indicate the ends of the embryo. The representation is based on original draws from the open source Wikipedia Archivo (cf. https://es.m.wikipedia.org/wiki/Archivo:Four_week_embryo_brain.svg; 2023-08).

1.2.2.2 From the Prosencephalon arises the eye

At the human eye's genesis, two optic evaginations form laterally at day 19 from the prosencephalon[35]. At day 25, they transform into optic vesicles (see **Figure 1.8**) and are visible on the ectoderm by the optic grooves[35, 37] (see **Figure 1.9-A**). Progressively, they extend and transform into tubes, the optic stalks, connected to the prosencephalon[35] (see **Figure 1.9-A 5.**). From the optic stalks will arise later in development the optic nerves[3, 4] (see **Figure *1.1***). On their distal side, theses tubes transform into bilayered cups with the most distal layer, named the inner layer, spousing the ectoderm internal side. The interactions between these two tissues leads to their progressive invagination and thickening[37] (see **Figure 1.9-A 2.** & **4.**). In human development, the thickening of the lens placode is visible from day 28, while its invagination, called the lens pit, is visible at day 33[38].

Quickly, the ectodermal invaginations differentiate toward pre-lens phenotypes, vascularised by the temporary hyaloid vessels (see **Figure 1.9-B 9.**), while the optic cup continues to enlarge[3, 31, 39] (see **Figure 1.9-B 7.** & **8.**). The hyaloid vessels will atrophy themselves later around the 6th week of gestation. At the same time, the lens-facing ectoderm transforms slowly into the corneal epithelium (see **Figure 1.9-C 10.**). The human lens completes its separation from the ectoderm at day 35[38], becoming the lens vesicle, (see **Figure 1.9-C 6.**). The lens vesicle completes its development later at day 56[37], making it one of the first operational organ of the human organism[4].

In the same time, the inner layer increases in size and thickness, progressively giving a pseudo-stratified form to the retina[40] (see **Figure 1.9-B 7.** & **-C 7.**). The first markers of retinal specification appear in the central inner layer around day 47[38]. Distribution of these markers extends progressively toward the peripheral cells as they start to differentiate while continuing to proliferate[38, 41, 42]. The retinal specification will continue over the development, rods and cones receptors being observables around the 15th week of gestation and after birth[38].

Retinal spread is mimicked by the outer monolayer (see **Figure 1.9-B 8.** & **-C 8.**), which proliferates in a parallel manner to the early retina while transforming into the RPE[38]. The pigmentation of the RPE starts to be visible around the 6th week of gestation[38]. Interactions between the RPE and the retina tissues plus their common origin supports transdifferentiation between them prior to the appearance of factors specifying their phenotypes[43, 44, 45]. The early lens and the periocular mesenchyme play a part in this process as they participate to respectively differentiate the retina and the RPE by using gradient factors[38]. Increased pigmentation develops toward the ventral side of the eye while epithelial cells proliferate in the optic cup periphery[46] (see **Figure 1.10**).

A. Human optic cup at day 33

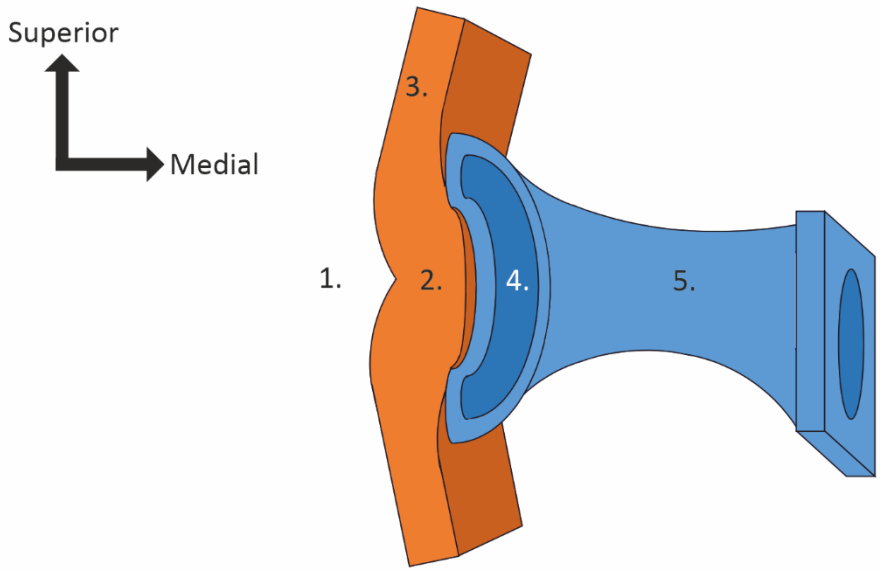

B. Human optic cup from day 33 to 35

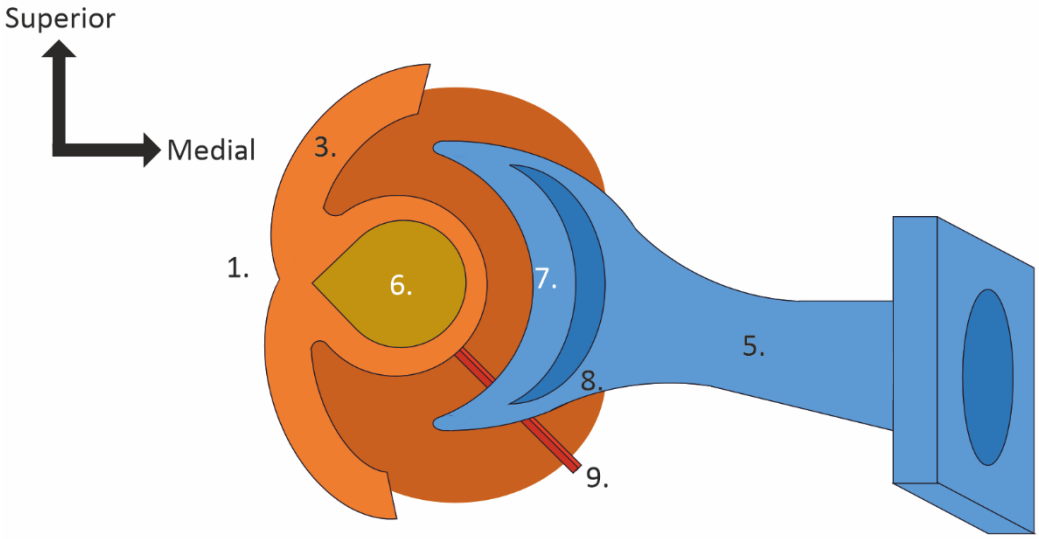

C. Human optic cup after day 35

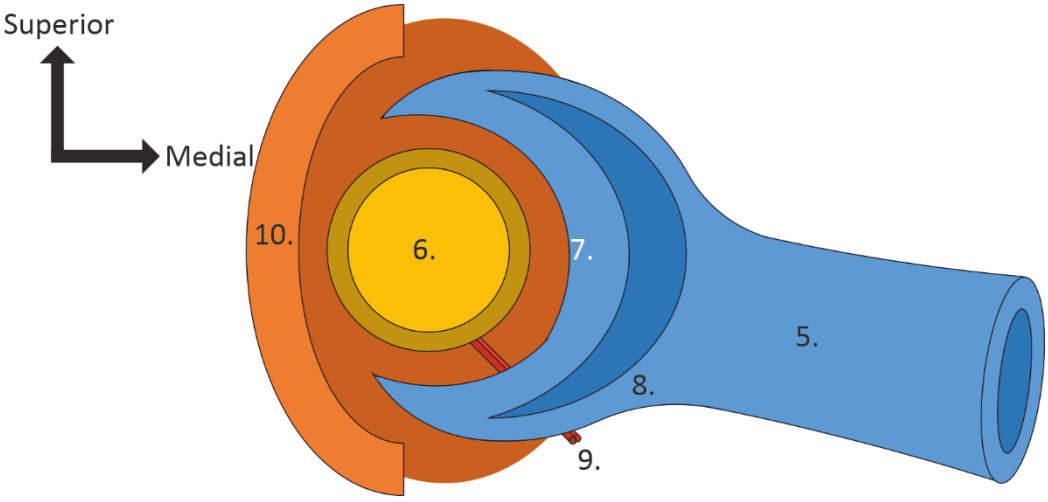

Figure 1.9: Human optic cup development: the lens development. Arrows in the superior left angles indicate the orientations of the plans. **A.** From the outside to the inside, the human optic cup at day 33 is firstly characterised by the lens pits (= 1.) the invagination of the lens placode (= 2.), which is a derivate of the ectoderm (= 3.). The optic cup (= 4.) follows this invagination while it develops a tube, the optic stalk (= 5) linking it to the prosencephalon. **B.** From day 33 to 35, the human lens (= 6.) continues its invagination, helped in its development by the transient hyaloid vessels (= 9.). At the same time, the optic cup has separated into two distinct layers, the inner one (= 7.) being the presumptive retina, and the outer one (= 8.) being the presumptive RPE. Transient lens invagination. **C.** Passed day 35, the lens vesicle has completed its separation from the ectoderm, which starts to differentiate into the corneal epithelium (= 10.). Tissues in place here will continue to grow until the fourth month of gestation, with some will mature well after birth[4, 38].

At the optic cup periphery, the human RPE and retina connect at the optic cup margin forming the ciliary margin zone around the 5th week of gestation[3, 38] (see **Figure 1.10-A 1.**). It takes the form of a distal tip-like ring and gives rise to new RPE cells, neurons and glial cells[181]. The arise of the CMZ is quickly followed by local pigment synthesis with the first granules being visible at the 5th week of gestation[47]. At the 8th week of gestation, the human ora serrata, pars plana and pars plicata (see **Figure 1.2-C**) appear, separating the early ciliary body and the retina[47]. The non-pigmentation of the inner ciliary body epithelial layer would come from its derivation from peripheral retinal cells while its pigmented counterpart arises from the RPE[46].

Oppositely on the lens anterior side, migrating mesenchymal cells are visible at the 6th week of gestation, where they regroup to form loose cell layers feeling the space between the early corneal epithelium and the lens[48]. Most of these cells will regroup into a single layer at the origin of the corneal endothelium. Shortly after, a new group of mesenchymal cells migrates between the corneal endothelium and the lens[3, 48]. They form the stroma of the CB, then the iris, along the proliferation and migration of the pigmented epithelial cells, which arise from the CMZ[3, 47, 48].

Finally, the IPE forms from the distal part of the CMZ, on the anterior side of the marginal sinus of the CMZ[47] (see **Figure 1.10-D 11.**). In humans, early IPE presence has been observed at the 13th week of gestation[47]. In the iris stroma, the sphincter muscle starts to express muscle specific proteins from the 18th week of gestation on[49]. In the IPE anterior layer, the dilator muscle starts to specifically express α-smooth actin from the 28th week on[49]. The iris stroma by itself completely recovers the lens anterior side on the contrary of IPE cells, which did not migrate in the presumptive pupil region[3]. At this point, this structure is called the pupillary membrane[3] (see **Figure 1.10-D 12.**). It will remain until the

fifth month of gestation[3]. Passed that point, vascularisation stops and local blood vessels atrophy[3]. This causes tissue degeneration and cell migration out of the pupillary membrane, from which the pupil enlarges until it gets close to the IPE[3].

A. Human optic cup at day 33

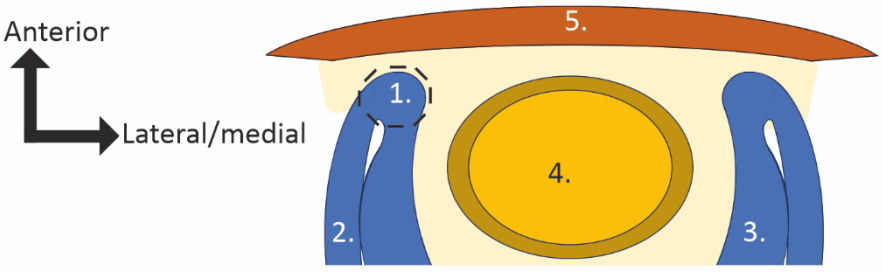

B. Human optic cup at the 8th week

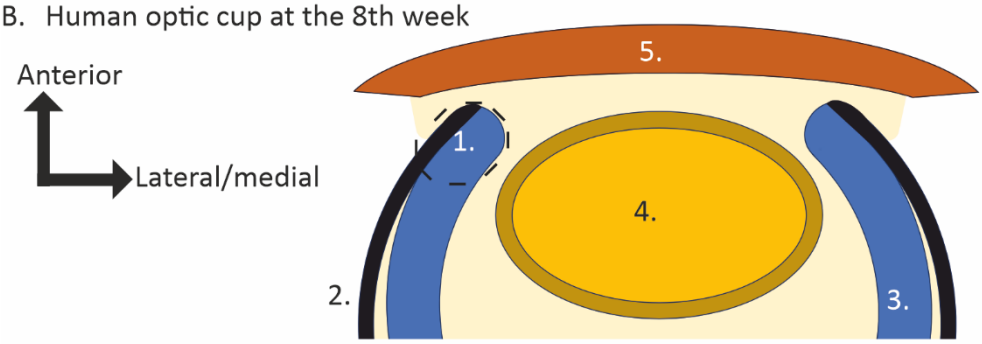

C. Human optic cup at the 12th week

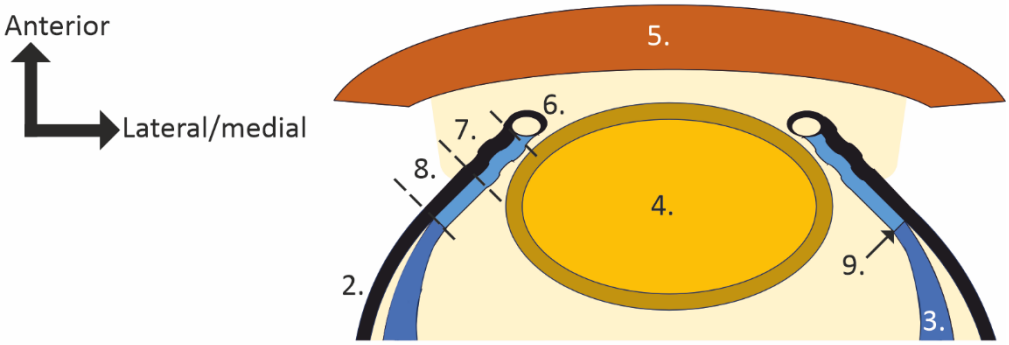

D. Human optic cup at the 13th week

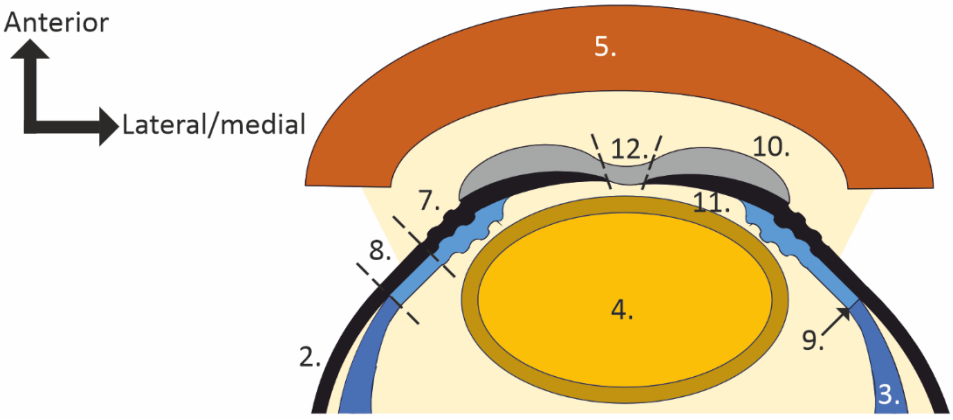

Figure 1.10: Representation of the human ciliary margin zone and its evolution from day 33 to the 13th week of development. Arrows in the superior left angles indicate the orientations of the plans. **A.** At day 33, the CMZ (= 1.) is the junction of the outer layer or presumptive RPE (= 2.) and the inner layer or presumptive retina (= 3.). They surround the lens (= 4.), recently detached from the presumptive cornea (= 5.). **B.** Later at the 8th week of gestation, both the RPE (= 2.) and the retina (= 3.) are differentiating and can be distinguished from each other[47, 50] but remain connected together at the CMZ (= 1.). **C.** At the 12th week of gestation, cell proliferation and tissue expansion have led to the development of the ciliary body which can be distinguished on its distal tip with the marginal sinus[47] (= 6.) covered by a thin pigmented portion of pigmented cells. Posterior to the marginal sinus are the Pars Plicata (= 7.), then the Pars plana (= 8.) with their pigmented and non-pigmented layers in direct continuity with the RPE (= 2.) and the retina (= 3.) respectively. As in adulthood, the Ora serrata (= 9.) connects the Pars plana and the retina. **D.** During the 13th week, a migration of extraocular mesenchymal cells set the basis of the iris stroma (= 10.) mimicking the evolution of the IPE cells (= 11.) moving close of and on the anterior side of the lens (= 4.). The pupillary membrane (= 12.) in the center of the iris stroma will remains free of epithelial cells until the fifth month where it starts to regress due to blood vessels atrophying. This will give rise to the pupil.

1.3 Age-related Macular Degeneration

1.3.1 Physiopathology

1.3.1.1 RPE and retina

To catch billions of photons and convert them into chemical signals is an intense and specific activity called phototransduction[4] and involve the RPE and the photoreceptors (see **Figure 1.11-A.**). The photoreceptors can be distinguished into the cones for the intense light and the rods for the low one[4]. The first ones can be even further distinguished into three subpopulations, each one having its own pigment catching a part of the visual spectrum. In the human eye, blue cones catch wavelengths at 420 nm, green cones run at 530 nm and red cones at 560 nm[3, 4]. The various colours observed over the visible spectrum result from the stimuli of different proportions of these subpopulations[4]. The rods on their side catches light at 500 nm as they contain only one pigment. The result of subsequent processing is a nuance of blue, perceived first in grey in the visual cortex[3, 4].

To run the phototransduction, photoreceptors require opsin, the protein responsible of the reaction and specific of wavelengths mentioned before, and an 11-*cis*-retinal, the photosensitive metabolite[4]. Both assemble and once the photon gets in touch with the

11-*cis*-retinal, the global structure changes, 11-*cis*-retinal is released as an all-*trans*-retinal metabolite[4]. As there is one 11-*cis*-retinal metabolite per phototransduction, thousands of them are required per day for a single photoreceptor[4]. Lacking the *cis*-*trans*-isomerase, photoreceptors send the all-*trans*-retinal to their neighbouring RPE counterpart, which runs their reconversion toward 11-*cis*-retinal. By doing so, RPE cells play a key step in the phototransduction[51].

A photoreceptor is organised in five distinct compartments described here from the retina to the RPE: **1**. the synaptic junction with the upper retinal layer; **2**. the internal fiber; **3**. the nucleus and surrounding body; **4**. the internal segment dedicated to energy production; **5**. the external segment where phototransduction occurs[4]. There, opsin and metabolites assemble into segments having a disk-like shape (see **Figure 1.11-A**). Ready-to-use segments are in the upper part of the compartment, while those used are close to the RPE. The RPE progressively detaches, degrades and phagocytoses the used segments. It is this RPE function that allows photoreceptors to work without mechanical disturbances[4, 51]. Each day, the RPE phagocytoses 10% of the photoreceptor outer segment (POS)[52]. With an average POS volume of 24 µm, around 100 million of photoreceptors and 5 million of RPE cells for one human adult eye, that represent 48 µm of POS to phagocytose per RPE cells on daily basis[4].

To ensure the retinal metabolism, the RPE developed a robust system of transport sat on highly polarised cytoplasm and plasma membrane[3, 4]. It is completed with an efficient paracellular resistance (parallel to the epithelial layer) maintaining the separation between the subretinal space and the choroid. The sum of these system allows RPE cells to transport nutrients, metabolites and electrolytes toward the retina, to evacuate the liquid in excess in the subretinal space and to maintain an appropriate pH over their cytoplasms and in the subretinal space[51].

To maintain this thin system over life, the RPE devolves a part of its energy to the secretion of various factors toward the retina and the choroid[51]. Among the main ones are: **1**. the pigmented epithelium-derived factor (PEDF) protecting retinal cells from apoptosis and stabilising the choroidal endothelium; **2**. the vascular endothelium growth factor, which essentially prevents endothelial cells to run apoptosis; **3**. the tissue-inhibitor of matrix metalloprotease maintaining an optimal Bruch's membrane organisation; **4**. the basic fibroblast growth factor, favouring retinal survival in case of injuries or light-induced damage; **5**. immunosuppressive cytokines to prevent immune cells to penetrate the eye[51].

In summary, the activity deployed by retinal and RPE cells is tremendous and the retina can not run itself. In absence of RPE cells, photoreceptors degenerate in only a few days and vision stops shortly after[53].

1.3.1.2 AMD in its wet and dry forms

AMD refers to the degeneration of photoreceptors in the macular area. This region being in charge of the central vision, symptoms are visible by the patient in a manner much more appreciable that in the rest of the retina[54, 55]. As the disease progresses, visual disturbances appear with straight lines looking curved in the central vision. Then, some holes in the vision rise and extend where the AMD progress. Two clinical forms exist: the wet/exudative form and the dry/geographic atrophy one.

The wet/exudative AMD:

The wet/exudative form is characterised by the vascularisation of the subretinal space of the posterior chamber. In a physiological situation, endothelia undergo a low proliferation to maintain their homeostasis and efficient blood supply. This is balanced by the secretion of pro-angiogenic factors by the RPE, and the secretion of anti-angiogenic ones, such as the PEDF[56]. In the case of exudative AMD, such balance is disrupted with an emphasis on the pro-angiogenic factors[57]. The generated vessels and increased blood flux favour micro-haemorrhages, which subsequently disrupt the homeostasis over the Bruch's membrane and in the subretinal space. In absence of treatments, oedemas form, the retina detaches from the RPE, which suffers fibrosis while photoreceptors degenerate[58]. If treated, this situation can be reversed to a certain degree that depends about the damages the RPE and the retina experienced[58].

The dry AMD/geographic atrophy:

On the contrary, the dry/geographic atrophy form, the one of interest in this PhD project, does not involve blood vessels but the delamination of the Bruch's membrane (see **Figure 1.11-B.**). Physiologically, this highly organised basal lamina polarises the RPE and filters blood exchanges between the RPE and the choroid[59]. Over development of the dry AMD/geographic atrophy, the Bruch membrane is progressively disbalanced by the growth and spread of drusens within it[60] (see **Figure 1.11-C.**). These elements are aggregates of lipids, proteins and metabolic wastes[61] originating from: 1. the POS RPE-

based phagocytosis; **2**. the blood supply and immune system; **3**. The choroid; **4**. the Bruch membrane itself[62]. To exemplify this diversity, Bergen *et al.* found in the literature at least 89 proteins in human drusens. Further, their progressive oxidation could solidify them as their proteolytic cleavage sites would be masked, so inactivated, by the ROS generated from the POS supramolecular elements[63]. To note, oxidation is not limited to protein-based proteolytic sites as ROS-based oxidation of lipids, also called lipoxidation[64], and generation of advanced glycation end-products, the oxidation of protein amine functions[65], have been observed in AMD[63].

The slow delamination of the Bruch membrane depolarises progressively the RPE, putting more stress on the thin organisation of its cytoskeleton[66] and its intracellular work. Over pathophysiological development, the delayed POS phagocytosis leads to the accumulation of lipofuscin granules in this region. Also named the "age pigment", it is mostly composed of lipids and proteins of phagocosomal, lysosomal and POS origin[56, 61]. Its slow accumulation in the Bruch membrane combines with an increased sensitivity to UVA light and high level of oxygen in the eye[67], and this combination results in a micro but chronic inflammation[56]. Ultimately, as drusens increase in number and size, they increasingly disrupt the exchanges between the RPE and the choroid[56].

Another major factor in geographic atrophy-based AMD is the single genetic polymorphism in an allele of the factor H, a component of the complement system[68]. Physiologically, the complement is an immune protein cascade involved in dead cell and waste cleaning, and pathogens removal[60]. In this process, factor H works to inhibit the activation of C3b and the subsequent alternative pathway of the complement[69]. At the physiological level in the eye, factor H has been observed from the baso-lateral side of RPE cells to the choroid[68] with other proteins from the complement system[60]. In 2005, Klein *et al*. identified a single genetic polymorphism in the sequence changing the tyrosine-histidine change at amino acid 402[68]. This change would be responsible of a lower affinity of the factor H for heparan sulfate-binding domains, decreasing its ability to bind to cell surface glycoaminoglycans[70]. This would ultimately result in a lower content of factor H in the Bruch membrane, favouring the risk of activation of alternative complement pathway, then the apparition of micro-inflammation in this region[60, 70]. To note, factor H plasma level is lowered in smokers, increasing the susceptibility of tissue to complement alternative pathway activation[69].

The deregulation of homeostasis from the choroid to the subretinal space, the growth of drusens amplified by metabolic disorders, the disorganisation of the Bruch membrane, combined with other risk factors (see **Table 1-2**) lead to the chronic degeneration of the retina and the atrophy of the RPE, resulting over time in vision loss[71].

A. RPE and retina in their physiological state

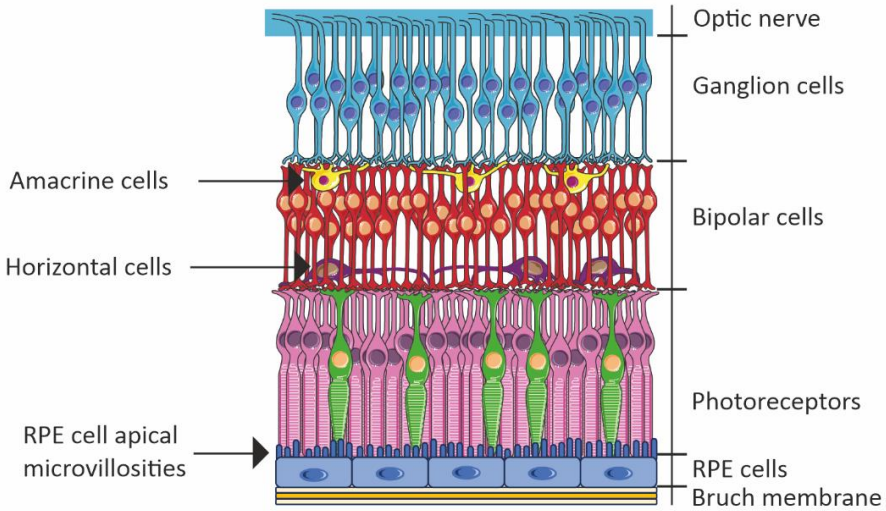

B. RPE and retina in early stage of AMD

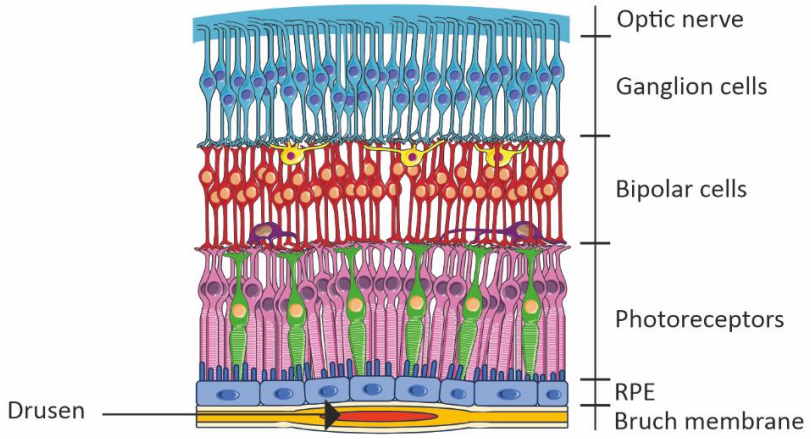

C. RPE and retina in late stage of AMD

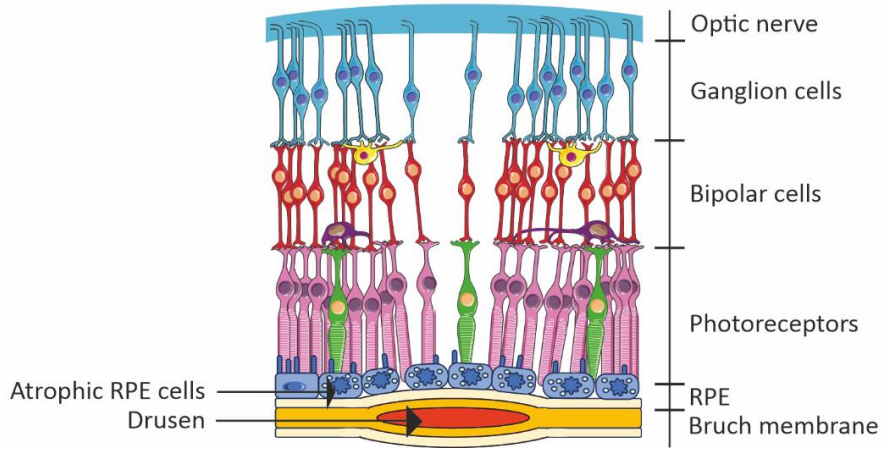

Figure 1.11: Representation of the human RPE and retina from a physiological situation to a late AMD one. A. RPE and retina in their physiological state. On the top of the retina is the optic nerve "in formation" and result from the assembly of ganglion cell axones[4]. Ganglion cells receive the influx from the bipolar cells below and bipolar cells receive the influx from the photoreceptors. Photoreceptors, where the phototransduction runs, are in direct contact with RPE cells, which set on the Bruch membrane. To phagocytose the POS, RPE cells use apical microvillosities, which participate the recognition and binding step, the first one of the phagocytosis followed by the internalization and finally the digestion[72]. At the junction between the photoreceptors and the bipolar cells are the horizontal cells, which modulate the influx transmission there by inhibitory feedbacks to the photoreceptors[73]. At the junction between bipolar cells and ganglion cells are the amacrine cells, which interact with bipolar cells, ganglions and between each other. By doing so, they create contextual effects, vertical integration and tasks more specific to each subtype of amacrine cells[73]. **B.** RPE and retina in early stage of AMD, with early drusens appearing in the Bruch membrane. Progressively, their mass lift the RPE and the retina, while them under homeostatic stress. **C.** RPE and retina in late stage of AMD. At this stage, the homeostatic stress is significant and led to retinal cell degeneration due to unsufficient supply from the RPE and deficient POS phagocytosis. The RPE cells exposed to a drusen-induced disruption of Bruch membrane plus suffering inflammatory conditions and homeostatic disbalances, suffer from atrophy. The representations are based on original draws from the open source Smart Servier Medical art (cf. https://smart.servier.com; 2023-08).

Table 1-2: Summary of AMD-associated risk factors[74]

Strength and association consistency	Risk factors	Description
Strong and consistent	Aging	AMD starts on a common basis after 55 years of age; prevalence increases exponentially with increasing age; incidence quadruples per decade[75, 76, 77]
	Cigarette	Risk is increased from 2 to 4-fold; smoking decreases the levels of high-density lipoproteins or the anti-oxidant in plasma; it increases oxidative stress, lipid peroxidation and inflammation[75, 78, 79]
	Cataract	Mostly associated with the exudative AMD, it increases retina susceptibility to light damage and favours post-operation inflammation[80, 81]
	Genetic	Development of AMD by heritability is estimated to 71% with two major loci on chromosome 1 and 10[75, 82, 83, 84]

Moderate and consistent	High body mass index	Due to increased pro-inflammatory factors in obese individuals, that favours AMD, especially the geographic atrophic form[85, 86]
	Cardiovascular disease	In a similar manner than atherosclerosis, lipid deposits in the choroid leads to reduce blood flow, increased hydrostatic pressure and potential leakages[87]
	Hypertension	As a systemic disease, hypertension decreases blood circulation in the choroid, thus disturbing the local homeostasis[88, 89]
Weak and inconsistent	Diabetes	Also a systemic disease, hyperglycemia and dyslipidemia would disturb retinal homeostasis by inducing inflammatory responses[90]
	Gender	Uncertain, the rate of progression of the disease would be higher in women than in men[91]
	Iris colour	A higher content in melanin in the iris could better protect the retina overtime[92]

1.3.2 Classification and techniques of diagnosis of AMD

The generic clinical classification of AMD is defined in three stages: the early, the intermediate and the late AMD[93]. The first one includes the presence of intermediate sized drusens from 63 to 125 µm. The presence of smaller drusens, called drupelets, is considered there as a normal sign of ageing. Presence of changes in the RPE can also be a part of the diagnosis[94]. Early AMD is finally described as asymptomatic at this stage. The intermediate stage is based on drusens bigger than 125 µm with pigmentation changes in the RPE, either increased or reduced[95]. Late AMD defines the geographic atropic or exudative form. It affects central vision and its rate of progression is important, effects being measurable over months in the exudative form, in years for the geographic atrophic one[93].

To diagnose AMD, optometrists and ophthalmologists image the back of the eye with four techniques[96]. The first one is a visual examination in an optometric office or an ophthalmologist one, where practitioners use an ophthalmoscope to observe the intraocular structures[96, 97]. The second technique is called Optical Coherence Tomography

Scan. This tool sends light waves into the patient eye to image at a high resolution the back of the eye in a cross-sectional manner over a few millimeters [96, 98]. The third technique, the fluorescein angiography, relies on an intravenous injection of fluorescein into the patient blood circulation prior to a rapid and intense serial photograph. This gives a consistent "picture" of the retinal blood circulation and surrounding tissues[96, 99].

1.3.3 Few words about the therapeutic arsenal against AMD

The form AMD takes impacts the panel of therapies that practitioners can use and the potential clinical outcome for the patient. So far, the wet form can be slowed with a large panel going from intraocular injections of anti-VEGF antibodies (see **Table 1-3**) to adenoviral vector-based therapies increasing production of PEDF and so, reducing the intra-ocular VEGF content[100].

The dry AMD is much more difficult to treat as the pathological epicentres, the drusens, are hard to reach by intra-ocular injections, while significant side effects can be induced if the treatment is not specific enough. An example of that were the initial *Thermal laser photocoagulation therapy with continuous wave* and the *Nanosecond pulsed laser*. Developed in the 90s, the first one used a subvisible laser energy and converted it into heat through the adsorption of the melanin in the RPE and choroid[101]. If that method proved to reduce drusen load, it impacted with various degrees the retina[102, 103]. Using the basis of the thermal laser photocoagulation therapy, the *Nanosecond pulsed laser* introduced a 3 nanosecond break between each pulse[101]; that proved beneficial as the therapeutic impact was more specific to pathological RPE cells with a lower thermal conductivity toward retinal cells plus an increased release of matrix metalloproteinase in the following week[104, 105]. With proved beneficial effects, these therapies remained still limited by the induced damages on the neighbouring cells and tissues[103].

A different strategy was developed by Dr Wong from St Pauls Eye Unit at the Royal Liverpool University Hospital in 2000. To counter choroidal neovascularisation secondary to AMD, Dr Lois and him redistributed the fovea out of the pathological region by inducing a retinal detachment[106], a retinotomy in medical term. To ensure the retina would then stabilise, perfluorocarbon and silicone oil were used. For 9 patients operated, 8 had successful reattachment of the retina and 2 experienced improved visual acuity. Later development saw improvements of the technique and its integration with the thermal

laser photocoagulation therapy in case of redundant foveal neovascularisation[107]. A broad investigation done the following year demonstrated that it was possible to select patients likely to experience improved visual acuity when operated by the macular relocation surgery protocol[108]. These publications demonstrate, with respect to the methods, their specifications and limitations, that the replacement of a pathological tissue by a healthy one can delay, block and even reverse in some cases the overall physiopathology with beneficial outcomes for the patient.

The therapeutic arsenal against AMD being vast, the reader is invited to consult the following reviews to get a broader but non-exhaustive clinical and scientific perspective:

- Lien *et al*. 2008[109] & Parravano *et al*. 2021[110] for their description of anti-VEGF-based therapies;
- Sarao *et al*. 2014 for their description of intravitreal steroids in the treatment of retinal diseases[111];
- Mozetic *et al*. 2019 for their broad analysis on many therapeutic options[112];
- Ammar *et al*. 2020 for their summarised description of the AMD clinical landscape[113];
- Khanani *et al*. 2022 for their description of gene therapies for AMD[114];
- Rizzolo et al. 2022 for their review of biomaterials for AMD[115].

Table 1-3: Antibodies-based anti-exudative AMD drugs summary[116, 117, 118, 119]

Drug	Format	Molecular weight (kDa)	Dose (mg)	Molecules per injection
Aflibercept	VEGFR1/2-Fc fusion protein	97-115	2.0	1.0
Bevacizumab	Full antibody	149	1.25	0.4-0.5
Brolucizumab	Single-chain antibody fragment	26	6.0	11.2-13.3
Faricimab	Full antibody	150	6.0	
Pegaptanib	Aptamer	> 40	0.3	
Ranibizumab	Fab fragment	48	0.5	0.5-0.6

1.3.4 Stem cells-based therapies against AMD

1.3.4.1 Prior to stem cells, cell lines-based cellular grafts

In the 1980s, clinicians and biologists worked to characterise human RPE cells with the aim to use them for RPE-related diseases[120, 121]. Quickly after, transplantations with primary cultivated RPE cells were conducted in animal models. In 1993, He *et al* grafted human primary RPE cells grown *in vitro* for 4-5 weeks into the subretinal space of albino rabbits[122]. Over the next 3 months, investigations revealed no signs of degenerations and low signs of inflammation only. Four years later, Castillo *et al* cultivated human RPE cells to observe potential protection of photoreceptors in the Royal college surgeon rat (RCS rat), an animal model of retinal degeneration, its immature RPE being unable to phagocytose the POS[123]. Compared with a sham control, the grafted RPE cells were able to phagocytose the rat POS, while photoreceptor cell number was three times superior 30 days after the process.

Trials on AMD-affected patients faced numerous ethical and technical barriers, among them the low knowledge of cell behaviour after graft and the limited autologous cell number prior to the graft[124, 125]. So, biologists started to develop cell lines. In 2001, Lund *et al* genetically modified RPE cells from a human donor to extend its *in vitro* lifespan and compare its performances with aRPE19 cell line into the RCS rat eye[125]. Both cell types developed and favoured local photoreceptors survival over 20 weeks without inflammatory or tumoral reactions. Still, the effects were limited in space and total preservation of the retina was not achieved[125]. Consequently, a larger view was developed with the aim to replace the defective RPE cells with competent RPE ones differentiated *in vitro* from pluri- and multipotent stem cells[126].

1.3.4.2 Stem cells in clinic

In a generic epithelium, replenishment of the cell pool requires a well-balanced system where cell proliferation is controlled and balanced with the needs of the tissue[127]. In that model, cell proliferation can be subdivided into transient amplifying cell population (TAC) and adult stem cells, the firsts originating from the seconds[128]. Adult stem cells are the primary source of the tissue cell pool, their state define the tissue life-span, except in wound healings[129, 130]. Related to that function, stem cells are classified according to their

plasticity (see **Table 1-4**), which is the first feature to consider in stem cells therapies development.

Table 1-4: Classification of stem cell according to their plasticity

Grade	Definition
Totipotent	Cell able to differentiate into the three germ layers and the embryonic annexes
Pluripotent	Cell able to differentiate into the three germ layers
Multipotent	Cell able to differentiate into multiple tissues from one germ layer
Oligopotent	Cell able to differentiate into two or more close/associated tissues
Unipotent	cell able to differentiate into one tissue

Adult stem cells:

Able to generate a range of cells belonging to their tissue of origin, or closely related with, adult stem cells reside in the organism over life-span where they maintain cell homeostasis[127, 131, 132]. The first stem cells therapy was the blood transplantation, already used in the end of the 50s to counter the aplasia that followed radiation-based incidents[133]. Haematopoietic stem cells from the bone marrow niche were then identified in the 1960s by Mrs McCulloch and Till[131]. The diversity of adult stem cells comes from their tissue of origin and their potency. So, generic names have been given to simplify their classification prior to detail them in-depth. Here is a non-exhaustive list of the most common stem cells: **1**. Mesenchymal stem cells, which can differentiate into bone cells, cartilage cells and adipogenic cells[132]; **2**. Neural stem cells are able to generate neurons, oligodendrocytes or astrocytes[132]; **3**. Haematopoietic stem cells form the various bloods cells[132]; **4**. Epithelial stem cells generating cells for epithelia and their annexes if present[134, 135, 136].

The RPE on its own is a post-mitotic epithelium, meaning that it does not undergo proliferation over its life-span and so, suffers the associated downside effects such as morphological changes, loss of melanosomes[137], cell number decreasing[138, 139] and so on. No stem cells were believed to reside in the human RPE until Salero *et al*. developed a protocol, from which were generated various *in vitro* sub-phenotypes from human post-

mortem RPE cells[140]. One particular sub-type was able to generate cobblestone monolayers in a clonal manner. The authors then experienced the potency these cells had and discovered that neural, adipogenic, chondrogenic and osteogenic profils could be generated from clonal cells[140]. No specific markers was identified by the authors but neural crest-associated and mesenchymal markers STRO-1, CD90 and CD105 were absent in the initial sub-populations. Later in 2020, Chen *et al*. used a different protocol based on 3D cell culture. Over the 3D culture of mouse RPE cells, the authors were able to generate both RPE cells and photoreceptors[141]. Then, the authors tagged these cells by an enhanced green fluorescent protein to follow their evolution in grafted mice with retinal degeneration. These cells disappear over 7 weeks, the authors suspecting an immune rejection from the host. However, they integrated the RPE, re-synthesize melanin, and in 3 of the 7 grafted mice, stabilised the vision[141].

Other cell sources for the RPE were identified in the adult ciliary body of various species[142]. However, despite their potential, no clinical try with autologous RPE stem cells seems to have been run so far.

Embryonic stem cells:

First major cell source suitable for *in vitro* manipulations, embryonic stem cells and their technologies arose from nearly 50 years of research on murine and human teratocarcinomas[143]. In the 2000s, cell culture methods to grow and derive human embryonic stem cells arose proportionally as the prospect to use them for clinical application[144, 145].

Quickly, protocols to drive ESC toward the RPE phenotype followed. In 2004, Haruta *et al* proved the principle by injecting primate ESC-derived RPE cells into the subretinal space of four weeks-aged RCS rats[146]. *In vitro*, the RPE cells demonstrated a hexagonal shape, a strong pigmentation and expressed RPE specific markers. *In vivo*, the injected cells preserved the retinal ones where they sat. In parallel, ESCs were used to study the developmental molecular mechanisms. As an example, Aoki *et al* generated eye-like bodies from primate ESC and grafted them in chick embryos to assess the role of the Wnt/β-catenin canonical pathway in the RPE specification[147]. These fundamental investigations feed the differentiation processes, which used Wnt agonists later to drive the RPE specification[148, 149]. Not alone to play a role in the ESC-derived RPE protocols,

many other factors were proved to be potent if added at the right time of the differentiation[150, 151].

With growing efficiencies in derivation processes, first clinical studies emerged. In 2014, a phase I/II clinical study measured the impact of ESC-derived RPE grafts in nine patients suffering from Stargardt's macular dystrophy and nine patients suffering from dry AMD over 37 months[152]. In AMD-treated patients, no adverse proliferation, rejection, ocular or systemic issues were detected and an improvement of visual acuity for 8 out of 9 patients was observed. In 2018, da Cruz *et al* observed the improvement of visual acuity in two patients affected by exudative AMD following the graft of human ESC-derived RPE sheets on fluocinolone supports[153]. A similar phase I/II clinical trial was performed on five dry AMD-affected patients with human ESC-derived RPE cells set on a parylene substrate with improvements or stabilisation of the visual acuity observed over the first four months[154]. However, ESCs face serious ethical limitations due to their origin, the human embryo, and potential immunological limitations on the side if the source is allogeneic[155].

Induced pluripotent stem cells:

Such barriers are released by the discovery of the pluripotency induction process by Takahashi *et al* in 2006 on murine fibroblasts and in 2007 on human ones[156, 157]. Allowing the reconversion of generic somatic cells toward pluripotent one, the cell source was not more limited to a very specific cell population in an organ at a specific time during development. The corollary is that the cell number available is much more substantial. One of the main concerns was the different gene expression profiles between the iPSCs and the ESCs, with studies reporting the presence of epigenetic traces in the induced cells[158, 159, 160]. With following reports demonstrating that these variations could be generated for a part of them by the lab protocols themselves, the sum of investigations finally showed both cells types to be similar in their gene expression and DNA methylation[161]. The number of clones used to define potential differences was the key feature: with a substantial number of clones for both types, no notable differences could be seen while on the opposite, with a low clone number, differences were notable[160].

With questions on the nature of iPSC wearing still traces of their origin, first protocols to generate RPE cells arose quickly. In 2009, Buchholz *et al* published a report about spontaneous differentiation of iPSCs into RPE cells[162]. Cells not exposed to FGF2 demonstrated melanin presence after the first month of culture. Later analysis

demonstrated specific RPE gene expression, production of proteins related to RPE functions and POS phagocytosis facilities at levels comparable with RPE-derived ESCs.

With improving protocols, the generation of iPSC-derived RPE cells aimed to reach clinical grade suitable for clinical implants, with success[163, 164]. These efforts led to pre-clinical and clinical studies over the last years. In 2021, Zhang *et al* demonstrated an efficient process of differentiation with cells able to rescue photoreceptors in RCS rats 6 weeks after subretinal injection[165]. No tumour formation was observed neither in immuno-deficient mice. Earlier in 2017, Mandai *et al*. published a clinical study with a graft-based iPSC-derived RPE surgery and the follow-up over one year in a patient with exudative AMD[166]. The cells were autologous and transformed from skin fibroblasts. No worsened or improved visual acuity was noticed except a brighter vision due to neovascular membranes removal.

Overall, iPSC and potentially ESC demonstrated great potential to replace degenerated RPE in AMD patients with initial clinical trials having demonstrated the safety of the process over the first post-surgery years. More significant, some measurable benefits could be already observed.

1.3.5 The IPE's plasticity and its potential to replace the RPE

Already known and studied before for its transformation facilities, the initial IPE investigations were conducted by Eguchi *et al* in 1971[167]. They observed the distribution of ^{3}H-thymidine in newt IPE cells after a lensectomy. Four days later after surgery, the authors observed a significant DNA synthesis from the dorsal section, a location comparable to the half-superior portion in mammals. Over the following 14 days, cell number increased gradually and formed a visible cell clump filling the pupil. More recently, Sousounis *et al* proved that the IPE ability to regenerate the newt lens was associated with an enriched content of ECM proteins, proteins involved in cell proliferation, migration and nuclear transcription factors[168].

Later, iris pigmented epithelial cells were regarded as a potential cell source to regenerate the RPE as these cells demonstrated potential to support RPE functions in AMD animal models. In the RCS rat, IPE grafts from seven to ten days old Long Evans rats transplanted into the subretinal space proved viable over three months while delaying photoreceptor degeneration[169]. These results were later confirmed by Schraermeyer *et al* who injected

Long Evans rat IPE cells into the subretinal space[170]. Still in 1997, another group demonstrated that *in vitro* porcine IPE cells can phagocytose POS at 64% of their RPE counterpart[171]. Later, Thumann *et al* used autologous grafts obtained by iridectomy to straightforward transplant them into the subretinal space[172]. The transplants attached to the underlying RPE and supported photoreceptor survival without immunological issues noticed by the authors. A similar investigation done on rabbits by Crafoord *et al* led to the same conclusion[173]. Finally, Abe *et al* demonstrated that monkey IPE cells cultivated in autoserum and injected into the subretinal space led to the same results than the previous ones cited before[174].

Another interesting point was made by the same group a year later with the injection of Long Evans rat IPE cells into the choroid of fourteen to eighteen days old RCS rats[175]. Six months later, retinal cells were numerous with a clear distinction between the different retinal layers in the transplanted eyes, while the control ones demonstrated nearly no surviving retinal cells. The authors supported that in absence of direct contact between retinal cells and injected IPE cells, the latter secreted factors favouring retinal cell survival. On the same trend, Arnhold *et al* observed that rat as human IPE and RPE cells produced at similar levels brain-neurotrophic factor, neurotrophin-3 and glial-derived neurotrophic factor, associated with neural growth[176].

All together, these investigations demonstrated that mammal IPE cells were able to work as RPE supports in cases of retinal degeneration. As suggested by Thumann *et al*, the close developmental link between the RPE and the IPE could be partly responsible for these results[177]. A point of view supported later by Bennis *et al* who investigated a significant portion of genes expressed in human IPE and RPE[178]. With stringent features, the group demonstrated that both tissues had close expression regarding pathways associated with epithelial functions. Oppositely, the authors observed that the phototransduction pathway related to the retinol metabolism was the most expressed pathway by the RPE on its own. Interestingly, the IPE counted a couple of pathways associated with human embryonic stem cell pluripotency or the Wnt/β-catenin pathway in its highest expressed pathways.

By the time at Bennis *et al* published their study, first clinical investigations had already started. In 1999, Abe *et al* injected autologous IPE cells cultivated for 27 to 60 days in the subretinal space of 8 patients suffering exudative AMD after removal of neovascular membranes[179]. Over the initial observation phase running from 1.5 to 8 months, visual

acuity improved for 6 patients and remained stable for the 2 others. The group published a year later observations on the same patient group, confirming their previous results[180]. A similar study was conducted by Lappas *et al*, who injected autologous IPE cells on 12 exudative AMD-affected patients[181]. With observations lasting over 6 months, the group did not observe increases in visual acuity. A broader study performed by the same group led to the conclusion that the injection of autologous IPE helps to preserve visual acuity in exudative AMD but do not improve it[182]. A three-year follow-up on 20 patients with exudative AMD confirmed that finding[183]. The IPE suspension was injected in the subretinal space straightforward after the iridectomy and the removal of neovascular membranes. Over the three years follow-up, stable vision was the main finding, the improvement and degradation of visual acuity being rare[183].

1.3.6 *In vitro* 2D versus 3D cell culture

Over the course of this project, primary porcine IPE cell culture has been an extended and evolving part with the use of 2D and 3D cell cultures. Both have advantages and disadvantages to consider prior to their use in primary stem cells culture.

In vitro, primary stem cells tend to lose their original features on generic adherent (= 2D) systems due to the loss of physical constraints, lack of specific factors present in the extracellular environment, specific cell-cell contacts and cell-basal lamina ones[134, 184, 185]. On a broader perspective, the 2D cell culture of primary cells often result in activities and observations irrelevant compared to the *in vivo* physiology[186]. The generic support consists in a flat surface of glass or polystyrene, which favours the adhesion of cells[186]. As cells form a monolayer, nutrients and growth factors distribution is homogeneous, favouring global cell proliferation to the expanse of the original (and potential) cell heterogenity[187]. Also, largely dependent of the medium used, the cell number or the surface coating, the flat and stretch surface has mechanical impact on cells[188], which adapt their gene expression and protein production[187].

So, different approaches have been developed to specifically grow primary stem cells from theirs differentiated counterparts, including 3D sphere cultures, ECM proteins-encapsulated hydrogels or decellularised native ECM[187, 189]. In this project aiming to identify porcine IPE stem cells, spheroid 3D cultures inspired from neurosphere assays were used[190].

In theory, cells in suspension are forced to adapt by forming spheres, otherwise they die. Once in culture, two patterns are possible. Firstly, all/most of the cells aggregate and establish new cell-cell contacts. By doing so, they reorganise around a core of differentiated cells, while peripheral cells in contact with growth factors tend to express stem cell markers[190]. In practice, that approach generates a great number of spheres despite important heterogeneity inside them. This heterogeneity is increased by the easy access to nutrient, growth factor and oxygen supply at the surface, while metabolic wastes and carbon dioxide accumulate at the core[191]. Secondly, cells plastic enough proliferate in a clonal manner to re-establish cell-cell contacts, while cells not able to survive without a basal-lamina anchor die[190], a phenomenon also called anoikis[192]. In this case, the potency cells demonstrate depends about the medium they are exposed to plus their original phenotype[190]. By doing so, spheres are highly homogeneous but their number depend of the original stem cell proliferation facilities[190, 193].

Despite the low sphere number generated or the low homogeneity between aggregates, 3D sphere assays have the advantage of a low number of intrinsic variables. Spheres are conditioned by the initial cell density seeded, the type of plate, the media used and cell movements induced over manipulations. This explains in part their successful use in the identification of primary stem cells from several tissues, including cancers[194, 195, 196, 197, 198, 199, 200].

1.4 In summary

Compared to the RPE, investigations to characterise the IPE are limited. The tissue is poorly characterised, its daily functional pathways being characterised by Bennis *et al* in 2017 only. The lack of mechanistic data made it also difficult to consider for a cell therapy prospect. Moreover, the rise of iPSC from human sources shifted the interest towards them.

Despite this, the clinical results demonstrated that autologous IPE transplantation was safe for the host immune system. The injection of generic autologous IPE cells without upstream selective cell culture processes further proved their suitability for RPE replacements. This view is completed by previous work done on the chick IPE by Asami *et al*, who proved that in specific cell culture conditions, mammalian IPE cells were able to generate photoreceptors, neurons and neuronal stem cells[201, 202]. The rise of

photoreceptor cells supports that at least some IPE cells, if appropriately monitored, can generate cells closely related from a developmental point of view. *In vitro* partial transformation of IPE cells toward lens ones further supports that IPE cells have regenerative potential[203].

Physiologically, the IPE conducts *in vivo* three functions: the control of the pupil diameter, the blockade of photons not in line with the pupil, and a permeability barrier with the posterior chamber. To do so, it is structured into two layers: **1.** the anterior one which includes a smaller content of melanosomes than the posterior one and smooth muscular fibres organised in a radial manner from the pupil to the iris root; **2.** the posterior one which is highly pigmented and forms a serrated layer to absorb the mechanical forces[149]. Developmentally linked to the RPE and the retina as it arises from the ciliary margin zone, IPE cells have been able *in vitro* to differentiate into neurons and perform critical functions conducted daily by the RPE. The various surgical experiments done so far demonstrated that these facilities were not limited to *in vitro* conditions as IPE-grafted/injected cells were able to conduct *in vivo* the RPE functions without generating physiological issues.

Thus, more fundamental knowledge about the IPE are required in first instance. This work is essential to then improve the outcome of IPE cell culture, characterisation, selection of IPE subpopulations and finally the identification of IPE stem cells. From there, future perspectives could be opened and IPE stem cells differentiated into functional RPE cells with the prospect to be added in the future in the anti-AMD arsenal.

1.5 Aim & objectives of the thesis

1.5.1 Aim

The aim of this project is to identify IPE stem cells, if they exist, from porcine tissue.

1.5.2 Objectives

To do so, the project is organised into three objectives:

1. To investigate fundamental features of the IPE *in vivo* by histological and immunohistochemical means.

2. To observe cell behaviour from porcine IPE cells *in vitro* with a neural stem cell-based protocol developed by the Kearns Group.

3. To observe and compare cell behaviour from porcine IPE cells *in vitro* with different medium-term protocols.

2 Chapter 2: materials and methods

2.1 Materials

Cell culture-related:

Amphotericin B solution (Sigma-Aldrich; A2942); Animal-free recombinant human epithelium growth factor (Peprotech; AF-100-15); Animal-free recombinant human basic fibroblast growth factor (Peprotech; AF-100-18B); aRPE19 cells (ATCC; CRL-2302); B27 supplement 50X (ThermoFisher; 17504044); 96-well plates (Corning; CC780); Costar® 12-/24-well TC-treated well plates (Corning; 3512; 3524); Culture flasks 75 cm^2 (Sigma-Aldrich; C7231); DMEM-F12 (ThermoFisher; 31331); BioFloat™ 96-well cell culture plate (FaCellitate; F202003); Heat-inactivated foetal bovine serum (LabTech; FB-100-500); Low attachment Nunclon Sphera 24-well plate (ThermoFisher; 174930); Oxoid™ Phosphate buffered saline tablets (ThermoFisher; BR0014G); Dulbecco's phosphate buffered saline solution (Sigma-Aldrich; D5773); Penicillin-Streptomycin (Sigma-Aldrich; P4333); Resazurin salts (ThermoFisher; R12204); Hydrophobic surface-based suspension plate (Greiner; 662102); TrypLE express enzyme (ThermoFisher; 12604021).

Embedding-cutting:

Microtome (Leica; RM2245); paraffin (Leica; 39601006); paraffin embedding station (Leica; EG1150H); Tissue processor (Leica; ASP-300); Superfrost® microscope slides (Sigma-Aldrich; Z692255).

FICC-related:

Bovine serum albumin (Sigma-Aldrich; A2153); CFSE cell labelling kit (Abcam; ab113853); DAPI (ThermoFisher; D1306); Cryostat (Leica; CM1900); Goat serum (Sigma-Aldrich; G9023); Neutral buffered formalin solution (Sigma-Aldrich; HT501128); Oxoid™ Phosphate buffered saline tablets (ThermoFisher; BR0014G); Superfrost Plus slides, ground edges (Epredia; J1800AMNZ); Tissue culture glass coverslip 13 mm (Sarstedt; 83.1840.002); Tissue freezing medium (Leica; 14020108926); Ultradisposable microtome blades, low profile (Epredia; 3053835); Vectashield antifade mounting medium (Vector Laboratories; H-1000-10); Multicolor Vybrant ™ cell-labelling solutions (ThermoFisher; V22889.

Histology – immunohistochemistry:

Acetone (Fisher Scientific; A/0600/PC17); acid alcoholic (Leica; 3803651E); avidin/biotin blocking kit (Vectorlabs; SP-2001); bovine serum albumin (Sigma-Aldrich; A2153); 4', 6-diamidino-2-phenylindole dihydrochloride (DAPI)(ThermoFisher; D1306); Goat serum (Sigma-Aldrich; G9023); Eosin Y (Leica; 3801600BBE); Ethanol 100% (Honeywell; 24194); ImmPACT® VIP peroxidase (HRP) substrate (Vectorlabs; SK-4605); Harris Haematoxylin (Leica; 3801560BBE); Histological coverslips (Leica; 3800141); 35% hydrogen peroxide (Sigma-Aldrich; 1086001000); methyl green (Vectorlabs; H-3402); Pertex Mounting medium (VWR; LEIC811); Neutral buffered formalin solution (Sigma-Aldrich; HT501128); Oxoid™ Phosphate buffered saline tablets (ThermoFisher; BR0014G); PAP pen for immunostaining (Sigma-Aldrich; Z377821-1EA); Sodium citrate tribasic dihydrate (Sigma-Aldrich; C8532); Triton –X100 (Sigma-Aldrich; 23472-9); Unitrieve (Innovex; NB325-500); Vectashield antifade mounting medium (Vector Laboratories; H-1000-10); Xylene (Fisher Scientific; X/0250/17).

Reverse transcription quantitative real-time PCR-related:

1kb DNA ladder (Sigma-Aldrich; D0428); 96 well plates for Roche Lightcycler 480 (Primer Design; BW-96480); Agarose (Sigma-Aldrich; A4718); DNA colorant for electrophoresis 6X (ThermoFisher; R0611); MicroAmp TM optical adhesive film (4360954; Thermofisher); Personalised transcripts (Eurogentec); Precision nanoscript2 reverse transcription kit (Primer Design; RT-nanoscript2); PrecisionPLUS qPCR master mix (Primer Design; PPLUS-machine type-10ML-SY); RNase/DNase free water (Primer Design); RNeasy mini kit (Qiagen; 74104); RNAse- & DNAse-free water (Primer Design; RNase/DNase free water), Safe SYBR green solution (ThermoFisher; S33102); Tris-acetate – EDTA (Sigma-Aldrich; 93295).

Tissue dissection-fixation:

Binocular microscope (Olympus; SZX12); Neutral buffered formalin solution (Sigma-Aldrich; HT501128); Oxoid™ Phosphate buffered saline tablets (ThermoFisher; BR0014G).

Western-blot:

β-mercapto-ethanol (Sigma-Aldrich; M3148); Acrylamide (Sigma-Aldrich; A4058); APS (Sigma-Aldrich; A3678); bromophenol blue (Sigma-Aldrich; B8026); Ethanol 100% (Honeywell; 24194); Glycerol (Sigma-Aldrich; G5516); Milk powder (Tesco); NaCl (Sigma-Aldrich; S3014); Nitrocellulose (Fisher Scientific; 10773485 & Cytiva; 10600047); Pierce™ BCA protein assay kit (ThermoFisher; 23227); Precision plus proteinTM dual color

standards (BioRad; 1610374); protease inhibitor cocktail (Sigma-Aldrich; P8340); Red ponceau (Sigma-Aldrich; P7170); RIPA lysis buffer 10X (Sigma-Aldrich; 20-188); SDS (Sigma-Aldrich; T3771); SupersignalTM west pico PLUS chemiluminescent (ThermoFisher; 34577); TEMED (Sigma-Aldrich; T22500); Transblot turbo 5X transfer buffer (BioRad; 10026938); Trizma (Sigma-Aldrich; T6066); Tween-20 (Sigma-Aldrich; P1379); Whatman paper 3MM (Fisher Scientific; 11935104 & Cytiva; 3030-704).

Human sample donors:

For histological investigations, post-mortem human eyes were provided by the Liverpool Royal Eye Bank and used according to the Liverpool Ethical Approval Statements (see **Table 2-1**).

Table 2-1: Human samples from the Liverpool Royal Eye Bank

Sample number	Sex	Age
LREB011	Female	86
LREB052	Male	60
LREB055	Female	85

2.2 Methods

2.2.1 Porcine eye dissection: from their reception to the eye opening

Prior to the contamination explained in part 4.4.1, porcine eyes were processed as follows. The globes were isolated by abattoir staff (Morphets; Widnes, UK) from porcine bodies on the day of slaughter and transported to the laboratory on ice a couple of hours later. In the laboratory, further manipulations were done in a class I hood. Extra-ocular muscles were removed with scissors (**see figure 2.1-A**). Eyes were opened with a scalpel on the back of the iris (**see figure 2.1-B**). Anterior and posterior parts were separated. Anterior parts were placed in PBS until next step. Then, either the iris was detached from the sclera by using a scalpel as a rake (**see figure 2.1-C**). Iris were placed in PBS until next step or the anterior chamber was processed without further manipulation. This protocol was used on a routine basis for all porcine eye dissections. Methods for both histological – immunohistochemistry and cell culture are indicated in sections **2.2.2** and **2.2.5** respectively.

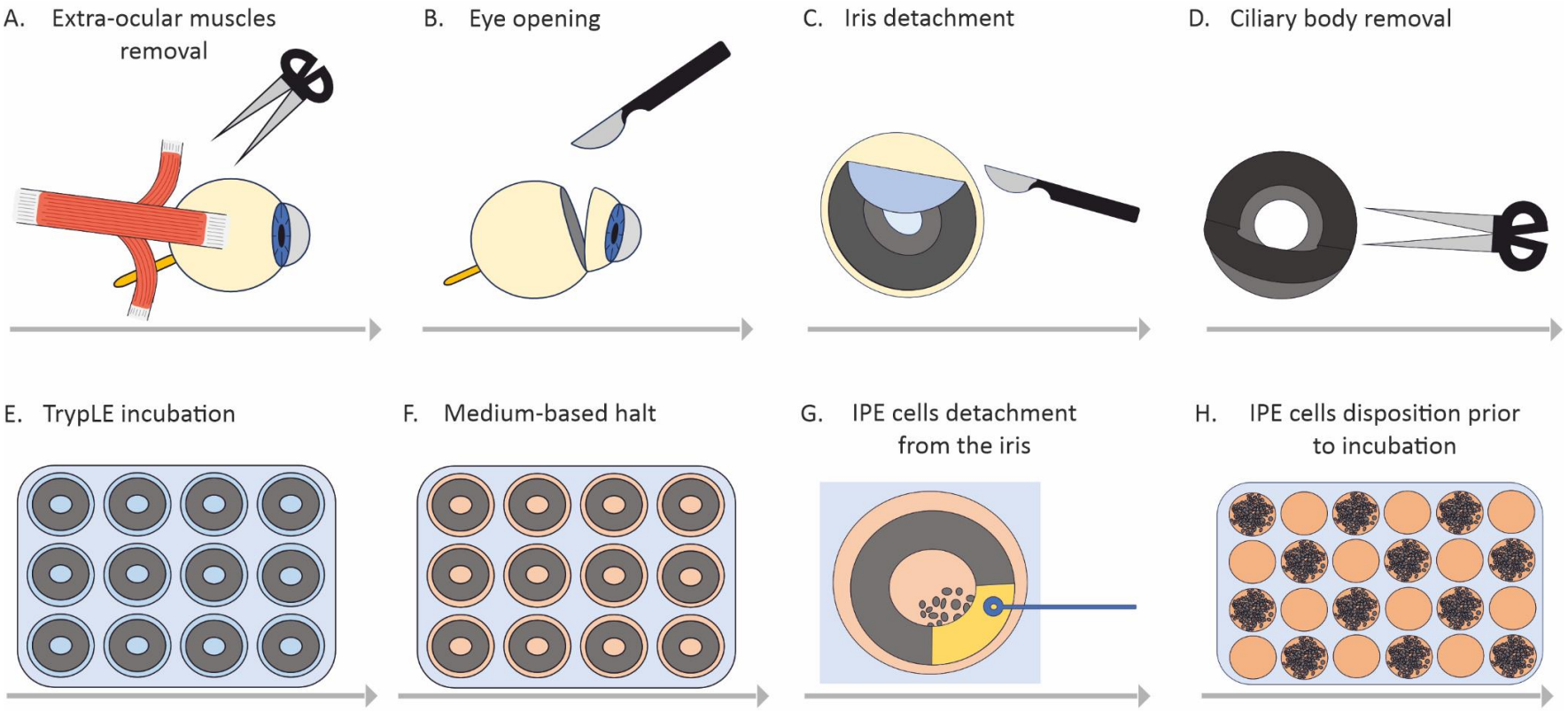

Figure 2.1: Diagram of the porcine eye generic dissection. All eyes were processed by steps A to D. Samples dedicated to cell culture were then processed by steps E to H. **A.** After reception in the dissection lab, extra-ocular muscles are removed using scissors. **B.** Once sclera cleaned of extra-ocular muscles, eyes are opened on the back of the iris with a scalpel. **C.** The iris is detached from the sclera by using the scalpel like a rake. **D.** Using a binocular loop, the ciliary body is separated from the iris by using micro-scissors. **E.** Iris are then incubated in pre-heated TrypLE for 40 min at 37°C. **F.** Iris are transferred into medium (DMEM-F12 20% FBS) to block the enzymatic reaction. **G.** IPE cells are gently detached from the iris by using an inoculation loop. **H.** IPE cell suspensions are seeded in 24 well plates with DMEM-F12 10% FBS prior to incubation at 37°C. Grey arrows indicate the pattern.

2.2.2 Histology & immunohistochemistry

2.2.2.1 Porcine eye dissection

In early investigations, the iris and other tissues such as the cornea were separated from each other and processed independently; process started passed figure 2.1-C (see **Figure *2.1***). Over the course of investigations, the anterior chamber (from the cornea to the iris) was kept together; process started passed figure 2.1-B (see **Figure *2.1***).

Tissues were then placed in formalin for 10 min in the first investigations only, then 24 hours the later ones. Following fixation, tissues were cleaned twice in PBS for 20 min each, then placed in the embedding machine. Embedding program is defined in **Table 2-2**.

Table 2-2: Cornea embedding program

Step	Component	Temperature (^{o}C)	Duration (min)
1	Ethanol 70%	Room temperature	40
2	Ethanol 90%	Room temperature	40
3	Ethanol absolute	Room temperature	40
4	Ethanol absolute	Room temperature	40
5	Ethanol absolute	Room temperature	90
6	Ethanol absolute	Room temperature	120
7	Xylene	Room temperature	60
8	Xylene	Room temperature	60
9	Xylene	40	120
10	Paraffin wax	62	75
11	Paraffin wax	62	60
12	Paraffin wax	62	180

Tissues were embedded in paraffin block with attention to not create air bubbles, and left to cool for half an hour. Sections were cut for 5 µm of thickness with a microtome and mounted into Superfrost ® slides. Slides were finally dried for the following 24 hours at 37^{o}C, then stored or used immediately.

2.2.2.2 H&E staining

Sections were deparaffinised in xylene for 5 min twice. Rehydration was then processed by pouring slides into 100%, 90% and 70% ethanol jars for 5 min each. Slides were rinsed for 1 min in running tap water. To stain nuclei, slides were incubated into haematoxylin for 4 min, then cleaned quickly in running tap water. To differentiate nuclei, slides were poured 10 times in acid alcoholic then cleaned in running tap water for 1 min. Slides were then incubated in eosin for 4 min to stain the mesenchyme and other cell components. A quick cleaning in running tap water followed. To complete the process, slides were dehydrated in progressive 70%, 90% and 100% ethanol gradients. Slides were finally mounted and sealed with nail polish.

2.2.2.3 Fluorescent/immunohistochemistry

Sections were deparaffinised in xylene for 5 min twice. Rehydration was then processed by pouring slides into 100%, 90% and 70% ethanol jar for 5 min each. Slides were cleaned for 1 min in running tap water.

Slides were then submitted to antigen retrieval either by sodium citrate solutions or by Unitrieve. The first solution was heated to 95^{o}C and slides were immersed in for 20 min. The second solution was heated at 60^{o}C and slides immersed from 30 to 60 min depending their targets according to the manufacturer instructions. Sections were then cleaned twice in PBS and permeabilised for 15 min by 1% Triton-X100 prior to be cleaned twice again in PBS.

Fluorescent method:

Sections were blocked for more than an hour in 10% normal goat blocking serum. Primary antibodies (see **Table 2-3**) were then applied overnight at 4^{o}C or at room temperature for 1 h only. Sections were then cleaned twice in PBS, incubated with secondary antibodies for 1 h and cleaned twice in PBS. Sections were incubated with DAPI at 1:10,000, then cleaned twice in PBS prior to be mounted in Vectashield medium and sealed with polish nail.

Colorimetric method:

Sections were then blocked with a 3% hydrogen peroxide – PBS solution, a biotin solution and an avidin one, each of them for 10 min. To complete the blocking, sections were incubated for more than an hour in horse blocking serum. Primary antibodies were then applied overnight at 4^{o}C. Sections were then cleaned twice in PBS, incubated with a pan-species secondary antibody and cleaned again twice in PBS. An HRP solution was then poured onto each section for 20 min, sections were cleaned twice in PBS. A specific attention was payed to remove any liquid at that point. Sections were then incubated with the ImmPACT VIP peroxidase substrate for 2 min then quickly cleaned in running tap water. To label nuclei, sections were incubated with an 80% methyl green solution for 5 min at 60^{o}C. Sections were then immersed for 15s into acetone, and finally incubated into xylene for 1 min. Slides were then mounted with mounting medium.

Table 2-3: Antibody list

Primary antibodies			
Target	**Product code; company**	**Host**	**Concentration***
A-smooth actin	ab7817 - Abcam	Mouse	5 µg/ml
Desmin	MA5-13259 - ThermoFisher	Mouse	1/200
Vimentin	ab8069; Abcam	Mouse	5 µg/ml
Nestin	NBP1-02419; Novus Biologicals	Rabbit	5 µg/ml
Pan-cytokeratin MNF-116	ab756; Abcam	Mouse	1/200
Pan-cytokeratin C-2931	C2931; Sigma-Aldrich	Mouse	1/200
PAX6	ab5790; Abcam	Rabbit	20 µg/ml
SOX2	ab97959; Abcam	Rabbit	4.5 µg/ml
N-cadherin	ab18203; Abcam	Rabbit	4 µg/ml
E-cadherin	ab15148; Abcam	Rabbit	0.6 µg/ml
ZO-1	61-7300; ThermoFisher	Rabbit	2.5 µg/ml
Collagen type IV	ab6586; Abcam	Rabbit	5 µg/ml
Pan-laminin	L-8271; Sigma-Aldrich	Mouse	1/200
Laminin-α4	SAB4501719; Sigma-Aldrich	Rabbit	5 µg/ml

Laminin-β1	PA5-27271; ThermoFisher	Rabbit	1 µg/ml
Laminin-β2	ab210956; Abcam	Mouse	1/600
GNL3	LS-C465526; LSBio	Rabbit	1/200
βIII-tubulin	ab7751; Abcam	Mouse	1/200
Tyrosinase	ab112231; Abcam	Rabbit	1/200
SNAIL/SLUG	ab180714; Abcam	Rabbit	1/200
Ki67	ab8191; Abcam	Mouse	1/100
PCNA	8580S; Cell Signalling	Mouse	1/100
ΔN-p63	ab172731 ; Abcam	Mouse	1/100

Secondary antibodies

Target	**Product code ; company**	**Dilution**
Alexa fluor 488 anti-mouse	A-11029; Invitrogen	pAb concentration / 2
Alexa fluor 514 anti-mouse	A-31555; Invitrogen	pAb concentration / 2
Alexa fluor 594 anti-mouse	A-11005; Invitrogen	pAb concentration / 2
Alexa fluor 488 anti-rabbit	A-11008; Invitrogen	pAb concentration / 2
Alexa fluor 594 anti-rabbit	A-11012; Invitrogen	pAb concentration / 2

*Dilutions are indicated in place of concentration when the original concentration was not provided by the manufacturer.

2.2.3 Western-Blot – samples preparation

2.2.3.1 Cell lysis

Cell lysis was carried out on samples at: **1**. day 6 DMEM-F12 with 10% FBS; **2**. day 14 DMEM-F12 with 10% FBS; **3**. day 14 DMEM-F12 with 1X B27; **4**. day 14 DMEM-F12 with 2X B27. To lyse cells, 10X RIPA lysis buffer was diluted in distilled water at 1X and placed at 4°C for a minimum of 2 hours prior to use. Lysis solution was completed at the last minute to 1% with phosphatase inhibitors.

Prior to extraction, adherent cells were washed in PBS and incubated in TryplE for 10 min at 37°C. Cell suspension was then centrifuged and cell pellet resuspended in RIPA-based lysis solution. To note, no more than 200 µl was used per sample to concentrate the

protein extract as much as possible. In addition, eyes being collected in pairs, IPE cells were processed by pair as well. Solutions were vigorously pipetted but care was taken to not induce bubbles in solutions. Solutions were then transferred into sterile 1.5 ml Eppendorfs. Tubes were then slowly agitated on a wheel for at least 90 mins at 4°C. Finally, Eppendorfs were centrifuged at 12,000 rpm for 10 min at 4°C. Supernatant were transferred into new tubes and stored at -20°C until quantification.

2.2.3.2 Protein quantification

Protein quantification was assessed using the Pierce BCA Protein assay kit. Prior to use, RIPA buffer was constituted as indicated in the previous section. A dilution series was then produced to constitute the standard curve. BSA (Sigma-Aldrich) was diluted in the 1X RIPA in distilled water by a dilution series ranging from 4 mg/ml to 0.03125 mg/ml. Next steps were processed as indicated by manufacturer's instructions. Two repeats per sample were analysed, 3 per standards. All samples were loaded into a 96 well plate. Absorbance was measured at 562 nm. Subsequent data were analysed and plates stored at 4°C.

2.2.4 Western-Blot - process

The day before processing, solutions were prepared as described below.

Resolving gel buffer :

- Trizma : 36.33 g
- Distilled water : 100 mL
- PH: 8.85.

Stacking gel buffer :

- Trizma : 3.028 g
- Distilled water : 100 mL
- PH : 6.8.

10% SDS :

- SDS : 10 g
- Distilled water : 100 mL.

5X running buffer :

- Trizma : 15.1 g
- Glycine : 94 g

- 10% SDS : 50 mL
- Distilled water : 1 L qsp.

10X TBS :

- Trizma : 24.2 g
- NaCl : 80 g
- Distilled water : 1 L qsp
- PH : 7.6.

Wash buffer:

- 10X TBS : 100 mL
- Tween-20 : 1 mL
- Distilled water : 899 mL.

Loading Laemmli buffer:

- Glycerol : 0.8 mL
- Distilled water : 3 mL
- Stacking gel : 2 mL
- B-mercapto-ethanol : 0.4 mL
- Bromophenol blue : one tip.

Stripping solution :

- Resolving gel buffer : 10.4 mL
- 10% SDS : 100 mL
- Distilled water : 500 mL
- PH : 6.7.

Transblot-turbo transfer 1X :

- Trans-blot turbo 5X transfer buffer : 200 mL
- Distilled water : 600 mL
- Ethanol 100% : 200 mL.

Milk blocking solution :

- Milk powder : 10 g
- Wash buffer : 200 mL.

2.2.4.1 Electrophoresis - gel preparation

Gels were prepared as follow. Two electrophoresis glass plates were placed into a clamp on a plastic support. To prevent leaks, a malleable plastic support was placed below the glasses and water was pipetted inside the gap as a leak test. Water was subsequently removed and glasses placed back vertically.

Resolving gels were first prepared by mixing 7 ml of distilled water, 5 ml of resolving gel buffer, 8 ml of acrylamide, 200 µl of 10% SDS solution, 200 µl of 10% APS solution and 20 µl of TEMED. The two last agents being polymerisers, 7 to 8 ml of the final mix were quickly poured into the glasses. To prevent bubbles formation and guarantee a horizontal level, 300 to 400 µl of isopropanol was added on the top of resolving gel buffers. Polymerisation then occurred for 1 hour at room temperature.

Stacking gels were obtained by mixing 3.7 ml of distilled water, 5 ml of stacking gel buffer, 1.3 ml of acrylamide, 100 µl of 10% SDS, 100 µl of 10% APS and 20 µl of TEMED. Prior to the addition of the polymerisers, isopropanol was removed from the glasses. Subsequent cleaning occurred with distilled water and a small piece tunnel paper ensured walls dryness. Once stacking gels were loaded, combs were added carefully to not introduce air bubbles. Polymerisation occurred over one hour. Finally, glasses and combs were placed in 1X running buffer overnight at 4^{o}C.

2.2.4.2 Electrophoresis run

The day of processing, samples were prepared for loading 10-20 µg protein per well. A volume of loading buffer representing one quarter of the sample volume was poured into each sample. When necessary, the total volume was adjusted with 1X RIPA buffer prepared at least 90 minutes in advance. Samples were then incubated at 95^{o}C for 5-10 min and stored on ice until use.

Gels were placed into electrophoresis tanks with the combs in. Tanks were filled with 1X running buffer to submerge the entire gel. Once this was completed, combs were carefully removed. Samples and ladders were finally loaded with attention to prevent contamination of neighbouring wells. When a well remained empty, loading buffer was added without any sample. Once gels were ready, tanks were closed and electrophoresis ran at 100 V until bromophenol blue reached the opposite side.

2.2.4.3 Protein transfer

Proteins were transferred from the polyacrylamide gel to a nitrocellulose membrane by semi-dry transfer or wet transfer. While electrophoresis was running, nitrocellulose

membranes, Whatman papers and sponge pads were soaked into Transblot turbo buffer 1X. Carefully, electrophoresis cassettes were removed from the tank with a specific attention to the distribution of samples within. After removal of the glasses, the right corner of each gel was cut for that purpose.

When transferred by the **semi-dry method**, polyacrylamide gels were then sandwiched in transfer cassettes as follows:

1. Sponge pad
2. Whatmam 3MM paper
3. Nitrocellulose paper
4. Polyacrylamide gel
5. Whatmam 3MM paper
6. Sponge pad

A roller was used at each new layer to remove air bubbles. Once sandwiches were prepared, they were placed in a Trans-blot Turbo transfer system (BioRad). Cassettes were closed and transfer ran at 100V for 7 min.

When transferred by the **wet method**, polyacrylamide gels were then sandwiched in transfer cassettes as follows:

1. Toward the positive electrode
2. White cassette wall
3. Sponge pad
4. Whatman 3MM paper
5. Nitrocellulose paper
6. Polyacrylamide gel
7. Whatman 3MM paper
8. Sponge pad
9. Black cassette wall
10. Toward the negative electrode.

A roller was used after each new layer to remove air bubbles. Once sandwiches were prepared, they were placed in a new tank toward the positive electrode. Tank was filled with transfer buffer and an ice pack was finally added. Tanks were closed and transfer ran at 100V for 1 hour 30 mins – 2 hours depending on the protein size.

2.2.4.4 Immunodetection

After transfers, cassettes were opened and membranes cleaned in TBS tween 20 buffer twice for 5 min. To ensure that transfer worked, a Ponceau S staining was performed with a ready-to-use Ponceau S solution. Membranes were incubated for 5 min and quickly imaged. When bands were observed, the process continued. Ponceau removal was processed by cleaning the membranes in TBS tween 20 buffer three times for 5 min each.

Once membranes were cleaned, they were blocked in blocking solutions according to manufacturers and previous investigator's instructions (**see Table 2-4**). Primary antibodies were applied overnight at 4^{o}C. Primary antibody dilution used was 1/5,000 for all.

Once overnight incubations were done, membranes were cleaned three times in TBS tween 20 for 5 min each. Membranes were subsequently incubated with a secondary antibody in 0.5% milk/BSA according to the primary antibody's species – TBS tween 20 for 1 hour at room temperature. Membranes were washed three times for 5 min each in TBS tween 20. Finally, they were incubated with Supersignal TM west pico PLUS chemiluminescent buffers mixed as a 1;1 solution for 2 min. Membranes were finally imaged using a BioRad Gel Doc XR+ System. Antibody solutions were used three times, then discarded.

Table 2-4: Blocking and antibody buffers

Antibody	Company	Concentration	Blocking		Antibody incubation buffer
			Buffer	Time	
Vimentin	Abcam – ab8069	5 µg/ml	5% milk – TBS tween 20	1 hour	0.5% milk – TBS tween 20
PAX6	Abcam – ab5790	20 µg/ml	5% BSA – TBS tween 20	1 hour	0.5% BSA – TBS tween 20
SOX2	Abcam – ab97959	4.5 µg/ml	5% milk – TBS tween 20	1 hour	0.5% milk – TBS tween 20
SNAIL/SLUG	Abcam – ab180714	1/200*	4% milk – TBS tween 20	1 hour	0.5% milk – TBS tween 20
GAPDH	Abcam – ab8245	2 mg/ml	5% BSA – TBS tween 20	1 hour	0.5% BSA – TBS tween 20

*Dilution are indicated in place of concentration when the original concentration was not provided by the manufacturer.

2.2.4.5 Stripping

To label the loading control GAPDH, membranes were stripped after imaging. Stripping buffers were heat prior to the imaging process to 55°C. Once membranes were imaged, they were quickly placed in TBS tween 20 and washed twice for 5 min. Prior to the stripping, 175 µl of β-mercaptoethanol was added to 25 ml of the stripping solution. Membranes were then immersed in the stripping solution and incubated at 55°C from 5 to 10 min maximum. Membranes were then washed three times in TBS tween 20 for 10 min each. Following processes restarted at the blocking stage as described in the previous section. Each membrane was stripped once only.

2.2.5 Cell culture

2.2.5.1 Primary IPE cell extraction – early protocol

Prior to contaminations explained in section **4.3.1**, porcine eyes were processed for the first steps as explained in section **2.2.1**.

Once iris were detached from the sclera by using the scalpel to separate the tissue (see **Figure 2.1-C**), they were placed in PBS until next step. If required by other users, posterior parts could be placed in PBS at 4°C.

In-house PBS was prepared upstream by mixing 1 PBS tablet in 500 ml distilled water. Mixture was then sterilised in the lab autoclave. Using a binocular loop and with the help of micro-scissors, iris were separated from surrounding epithelia and ciliary bodies (see **Figure 2.1-D**), then placed in in-house PBS at room temperature until next step. To detach the IPE from the stroma, each iris was incubated in 2ml of TryplE for 40 min at 37°C (see **Figure 2.1-E**). Tissues were placed back in DMEM-F12 20% FBS 1% P/S/F (see **Figure 2.1-F**). Separation between the iris stroma and the IPE was done under a binocular loupe with the help of an inoculation cove (see **Figure 2.1-G**). Stroma were removed and IPE suspensions kept in their respective wells in DMEM-F12 20% FBS 1% P/S/F until next step.

Samples were transferred into a class II hood. IPE suspensions were transferred into Falcon 15 ml containing 5 ml of PBS. Centrifugation was run for 5 min at 1,000 rpm in a Sigma 2-6E centrifuge. Pellets were resuspended in 1 ml of DMEM-F12 10% FBS completed with antibiotics at 1% for initial cultures, then at 2%. IPE suspensions were finally seeded in 24 well plates with one IPE suspension for one well (see **Figure 2.1-H**). Plates were placed in incubation at 37°C with 5% CO_2.

To note, in initial cultures, the 24 wells of a 24-well plate were fulfilled with IPE suspensions. That resulted in poor cell adhesion, proliferation or medium quick acidification visualised by the DMEM colouring in yellow. Quickly, the protocol was adapted and only 12 wells on 24 were used, which resulted in much more cell adhesion and proliferation (see **Figure *2.1*-H**).

2.2.5.2 Primary IPE cell extraction – late protocol

This protocol results from investigations led in section **4.3.1**.

The *late protocol* followed the same pattern than the *early protocol* (described in the previous section) but focused on improving the asepsis and reducing the microbial load. In-house PBS was prepared upstream by mixing 1 PBS tablet in 500 ml distilled water. Mixture was then sterilised in the lab autoclave.

Porcine eyes were processed as followed. The globes were isolated by the abattoir staff from dead pigs on the day of slaughter and transported to the lab on ice in the following hours. Further manipulations were done in a class I hood. Extra-ocular muscles were removed with scissors. Eyes were then cleaned in PBS 2% P/S/F, PBS 10% Iodine and PBS alone for 2 min each. Eyes were opened with a scalpel on the back of the ora serata. Anterior and posterior parts were separated. If required by other users, posterior part could be placed in PBS at 4°C. Anterior parts were placed in PBS until next step. Using the scalpel as a scraper, epithelia and iris were detached from the sclera and placed in in-house PBS until next step.

Using a binocular loop and with the help of micro-scissors, iris were separated from surrounding epithelia and ciliary bodies, then placed in DMEM-F12 20% FBS 1% P/S/F until next step. To detach the IPE from the stroma, each iris was incubated in 2ml of TryplE for 40 min at 37°C. Tissues were placed back in DMEM-F12 20% FBS 1% P/S/F. Separation

between the iris stroma and the IPE was done under a binocular loop with the help of an inoculation cove. Stroma were removed and IPE suspensions kept in their respective wells in DMEM-F12 20% FBS 1% P/S/F until next step.

Samples were transferred into a class II hood. IPE suspensions were transferred into 15 ml Falcon containing 5 ml of PBS 2% P/S 2% F for 10 to 15 min. Centrifugation was run for 5 min at 1,000 rpm in a Sigma 2-6E centrifuge. Pellets were resuspended in 1 ml of DMEM-F12 10% FBS 2% P/S 2% F and finally seeded in 12 well plates with one IPE suspension for one well. Plates were placed in incubation at 37°C with 5% CO_2.

2.2.5.3 Adherent and suspended cultures used in Chapter 4

Cells were grown for 8 days on adherent plates in DMEM-F12 10% FBS 2% P/S 2% F. Medium was refreshed at day 3 and day 6. At day 8, cells were incubated in TryplE for 15 to 20 min at 37°C to detach them from the bottom surface. Each IPE suspension was then transferred in a dedicated Falcon 15 ml containing 5 ml sterile PBS. Tubes were centrifuged at 1,000 rpm in a Sigma 2-6E centrifuge and pellet resuspended in 1 ml DMEM-F12 20 ng/ml EGF, 40 ng/ml bFGF and 1X B27 2% P/S 2% F. Cell number was counted with a haemocytometer to adjust cell concentration to 15 cells/µl. Cells were seeded in 24 wells Nunclon Sphera plates, medium was added to give a total volume of 800 µl. To ensure the cells had sufficient amounts of growth factors, 100 µl of the medium was replaced on daily basis. Spheres were grown for 8 days.

Pictures were taken prior to each medium change by an Axiovert S100 microscope and processed with the open-source FIJI software[53].

2.2.5.4 Adherent cell culture used in Chapter 5

Cells were grown for 14 days in total in the adherent plates they were seeded in. Medium changes occurred at day 3 and 6 after the extraction. At day 6, specific media were used and changed every two days until the end of the process. Media were prepared in 50 ml Falcon tubes by adding 1 ml or 2 ml of 50X B27 in 49 ml and 48 ml of DMEM-F12 with 2% P/S 2% F, or 5 ml of FBS into 45 ml of DMEM-F12 with 2% P/S 2% F.

Pictures were taken prior to each medium change by an Axiovert S100 microscope and processed with the FIJI software.

2.2.6 Reverse transcription-quantitative real time PCR

2.2.6.1 Transcript design

Porcine reference and investigated transcripts were designed on Pubmed primer design Primer-BLAST. Gene sequences were selected with the following features: **1**. transcripts must span an exon-exon junction; **2**. annealing temperature difference between the forward and the reverse transcripts must be lower than 1°C; **3**. the total annealing temperature must turn around 60°C; **4**. GC content must be between 40 to 60%; **5**. avoid complementary regions between the two primers. Two to three transcript pairs were finally ordered to ensure that one works. They were assessed on RNA samples from IPE adherent cells and/or IPE spheres. Compositions are indicated in **Table *2-6***.

2.2.6.2 RNA extraction

Prior to extraction, adherent cells were washed in sterile PBS and incubated in TryplE for 10 min at 37°C. Cell suspension was then centrifuged and cell pellet resuspended in 350 µl of RLT lysis buffer from RNeasy kit. IPE agrgegates were directly centrifuged and cell pellet resuspended as indicated above. 350 µl of ethanol 70% were then added. Samples were placed on ice until next step.

Once ready, 700 µl of the RNA extract were placed in RNeasy spin columns from the RNeasy kit and tubes were centrifuged at 8,000 g for 15 s. Supernatant from the collection tube was discarded and 700 µl of RW1 buffer from RNeasy kit were poured into each column. Centrifugation was run at 8,000 g for 15 s. Again, supernatant from collection tubes were discarded and 500 µl of RPE1 buffer from RNeasy kit poured into each column. Tubes were centrifuged at 8,000 g for 15 s, 500 µl of RPE1 buffer poured again and columns centrifuged at 8,000 g for 2 min. Supernatants from collection tubes were discarded again and a final centrifugation at 8,000g for 1 min was done to remove the remnant buffer.

Spin columns were then transferred into 1.5 ml Eppendorf tubes. 30 µl of RNase- and DNase-free water from RNeasy kit was poured into the column and samples were centrifuged at 8,000 g for 1 min. Eppendorfs were then placed on ice and spin columns placed into new eppendorfs. 20 µl of RNase- and DNase-free water from RNeasy kit was added into each column, then tubes were centrifuged at 8,000g for 1 min. Eppendorfs were finally placed on ice. Samples were finally quantified by Nanodrop 2000 and stored at -80^{o}C to conserve RNA integrity.

2.2.6.3 Reverse transcription

Complementary DNA (cDNA) were generated with the Precision nanoScript2 Reverse transcription kit and RNAse- & DNAse-free water from Primer design. RNA solutions were mixed with 1 µl of retro-transcription random nonamer and oligo-dT primers completed to 10 µl with RNAse- & DNAse-free water in a PCR tube. Samples were heated to 65^{o}C for five minutes in a Bio-Rad Thermal cycler T100 for the binding step. Solutions were completed with 5 µl of Nanoscript2 4X buffer, 1 µl of a dNTP mix, 3 µl of RNAse- & DNAse-free water and 1 µl of nanoscript2 enzyme. Solutions were quickly mixed, spinned and processed as followed for the cDNA extension: **1**. 5 minutes at 25^{o}C; **2**. 20 minutes at 42^{o}C; **3**. 10 minutes at 72^{o}C. CDNA generated was measured by Nanodrop 2000 and stored on ice or at -20^{o}C to conserve DNA structure.

2.2.6.4 Quantitative real-time PCR

Samples were prepared using the PrecisionPLUS qPCR SYBR green master mix Quantitative real-time and RNAse- & DNAse-free water from Primer Design, and transcripts from Eurogentec. PCR was processed by diluting cDNA samples in RNAse- & DNAse-free water. Initial assessments started at 1/3, 1/9, 1/27 and 1/81 mixing, later ones at 1/20, 1/40, 1/80, 1/160 and 1/320. QPCR mix was composed as followed: 5 µl of PrecisionPLUS qPCR SYBR green master mix, 0.12 µl of the forward and reverse transcripts, 2.5 µl of the cDNA sample and 2.44 µl of RNAse- & DNAse-free water. Solutions were placed in 96 well plates, closed by MicroAmp TM optical adhesive film and plates placed in Roche LightCycler 96. Features of the PCR process are summarised in **Table 2-5**. Measures of fluorescent transcripts generated were done at the annealing-polymerisation step.

Table 2-5: qPCR features

Step	N cycles	Temperature (°C)	Time (seconds)
Preincubation	1	95	120
Annealing	45	Specific to the transcripts (see **Table 2-6**)	10
Polymerisation	45	60	30
Denaturation	45	95	10
Melting	1	95	10
	1	60	60
	1	97	1
Cooling	45	37	30

Table 2-6: Porcine transcripts

Gene targeted	Sequences	Annealing temperature	Efficiency
	Reference transcripts		
HPRT1	F: CCCAGCGTCGTGATTAGTG	Tested at 60°C	91%
	R: GGCCTCCCATCTCTTTCATC		
β2-microglobulin	F: AACCACTTTTCACACCGCTC	Tested at 60°C	99%
	R: TGGCGTGAGTAAACCTGAAC		
β-tubulin	F: ACTCAGACACAAAGCAAGGA	Tested at 60°C	70%
	R: GCACGTATTTCTTACCGTGG		
TBP	F: GCCAGGAGTTCTGTAGGGTC	Tested at 60°C	138%
	R: GCAAGAAAGAGTGATGCTGGAG		
UBC	F: TGGCTATATAAGGAAGCACCG	Tested at 60°C	
	R: AAGATCTGCATTGTCAGGTGG		
	Pigmentation transcripts		
Tyrosinase	F: CTTCTCCTCTTGGCAGATCAT	Tested at 60°C	88%
	R: CTGGATTTGTCGTGGTTTCC		

TYRP-1	F: AAGGTTCTCACAGTCAGGAG	Tested at 60^{o}C	138%
	R: AAATTGTGGTGTGTTGCCAT		
TYRP-2	F: ATCCTGTTTTCGTGGTCCTT	Tested at 60^{o}C	125%
	R: CATTCGATTGTGACCGATGG		
Recombinant transcripts			
C-Myc	F: GGATAGTGGAAAACCCGGCTG	Tested at 60^{o}C	101%
	R: GAAGTTCTCCTCCTCGTCGC		
GNL3	F: GCACGCAGCATACAAGCTATC	Tested at 60^{o}C	113%
	R: TGTCAACACTTTCTTGGTCGGT		
WNT/β-catenin canonical & non-canonical pathways-associated transcripts			
WNT2B	F: ACACGTCCTGGTGGTACATC	Optimised at 62^{o}C	98%
	R: GAGCGCATGATGTCTGGGTA		
WNT5A	F: GACTGACCCAACCGAGTCTG	Tested at 60^{o}C	108%
	R: ATTCCAATCGACTTCTCCTCCG		
β-catenin	F: TAAGCCTCTCGGTCTGTGGC	Tested at 60^{o}C	77%
	R: TGTACTTCAGAGATCCTCAGGGG		
Ocular developmental transcripts			
PAX6	F: GTAGAACGCGGCTGTCAGAT	Tested at 60^{o}C	99%
	R: GAGAGCAATTCTCAGATCCCTGG		
SOX2	F: ACAGCTACGCGCACATGAAT	Optimised at 59^{o}C	94%
	R: CGAGCTGGTCATGGAGTTGT		
Nestin	F: TCTCTCAGCATCTTGGACCCTA	Tested at 60^{o}C	95%
	R: GGTGTGTCAAGGGTATCGGG		
Retinal pigmented epithelial transcripts			
MITF	F: ATGGCGAATACGTTACCCGT	Optimised at 52^{o}C	84%
	R: TGTGAGCTCCCTTTTGATGTTG		
OTX1	F: CTACCTTCACGCGCTCTCAG	Optimised at 62^{o}C	106%
	R: GGTTCTTGAACCAGACCTGGAC		
MAFB	F: CCGAACAGAAGACCCACCTC	Tested at 60^{o}C	87%
	R: GTAGTTGCTCGCCATCCAGT		

2.2.6.5 DNA electrophoresis

To ensure that the quantitative real-time PCR generated only targeted sequences, PCR products were run on agarose gel. Features to observe were the number of bands generated and their size. If multiple bands were observed, the reaction was not specific. If bands were not equivalents in size, the reaction was not specific neither.

Gels were prepared by mixing 4 mg of agarose in 200 ml of 1X TAE buffer: 40 mM Tris-acetate 1 mM EDTA. Solutions were mixed and melted in the micro-wave until dissolution of the powder was achieved. 10 ul of Safe SYBR green solution was added to the solution, which was then versed into a container for electrophoresis gel. A comb was finally placed in the liquid gel prior to its solidification.

After solidification, 100 ml of 1X TAE buffer was placed into the cast. DNA samples were then prepared by adding 3 ul of DNA coloured loading dye for each cDNA sample. The comb was removed and samples loaded into the gel, completed with a DNA ladder. Once lid was placed, the electrophoresis was started. The process was stopped once an appropriate distance was reached by the samples, around 3 cm. Gels were finally imaged under UV light in a BioRad Gel Doc XR+ System.

2.2.6.6 Analysis by computer

Measures of fluorescent transcripts were processed by the Roche LightCycler 96. Once the reaction was over, data were transferred and processed on computer by the LightCycler® 96 software. Fluorescence developed in each well was summarised by a CT value. Each sample was assessed in three wells for one transcript. From these three CT values was calculated a mean of expression. Then, investigated transcript means were plotted against the reference transcript means. The difference was finally set by the following equation: $2^{-\Delta CT}$.

2.2.6.7 Statistics

Results were summarised by conditions in GraphPad Prism 8 and analysed by the Student paired T-test for initial reference transcript validation, and a Welch ANOVA test for investigated transcripts.

2.2.7 Adherent IPE cell staining on 13 mm glass slides

2.2.7.1 Cell extraction and culture

To label adherent cells, cells were seeded on 13 mm glass slides after their extraction from porcine eye. 13 mm glass slides were sterilised under UV light for 15 min, then placed in 24 well plates.

Cells were extracted from porcine eyes as indicated in section **2.2.5.2**. However, to improve the imaging quality, cells were seeded on sterile 13 mm glass coverslips instead of 12 well plates. During dissection, once IPE cells were detached from the iris stroma, IPE suspensions were transferred into Falcon 15 ml completed with 5 ml PBS. Tubes were centrifuged for 5 min at 1,000 rpm in a Sigma 2-6E centrifuge. Then, pellets were resuspended in 200 µl of DMEM-F12 10 % FBS instead of 1 ml. Glass coverslips were then placed into 12 well plates prior to the cell seeding. The seeding was carefully processed by pipetting 100 µl of IPE suspension on one glass. IPE suspensions rested in that state for 30 min. Finally, 900 µl was slowly carefully added in each well.

ARPE19[204] cells were grown following the same process. The only difference between the two cell types was the medium which contained 1% of antibiotics for ARPE19 cells and 2% for IPE cells.

Medium was changed at day 3 and day 6. At day 8, plates were brought into a chemical hood. Medium was removed and cells were fixed with Formalin 4% for 10 min. Cells were then washed with PBS twice. A final volume of 500 µl PBS was added in each well until use, plates were conserved at 4°C.

2.2.7.2 Staining and imaging

Cell labelling started with a PBS wash and a permeabilisation in Triton X100 1% for 10 min. Normal goat blocking serum 10% was then used for more than an hour prior to primary antibody incubation overnight at 4°C. The following day, cells were incubated in a secondary antibodies solution for one hour and counterstained by DAPI for 20 min. Finally, glasses were mounted on Superfrost® microscope slides with Vectashield antifade media and sealed with nail vanish. Images were acquired using a Zeiss confocal laser

scanning microscope 800 and the Zen Lite 3.1 blue edition (Zeiss) software. FIJI was finally used to process the images, reduce the background and increase the contrast.

2.2.8 Adherent IPE cell staining on 24 well plates

2.2.8.1 Cell extraction and culture

Cells were extracted from porcine eyes as indicated in section **2.2.5.2**. Once IPE samples were detached from their stroma, cell suspensions were transferred into 15 ml centrifuged tubes containing with 5 ml 2% P/S/F PBS. Tubes were centrifuged for 5 min at 1,000 rpm in a Sigma 2-6E centrifuge. Then, pellets were resuspended in 1 ml of DMEM-F12 10 % FBS. Cell solutions were then seeded into 24 well plates with 2 wells for each IPE extraction. Volumes were made up to 1 ml.

Media were changed according to the process described in section **2.2.5.4**. At day 14, plates were brought into a fume hood. Medium was removed and cells were fixed with 10% formalin for 10 min. Cells were then washed twice with PBS. A final volume of PBS was added to cover the samples until use, plates were stored at 4^{o}C.

2.2.8.2 Staining and imaging

Cell labelling started with a PBS wash and a permeabilisation step in Triton X100 1% for 10 min. 10% normal goat blocking serum was then used for more than an hour prior to primary antibody incubation overnight at 4^{o}C. The following day, cells were incubated in a secondary antibody solution for one hour and counterstained with DAPI for 20 min. Finally, 200 µl of PBS was added to each well. Samples were then stored at 4^{o}C protected from light and imaged in the following 24 hours.

2.2.9 IPE aggregates staining

2.2.9.1 Cell culture

To label IPE spheres, cells were cultivated as indicated in section **2.2.5.3**. After 8 days of culture in suspension, spheres were transferred into Falcon 15 ml completed with 2 ml of

PBS. Tubes were centrifuged for 3 min at 1,000 rpm in a Sigma 2-6E centrifuge, then brought in a chemical hood. There, supernatant was removed and pellet resuspended in Formalin 4% for 15 min. Then, 5 ml of PBS was added to dilute the fixative. Tubes were centrifuged for 3 min at 1,000 min in a Sigma 2-6E centrifuge and pellet resuspended in 5 ml of PBS. The manipulation was repeated again.

To prepare spheres to the OCT embedding, pellets were resuspended in a 15% glucose-PBS solution for 2 hours at 4°C. Spheres were then conserved in a 30% glucose-PBS solution at 4°C. Samples were embedded in Tissue freezing medium in a slurry containing dry ice. Blocks were then sectioned at 5 µm and collected onto Superfrost Plus slides. They were immediately placed at -20°C until use.

2.2.9.2 Staining and imaging

Prior to label, slides were placed at room temperature for 30 min in a covered slide racker with wet paper towel. Once ready, sections were incubated in Triton X100 1% for 15 min followed by an incubation in normal goat blocking serum 10% for at least an hour. Sections were then incubated overnight at 4°C with primary antibody solution. The following day, sections were incubated with secondary antibody solutions for 1 hour and counterstained with DAPI for 20 min. Slides were mounted with VectaShield antifade media and sealed with nail polish. Images were acquired using a Zeiss confocal laser scanning microscope 800 and the Zen Lite 3.1 blue edition (Zeiss) software. FIJI was finally used to process the images, reduce the background and increase the contrast.

2.2.9.3 CFSE and DiD-/DiI Vybrant staining and imaging

IPE cells were cultivated as indicated in section **2.2.5.3**. At day 8 prior to be seeded on suspension plates, they were incubated in 10nM CFDA-SE-sterile PBS for CFSE staining or in DiD- or DiI- sterile PBS, prepared at 5 µl for 1 ml for Dies Vybrant staining. Incubations lasted from 15 to 20 min at 37°C in a sterilised Eppendorf 1.5 ml. Cells were then transferred into a Falcon 15 ml with 5 ml of sterile PBS and centrifuged at 1,000 rpm in a Sigma 2-6E centrifuge for 5 min. Pellets were resuspended in 5 ml sterile PBS and centrifuged again with the same settings. Cells were counted with a haemacytometer, seeded and cultivated according to the protocol detailed in section **2.2.5.3**. Spheres were

grown for eight more days. They were then fixed and processed according to the protocol detailed in section **2.2.9**. The day of imaging, sections were placed at room temperature for 30 min in a closed slide racker with wet paper towel. Once ready, sections were incubated in Triton X100 1% for 15 min and cleaned twice in in-house PBS. Sections were then incubated in DAPI for 20 min, cleaned twice in in-house PBS and mounted in Vectashield medium. Images were acquired using a Zeiss confocal laser scanning microscope 800 and the Zen Lite 3.1 blue edition (Zeiss) software. FIJI was finally used to process the images, reduce the background and increase the contrast. Sections were conserved at -20^{o}C after imaging. **Table 2-7** summarises the dyes used.

Table 2-7: Summary of dyes used

Name	Description	Purposes
Carboxyfluorescein succinimidyl ester (CFSE)	Product of the cleavage of CFDA-SE by intracellular esterases, CFSE covalently binds to protein free amines and remains in the cytoplasm. Excitation: 492 nm – Emission: 517 nm	To assess cell proliferation
Vybrant® DiD	Lipophilic, this compound diffuses and stick to the plasma membranes. Excitation: 649 nm – Emission: 671 nm	To assess cell aggregation in couple with Vybrant DiI®
Vybrant® DiI	Lipophilic, this compound diffuses and stick to the plasma membranes. Excitation: 552 nm – Emission: 569 nm	To assess cell aggregation in couple with Vybrant DiD®

2.2.10 Resazurin-based metabolic assessment

Resazurin stock solution was prepared from resazurin sodium salt in sterile 2% P/S/F PBS to reach a 0.1 mg/ml concentration. This solution was then filtered twice through 0.22 µm filters and stored at 4^{o}C protected from light.

Measurements were undertaken at time points when media was changed. Prior to assessment, stock solution was diluted in the three media types (see **Figure 5.1**) at a ratio of 1:10. Cell media were replaced by resazurin-containing media. Plates were returned to the incubator for 2 hours. Media were then transferred into sterile eppendorfs and the

latter were placed on ice immediately. Cells were carefully washed three times in PBS and 2 ml of fresh media was then added in each well. Plates were replaced in the incubator at 37^{o}C 5% CO_2.

Once cell culture was completed, 200 µl of each sample were placed into black 96 well plates. Plates were then read for their fluorescence at 560 nm in a BMG Labtech FLUOROstar Optima plate reader. To get a complete view, gains were read from 1,000 to 1,700-1,800. Numerical data were processed using Excel.

2.2.11 Statistics

Statistics for cell culture

For section **4.3.1**, the aim was: to compare the two cell culture processes. So, raw data from 36 cell counts were reproduced in Excel, 18 cells concerned 18 independent IPE cells samples grown by the original process (see **Table 4-1**), the 18 others were grown by the condition 4 (see table 18 – condition 4). Data were then plotted together by the GraphPad Prism 8 software. As each IPE sample was independent, only the mean from all samples in one condition was considered. So, the T-test was set up as unpaired. The number of samples per conditions being low, data were test positive for Normality at p value = 0.05 by the Shapiro-Wilk test. A gaussian distribution being assumable but the standard deviations between the two conditions being different, the parametric unpaired T-test with Welch correction was set up.

For section **4.3.2**, the aims were:

1. To compare the means of spheres generated per plate types: 6 independent samples grown on Greiner suspension plate were plotted against 6 independent samples grown on Nunclon sphere plates; the process run was the same than the one in section 4.3.1;
2. To compare the sphere size per plate type: for both Greiner suspension plates and Nunclon Sphera plates, 3 independent samples grown for three days plus 3 grown for six days were used. Sphere sizes were measured from pictures with FIJI for an arbitrary unit (a.u.). Samples were of unequal size with more spheres measured in Nunclon Sphera plates. Data were then collected in Graphpad Prism and a one-way ANOVA was selected. Due to data sets being different, a “no matching or pairing” analysis was set up. Shapiro-Wilk test resulted negative, so a gaussian

distribution could not be assumed. So, a non-parametric Kruskal-Wallis test was selected.

3. To compare the number of spheres attached versus spheres in suspension for Greiner suspension plates only: 2 independent samples were imaged at day 4 and day 8 after being seeded in Greiner suspension plates. 12 wells per samples were run and count was taken distinguishing suspended spheres and attached ones. Data were plotted in Graphpad Prism and a one-way ANOVA was selected. Due to data sets being different, a "no matching or pairing" analysis was set up. Shapiro-Wilk test resulted negative, so a gaussian distribution could not be assumed. So, a non-parametric Kruskal-Wallis test was selected.

Statistics for CFSE-labelled IPE cells:

For section **4.4.1**, the aim was: to measure the fluorescence intensity from CFSE-labelled aggregates. Data were summarised as pixel number and colour value over a scale of 256 shades of green by the software. Data were then transformed into graphs by GraphPad Prism8. Means and standard deviations per pixel value were obtained from the five sections investigated.

3 Chapter 3: Characterisation of the porcine IPE tissue

3.1 Overview

The IPE lies on the back of the iris stroma, taking the form of a thin pigmented layer. From there, it participates in mydriasis, the opening of the pupil, while its pigmentation absorbs scattering light not in line with the pupil-lens axis. So far, few investigations only investigated the IPE protein content *in vivo* and none were related to stem cells. One the reason being the IPE intrinsic pigmentation, making it difficult to observe by histology and immunohistochemistry. Therefore, that work was dedicated: 1. to fulfil that knowledge gap by integrating a melanin-removal step in H&E and IHC protocols; 2. to observe fundamental proteins related to: the cytoskeleton, the basal lamina, the cell-cell junction and the proliferation. 3. To observe the presence of generic stem cells markers and proteins associated with development. The summary of this work helped to distinguish specific compartments in the porcine IPE, including cell proliferation. However, none of the markers used for stem cells was observed, on the contrary of those associated with the development of the eye.

3.2 Aim & objectives of the chapter

The aim of this chapter was to distinguish different regions in the IPE *in vivo* and focus on the area(s) involved in proliferation.

The objectives were:

- To establish a robust method to remove the melanin from formalin-fixed paraffin-embedded (FFPE) porcine IPE sections;
- To investigate the components of porcine IPE cytoskeleton, basal lamina and cell-cell junctions;
- To assess proliferation in native IPE;
- To identify areas of stem cell and development-related proteins expression.

3.3 Depigmentation of the porcine IPE

3.3.1 H_2O_2-based depigmentation runs well into a haematoxylin and eosin staining protocol

The first objective was to integrate the process from Manicam *et al*[205] into the institute's *in-house* H&E protocol on porcine ocular sections (see **Figure 3.1-A**). To depigment, a 10% H_2O_2 PBS solution was heated at 60°C in which formalin-fixed paraffin-embedded tissue sections were incubated after their rehydration. Sections were cleaned in running tap water prior and after the depigmentation. Several time points were studied to observe how the hydrogen peroxide would: **1**. remove the melanin; **2**. damage the tissue (see **Figure 3.1-B**). Tissue sections used there were among the first processed by the writer, and so did not reflect on the IPE specifically but on porcine ocular pigmented tissues in general. Investigations coming after this one will focus on the IPE specifically.

All sections were stained as expected: haematoxylin marked cell nuclei, eosin marked cytoplasm and mesenchyme. Melanin was progressively removed, the first nuclei in the pigmented epithelia appearing after 20 minutes of incubation. That was the minimum time required to observe an intracellular structure.

It was also observed that the longer the incubation, the more damaged the sections. Distinction between tissues in a single section was easy to do with a short (10 min) to medium incubation (30 min; see **Figure 3.1-B**). Incubations longer than that suffered damages from excess oxidation. Cytoplasmic and stromal elements could be observed but demonstrated a loss in consistency compared to the controls. Only nuclei seemed to remain consistent. Overall, the depigmentation was easily integrated into the H&E protocol, the optimal window being between 20 and 30 minutes of incubation.

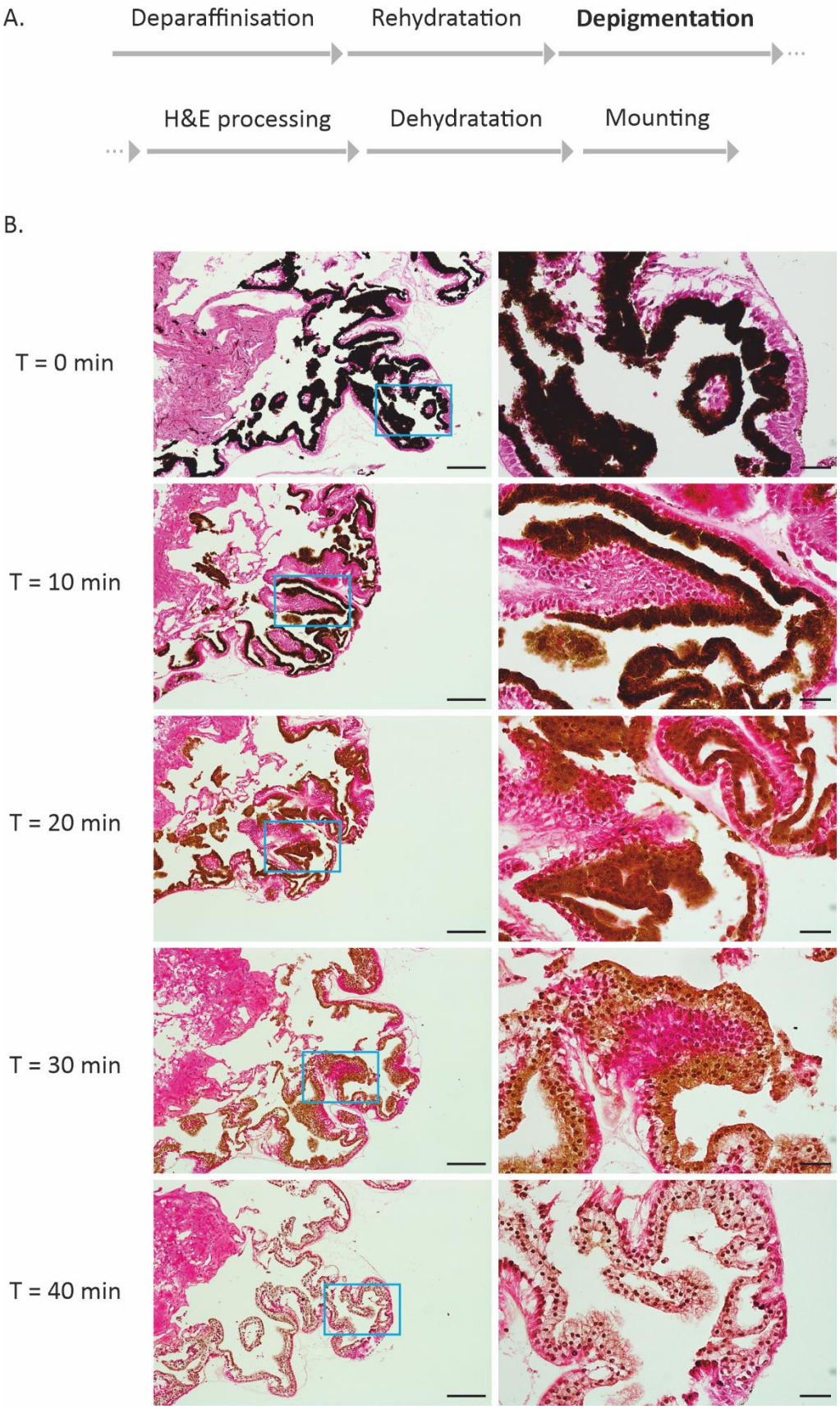

Figure 3.1: H&E analysis of porcine ocular pigmented epithelial sections depigmented by a 10% H_2O_2-based solution. A. Diagram representing the different steps of the processed H&E with the depigmentation included in. **B.** Representative images of porcine

ocular sections depigmented by a 10% H_2O_2-based solution for times indicated on the left. Melanin in epithelia has been progressively removed with cell nuclei being visible at T = 20 min. However, in the meantime, tissues demonstrated damages. The Blue boxes on left pictures indicate higher magnifications on right pictures. On the left pictures, SB = 200 µm. On the right pictures, scale bars = 100 µm.

3.3.2 H_2O_2-based depigmentation requires optimisation to run into fluorescent immunohistochemistry

The second objective was to assess the compatibility between the depigmentation and fluorescent immunohistochemistry. To get a signal throughout the assessment, a robust protein present in the IPE was necessary. So, desmin, a type III intermediate cytoskeleton protein[206], was selected. Desmin has the advantage to be present through the dilator muscle, the non-pigmented part of the IPE[207]. So, it is not masked by melanin and non-depigmented sections could be used as positive controls.

Depigmented sections were processed in a similar fashion than the assessment done in section **3.3.1**. Briefly, tissue sections were de-waxed in xylene, rehydrated in progressive diluted ethanol solutions and depigmented in 10% H_2O_2 solution at 60°C. They were then processed for fluorescent immunohistochemistry (see section **2.2.2.3**).

The first desmin-based investigation in the porcine eye correlated with observations done in the human eye[206]. Non-depigmented sections demonstrated desmin along the IPE anterior layer, which shaped as fibres (see **Figure 3.2-D**). No fluorescence from the green channel was detected from the pigmented layer. Conversely, DAPI-labelled nuclei were observed in both layers. Other fibres in the iris stroma were labelled, which shall correspond to the sphincter muscle.

In depigmented sections, only DAPI-stained nuclei were observed (see **Figure 3.2-E**). Nuclei were labelled in the iris stroma, the IPE and the ciliary body. Background from the green channel was observed in the stroma. The depigmentation made the IPE cell nuclei much more observable than those from the pigmented sections. That proves that the process for fluorescent investigation worked but required adjustments depending of the cell structure to stain and its chemical composition.

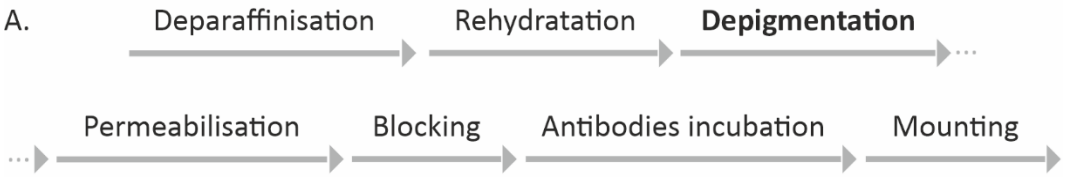

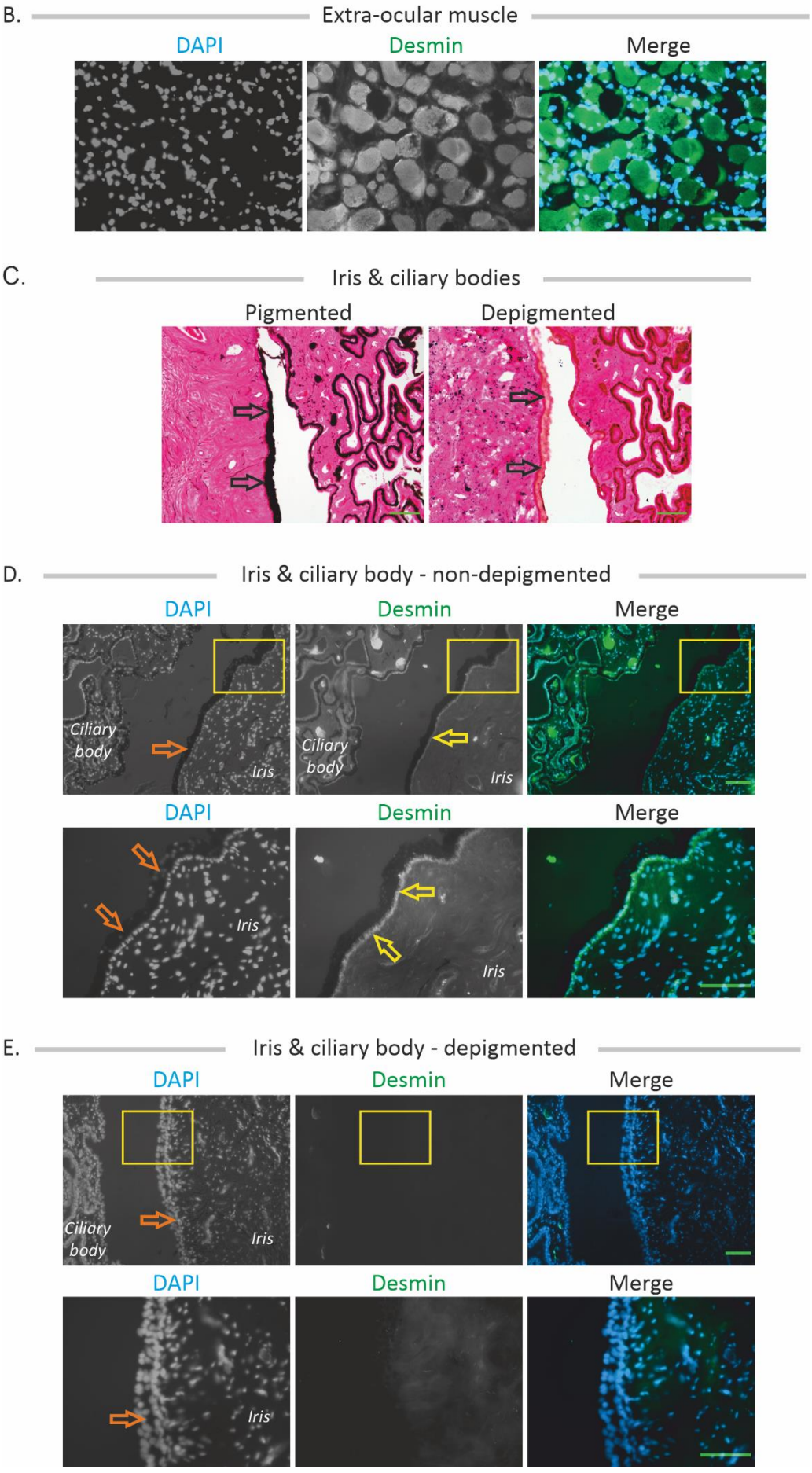
B.
Extra-ocular muscle
DAPI
Desmin
Merge
C.
Iris & ciliary bodies
Pigmented
Depigmented
D.
Iris & ciliary body - non-depigmented
DAPI
Desmin
Merge
Ciliary body
Iris
DAPI
Desmin
Merge
Iris
Iris
E.
Iris & ciliary body - depigmented
DAPI
Desmin
Merge
Ciliary body
Iris
DAPI
Desmin
Merge
Iris

Figure 3.2: Representative pictures of desmin in porcine iris sections depigmented by a 10% H_2O_2 solution. A. Diagram representing the different steps of the processed FIHC with the depigmentation included in. **B.** Porcine extra-ocular muscle section used as positive control for the anti-desmin antibody. Muscle fibers reacted well with the anti-desmin antibody, revealed by an AF 488 secondary antibody. **C.** H&E of pigmented & depigmented porcine iris sections. **Black arrows** indicate the IPE. SB = 100 µm. **D. & E.** Porcine iris sections non-depigmented and depigmented respectively. Desmin was labelled in the IPE anterior layer and revealed by an AF 488 secondary antibody on the non-depigmented section (= **yellow arrows**). No signals were observed on the depigmented section. **Orange arrows** indicate the IPE. Yellow boxes show higher magnifications below. Tissues are labelled by the white and italic writing. DAPI is in blue, desmin in green. Small scale bars = 100 µm, tall scale bars = 50 µm.

3.3.3 Desmin was labelled on depigmented section with an appropriate fixation of the original tissue

To label desmin on depigmented sections, several experiments were done to identify one or more parameter(s) to adjust. Changes were implemented in the process described earlier (see section **2.2.2.3**) with the same anti-desmin antibody. Results are summarised in the following **Table 3-1**. Experiment A is shown in the Appendices (see section **7**) as an example of negative result (see **Figure 7.1**).

Table 3-1: Scheme of optimisation

Original process:	**Chemicals**	**Incubation time**	**Temperature**
	10% H2O2 in PBS	20 min	60°C

Experiment:	**H_2O_2 (in %)**	**Tissue depigmented for**	**Tissue fixed for**	**Temperature (°C)**	**Desmin label**
A.	10%	5, 10 & 15 min	10 min	60°C	No
B.	5%	20 min	10 min	60°C	No
C.	10%	20, 25 & 30 min	10 min	45°C	No
D.	15%	5, 10 & 15 min	10 min	60°C	No
E.	20%	5, 10 & 15 min	10 min	60°C	No
F.	10%	10, 20, 30, 40, 50 & 60 min	25 min	60°C	No
G.	10%	30 & 60 min	24 hours	60°C	Yes

Experiment G was designed to give long time to the formalin to fix the tissue in a deeper manner. That was thought to be large enough to protect desmin from the hydrogen peroxide but could also severely reduce the depigmentation efficiency. The following protocol did not vary, H_2O_2 incubations were done over 30 and 60 minutes. As a result, desmin was labelled on depigmented sections incubated for 30 minutes (see **Figure 3.3-A**). A dotted line was observed, which followed the invaginations of the posterior side of the iris. IPE nuclei were clearly labelled by the DAPI, on the opposite of the iris stromal ones. For sections incubated for 60 minutes, some desmin signals were observed but no DAPI remained in the IPE (see **Figure 3.3-B**). Two experiments were done from other tissues fixed for 24 hours in 4% formalin and confirmed that result.

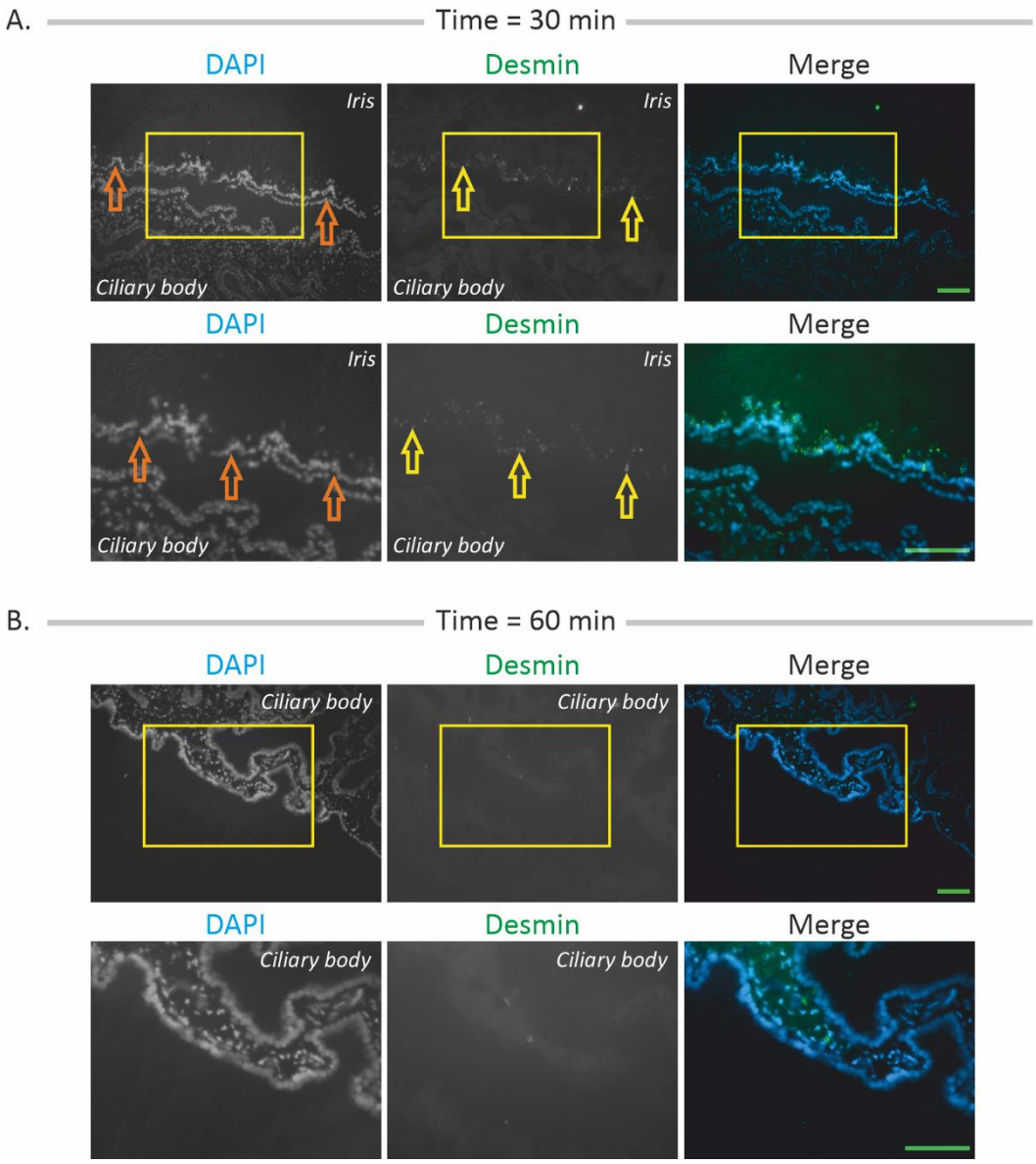

Figure 3.3: Representative pictures of the experiment G. Porcine iris tissue was fixed in 4% formalin for 24 hours prior to the tissue embedding. Sections were then labelled with

an anti-desmin antibody and an AF 488 secondary antibody. **A.** Sections depigmented for 30 min. Desmin (= **yellow arrows**) is labelled in the IPE anterior layer. **Orange arrows** indicate the IPE. **B.** Sections depigmented for 60 min. No signals, both DAPI and desmin, were observed in the IPE. Yellow boxes show higher magnifications below. Tissues are labelled by the white and italic writings. DAPI is represented in blue, desmin in green. Small scale bars = 100 µm, tall scale bars = 50 µm.

3.3.4 Investigation of the chemicals, the time of the process and the pH

Despite having successfully depigmented porcine IPE sections and labelled desmin on them, fluorescent and H&E sections showed extensive damages from the depigmentation. To get an efficient depigmentation with preserved sections, the reaction required optimisation. Results were categorised according to: **1**. the presence of desmin and DAPI labelled over the tissue; **2**. the signals observed; **3**. the quality of the depigmentation assessed by H&E staining; **4**. the observed H&E staining.

Four solutions were experimented with features showed in **Table 3-2**. Disodium phosphate (Na_2PO_4) has been successfully combined as a diluent with H_2O_2 to depigment tissue sections, including the human IPE[206, 207]. Therefore, its suitability in the developed protocol was experimented. Sections were processed in different conditions: 20 min, at 60°C; 18 hours, at room temperature. Sections were finally labelled for desmin and counter-labelled by DAPI. Results are summarised in **Table 3-3**.

This section shows the results from the selected composition, process and pH selected: 3% H2O2 at 60°C for 20 min & at pH9. Result from the short depigmentation with a 10% H_2O_2-1% Na_2Po_4 solution is shown in the Appendices as an example of non-selected protocol (see **Figure 7.2**).

Table 3-2: Hydrogen peroxide solutions

Components	Composition
Hydrogen peroxide only	3% H_2O_2 in PBS (v/v)
	10% H_2O_2 in PBS (v/v)
Hydrogen peroxide and disodium phosphate	3% H_2O_2 1% Na_2Po_4 in PBS (v/v; w/v)
	10% H_2O_2 1% Na_2Po_4 in PBS (v/v; w/v)

Table 3-3: Summary of short and long depigmentations with different H_2O_2 solutions

Short depigmentation: 60°C; 20 minutes				
Solution	**3% H_2O_2 in PBS**	**10% H_2O_2 in PBS**	**3% H_2O_2 1% Na_2Po_4 in PBS**	**10% H_2O_2 1% Na_2Po_4 in PBS**
Desmin & DAPI	Positive	Positive	Positive	Positive
Signals observed	Desmin: fibres DAPI: nuclei	Desmin: dots DAPI: nuclei	Desmin: dots DAPI: Nuclei	Desmin: dots DAPI: nuclei
Depigmented	Partly	Fully	Fully	Fully
H&E quality	Good	Good	Non-usable	Non-usable
Long depigmentation: room temperature; 18 hours				
Solution	**3% H_2O_2 in PBS**	**10% H_2O_2 in PBS**	**3% H_2O_2 1% Na_2Po_4 in PBS**	**10% H_2O_2 1% Na_2Po_4 in PBS**
Desmin & DAPI	Desmin: negative DAPI: positive	Desmin: positive DAPI: positive	Desmin: negative DAPI: positive	Desmin: negative DAPI: negative
Signals observed	Desmin: background DAPI: nuclei	Desmin: remnants of fibres DAPI: remnants of nuclei	Desmin: nothing DAPI: remnants of nuclei	Desmin: background DAPI: background
Depigmented	Fully	Fully	Fully	Fully
H&E quality	Non-usable	Non-usable	Non-usable	Non-usable

At 3% at 60°C and for 20 min, H_2O_2 removed only a part of the melanin, the IPE remaining strongly brown. The overall H&E staining was good with iris stromal fibres, cells and vessels being clearly differentiated by eosin. Moreover, haematoxylin labelled clearly cell nuclei, except in the IPE due to the melanin (see **Figure 3.4-A**). The anti-desmin antibody gave a consistent signal starting from the ciliary body and going all along the IPE. The DAPI labelled more cells from the ciliary body and few from the IPE, none from the iris stroma (see **Figure 3.4-B**). As both the H&E and fluorophore labels were at an appreciable quality, a fair balance between section quality and melanin removal seemed to be reached. Thus, further histological and FIHC-based investigations would rely on a 3% H_2O_2 solution, with the depigmentation run at 60°C for 20 min.

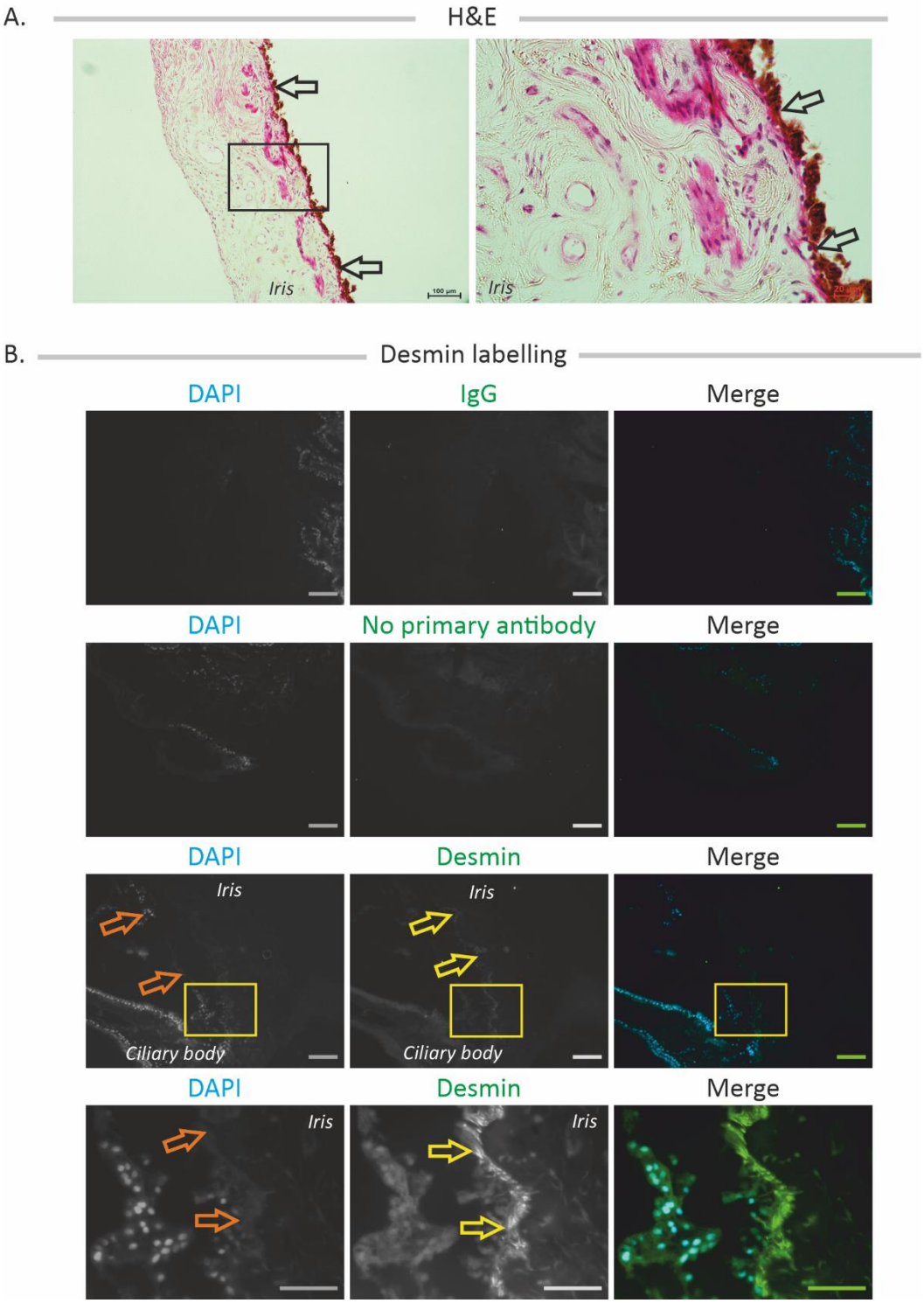

Figure 3.4: Porcine iris sections depigmented by 3% H_2O_2 at 60°C for 20 min. A. H&E-stained sections. **Black arrows** indicate the IPE. The black box indicates higher magnification on the right. SB are indicated in the right bottom corner. **B.** Anti-desmin FIH. Desmin was labelled with an AF 514 and is indicated in the IPE anterior layer (= **yellow arrows**). **Orange arrows** indicate the IPE. Boxes show higher magnifications below. Tissues are labelled by the black (H&E) / white (FIHC) and italic writings. DAPI is represented in blue, desmin in green. Small scale bars = 100 µm, tall scale bars = 50 µm.

In 1995, Shi *et a*l. investigated the pH of antigen retrieval solutions to label different proteins[208]. With the same spirit, H_2O_2-based depigmentations were performed with three different pHs. The aim was to observe potential benefits on the process efficiency or/and the staining quality. The original 3% H_2O_2 solution pH was ≈6.9, so the spectrum was sprayed from 5 to 9 using chlorhydric acid (HCl) and sodium hydroxide (NaOH). Three factors were set to analyse the pictures: the melanin content; the H&E quality; the desmin and the DNA quality staining. Results are summarised in **Table 3-4**.

Table 3-4: Summary of pH-based depigmentation

PH	**5**	**7**	**9**
Melanin content	High	Null	Null
Desmin labelling	Low	Low	High
Desoxyribonucleic acid labelling	Null	Null	Null

3% H_2O_2 at pH 9 depigmented the iris, the IPE and the CBPE (see **Figure 3.5-A**). No melanin remained visible. That said, sections on the H&E were bleached at a high level. Iris stromal fibres were each distinguishable from the others and eosin-stained cytoplasms were absent or nearly from the IPE. Red blood cells and dense area of CB stroma and epithelia were properly labelled. Hematoxylin-stained nuclei were well visible, differentiating the epithelia from the stroma. On the fluorescent assessment (see **Figure 3.5-B**), desmin was clearly labelled from the ciliary bodies – iris junction to the pupillary extension with dilator fibers properly labelled. Again, the blue channel did not show nuclei-based DNA but an important background over the entire section. So, higher pH increased the efficiency as sections were nearly or completely melanin-free, participating to make brighter signals from the anti-desmin labelling. Thus, more structures could or would be marked in later investigations by using 3% H_2O_2 at pH 9.

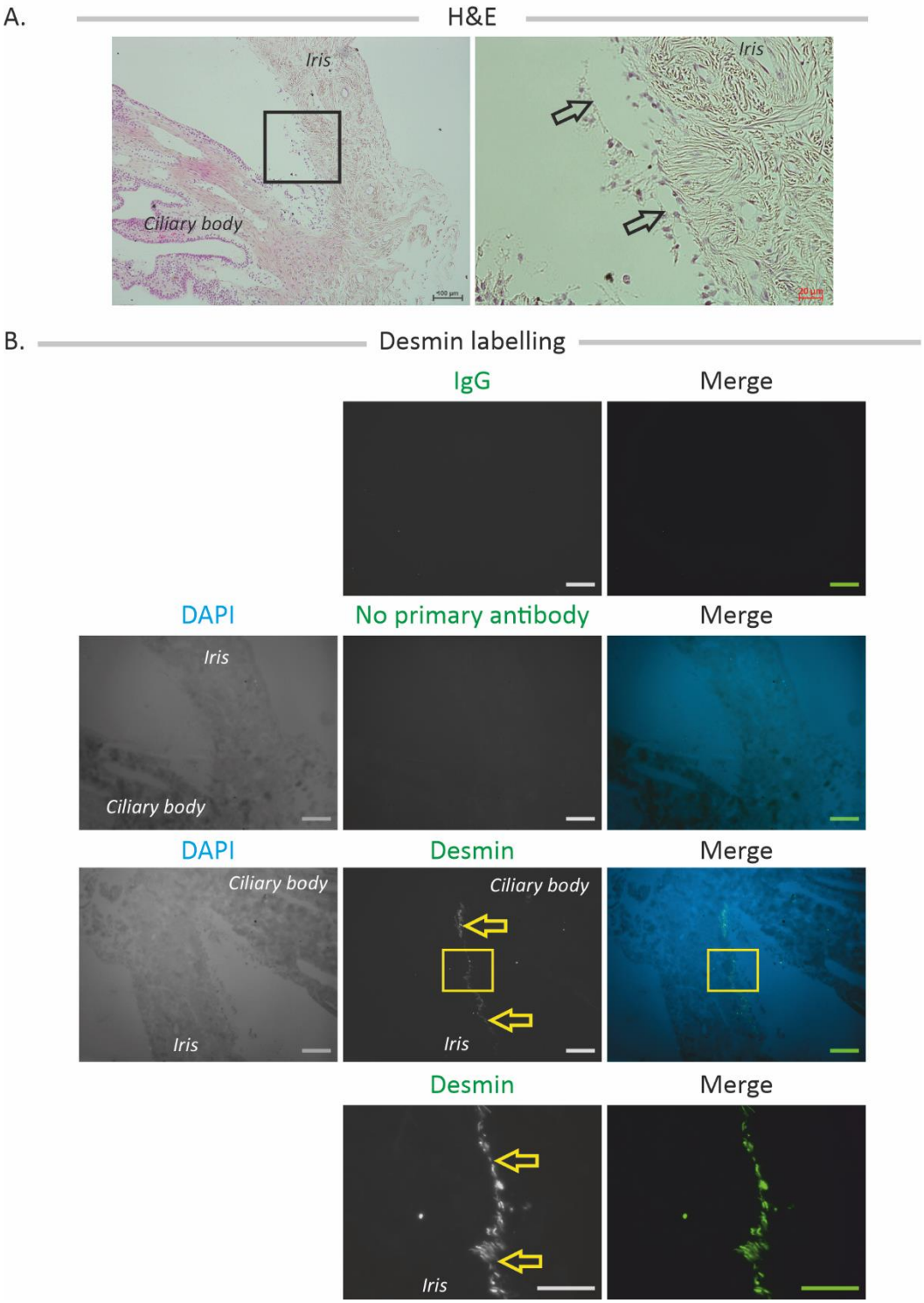

Figure 3.5: Porcine iris sections depigmented by 3% H_2O_2 at pH 9. A. H&E-stained sections. **Black arrows** indicate the IPE. The black box indicates higher magnification on the right. SB are indicated in the right bottom corner. **B.** Anti-desmin FIH. Desmin was labelled with an AF 514 and is indicated in the IPE anterior layer (= **yellow arrows**). Boxes show higher magnifications below. Tissues are labelled by the black (H&E) / white (FIHC) and italic writings. DAPI is represented in blue, desmin in green. Small SB = 100 µm, tall SB = 50 µm.

3.4 Porcine IPE cytoskeleton assessment

3.4.1 Intermediate filaments

3.4.1.1 Vimentin is present in human and porcine irises

Originally discovered in murine 3T3 fibroblasts, vimentin was described as a wickerwork network, *vimentum* in Latin, which distinguished itself from cytokeratins type I and II[209]. Its fibrous structure is based on a set of three coil domains holding together by hydrophobic and ionic charges. This allows quick filaments formation and dynamic rearrangements, comparable to those of actin and microtubules filaments[210]. In line with iris movements, vimentin has been found as the main intermediate filament in the human IPE[207]. So, investigations were run on porcine iris pigmented and depigmented sections and with human ones as positive controls.

On human pigmented sections, IgG control pictures show a certain background in the ciliary and the IPE regions (see **Figure 3.6-A**). When incubated with anti-vimentin antibody, this background is still present but specific marks taking the form of fibres are labelled as going along a posterior-to-anterior axis and from a central-to-peripheral direction. Some cells from the stroma were labelled as well.

On human depigmented sections (see **Figure 3.6-B**), vimentin fibres were labelled all along the IPE, mostly in its anterior part. A nearly empty space seemed to remain vimentin-free and what might be plasma membrane are visible as well. The iris stroma was strongly labelled on the opposite of what was observed earlier, especially in its anterior part. DAPI was observed in the IPE only.

On porcine pigmented sections (see **Figure 3.6-C**), no vimentin was observed along the IPE. Similarly to what was observed on human pigmented sections, a background was observable on both IPE and CBPE, showing them by contrast in grey. No stromal or endothelial cells were labelled. The same statement applied for the porcine depigmented sections with no observed vimentin but an important background instead (see **Figure 3.6-D**).

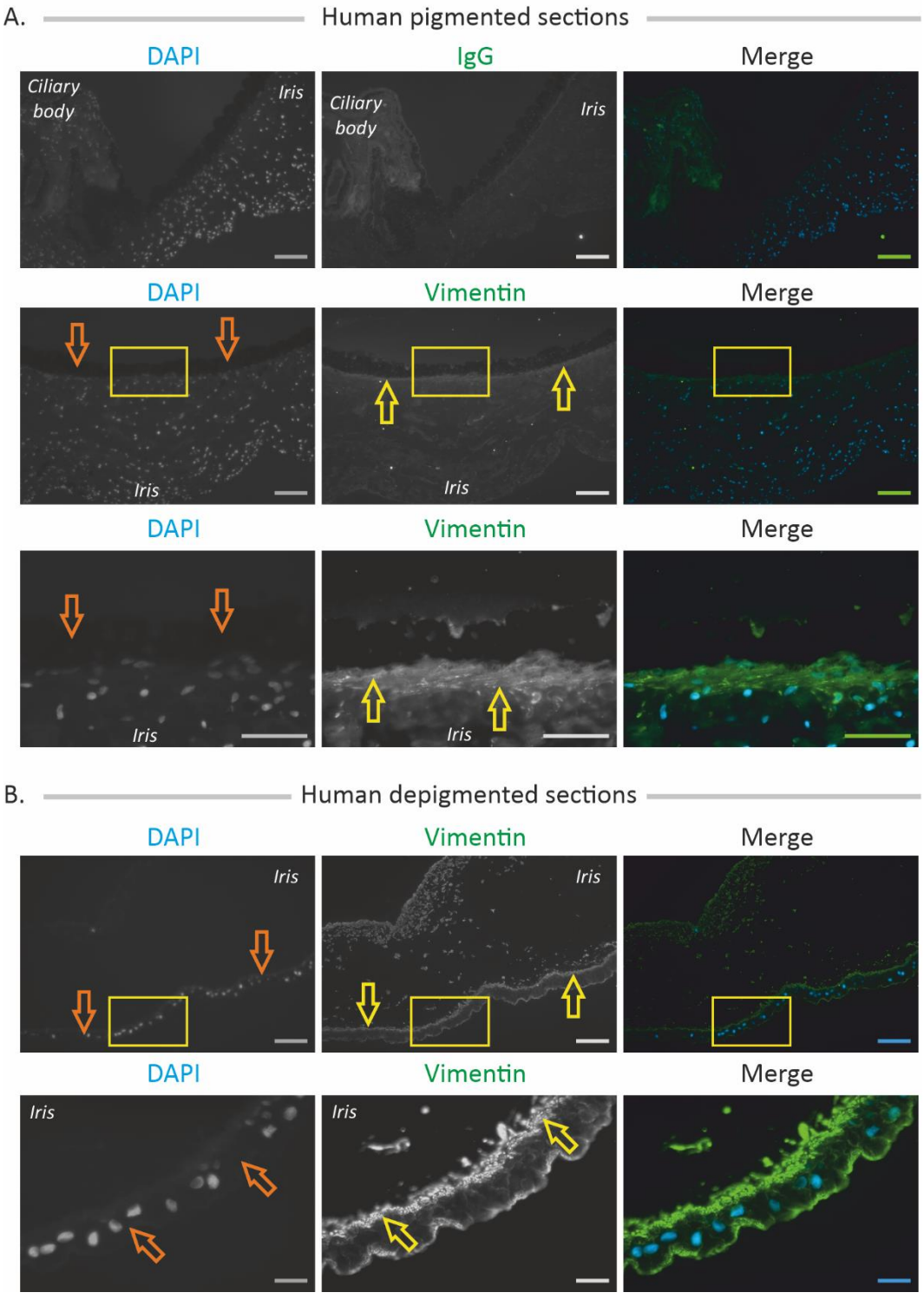
A.
Human pigmented sections
DAPI
IgG
Merge
Ciliary body
Iris
Ciliary body
Iris
DAPI
Vimentin
Merge
Iris
Iris
DAPI
Vimentin
Merge
Iris
Iris
B.
Human depigmented sections
DAPI
Vimentin
Merge
Iris
Iris
DAPI
Vimentin
Merge
Iris
Iris

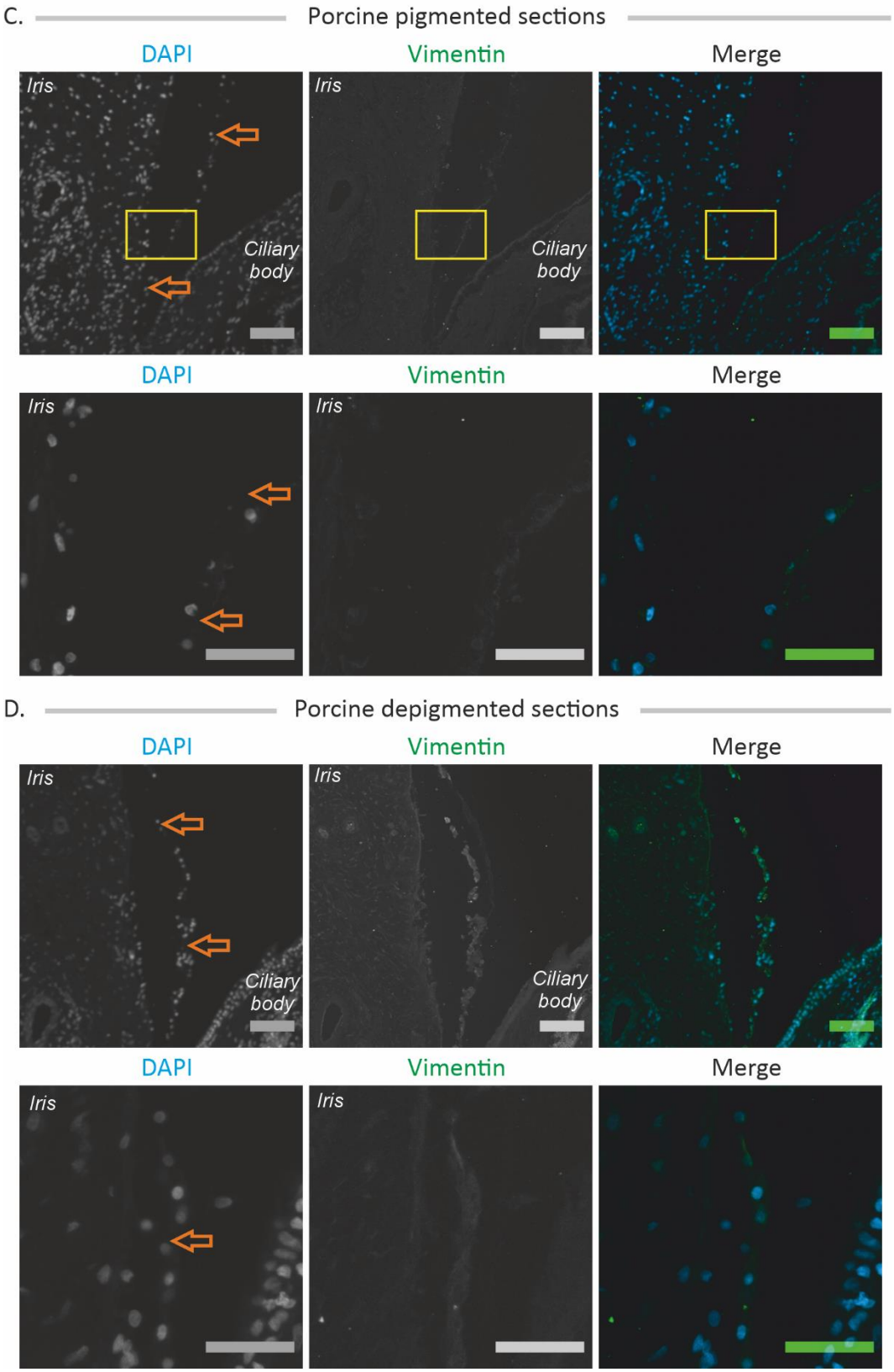

Figure 3.6: Representative pictures of vimentin in human and porcine iris sections. A. Human pigmented iris sections. **B.** Human depigmented iris sections. **C.** Porcine pigmented iris sections. **D.** Porcine depigmented iris sections. Vimentin (= **yellow arrows**) was labelled in all human sections but remained absent from all the porcine ones. **Orange arrows** indicate the IPE. Yellow boxes indicate higher magnifications below. Anti-vimentin

primary antibodies were labelled with an AF 488 secondary antibody. Tissues are labelled by the white and italic writings. DAPI is represented in blue, vimentin in green. Small scale bars = 100 µm, tall scale bars = 50 µm.

As vimentin detected on both human and porcine sections was low and absent respectively, two different methods were used. The objectives were to assess the suitability of the antibody to mark vimentin and check its polyvalence on different species as indicated by the manufacturer. So, vimentin in human sections was assessed by colorimetric IHC using the ImmPACT® VIP peroxidase (HRP) substrate, which generates a purple signal. Vimentin from porcine IPE was assessed by Western-Blot.

On IHC-processed human sections (see **Figure 3.7-A**), not depigmented, vimentin bands were detected in the iris stromal anterior part, the stromal posterior one and in the IPE anterior layer. The use of a purple colorimetric dye allowed a better distinction with the pigment than a DAB-based. Methyl green was used as nuclear staining. So, the suitability of the anti-vimentin antibody was confirmed and vimentin in the IPE well observed.

On WB-processed porcine tissue samples (see **Figure 3.7-B**), vimentin was detected at a high degree in the IPE sample considering the low GAPDH band corresponding. However, further postulates about the vimentin content in the IPE are technically impossible due to the difference between the GAPDH contents. Different bands were observed running from 50 kDa to 38 kDa, which shall correspond to the different forms vimentin filaments can take[210]. That result was reproduced with these little bands always labelled.

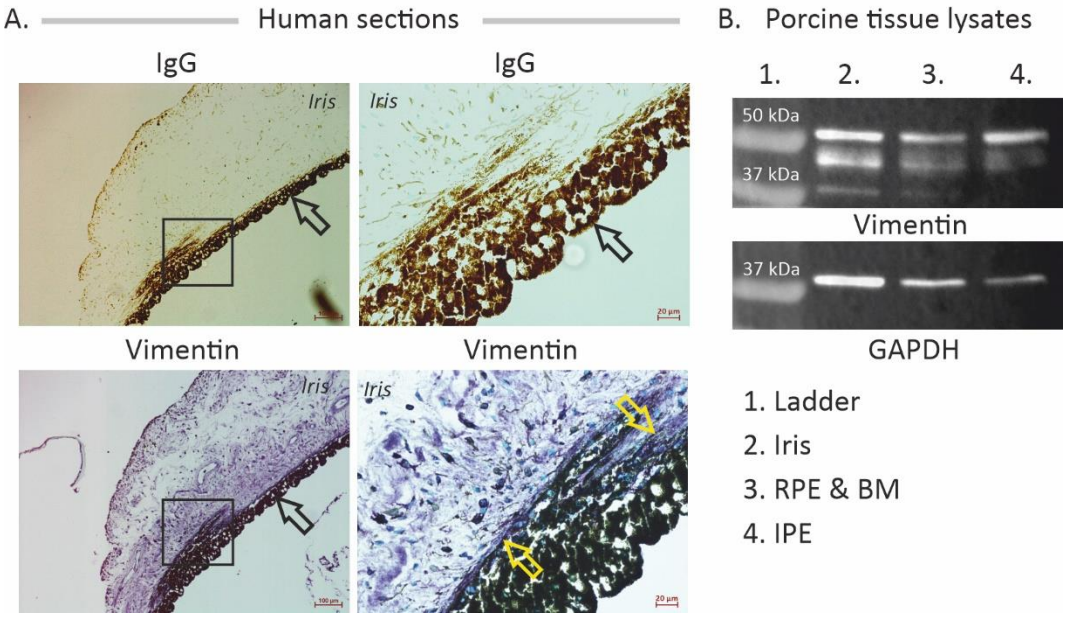

Figure 3.7: Representative pictures of vimentin in human iris section and on porcine ocular protein extract. A. Human iris section. Vimentin is in purple, nuclei in methyl green. Vimentin is present over the main body of the iris and in the IPE anterior layer (= **yellow arrows**). **Black arrows** indicate the IPE. Boxes show higher magnifications on the right. Anti-vimentin primary antibodies were labelled by solutions of the ImmPACT® VIP peroxidase (HRP) substrate kit. Tissues are labelled by the black and italic writing. Scale bars = 100 µm (left pictures) and 20 µm (right pictures). **B.** Vimentin content in proteins extracted from pig eyes. 20 µg of proteins were loaded per well. GAPDH was used as a loading control. Anti-vimentin antibodies were bind to Numbers indicate the samples loaded and described above.

Thus, vimentin was properly labelled on human sections as done before[207]. Its presence on porcine sections was not possible to detect by IHC means but a high content was present in protein samples assessed by WB.

3.4.1.2 Cytokeratins type I and II are absent

According to previous unpublished investigations from the Kearns group, IPE cells grown *in vitro* expressed cytokeratins type I and II, which were assessed by a pan-cytokeratin antibodies[211]. So, investigations were done to assess the presence of cytokeratins in the tissue with two pan-cytokeratins antibodies (see **Table 2-3** and **Table 3-5**). That investigation was run concomitantly with the depigmentation optimisation. Tissues were fixed in formalin for 24 hours and sections were depigmented in 10% H_2O_2 for 30 min without further adjustments.

Table 3-5: Pan-cytokeratin antibodies targets

Pan-cytokeratin antibodies	Cytokeratins recognized
Clone C-11 2931	4, 5, 6, 8, 10, 13 & 18
MNF-116	5, 6, 8, 17 & 19

Control pigmented iris sections revealed no cytokeratins labelled by C-11 (see **Figure 3.8-A**). Few dots were observed in the iris stroma, potentially around capillaries to confirm with specific antibodies. Depigmented iris sections also demonstrated the absence of targeted cytokeratins in the IPE (see **Figure 3.8-B**). Surprisingly, on control pigmented iris section (see **Figure 3.9-A**), MNF-116 marked the anterior layer of the IPE and several other structures in the iris stroma: vessels, capillaries and stromal cells. No fibres were observed, marks taking a dotty form instead. These marks were not found on depigmented iris sections (see **Figure 3.9-B**).

As the IPE was positive for the first MNF-116 investigation, the IPE would produce cytokeratins type I and II, desmin and vimentin. So, the IPE would have cytoskeletal proteins running opposite functions. This statement being contradictory, the experiment was reproduced on pigmented iris sections processed from different eyes and new solutions (see **Figure 3.10-A**). To ensure the rightness of the result, adult porcine corneal sections were added as control tissue (see **Figure 3.10-B**). Expressing cytokeratins 3 and 12[212], not targeted by MNF-116 (see **Table 3-5**), that control was expected to be negative. As a result, no cytokeratins were labelled in the iris stroma, in the IPE anterior layer or in the corneal epithelium.

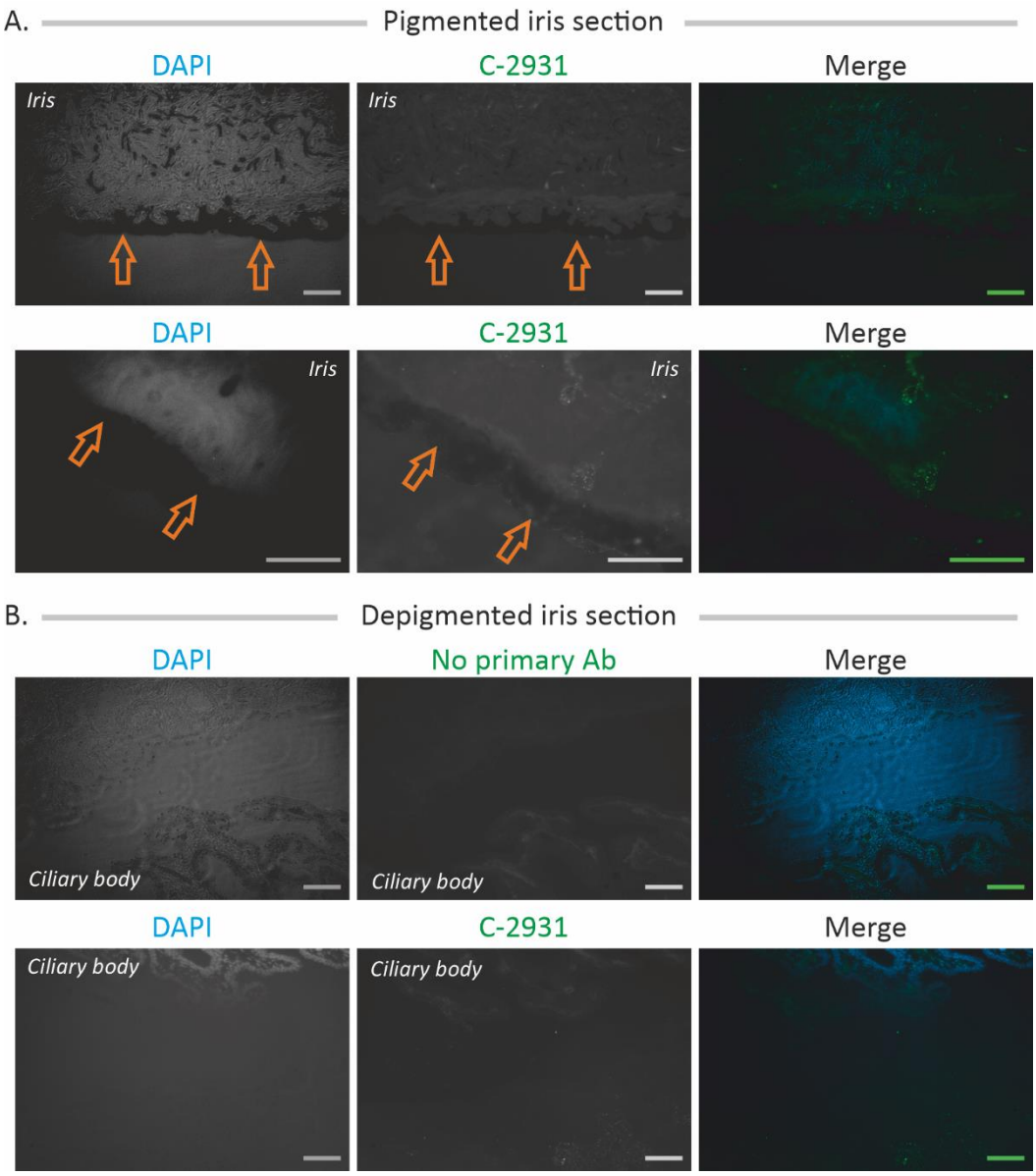

Figure 3.8: Representative images of C-11 2931-labelled porcine iris sections. A. Pigmented iris section. **B.** Depigmented iris section. No signals were observed in both types of sections. **Orange arrows** indicate the IPE. Anti-C-2931 primary antibodies were labelled with an AF 488 secondary antibody. Tissues are labelled by the white and italic writings. DAPI is represented in blue, C-2931 in green. Small scale bars = 100 µm, tall scale bars = 50 µm.

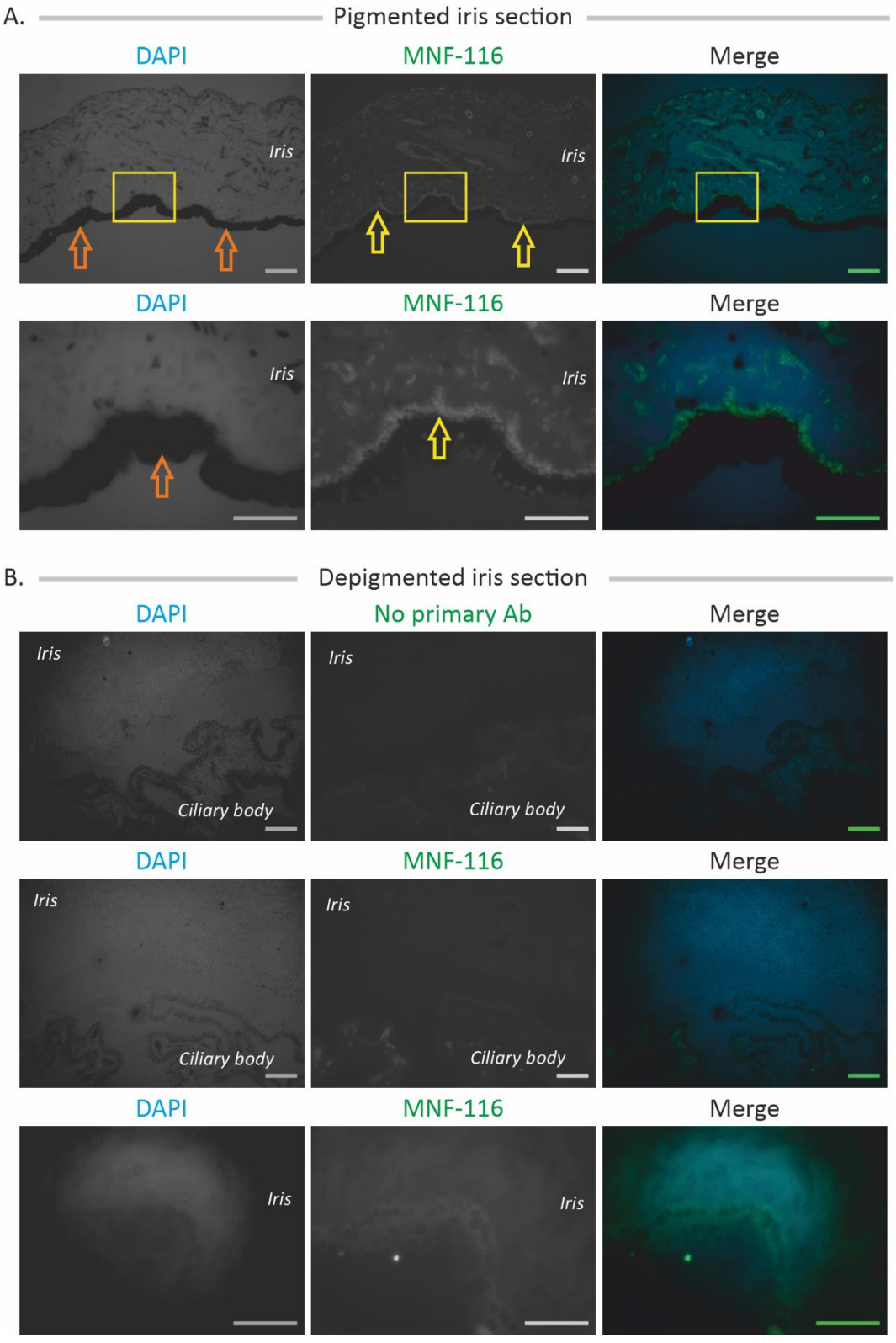

Figure 3.9: Representative images of MNF-116-labelled porcine iris sections. A. Pigmented iris section. **B.** Depigmented iris section. MNF-116 (= **yellow arrows**) signals were observed in the pigmented sections in the iris and in the IPE anterior layer. No signals were observed on the depigmented sections. **Orange arrows** indicate the IPE. Boxes show higher magnifications below. Anti-MNF-116 primary antibodies were labelled with an AF 488 secondary antibody. DAPI is in blue, MNF-116 is in green. Tissues are labelled by the white and italic writings. Small scale bars = 100 µm, tall scale bars = 50 µm.

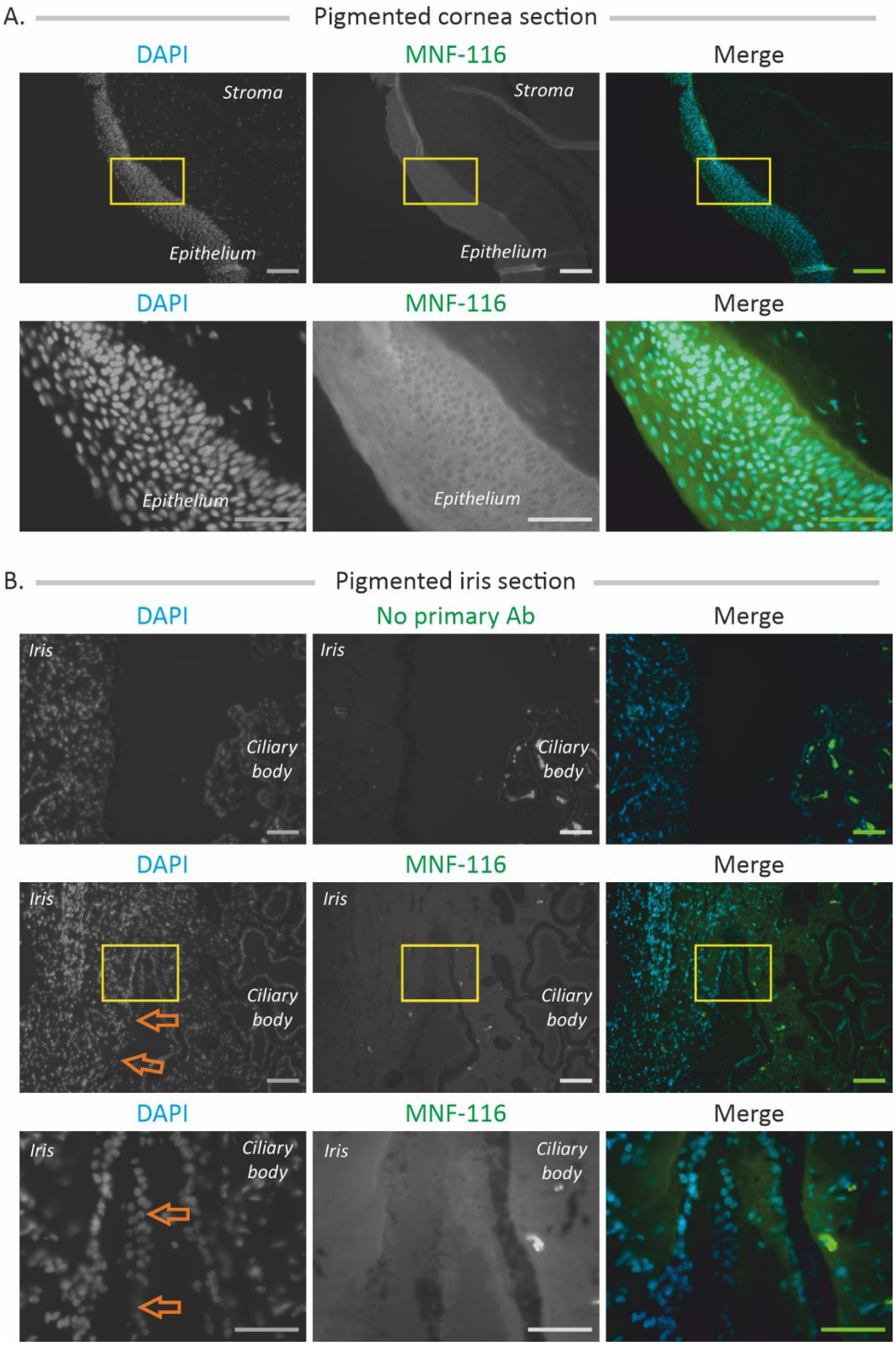

Figure 3.10: Second assessment of MNF-116-labelled porcine cornea and iris sections. A. Cornea section. No signals were observed on the green channel. **B.** Pigmented iris section. No MNF-116 signals were observed in both tissues. Boxes show higher magnifications below. **Orange arrows** indicate the IPE. Anti-MNF-116 primary antibodies were labelled with an AF 488 secondary antibody. DAPI is represented in blue, MNF-116 in green. Tissues are labelled by the white and italic writings. Small scale bars = 100 µm, tall scale bars = 50 µm.

Thus, absence of cytokeratins was confirmed in iris sections. Further investigations using MNF-11- confirmed the second results, so the probable reason to these variations shall lie in the solutions used.

3.4.1.3 Nestin is present in the ciliary bodies – IPE junction

Nestin is a type IV intermediate filament found in neuronal stem cells of the developing and adult brains[213]. Its structure looking to both type III and type IV, it makes it difficult to definitely classify it[214, 215]. As this project aims to identify cells with a certain degree of plasticity, nestin was deemed appropriate. It has been found in murine post-natal IPE tissue with expression being detected 21 days after birth. *In vitro*, its expression was restored when cells were subjected to neurospheres conditions[201]. Thus, nestin was assessed in adult porcine IPE sections.

On pigmented iris sections, nestin was not observed, except in the iris - ciliary body junction, where a small part of the IPE was labelled (see **Figure 3.11-A**). Specifically, marked cells were part of the IPE posterior layer, which has probably detached from the stroma during the sectioning. Some signals were observed in the IPE – iris stroma region marking either IPE cells or stromal ones. Stromal structures reacted as well such as capillary vessels in the middle of the stroma or stromal cells with fibres surrounding nuclei.

On depigmented section, most of the tissues reacted to the antibody except the IPE (see **Figure 3.11-B**). Few signals were gained from the posterior layer while the anterior layer as stromal structures strongly reacted. In absence of a positive control for the antibody, the observed brightness in these sections seemed irrelevant, potentially resulting from random binding following the depigmentation.

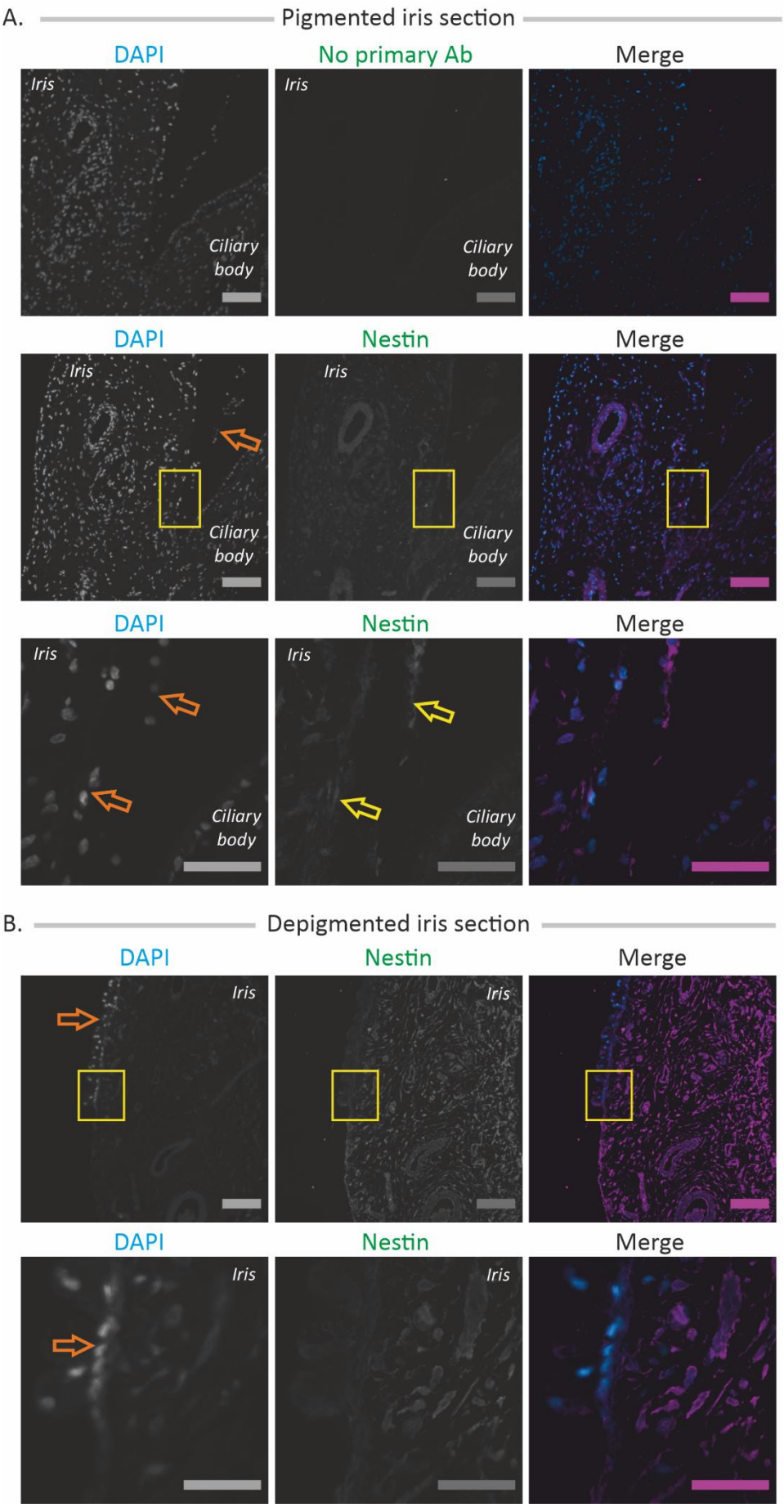
A.
Pigmented iris section
DAPI
No primary Ab
Merge
Iris
Ciliary body
DAPI
Nestin
Merge
Iris
Ciliary body
DAPI
Nestin
Merge
Iris
Ciliary body
B.
Depigmented iris section
DAPI
Nestin
Merge
Iris
DAPI
Nestin
Merge
Iris

Figure 3.11: Representative images of nestin-labelled porcine iris sections and nestin-labelled porcine ocular protein samples. A. Pigmented iris sections. Nestin (= **yellow arrows**) is present in the ciliary body – IPE junction **B.** Depigmented iris sections. Unspecific signals were observed over the section. **Orange arrows** indicate the IPE. Anti-nestin primary antibodies were labelled with an AF 594 secondary antibody. Boxes show higher magnifications below. DAPI is represented in blue, nestin in purple. Tissues are labelled by the white and italic writings. Small scale bars = 100 µm, tall scale bars = 50 µm.

Thus, nestin was found in IPE cells near the IPE – CB junction only. The antibody marked a small, limited area and mostly in the posterior layer.

3.4.2 Micro-filaments are linked to smooth muscle activities

Also called "stress fibres", micro-filaments are polymerised networks of different actin isoforms mixed with actin-cross-linking proteins. Some networks last for few seconds only, this is the case for lamellipodia where depolymerisation releases actin monomers. Other last longer such as myofibrils which are observables for days[216]. Three major classes have been identified: α-, β- and γ-. Each have their own specificities with the α-one being present in muscles only (α-cardiac, α-skeletal and α-smooth). Previous investigations discovered that α-smooth actin (α-SMA) was present in the human IPE anterior layer from which the pupil dilator muscle takes its roofs[206, 207]. Thus, α-SMA was investigated in the porcine IPE.

On pigmented iris sections (see **Figure 3.12-A**), α-SMA was labelled over the length of the IPE anterior layer. Fibres were clearly marked and easy to dissociate from each other. In the same manner than observed in **Figure 3.6-A**, fibres demonstrated an orientation going toward the iris periphery along a posterior-to-anterior axis. On higher magnification, some were running from the posterior pigmented layer and signals were coming from the posterior layer itself. Stromal iris vessels were marked by the antibody.

On depigmented iris section (see **Figure 3.12-B**), α-SMA was marked again along the IPE anterior layer. The IPE posterior layer seemed absent as no DAPI was observed there. As for previous investigation of this chapter, it is possible that the IPE detached during the sectioning. That issue concerned all sections harvested in that investigation. A-SMA was labelled as well in iris vessels with several small capillaries visible. As seen before, no or few stromal nuclei only were marked by DAPI.

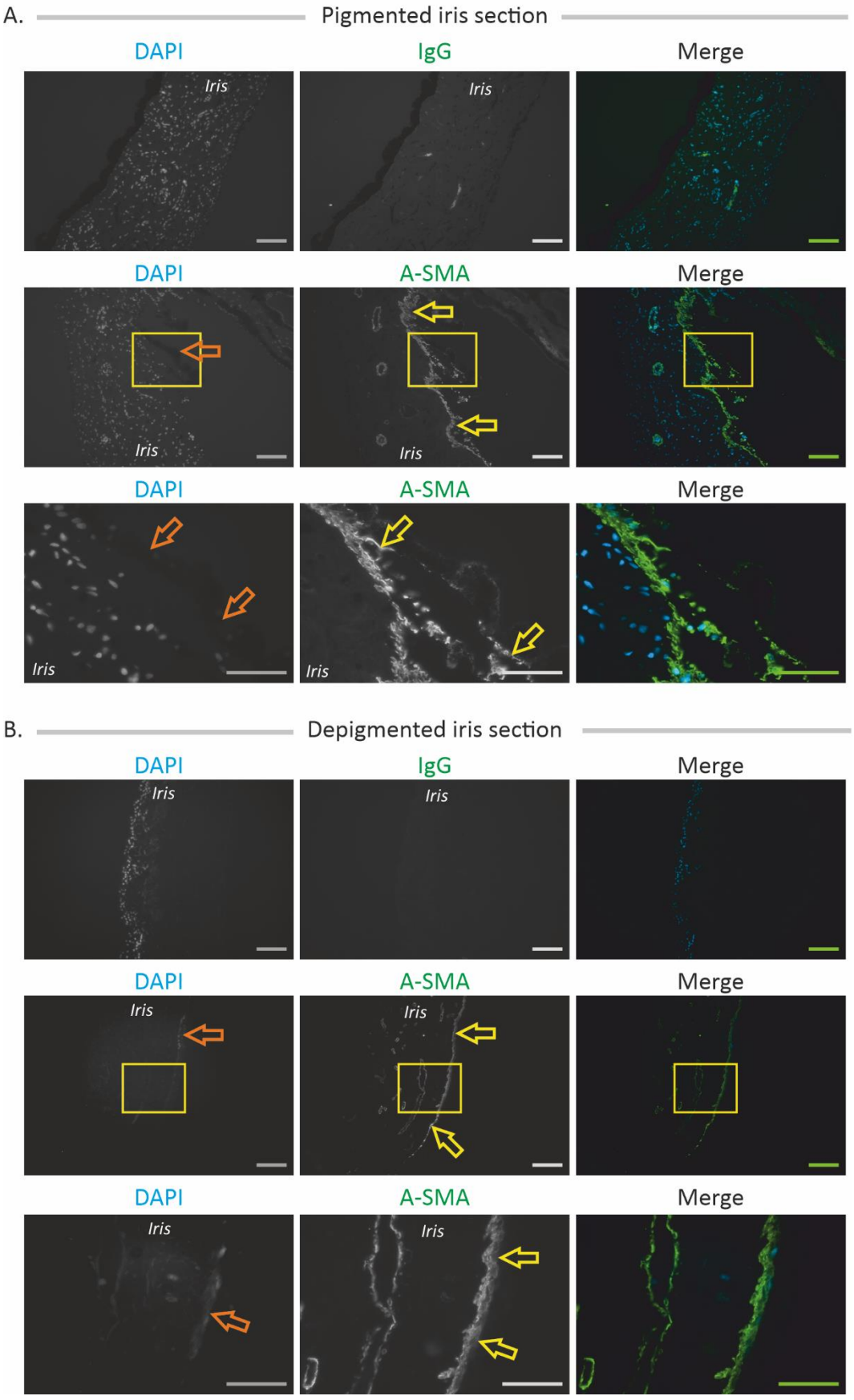

Figure 3.12: Representative images of α-SMA-labelled porcine iris sections. A. Pigmented iris sections. **B.** Depigmented iris sections. A-SMA (= **yellow arrows**) was

labelled in both types of sections over the IPE length. Boxes show higher magnifications below. **Orange arrows** indicate the IPE. DAPI is represented in blue, α-SMA in green. Tissues are labelled by the white and italic writings. Anti-A-SMA primary antibodies were labelled with an AF 514 secondary antibody. Small scale bars = 100 µm, tall scale bars = 50 µm.

Thus, α-SMA was found in the anterior layer along the length of the dilator fibres in a fashion similar to desmin. Its presence in the posterior layer is also probable.

3.5 Porcine IPE basal lamina assessment

3.5.1 Collagen type IV

Ubiquitous components of basal lamina with laminins, collagen type IV is defined as a non-fibrillar collagen[217]. It is encoded by 6 different genes and so forms 6 different chains more or less specific of the tissue they support. Structurally, collagen type IV chains associate in trimers to form a helix with multiple breaks inside it. This gives to the molecule multiple curved shapes[217]. Once polymerised with other collagen type IV, the network absorbs mechanical pressures and helps supporting the tissue it associates with[127]. Previous work showed that collagen type IV surrounds the IPE on its anterior and posterior side[32]. Investigations were run here to assess that statement in the porcine IPE basal lamina.

Here, human cornea was used as positive control (see **Figure 3.13-A**). Marks were observed on the basal side of the corneal epithelium to the limbus. Some background in the stroma were observed. Still, the intensity of the purple signals and their localisation at the basal side were good.

Porcine cornea section was then used to demonstrate that the anti-collagen type IV antibody worked on porcine section (see **Figure 3.13-B**). The antibody marked the basal lamina along the corneal epithelium. Marks went progressively less intense in the limbal region where methyl green-stained nuclei are much more visible. Background intensity was lower except in one stromal area and along the corneal epithelium, despite the hydrogen peroxide-based blocking.

Porcine pigmented iris sections demonstrated much stronger collagen type IV content (see **Figure 3.13-C**). The IPE anterior basal lamina was intensely marked along its length. Multiple vessel-based basal lamina were marked as an important number of stromal

fibres. No marks could be observed on the posterior side of the IPE due to the pigment or potentially the absence of collagen type IV there.

Porcine depigmented iris sections showed a similar picture (see **Figure 3.13-D**). Collagen type IV was again marked along IPE length on its anterior side. Moreover, where the IPE was present, collagen type IV was labelled on its posterior side at lower degree. Other iris stromal structures were clearly marked with vessels and capillaries easy to distinguish. Some fibres were labelled on the iris stromal anterior side. Methyl green-stained stromal nuclei were not distinguished on the contrary of IPE ones.

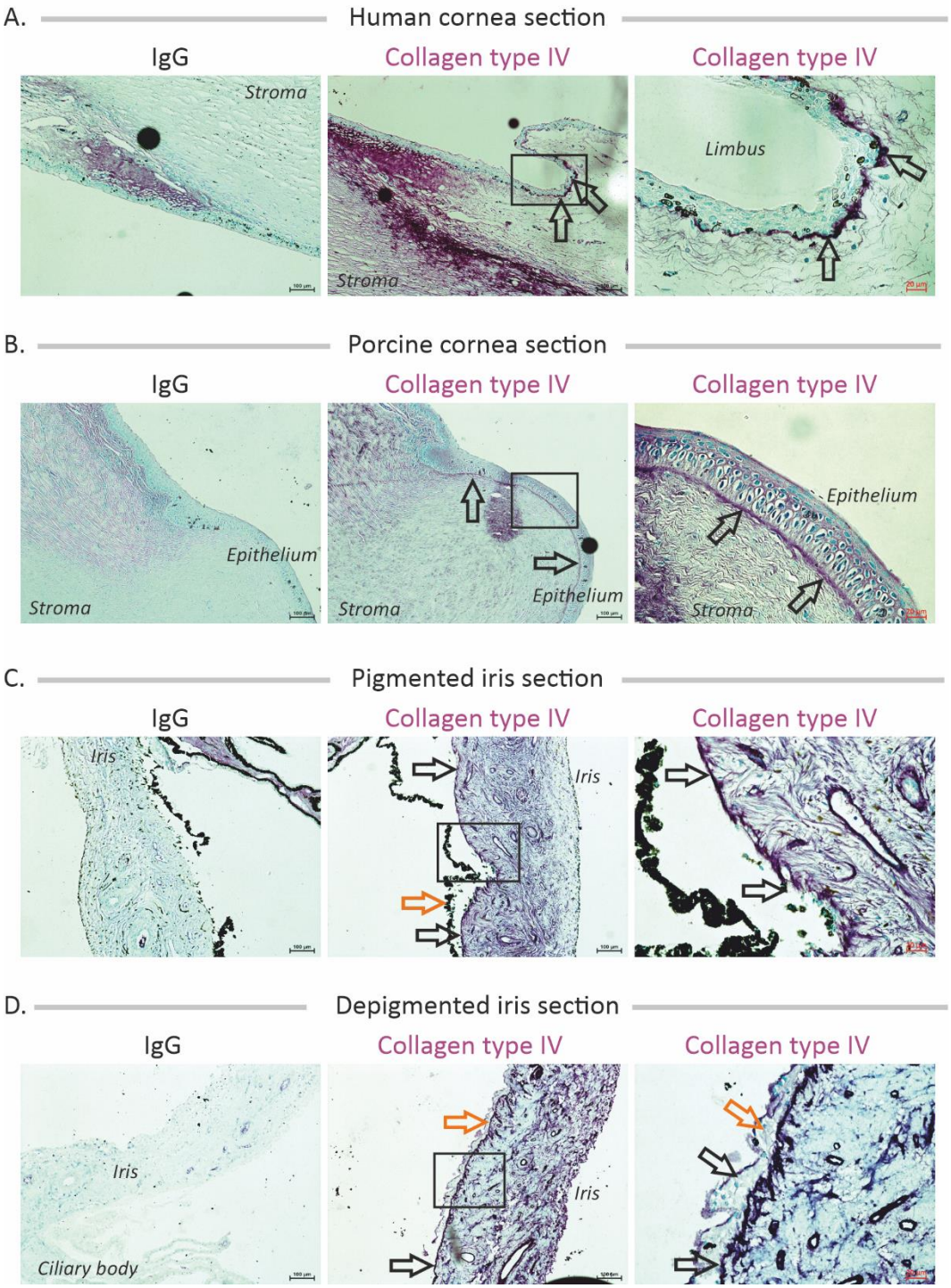

Figure 3.13: Representative images of collagen type IV-labelled human and porcine ocular sections. A. Human cornea section. **B.** Porcine cornea section. **C.** Porcine pigmented iris section. **D.** Porcine depigmented iris section. Collagen type IV (= **black arrows**) was labelled in all sections in the basal lamina of epithelia, iris endothelia and in iris stromal fibres. **Orange arrows** indicate the IPE. Black boxes represent higher magnifications on the right. Anti-collagen type IV antibody were labelled by solutions from the ImmPACT® VIP peroxidase (HRP) substrate kit. Tissues are labelled by the black and italic writings. Cell nuclei are in methyl green. Collagen type IV is in purple. Black scale bars = 100 µm, red scale bars = 20 µm.

So, the porcine IPE is surrounded anteriorly and posteriorly by a collagen type IV basal lamina.

3.5.2 Laminins

Another major component of the basal lamina, laminins are triple chains-based proteins. The core α chain defines the N- and C- terminals. β- and γ-chains associate with the α- one on its C-terminal and dissociate near the N-terminal, giving to the protein a cross-based form[127]. The C-terminus connects with integrins from the cells, N-terminus with other proteins from the basal lamina such as nidogens or heparan sulfate proteoglycans. To note, these two proteins are key binders between laminins and collagen type IV[127, 218, 219]. Five α chains, four β ones and three γ ones exist and assemble specifically depending the nature of the tissue and the cells they connect with. Laminin 111 for example, α1-β1-γ1, appears early during the development to then be replaced by more specific ones[220]. So, laminin composition are indicative of the cell functions, an epithelial stem cell requiring specific laminin 511 for example[221, 222].

Laminins have not been identified in the IPE basal lamina to our knowledge. So, investigations were run with a range of anti-laminin antibodies.

3.5.2.1 Porcine ocular sections did not react to the pan-laminin antibody

A general investigation was run over porcine tissues with a pan-laminin antibody (see **Table 2-3**) to assess the general laminin repartition in porcine cornea and iris (see **Figure 3.14**). As a result, no staining were observed on the cornea section, neither on the pigmented iris one. Instead, background was observed through the green channel corresponding to the anti-pan-laminin antibody. As no background was observed on IgG controls, that phenomenon did not result from random binding from the secondary antibodies used. A second investigation with a different pan-laminin antibody is advisable prior to further conclusions.

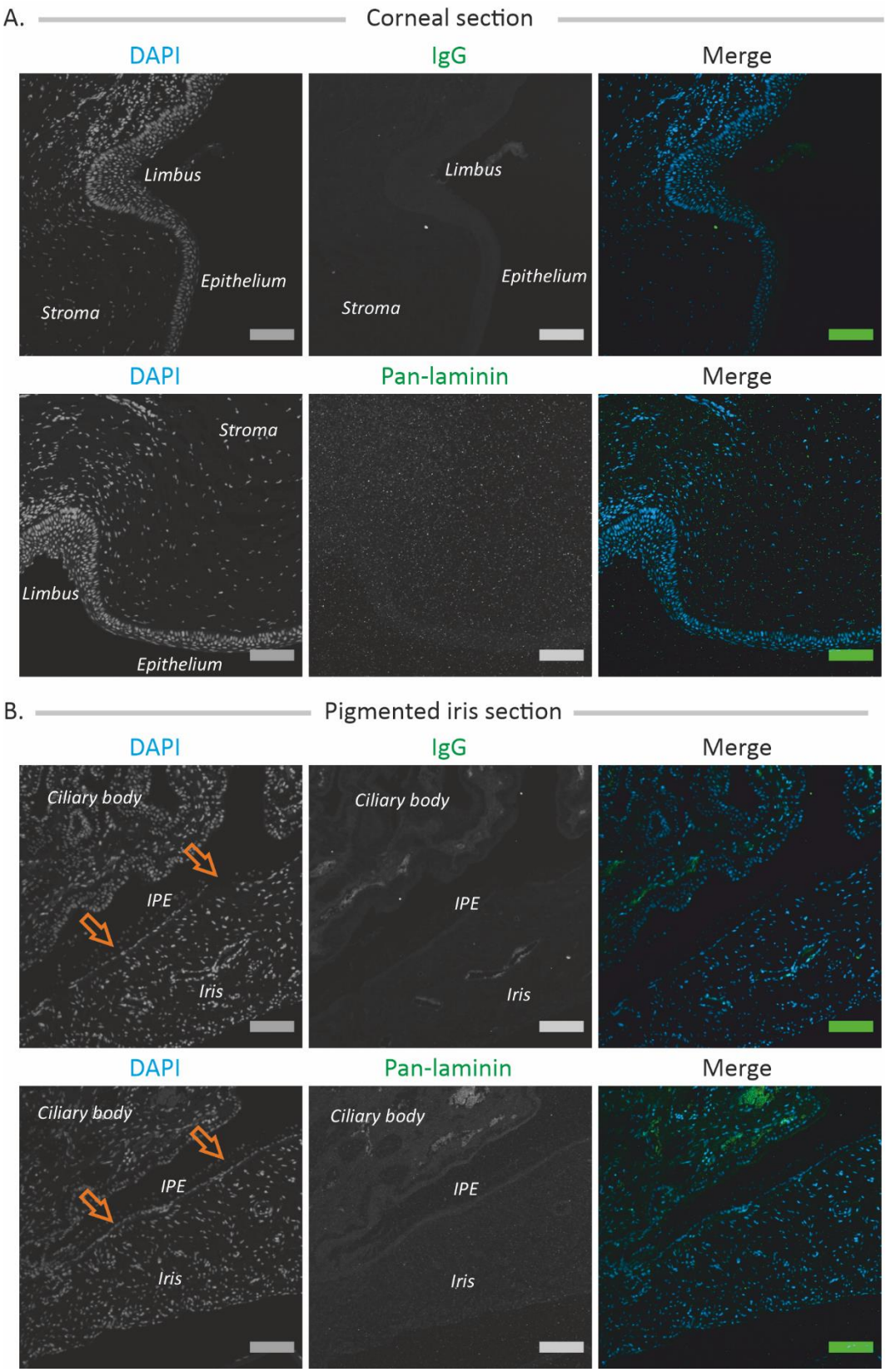

Figure 3.14: Representative images of pan-laminin-labelled porcine sections. A. Corneal sections. **B.** Pigmented iris section. Not laminins were observed on both tissues. **Orange arrows** indicate the IPE. DAPI is represented in blue. Laminins are in green. Tissues are labelled by the white and italic writing. Scale bars = 100 µm.

3.5.2.2 Laminin α4 was marked on human sections only

Laminin-α4 chain is associated with smooth muscles and endothelial basal lamina[223]. So, it was expected to observe it over the IPE anterior basal lamina where lies the dilator fibres. Laminin α4 could also stop when approaching the ciliary body – IPE junction, suggesting that cells would run functions different than the smooth muscular ones.

On human iris section (see **Figure 3.15**), the anti-laminin α4 antibody marked basal lamina over a precise area. Laminin α4 was absent in IPE areas close from the ciliary body. Oppositely, it was marked over the rest of the IPE basal lamina on its anterior side in contact with iris stroma (see **Figure 3.15-C.**). None were detected on the posterior side. Small stromal vessels were marked as well.

Oppositely on porcine sections (see **Figure 3.16**), no staining was observed over the anterior basal lamina. Instead, several stromal cells were marked, dots corresponding with DAPI nuclear staining. Higher magnifications revealed multiple dots co-localising on cell structures. Several staining were also present in stromal regions without cells around them as showed by the lack of DAPI.

The overall “dotty” distribution of signals on porcine sections contrasts with the human ones. So, if laminin-α4 is present in the human IPE anterior basal lamina, its place in porcine iris remains to confirm and would require a different anti-laminin α4 antibody.

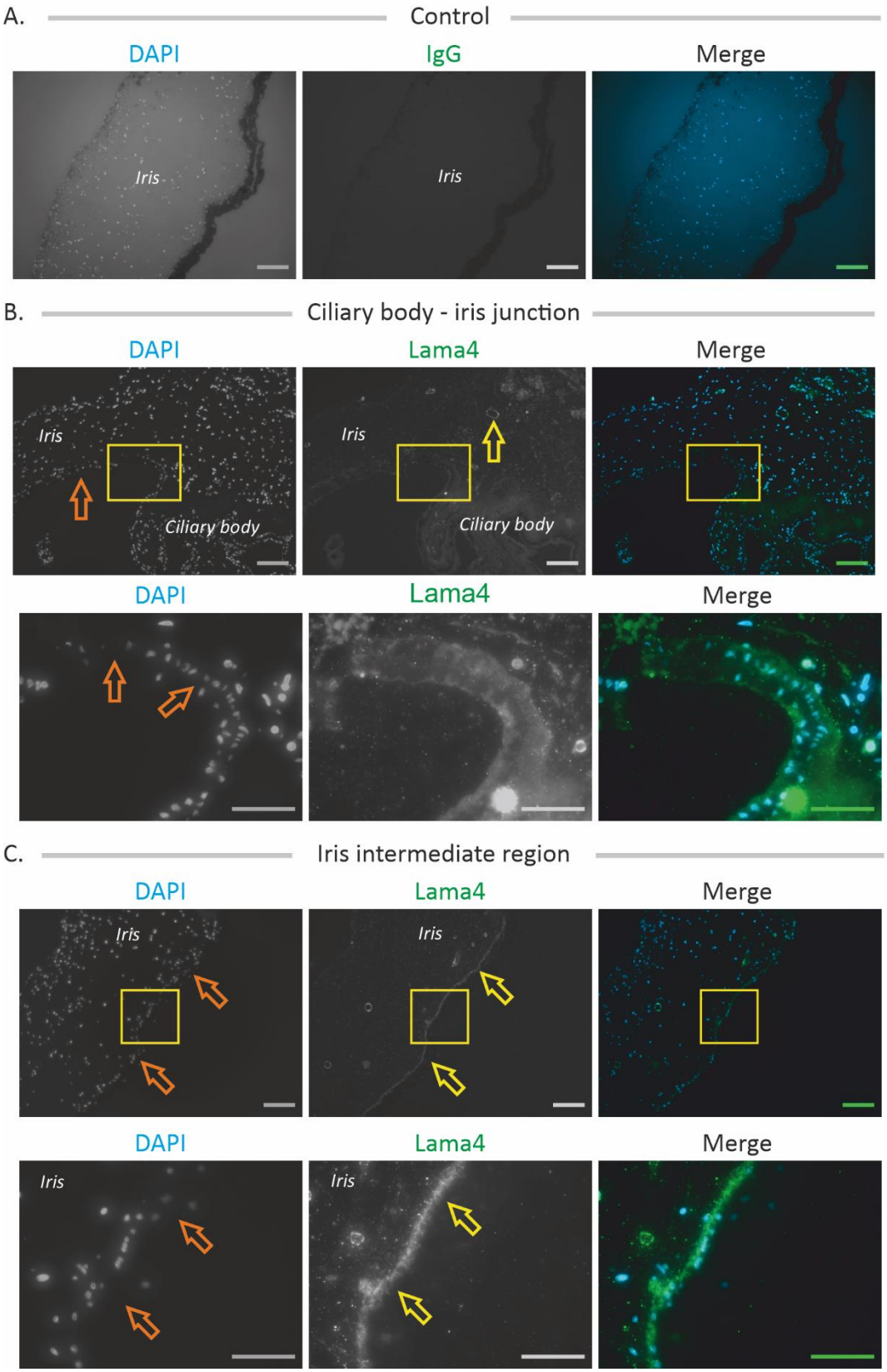

Figure 3.15: Representative images of laminin-α4--labelled human sections. A. Control sections labelled with IgG antibodies. **B.** Ciliary body – iris junctions. **C.** Iris intermediate region. Laminin α4 (= **yellow arrows**) is present in the IPE anterior basal lamina in area far from the ciliary body-IPE junction. **Orange arrows** indicate the IPE. Yellow boxes indicate

higher magnifications below. Tissues are labelled by the white and italic writings. DAPI is in blue, laminin α4 is in green. Small scale bars = 100 µm. Tall scale bars = 50 µm.

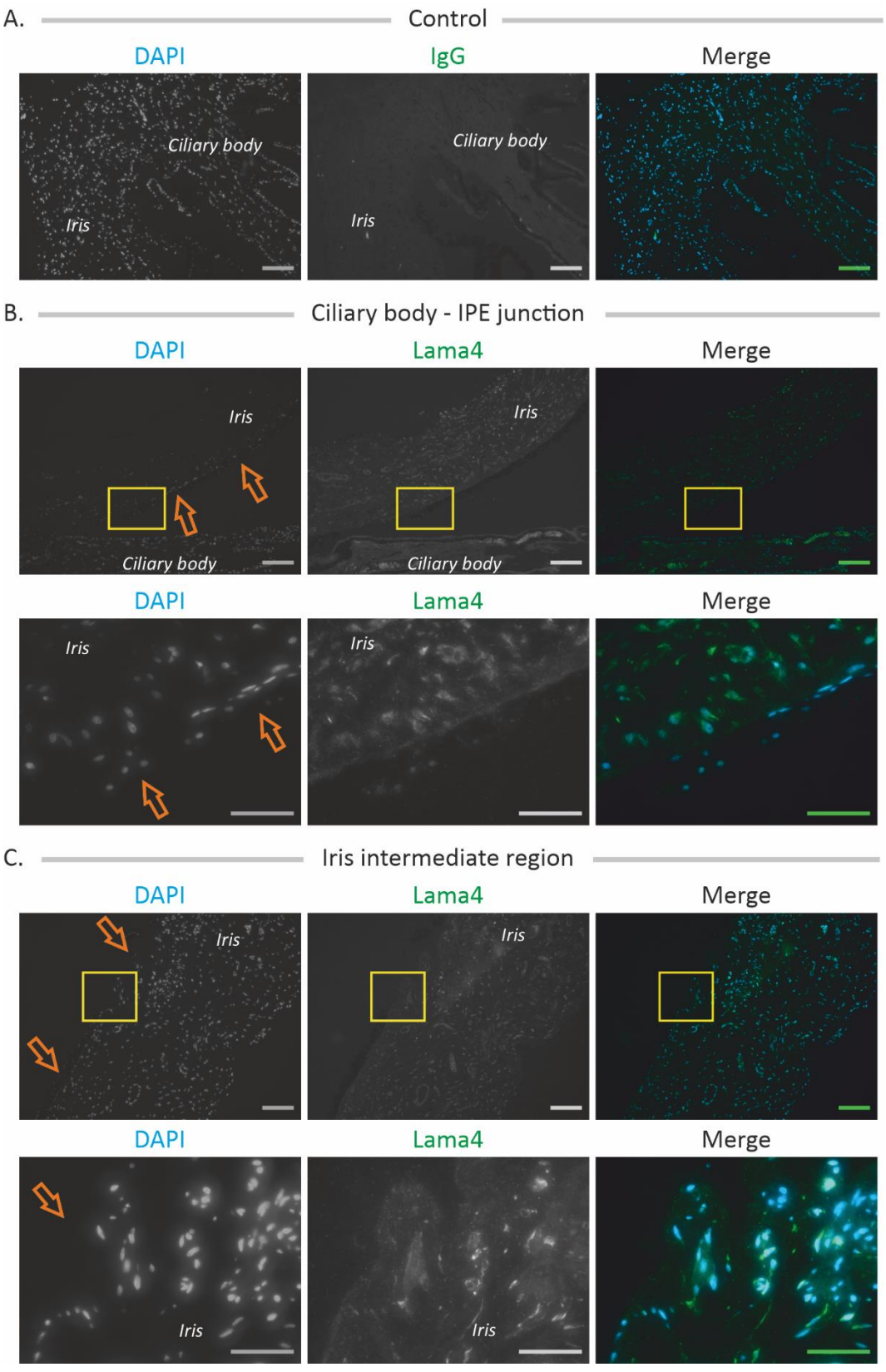

Figure 3.16: Representative images of laminin-4-labelled porcine sections. A. Control sections labelled with IgG antibodies. **B.** Ciliary body – iris junctions. **C.** Iris intermediate region. Sections remained free of anti-laminin α4 antibodies. **Orange arrows** indicate the IPE. Yellow boxes indicate higher magnifications below. Tissues are labelled by the white and italic writings. DAPI is in blue, laminin α4 is in green. Small scale bars = 100 µm. Tall scale bars = 50 µm.

3.5.2.3 Laminin-β1 & laminin-β2

Laminin-β1 and –β2 have been found in the limbus where they support limbal stem cell niches[221]. So, their presence in a specific part of the IPE would be an element in favour of the existence of stem cells in the IPE. Human limbus sections were used as positive controls (see **Figure 7.3**). None sections exhibited positive staining; background staining was present in the subjacent scleral region and corneal stromal one. So, results being potentially invalids (see **Figure 7.3**), further statements would be inconsistent. As a quick summary, no signals were observed from the anti-laminin-β1 labelled iris. For anti-laminin-β2 labelled iris sections, signals were observed on the top of the ciliary body non-pigmented epithelium, facing the lens. No other tissues reacted with the antibody.

3.6 Cell-cell junctions in the IPE

3.6.1 Cadherins

Porcine cornea was used as positive controls for N- and E-cadherins[224]. Specifically, the limbal basal layer was expected to be positive to N-cadherin and upper layers from both limbal and corneal epithelium positive to E-cadherin. N- and E-cadherins were investigated on porcine pigmented and depigmented iris sections.

3.6.1.1 N-cadherin was the major cadherin used in the IPE

On porcine cornea sections, the epithelial basal layers from the scleral epithelium, the limbal one and the corneal one stained positively for N-cadherin (see **Figure 3.17-A**). Signals were also observed in superior limbal epithelial layers with a lower fluorescence intensity.

On pigmented iris sections, N-cadherin was observed in the IPE despite the pigment (see **Figure 3.17-B**). At higher magnification, cell delimitations are visible in the IPE anterior layer. An intense fluorescence is observable at the CB-IPE junction and over the CB non-pigmented epithelium. Multiple iris stromal cells, iris stromal vessels and the corneal endothelium were labelled.

On depigmented iris sections, anti-N-cadherin staining was observed from the IPE and what could be the sphincter muscle (see **Figure 3.17-C**). However, fluorescence was not emitted from specific cell structures but seemed diffused instead. Some elements at the surface were labelled with the IPE having a "granular" aspect visible on the higher magnification. The sphincter was also labelled in this manner, suggesting that the labelling has been labelled in an unspecific manner.

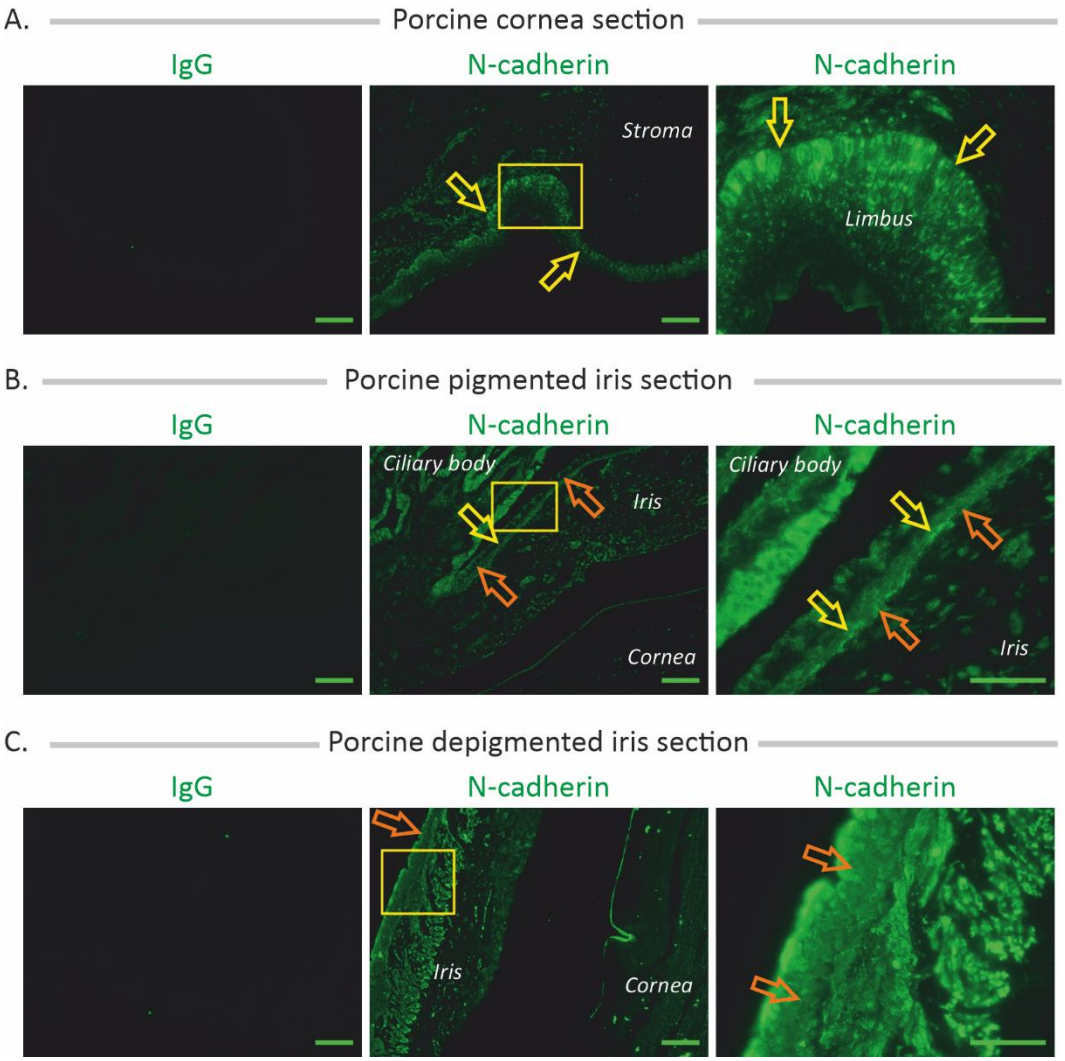

Figure 3.17: Representative images of N-cadherin-labelled porcine ocular sections. A. Cornea section. **B.** Pigmented iris section. **C.** Depigmented iris section. N-cadherin (= **yellow arrows**) is labelled: in the basal layers of the scleral, limbal and corneal epithelia

for the positive controls; in the IPE and the both ciliary body epithelia for investigated tissues. **Orange arrows** indicate the IPE. Yellow boxes indicate higher magnifications on the right. Tissues names are labelled by the white and italic writings. N-cadherin is in green. Small scale bars = 100 µm, tall scale bars = 50 µm.

3.6.1.2 E-cadherin investigation demonstrated unclear/irrelevant distributions

On cornea section, anti-E-cadherin antibody marked as expected cells in limbal superior layers over several layers, in scleral basal ones and in corneal epithelial superior layers (see **Figure 3.18-A**).

On porcine iris sections, some signals were observed close from the IPE (see **Figure 3.18-B**). High magnification revealed these marks at the junction with iris the stroma, where the dilator fibres set. Melanin prevented observations on the posterior one. Oppositely to the IPE, the CBE was marked but epithelial cell shapes were difficult to observe. Signals from iris stromal cells and vessels were observed as well.

Depigmented IPE was labelled along its length and no cell-cell distinctions could be made (see **Figure 3.18-C**). Only methyl green-stained nuclei could be weakly observed at high magnification. That observation applied for the CB, pigmented and non-pigmented epithelia. Again, what could correspond to the sphincter muscle was labelled. Iris stromal cells and vessels reacted as well, suggesting that again the antibody labelled elements in an unspecific manner.

So, E-cadherin observations at the IPE – iris stroma border was unexpected as this specific region holds smooth muscular structures and its associated basal lamina. For what has been observed from the writer on sections showed here and others, E-cadherin and N-cadherin localisations did not have the same localisations. Further investigations shall confirm or infirm this observation. A search for the partners of N-cadherin and those of E-cadherin, then the superposition of these results could help.

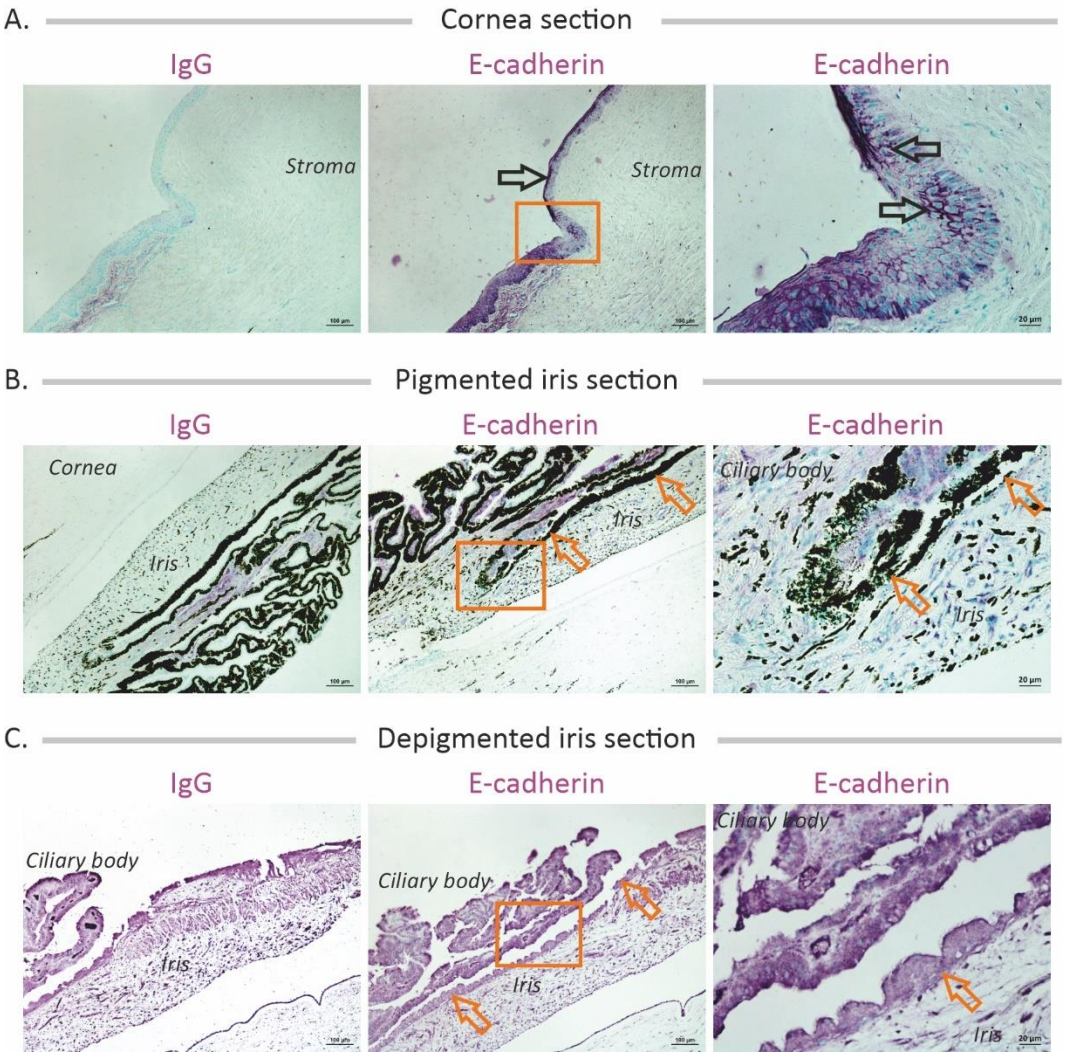

Figure 3.18: Representative images of E-cadherin-labelled porcine ocular sections. A. Cornea section. **B.** Pigmented iris section. **C.** Depigmented iris section. E-cadherin (= **black arrows**) was observed in the limbal, the corneal, the scleral and the CB non-pigmented epithelia, plus at the border between the IPE and the iris stroma. **Orange arrows** indicate the IPE. E-cadherin is in purple, cell nuclei in methyl green. Orange boxes indicate higher magnifications on the right. Tissues are labelled by the black and italic writings. Left and middle scale bars = 100 µm, right scale bars = 20 µm.

3.6.2 Tight junctions

Fundamentally, tight junctions control passage of nutrients and ionics between cells plus ensure the right position of lipids in plasmic membranes[127]. As on the back of the IPE lies a lumen coming from the aqueous humour secreted by the ciliary body, the IPE shall be selectively permeable to the aqueous humour and ensure it does not disperse into the iris stroma. So, ZO1, a well-known the tight junction protein expressed in epithelia[225], has been investigated.

On pigmented iris sections, ZO1 signals were observed in the IPE anterior layer, in iris stromal vessels and in the CBNPE (see **Figure 3.19-A**). Higher magnifications revealed its presence in IPE posterior pigmented layer as well. The IPE anterior layer was well marked but did not shape as plasma membrane proteins. Similar observations can apply to vessels structures observed in the iris stroma. Stromal cells were finally marked.

Depigmented iris sections revealed that ZO1 was present through the IPE on its entire width (see **Figure 3.19-B**). Both IPE and CBE cell shapes were defined and looked similarly, taking the form of small epithelial cells continuous between both tissues. Finally, the cell number marked there was high.

Thus, IPE cells use numerous ZO1-based tight junctions through the length of the tissue. Cells from the anterior layer looked longitudinal, which could correspond to their muscle activity while cells from the posterior one were more round-shaped.

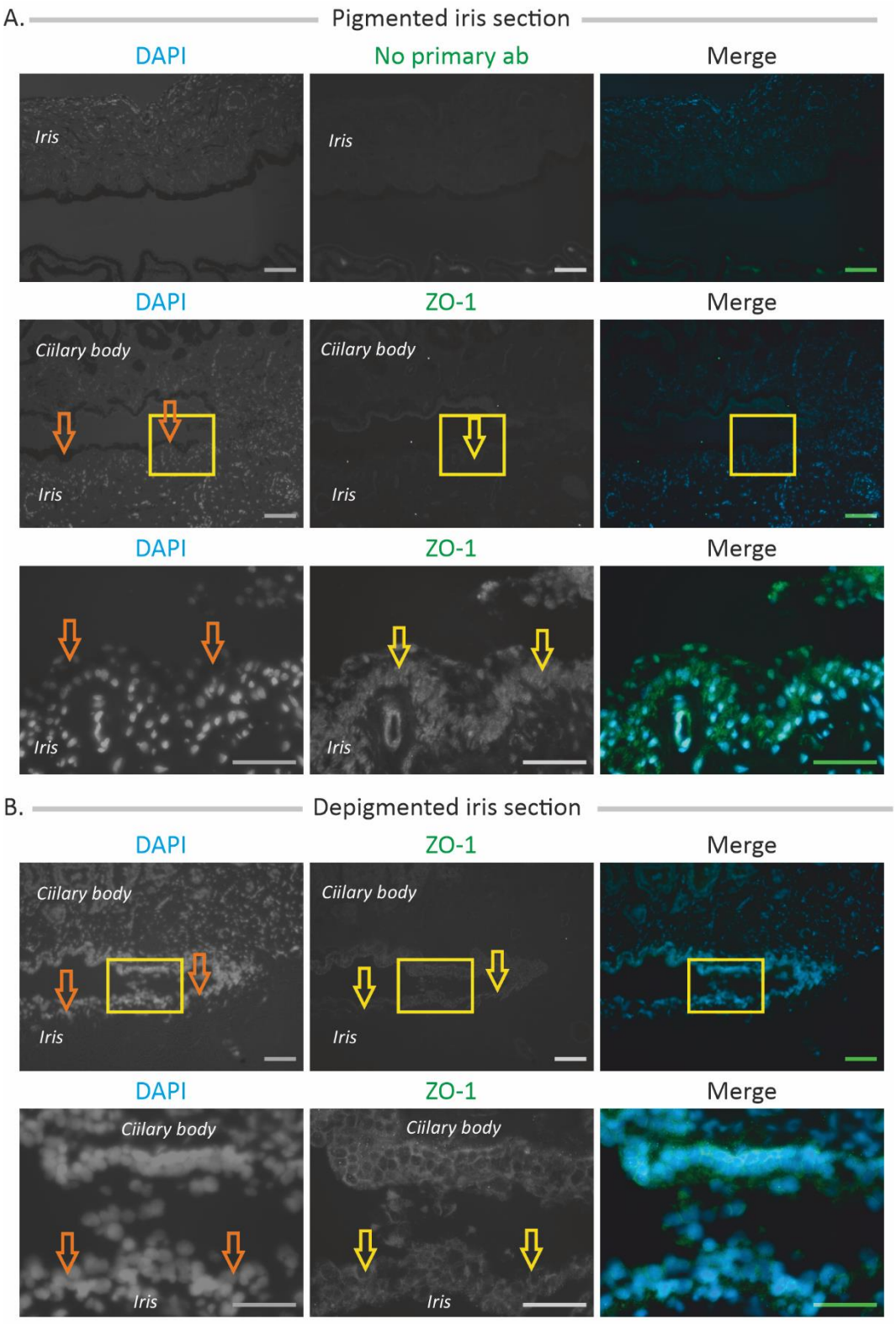

Figure 3.19: Representative images of porcine IPE-labelled for ZO-1. A. Pigmented iris section. **B.** Depigmented iris section. ZO1 (= **yellow arrows**) is labelled in both pigmented and depigmented sections and was observed through both anterior and posterior IPE layers (= **orange arrows**). ZO1 is represented in green, DNA in blue. Yellow boxes indicate higher magnification below. Tissues are labelled by the white and italic writings. Small scale bars = 100 µm, tall scale bars = 50 µm.

3.7 Proliferation in the IPE

3.7.1 PCNA labelled few cell cycle S-phase only

To control the anti-PCNA antibody suitability on porcine depigmented tissues, a corneal-limbal-scleral section was depigmented and used as positive control (see **Figure 3.20-B**). However, the signals intensity was low, making them barely visible and at high magnification only. Still, signals came from the limbal basal layer and upper ones. The number of nuclei marked by the antibody was low while the absence of DAPI counterstaining suggests that the limbus suffered from the depigmentation.

At the iris-ciliary body region, no signals from nuclei were observed. A-SMA was used there to mark specifically the IPE. However, only the α-SMA labelling was observed (see **Figure 3.20-C**). No PCNA signals was observed over the IPE length.

With few limbal basal cells labelled by the PCNA antibody, plus the low signal observed on the green channel, it is possible that the PCNA – AF conjugated antibody shall have been used at a higher concentration. That would have generated brighter fluorescence. Moreover, the use of limbus sections as positive controls for nuclear targets was reconsidered when the depigmentation was required.

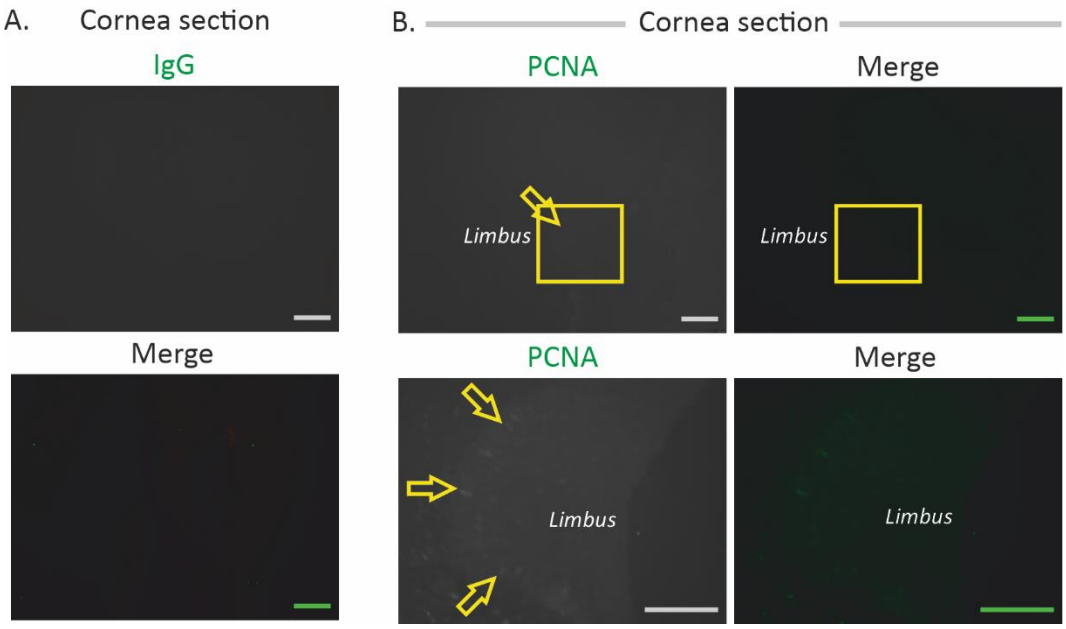

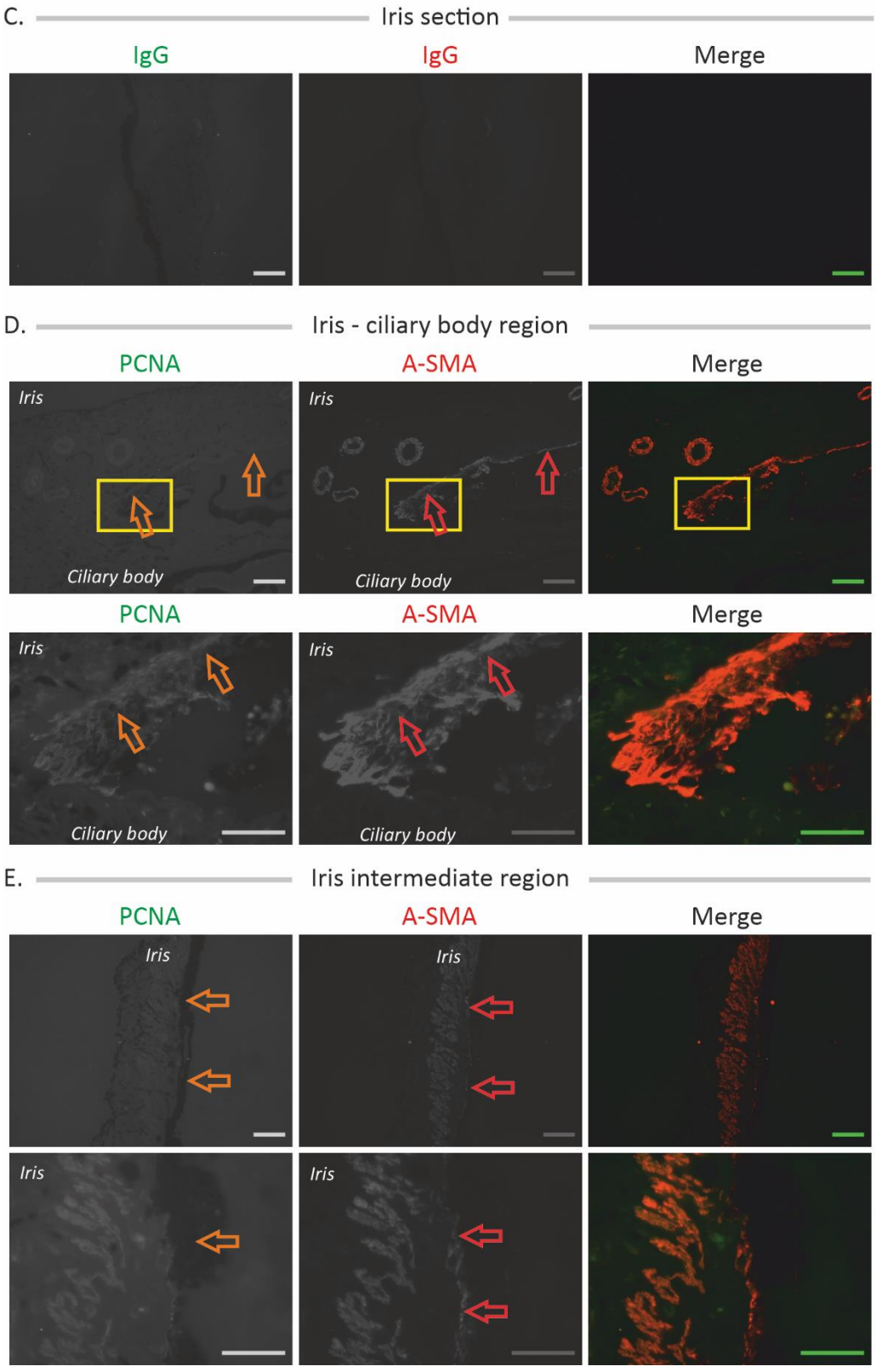
C.
Iris section
IgG
IgG
Merge
D.
Iris - ciliary body region
PCNA
A-SMA
Merge
Iris
Ciliary body
PCNA
A-SMA
Merge
Iris
Ciliary body
E.
Iris intermediate region
PCNA
A-SMA
Merge
Iris
Iris
Iris
Iris

Figure 3.20: Representative images of PCNA-labelled porcine ocular anterior chamber. **A.** IgG-labelled cornea section. **B.** PCNA-labelled cornea section. **C.** IgG-labelled iris section. **D.** PCNA and A-SMA-labelled iris section at the iris-ciliary body region. **E.** PCNA and A-SMA-labelled iris intermediate region. PCNA (= **yellow arrows**) was observed on cornea section in the basal layer of the limbus but not in the IPE. A-SMA (= **red arrows**) was used to distinguish the IPE (= **orange arrows**) from the iris. Yellow boxes indicate higher magnifications below. PCNA was in green, A-SMA in red. Tissues are labelled by the white and italic writings. Small scale bars = 100 µm, tall scale bars = 50 µm.

3.7.2 Ki67 marked differentially the IPE depending the location

Investigations were executed on complete anterior chamber sections. No depigmented sections were used there as past investigations showed that the limbus, used as a positive control here, demonstrated poor resistance to the depigmentation.

As expected, the limbus was marked from its basal to its fifth or sixth layer. The basal corneal epithelial layer was also labelled on most of the corneal epithelium length, corresponding with previous investigations[226] (see **Figure 3.21-B**).

At the iris-ciliary body junction, a strong fluorescence was observed in the IPE and the CBE, bypassing the melanin (see **Figure 3.21-C**). In the IPE, signals came from both anterior and posterior layers with different intensities. The closer from the junction, the brighter the fluorescence, suggesting a potential higher content of Ki67 in these areas. To note, the antibody marked both cytoplasm and nuclei in that region in a similar fashion to the limbal basal epithelial cells (see **Figure 3.21-B**).

Near the pupil, differences were visible (see **Figure 3.21-C**). Signals were arising mainly from cell cytoplasm in the anterior layer surrounding nuclei. On the posterior layer, signals were arising from cell nuclei where the pigment was less important or absent. Several stromal structures reacted as well.

Thus, a strong content of Ki67 was observed near and at the IPE-CBE junction, suggesting that several cells in this area are running through mitosis. It is then observed over the IPE length at a lower intensity. Finally, Ki67 and DAPI signals were observed deep into the stroma.

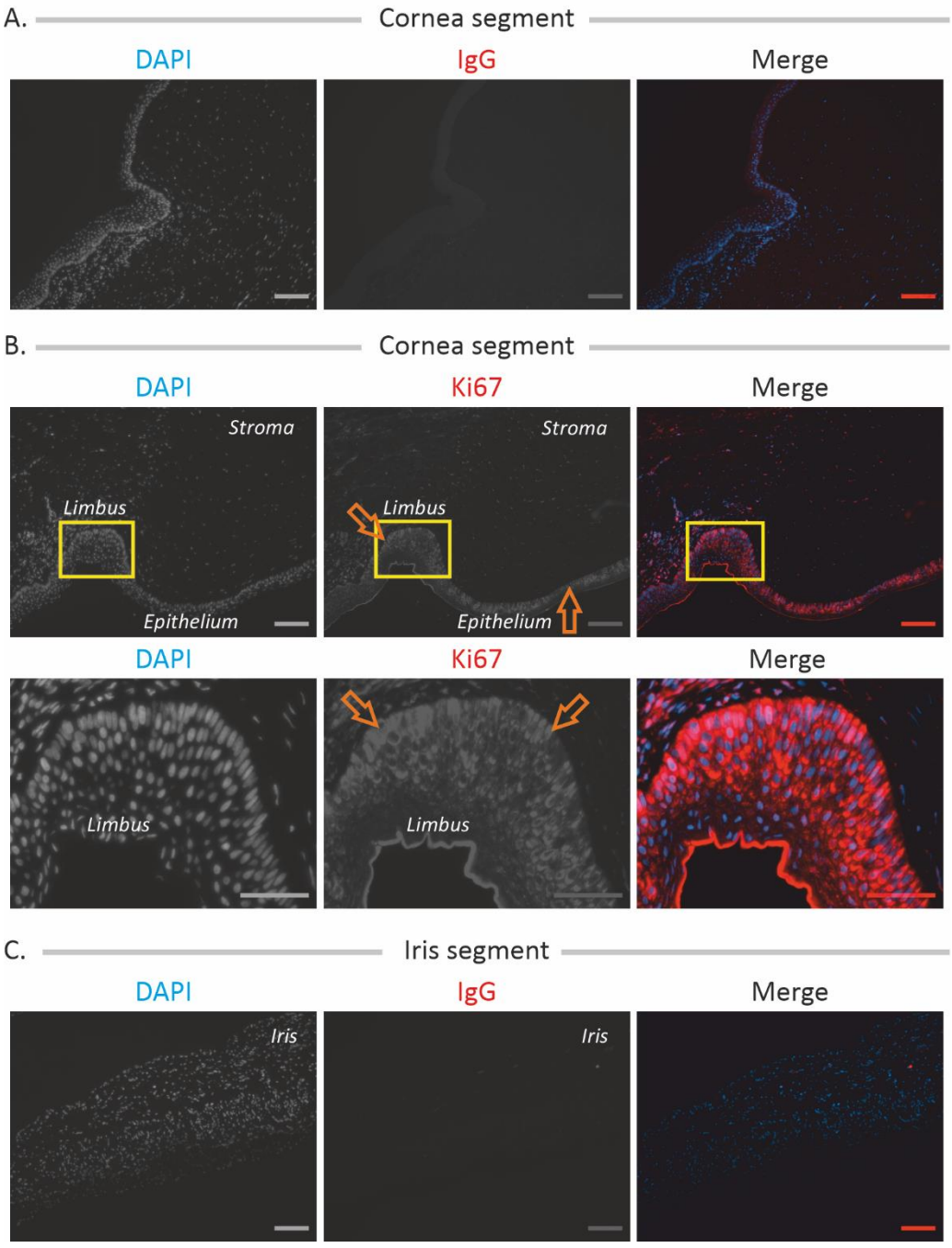
A.
Cornea segment
DAPI
IgG
Merge
B.
Cornea segment
DAPI
Ki67
Merge
Stroma
Limbus
Epithelium
Stroma
Limbus
Epithelium
DAPI
Ki67
Merge
Limbus
Limbus
C.
Iris segment
DAPI
IgG
Merge
Iris
Iris

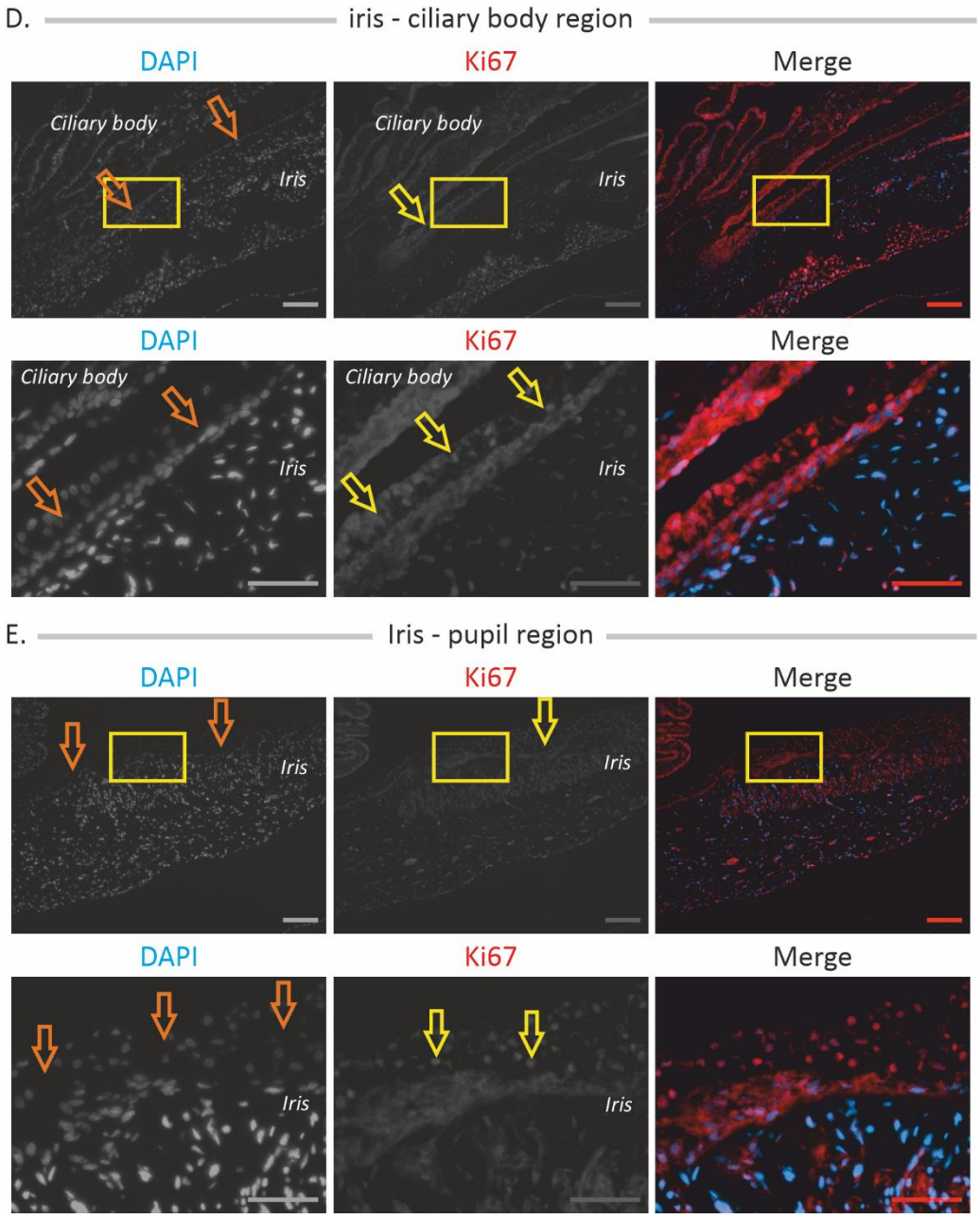

Figure 3.21: Representative images of Ki67-labelled porcine ocular anterior chamber. A. IgG-labelled cornea section. **B.** Ki76-labelled cornea section. **C.** IgG-labelled iris section. **D.** Ki76-labelled iris – ciliary body region section. **E.** Ki67-labelled iris - pupil region. Ki67 (= **yellow arrows**) was observed in multiple layers of the limbus, in the corneal epithelium and in the IPE (= **orange arrows**). In the IPE, Ki67 fluorescence intensity was higher in the iris – ciliary body region than in the iris – pupil region. Yellow boxes indicate higher magnifications below. DAPI is in blue, Ki67 in red. Tissues are labelled by the white and italic writings. Small scale bars = 100 µm, tall scale bars = 50 µm.

3.8 No IPE cells expressed the stem cell marker ΔN-p63 *in vivo*

That investigation was among the firsts done over that PhD. So, protocols related to the depigmentation were not optimised at that time.

To assess the anti-ΔN-p63 antibody suitability, human and porcine limbii were investigated as positive control[227, 228] (see **Figure 7.4** and **Figure 3.22-A**). Nuclei from the limbal basal layer and some from the upper ones were labelled by the antibody. So, the antibody was proved to work on porcine tissue and was assessed on the CBE-IPE junction. Investigations were run only on depigmented iris sections (see **Figure 3.22-B**). As a result, no marks were observed in the CBE-IPE junction. Instead, the background from the IPE contrasted with the iris, making it visible over its length. Thus, no ΔN-p63-positive cells were detected in the IPE.

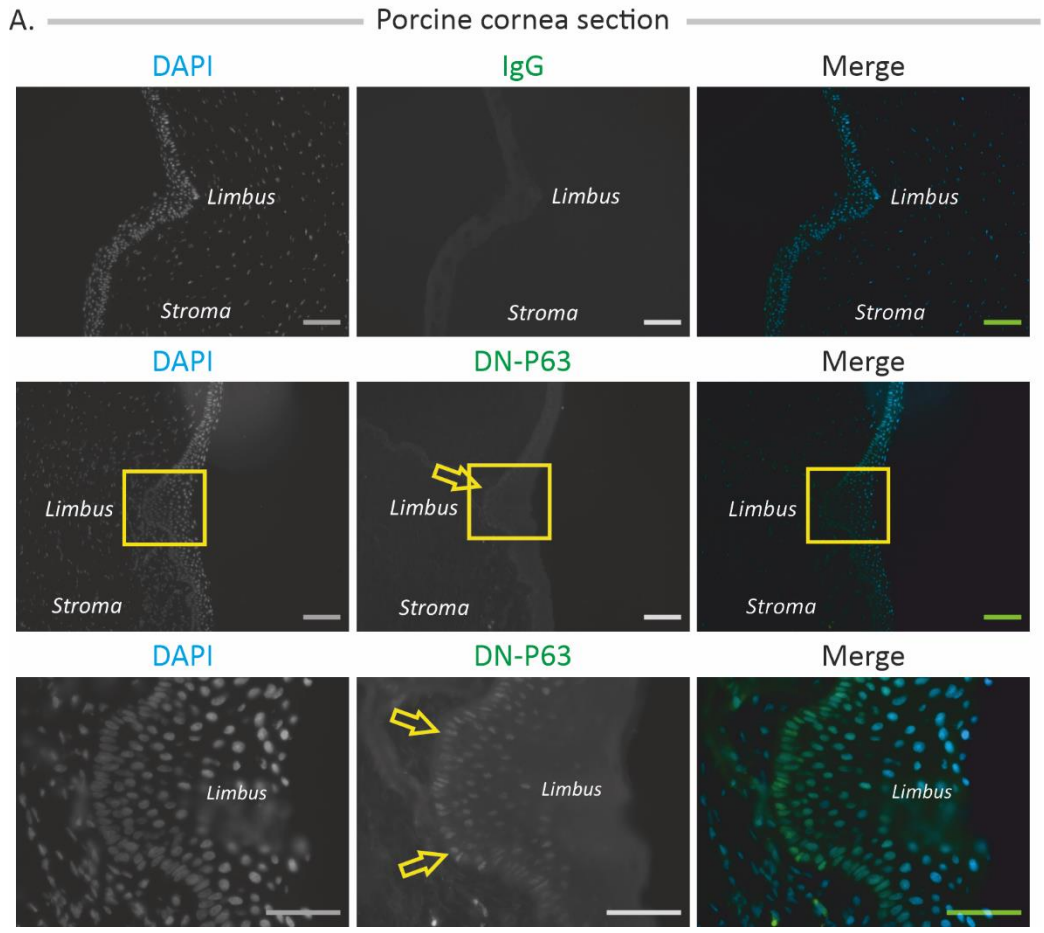

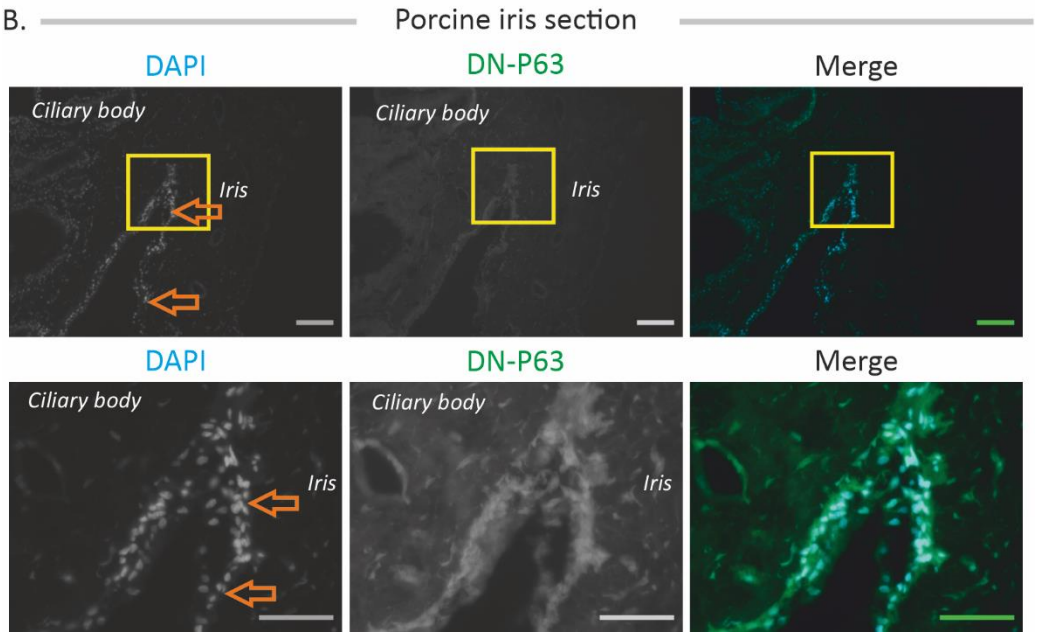

Figure 3.22: Representative pictures of porcine ocular sections labelled for ΔN-p63. A. Cornea section. **B.** Iris section. ΔN-p63 (= **yellow arrow**) was labelled in the basal layer of the limbus but not in the IPE at its junction with the ciliary body epithelia. Yellow boxes indicate higher magnifications below. **Orange arrows** indicate the IPE. DAPI is in blue. ΔN-p63 is in green. Tissues are labelled by the white and italic writing. Small scale bars = 100 µm, tall scale bars = 50 µm.

3.9 Developmental markers in the IPE

3.9.1 PAX6 is present in the IPE and the iris

Human and porcine iris sections showed similar PAX6 distributions. On the human section (see **Figure *3.23*-A**), a strong brightness emerged from the IPE anterior layer in a location close to the CBE-IPE junction and going to the pupil. Some cells from the posterior layer were also stained by the antibody, plus some areas of the CBE. Several structures in the iris stroma were marked as well, mostly nuclei peripheral regions.

Porcine pigmented sections demonstrated a lower intensity with both anterior and posterior IPE layers being positive (see **Figure *3.23*-B**). Higher magnifications revealed several proteins surrounding nuclei again. Other stromal structures, especially vessels, also reacted.

Thus, PAX6 was labelled as expected in both human and porcine IPE at the CBE-IPE junction and over the IPE length as well. CBE and iris stromal cells were also labelled. Finally, PAX6 was similarly distributed between both species.

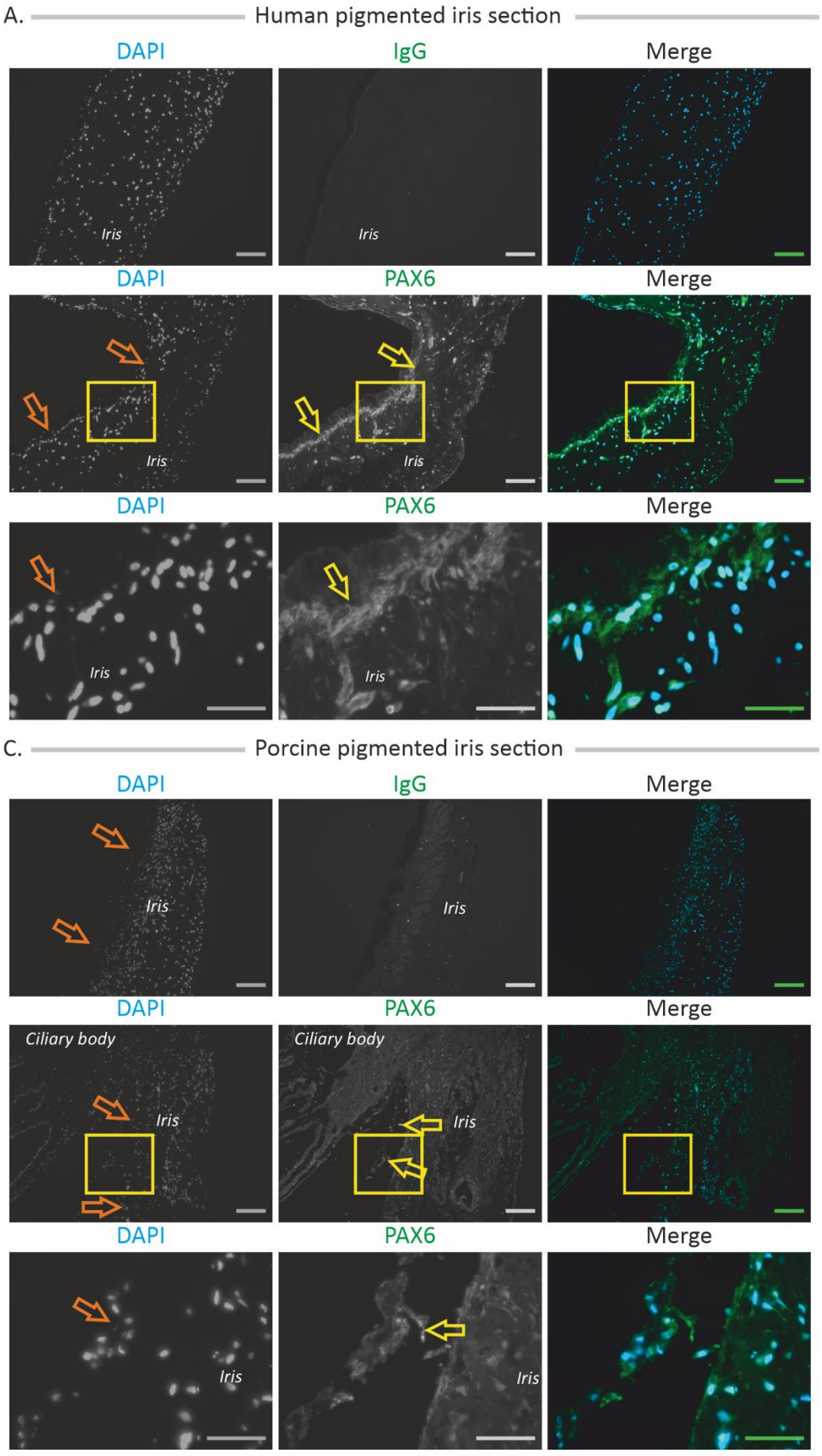
A.
Human pigmented iris section
DAPI
IgG
Merge
Iris
Iris
DAPI
PAX6
Merge
Iris
Iris
DAPI
PAX6
Merge
Iris
Iris
C.
Porcine pigmented iris section
DAPI
IgG
Merge
Iris
Iris
DAPI
PAX6
Merge
Ciliary body
Iris
Ciliary body
Iris
DAPI
PAX6
Merge
Iris
Iris

Figure 3.23: Representative images of PAX6-labelled human and porcine iris sections. A. Human pigmented sections. **B.** Porcine pigmented sections. PAX6 (= **yellow arrows**) was labelled in all sections. **Orange arrow**s indicate the IPE. Yellow boxes indicate higher magnifications below. DAPI is represented in blue, PAX6 in green. Tissues are labelled by the white and italic writings. DAPI is in blue, PAX6 is in green. Small scale bars = 100 µm, tall scale bars = 50 µm.

3.9.2 SOX2 is present in the IPE cell cytoplasm

To assess the anti-SOX2 antibody suitability, cornea sections, and specifically the limbus, were used[304] (see **Figure 7.5**). Surprisingly, the antibody labelled the cytoplasm with multiple dots but nothing related to nuclei as it shall be[229]. Brightness also raised from the basal lamina. The brightness was stronger in the limbal upper layers than in the basal one. As for laminins, results being potentially invalids, further statements would be inconsistent. As a quick summary for IPE investigations, the anti-SOX2 antibody also marked cytoplasms not in nuclei. Finally, several iris and ciliary body stromal cells were marked.

3.10 Discussion

The aim of this chapter was to distinguish different regions in the porcine IPE *in vivo* and focus on the ones involved in proliferation. To do so, the development of a robust method to remove the melanin was set up, prior to the investigations of various features related to the cytoskeleton, the basal lamina and the cell-cell junction. Finally, proteins involved in proliferation, stem cell maintenance and embryogenesis were investigated.

3.10.1 Depigmentation, a process to deepen

Melanin, from melanos meaning dark in Greek, is the major pigment of surface tissues exposed to the sunlight[230]. The molecule absorsbs the visible light, wavelengths from 700 (red) to 400 nm (purple), plus ultra-violets rays of shorter wavelengths. Once molecules are packed in organelles, the melanosomes, they surround nuclei shielding the DNA from ultra-violet-induced damages[231]. When a photon is catch by melanin, the energy from the

photon transfers to the melanin phenol ring, which then dissipates the energy by heating[232].

In that section, the objective was to develop a depigmentation process able to remove the melanin from formalin-fixed paraffin-embedded IPE sections as specific fluorescence signals would be otherwise unreliable. The two most widely-reported agents are the hydrogen peroxide (H_2O_2) and the permanganate potassium-oxalic acid ($KMnO_4$). Previous investigations reported they could be integrated into various protocols fairly simply[205]. However, $KMnO_4$ treatment severely diminishes tissue integrity and antigen structures, meaning a large panel of antibodies can no longer be used[216]. On the other hand, H_2O_2 bleaching has been successfully included in immunostaining protocols, making it the choice of preference in this study[205].

Quickly, it appeared that to use H_2O_2 as a melanin removal required adjustments to improve the overall quality of the results.

3.10.1.1 Initially, depigmentation produced the desired result

The first depigmented sections exhibited structures that were easy to distinguish, and a melanin content reduced enough to observe nuclei and cytoplasms in pigmented epithelia after 20 min of incubation (see **Figure 3.1**). Longer incubations demonstrated a decrease in eosin staining. So, as well as degrading the melanin structure, depigmentation also changed progressively the tissue chemistry, potentially the pH. Indeed, eosin is an acidic negatively charged dye which targets cytoplasms, mitochondria, collagens or intermediate filaments, all major basophilic intra- and extracellular components[233, 234]. So, the decreased eosin staining could result from a progressive acidification of the section.

On the other hand, haematoxylin is a basophilic dye staining the acids, the glycosaminoglycans and the glycoproteins[233, 234]. However, the purple-blue from haematoxylin would be more prominent if section suffered acidification. Thus, it is probable that the reduced eosin staining resulted from an increased sensitivity and subsequent degradation from basophilic elements exposed to the hydrogen peroxide. Those observations were not reported by previous investigations[235, 236].

3.10.1.2 Initial desmin FIHC being negative, adjustments were required

Initial depigmented sections labelled with the anti-desmin antibody demonstrated negative results, while normal sections demonstrated positive results (see **Figure 3.2**). *In vitro*, assembly experiments demonstrated that with pH lowering, desmin unit length filaments formed larger complexes. Sedimentation measurement confirmed then a much higher sedimentation facility as pH lowered[237]. To note, among intermediate filaments, only cytokeratins type I and type II are classified as acidic and basic respectively[238].

Desmin clearly changed from its exposure to H_2O_2 (see **Figure 3.2**). Either its three-dimensional structure changed, either it suffered chemical damages by the hydrogen peroxide, either both factors ran together. So, the first improvement in the protocol was the extension of formalin-based fixation from 10 minutes to 24 hours (see **Figure 3.3**). As explained by Ramos-Vara *et al*, fixation by formalin occurs in three steps[239]:

1. the penetration, the quickest;
2. the covalent binding to peptide sequences, running twelve times slower than the penetration;
3. the cross-linking between covalent bonds, running four times slower than the covalent binding.

So, with initial fixation lasting 10 min, in an utopic scenario with the iris penetrated by formalin at 100%, samples would be covalently bound at 8.3% and cross-linked at 2.75%. That was clearly insufficient. In regard of previous publications, positive results obtained at the experiment G (see **Table 3-1**) can be considered as a normal fixation[236, 240, 241, 242].

The second essential adjustment was the selection of appropriate chemical components to synchronise with the temperature/time factor. Over investigations, it became clear that the most balanced result was reached with 3% H_2O_2 in PBS only (see **Figure 3.4**). That was considered good for FIHC as melanin did not quench the DAPI signals from the IPE. In addition, the temperature and the time of incubation in H_2O_2 worked together in an inverse relationship. As temperature (= energy) increased, the time necessary to break melanin reduced. Reciprocally, as temperature lowered, the time increased (see **Table 3-2** & **Table 3-3**).

Regarding the pH, desmin only is not enough to justify the pH of H_2O_2 in the process (see **Table 3-4**). In a similar manner to eosin, some proteins can be sensitive to a certain pH. The enhanced GFP for example loses its fluorescence in lysosome, where the pH lies below

5[242, 243]. Thus, that feature could be adjusted depending the location and the intrinsic features of the targeted protein.

In conclusion, the depigmentation developed in this chapter worked well to depigment the IPE and label desmin in. However, it could also produce wrong positive results as demonstrated with nestin for example (see **Figure 3.11**). So, the process being subtle to balance, it shall be adapted or adjusted to the protein of interest (see **Figure 3.24-B**) and also to the tissue to stain. Melanoma for example could demonstrate opposite reactions to the H_2O_2-depigmentation than the IPE[244, 245]. Changes in the protocol shall always be considered in the equation "melanin removal versus section damages" (see **Figure 3.24-A**). Finally, these investigations shall include monoclonal antibodies only as their recognition of a single epitope would limit the number of wrong positive results. The depigmented sections shall also include all the technical controls routinely used (IgG, no primary & secondary antibodies). More features could be experimented to complete the panel, such as the light exposure[246] and the chemistry of the buffer[247].

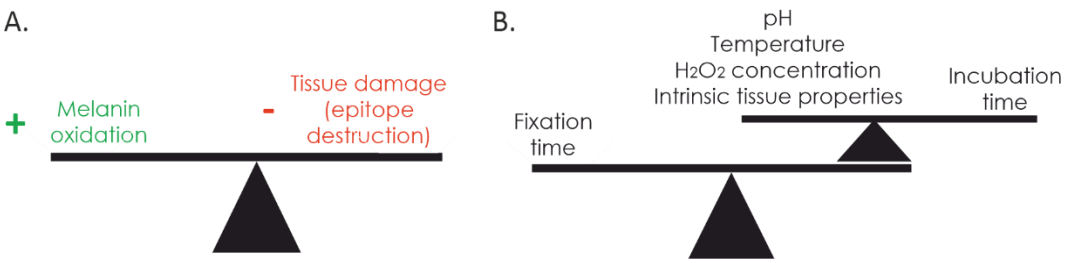

Figure 3.24: Balance of the depigmentation technical investigation. A. Balance advantages/disadvantages. **B.** Layout of the features to adjust.

3.10.2 Features of the IPE tissue

In that section, the objectives were: **1**. To define intrinsic features of the porcine IPE in vivo, which could be commonly found in IPE cells in later investigations; **2**. To investigate more specific markers susceptible to be present in some IPE segments only.

3.10.2.1 IPE has a mesenchymal cytoskeleton

In vivo, the nature of the cytoskeleton defines partly the phenotype. Those proteins ensure multiple functions going from chromosomic separation during mitosis to cell shape maintenance and resilience to mechanical pressures[127].

Desmin, vimentin, nestin and α-SMA were found in the porcine IPE. Distributions varied: desmin was limited to the IPE anterior layer in contact with the iris stroma; nestin was found only at the CBE – IPE junction region in the posterior layer; vimentin and α-SMA were found through both layers in the human IPE.

Desmin was present from the ciliary body – IPE junction to/near: the pupil depending the section (see **Figure 3.2**); the sphincter in the iris stroma. To note, the sphincter is supposed to limit the spread of the dilator muscle around the pupil[3]. Finally, desmin observation over the IPE was in line with previous publications stating the IPE anterior layer as the roof of the dilator muscle[207].

A-SMA was distributed through both anterior and posterior layers (see **Figure 3.12**). This protein is involved in mechanotransduction in various tissues, including smooth muscles, so it demonstrates that the porcine IPE integrates the smooth muscle-based mechanisms induced by mydriasis[248, 249].

Nestin was detected on a limited part of the posterior IPE, quite close to the ciliary body-IPE junction (see **Figure 3.11**). Its distribution over ontogenesis was not possible to establish as Asami *et al* did, due to the age of samples being unknown[201]. Nestin presence in that region still suggests the following points:

- Cells in that area shall also use vimentin as nestin requires a different intermediate filament to polymerise, which is not desmin in the IPE posterior layer[250];
- Cells in that area shall be mechanically resilient as nestin is also associated with mechanical flexibility[251];
- Those cells could be phenotypically more plastic/less differentiated than IPE cells in other regions[252, 253, 254, 255];
- That distribution correlates with the intense Ki67 distribution in that area and PAX6 (see **Figure 3.21** & **Figure 3.23**).

Finally, nestin and desmin specific distributions suggest that the IPE is an organised tissue not only polarised by the anterior-posterior axis but with potential sections devolved to functions other than dilator contractions and pigment synthesis.

Vimentin being undetected from porcine sections created confusion until WB was used (see **Figure 3.6** & **Figure 3.7**). There, the strong content of vimentin detected would suggests that vimentin is a major intermediate filament of the IPE. This is correlated by the human sections positive for vimentin. Reasons why the FIHC failed remain unknown. Indeed, the antibody was predicted to work on porcine tissues; human and porcine sequence compositions are similar at 98% (Uniprot entry numbers: P08670 & P02543); WB using that antibody labelled vimentin from porcine iris and IPE protein extracts; later vimentin-based investigations using that antibody were positive (see Chapter **4**). A different antibody would be determinant to solve that issue.

In summary, the presence of smooth muscular and mesenchymal cytoskeletal proteins demonstrates a protein content similar between the human and the porcine IPE.

3.10.2.2 Basal lamina contains collagen type IV and laminin-α4

The basis of metazoan biology relies on a set of cells setting on a layer of extracellular matrix protein. In mammals, the specialised basal lamina forms on basolateral side of the epithelia, endothelia, axons, etc. With a thickness of 40 to 120 nm, it first anchors cells and then polarises them. From that arises cell structural support, a modulation of cell behaviour, the promotion of tissue healing, maintenance of stem cell niches or the filtration of growth factors and nutrients[127, 221, 256, 257, 258].

On the basal side, **collagen type IV** was present over the IPE length in contact with the iris stroma and on the IPE posterior side (see **Figure 3.13**). That is in line with previous observations of the IPE and general metazoan biology[32, 259, 260]. Collagen type IV presence on both sides participates to maintain the bilayered polarity and preserve the IPE integrity through mydriasis and myosis, explaining the IPE facilities to pass from a multifolded state to a flat one without disturbances[261].

Laminins on the other side were difficult to label (see **Figure 3.14**). The anti-laminin α4 was the only antibody to work and only on human sections. In that case, laminin α4 was found over the length of the IPE anterior layer except at the ciliary body–IPE junction. As that chain is a major component of laminin-associated smooth muscles, its presence

further supports that muscular activities are run by the IPE[262, 263] (see **Figure 3.15**). One possible reason for the porcine investigated iris sections to be negative could be technical as the manufacturers did not mention porcine tissues as suitable for this antibody.

Considering the complete absence of results on porcine sections, plus the similarities between both human and porcine IPE, laminins shall be reinvestigated with appropriate antibodies. Furthermore, if laminin-β1 and -β2 chains in the IPE are indeed absent, the IPE would lack two major components of stem cell niche basal laminas[219, 222, 259] (see **Figure 3.16**).

3.10.2.3 N-cadherin was the adherent junction protein detected

Cell-cell junctions and attachments are critical features of epithelia to keep tissue integrity. Originally, N-cadherin was found in the retina, the heart and the brain, giving its name of Neural-cadherin[264]. Later, it was found in multiple tissues including skeletal and smooth muscles, vascular tissues or conjunctive cells[265]. Because it allows cells to form adherent junctions without the strength of E-cadherin, giving cells a certain mobility, it is a major component in the development of several tissues[266, 267, 268].

In light of this, its distribution over the IPE length makes sense (see **Figure 3.17**). The IPE is indeed subjected to muscle contraction from the dilator and relaxation from the sphincter. To maintain cell-cell junctions in this mobile environment requires therefore a junctional system maintaining structural integrity between cells with a certain flexibility.

3.10.3 So, the IPE exhibits the features of a smooth muscle

Overall, vimentin is an ideal intermediate filament for the IPE as its molecular structure allows dynamic rearrangements along the filament[210]. Indeed, the filament is based on the assembly of vimentin polypeptides into dimers then tetramers. Further assembly leads to the unit-length filament, composed of eight tetramers. A certain number of these unit-length units then interact together to form the vimentin filaments[210]. As these elements hold together by ionic and hydrophobic interactions, their assembly and disassembly, observed *in vitro* but applying potentially *in vivo*, can be spontaneous[210]. So, the rearrangements occur by the removal or the shift of some polypeptides from the

filament. This makes the vimentin filament flexible and adaptable without the need to disassemble the entire filament to then reassemble it in a different location. For these reasons, vimentin is found in many motile organs including the lung and the kidney[210]. And so, considering the iris function in the ocular system[3], it is logical to find it in the porcine IPE, after being observed in the human one[207].

Moreover, vimentin could specifically participate in the dilator activities as it can assemble with desmin at the dimer level, the tetramer one, the unit-length filament and the filament[237]. Based on a specific polypeptidic sequence but organised in the same manner as vimentin[238], desmin connects with the mitochondria, the contractile filaments, the desmosomes and the nucleus[269]. By doing so, it maintains the cell structural integrity, the energy supply and the cell-cell connections upon contraction/relaxation of the myosin filaments in smooth and skeletal muscles[270, 271]. So, similar to vimentin, its presence in the porcine IPE tissue makes sense in regards to the critical functions its supports.

A-smooth muscle actin is also critical in this function. On a general basis, actin proteins form dynamic filaments from a pool of cytosolic actins toward a specific direction[272]. The polymerisation happens toward the direction of interest, this end being called the barbed/plus end[248]. Meanwhile, on the other side, the pointed/minus end depolymerises to recycle actin polypeptides. The actin filaments, also called stress fibres/thin filaments, form in a parallel manner to then intercalate with the myosin filaments[4]. The myosin heads attach to the thin filaments, then balance the myosin filament toward the barbed end. Six actin isoforms have been identified so far, the amino acid sequence composing them is identical at 95%[248]. One of the major factors of each isoform is the N-terminal domain, which is believed to drive the polymerisation rate and the length of the filament[273]. The six isoforms have been identified in distinct tissues, except the α-SMA, identified in smooth muscles, vascular endothelial walls and myofibroblasts[248, 274]. The reason is that the α-SMA would increase the cell traction forces as demonstrated by Chen *et al*[275]. So, the α-SMA in the IPE would integrate the dilator muscular system there by favouring the contraction of the iris toward its periphery.

Not detected in the porcine sections but in the human ones only, likely due to the non-suitability of the antibody on porcine tissues, the laminin-α4 was present in the basal lamina from the anterior layer only. This chain associates with cardiac and smooth muscle fibres, plus vascular endothelial vessels in various tissues[262]. The presence of a single laminin-α chain over the length of the IPE seems few in regard of the various laminins

found over smooth muscles in general[223, 276]. However, its unusual structure makes it relevant there. Indeed, its N-terminal is trunked, making the subsequent laminin network flexible compared with other laminins[277]. As the iris contracts and relax, multiple folds appear on its posterior side, as demonstrated by Freddo *et al*[32]. So, the flexibility of the basal lamina there is probably a key factor to support the integrity of the tissue in the multi-folded configuration. Another example of flexible tissue suffering different configurations are the endothelial vessels, which also use laminin-α4 as their major laminin-α chain[219].

In regard of the general structure of the iris and the eye, the presence of a smooth muscle lengthening the iris posterior side makes sense. The dilator, as a smooth muscle, can contract the iris within half a single cell layer over a large surface in a synchronous and autonomous manner without highly specific needs with the exception of its neural regulation, on the contrary of skeletal and cardiac muscles[3, 4].

Skeletal muscles are called voluntary muscles and compose with the skeleton to move the organism or the eye in the case of extraocular muscles[4]. Muscle fibers there are organised in a cylindric and longitudinal manner containing multiple nuclei, glycogen-containing granules and pools of myogloblines, the oxygen reservoir of these muscles[4]. Taking together, skeletal muscle fibers form a proper syncytium contracting and relaxing around their myosin and actin contractile filaments. Dimensions of skeletal muscles are also one of their specificities as their diameter range between 10 and 100 µm over distances going to 35 cm[4]. Physiologically, skeletal fibers are under the control of the somatic nervous system which decides the movements[4]. Its fibers distribute over the organism and connect in the cortex of the frontal lobe, the most anterior part of the brain[4]. If such system was applied to the iris, the pupil movements would not necessarily match with the environmental light intensity. And so, the intra-ocular light intensity would not necessarily match the physiological requirements of retinal cells[4].

The second system is the cardiac one, a striated muscle as the skeletal muscles, but under the control of the autonomous nervous system[4]. Cardiac fibers contract around myosine and actin filaments, which are structured in a striated manner to generate the tissue contraction. The anatomy of the cardiac muscle fibers differs from the skeletal ones by their shorter spread and a higher number of desmosomes and GAP junctions thanks to their plasmic membranes, which spouse the form of their facing counterpart[4]. This cell organisation favours the muscle fibers to contract and relax in a highly synchronised

manner, some authors describing it as well as a syncytium-based muscular system[4]. The main specificity of the cardiac system is its depolarisation and contraction capacity, autonomous of any neural regulations despite the significant number of neural-to-cardiac terminations[4]. The cardiac independent activity, also called intrinsic activity, relies on the fibers structures and the presence of the cardionector system, composed of non-contractile cell. The autonomous nervous system "regulates" the intrinsic system by accelerating or braking it[4]. This thin regulation makes the cardiac muscle a very specific system devolved only to the appropriate blood circulation[4].

So, the sum of proteins identified in that work supports that the porcine IPE anterior layer can be rightly compared with a smooth muscle as each cytoskeletal protein, plus the laminin-α4, supports the functions of the others. The probability to identify further proteins involved in mechanotransduction, smooth muscle regulation and smooth muscle activities in the human and porcine IPE anterior layers is therefore high.

3.10.4 Proliferation could occur at/near the ciliary body–IPE junction

In a tissue, two strategies exist to keep homeostasis. Either new cells arise to replace apoptotic ones, or the same cells remain over the life time.

In the first strategy, proliferating cells are generally specifically distributed to control their activity. The limitation of proliferation to specific areas is related to the function of epithelia. To form specialised barriers requires specialised cells that cannot maintain cell cycle activities at the same time[127]. So, special areas dedicated to the proliferation and its control are common. In the limbus, stem cells generate transient amplifying cells (TAC) on the basal layer, from which more cells arise and move toward the cornea centre[278]. A similar strategy is used by epidermal stem cells located on the top of dermal papillary. While they move toward the bottom of it, they transform into TAC to then leave the basal lamina and integrate the upper layers[279].

Less common are tissues which develop over embryogenesis and remain in that state over life. The RPE is a good example of such a tissue. It maintains its homeostasis by a long-term cell survival strategy, so without stem cells and without cell cycles. Instead, cells become hypertrophic to keep an epithelial continuum as RPE cell number decreases with ageing[138, 139].

So, it was originally expected that cell proliferation would localise at/near the ciliary body–IPE junction as a result of original stem or progenitor cell proliferation starting from the bottom of the ciliary body–IPE junction. Indeed, this region has the structural features of a stem cell niche. By comparison, the intestinal stem cell niche localises at the bottom of intestinal villi in a similar structural complex, which protects them from external environment issues, filters the nutrient supply and maintain their homeostasis through ontogenesis[280, 281, 282, 283]. In regard of the architecture of the eye, the ciliary body-IPE junction seemed ideal for that purpose.

As a result, the proliferation marker **Ki-67** was observed in cells at and near the ciliary body–IPE junction over both layers (see **Figure 3.21**). This can be translated as a cell pool in reserve maintaining the IPE from there. As fluorescence intensity reduced with increasing distance from that region, Ki67 proportion diminished and potentially the proliferation with[284]. It is tempting to hypothesise that a certain number of cells, close to the ciliary body-IPE junction and demonstrating intense Ki-67 fluorescence would correspond to transient amplifying cells (TACs) from which rise new IPE cells. These new cells would then move progressively toward the pupil to finally degenerate, as already suggested for the human IPE[3].

3.10.5 Developmental markers: PAX6 present, SOX2 absent?

3.10.5.1 PAX6 distributed over the IPE length, for what purpose?

PAX6 is a protein playing important functions during development. This transcription factor is involved in the RPE proliferation and maturation, the iris development, the production of crystalline in the lens, the retinal specification, the development of the forebrain, the cerebellum, the pancreatic islets, the lens, the cornea[285, 286, 287, 288, 289, 290, 290, 291]. Finely regulated with multiple regulatory sequences at the genetic level, PAX6 is often dependant of the form used and the amount present in an area. Its mutations can lead to severe pathological phenotypes due to abnormal development, such as the aniridia[292, 293].

So, as PAX6 was present in the IPE, the question of its use was asked (see **Figure 3.23**). In the iris, periocular mesenchymal cells migrate along the iris epithelium and differentiate into the iris stroma[48]. Iris continues to mature during postnatal time and a PAX6 gradient appears with high levels observed in non-neuronal cells destined for iris specification[294].

Developmental studies revealed that PAX6 haploinsufficiency would be the cause of aniridia. The inactivation of one of its alleles decreases the size of iris progenitor pool. With less progenitor cells, less tissue is generated and delays in formation of subjacent tissues appear[294, 295]. An example of consequent inactivation of PAX6 is the subsequent inactivation of BMP4, involved in the IPE polarisation[296, 297]. Following its inactivation, the IPE posterior IPE layer is thinner, the anterior one disorganised and the ciliary bodies absent.

So, in that investigation, PAX6 was found in both human and porcine sections from the ciliary body-IPE junction to a point close from the pupil (see **Figure 3.23**). A potential reason for adult IPE cells to use PAX6 at/near the ciliary body–IPE junction could be that it participates to the cell proliferation. Moreover, its spread over most of the IPE suggest that it could also participate to maintain several IPE functions. Next investigations could focus on its specific downstream targets involved in more specialised functions[298].

3.10.5.2 Further investigations are required for SOX2

SOX2 is another critical developmental regulator, identified in its mutated form in several anophthalmia and microphthalmia cases[299]. During development, SOX2 is associated with the lens formation and the retinal development[300, 301, 302]. In retinal progenitors, SOX2 plays the opposite function to PAX6, as ablation of the first drives an immediate upregulation of the second in progenitor cells, which transform toward non-neurogenic cells. When SOX2 expression is investigated on foetal mouse eye, it is found in the retina but not in the RPE, the CBE and the IPE. However, RPE cells exposed *in vitro* and *in vivo* to SOX2 convert into retinal cells[303, 304, 305].

In regards of the general literature, results from SOX2 investigation were at least unexpected (see **Figure 7.5**). In the limbus, SOX2 associates with ΔN-p63 to help the stem cell proliferation and prevent their differentiation[229]. On a general prospect, stem cells maintain SOX2 in the nucleus to interact with heterogeneous nuclear ribonucleoproteins, DNA repair proteins and helicases when it is not with other transcription factors such as OCT4[229, 306, 307, 308]. So, a transcription factor present in number in cell cytoplasm of a stem cell niche as observed there could reflect a sequestration from nuclei. The SOX2 amino acid structure contains indeed a nuclear export signal, which leads to its expulsion from the nucleus when that sequence is acetylated[309].

However, it was impossible to assess specifically this post-translational modification. Biologically, if limbal stem cells expulsed SOX2 as showed there, they would differentiate without renewing their pool leading to degeneration of the corneal epithelium. No event like that from porcine limbii has been physiologically observed so far. So, a straight reason would be that the antibody, predicted to work on porcine tissues, did not recognise SOX2. Thus, it is necessary to reinvestigate porcine tissues with a new anti-SOX2 antibody.

3.11 In conclusion

In total, the sum of proteins found in the porcine IPE is in accordance with the functions described in other mammal species, supporting that it physiologically runs as a myoepithelium. The porcine IPE seems not only to be polarised along the anterior – posterior axis as demonstrated by the distinct muscular and pigmented compartments. Cell homeostasis is probably organised along a peripheral-to-central axis with proliferation potentially limited at the IPE periphery, while cells at the centre would degenerate and be evacuated by the aqueous humour flux. In that regard, the aim of the chapter to distinguish different sections inside the porcine IPE could be considered as partly completed. Further investigations using other protein targets would bring more values to this postulate.

Furthermore, some elements associated with stem cells were observed in the ciliary body-IPE junction. In absence of specific markers so far, next investigations shall focus on such generic stem cell-associated proteins. Finally, to understand the rationales behind PAX6 spread in the adult IPE could complete the understanding of the IPE homeostasis.

4 Chapter 4: Porcine IPE cells in neurogenic conditions develop specific neuronal proteins

4.1 Overview

As explained in section **1.3.6**, neurosphere assays were used in this project with the expectation that IPE stem cells would arise from them. In the past, IPE-derived spheres have been successfully generated from some animal models including chicken, rat and pig[201, 202, 310]. So, the Kearns group developed a protocol to generate spheres from fresh pig eyes (unpublished data). That protocol served as the starting point for following investigations using Nunclon Sphera© plates. However, quickly after investigations began, the COVID outbreak raised and then resulted in a plastic shortage, limiting the access to these plates.

4.2 Aim & objectives of the chapter

The aim of that chapter was to investigate the behaviour of IPE cells placed in generic neurospheres conditions.

The objectives were:

- To investigate protocols and materials able to generate spheres or aggregates
- To investigate the way IPE spheres or aggregates form
- To investigate the epithelial and muscular markers initially found in chapter III
- To investigate potential cell transformations.

4.3 Development of cell culture processes

As investigations were starting, a systematic microbial contamination arised from the IPE cultures. Despite the attempts to clean the hoods, the incubators and the materials used, microbial contamination persisted. So, the protocol required updates in first instance.

Moreover, the COVID outbreak resulted in a plastic shortage, limiting the access to the Nunclon Sphera© plates. So, other plates were considered.

4.3.1 IPE contamination was resolved by an increased antibiotic concentration in the cell culture medium

Based on the Institute *in-house* protocol, steps were included while some solutions changed. The final protocol was the addition of the original one plus all changes investigated. Protocols investigated are summarised in **Table 4-1**.

Table 4-1: Summary of changes included

Original process	**Condition 1**	**Condition 2**	**Condition 3**	**Condition 4**
		In dissection hood		
1. Extra-ocular muscles removed	**1.** Extra-ocular muscles removed	**1.** Extra-ocular muscles removed	**1.** Extra-ocular muscles removed	**1.** Extra-ocular muscles removed
2. Separation between anterior and posterior chambers	**2. Eyes cleaned in PBS 1% P/S/F + PBS 10% Iodine + PBS**	**2.** Eyes cleaned in PBS 1% P/S/F + PBS 10% Iodine + PBS	**2. Eyes cleaned in PBS 2% P/S/F + PBS 10% Iodine + PBS**	**2.** Eyes cleaned in PBS 2% P/S/F + PBS 10% Iodine + PBS
3. Anterior chamber placed in PBS	**3.** Separation between anterior and posterior chambers	**3.** Separation between anterior and posterior chambers	**3.** Separation between anterior and posterior chambers	**3.** Separation between anterior and posterior chambers
4. Iris detached from sclera and separated from surrounding epithelia	**4.** Anterior chamber placed in PBS	**4.** Anterior chamber placed in PBS	**4.** Anterior chamber placed in PBS	**4.** Anterior chamber placed in PBS
5. Iris placed in DMEM-F12 20% FBS 1% P/S/F until all eyes are processed	**5.** Iris detached from sclera and separated from surrounding epithelia	**5.** Iris detached from sclera and separated from surrounding epithelia	**5.** Iris detached from sclera and separated from surrounding epithelia	**5.** Iris detached from sclera and separated from surrounding epithelia
6. Incubation in TryplE for 40 min at 37^{o}C	**6.** Iris placed in DMEM-F12 20% FBS 1% P/S/F until all eyes are processed	**6.** Iris placed in DMEM-F12 20% FBS 1% P/S/F until all eyes are processed	**6.** Iris placed in DMEM-F12 20% FBS 1% P/S/F until all eyes are processed	**6.** Iris placed in DMEM-F12 20% FBS 1% P/S/F until all eyes are processed

7. Tissues placed back into DMEM-F12 20% FBS 1% P/S/F	**7.** Incubation in TryplE for 40 min at 37°C	**7.** Incubation in TryplE for 40 min at 37°C	**7.** Incubation in TryplE for 40 min at 37°C	**7.** Incubation in TryplE for 40 min at 37°C
8. IPE separated from the stroma	**8.** Tissues placed back into DMEM-F12 20% FBS 1% P/S/F	**8.** Tissues placed back into DMEM-F12 20% FBS 1% P/S/F	**8.** Tissues placed back into DMEM-F12 20% FBS 1% P/S/F	**8.** Tissues placed back into DMEM-F12 20% FBS 1% P/S/F
9. IPE's suspension transfered in sterile PBS and centrifuged	**9.** IPE separated from the stroma	**9.** IPE separated from the stroma	**9.** IPE separated from the stroma	**9.** IPE separated from the stroma
In safety cabinet type 2				
10. IPE's pellet resuspended and seeded in DMEM-F12 10% FBS 1% P/S/F	**10.** IPE's suspension transfered in sterile PBS and centrifuged	**10. IPE's suspension transfered in sterile PBS 1% P/S/F for 10-15 min**	**10. IPE's suspension transfered in sterile PBS 2% P/S/F for 10-15 min**	**10.** IPE's suspension transfered in sterile PBS 2% P/S/F for 10-15 min
	11. IPE's pellet resuspended and seeded in DMEM-F12 10% FBS 1% P/S/F	**11.** IPE's pellet resuspended and seeded in DMEM-F12 10% FBS 1% P/S/F	**11.** IPE's pellet resuspended and seeded in DMEM-F12 10% FBS 1% P/S/F	**11. IPE's pellet resuspended and seeded in DMEM-F12 10% FBS 2% P/S/F**

In IPE cultures cultivated by the original process (see **Table 4-1**), cells originated from black aggregates (see **Figure 4.1-A**). Over one week, their number grew to pass 100,000 cells for most samples (see **Figure 4.1-C**). Morphologies were filiforms or cuboidal. The high content of melanin facilitates the distinction of cells and their nuclei. When contaminated, IPE cells look degenerated or atrophied, with a lower cell number and the presence of an opaque suspension in the medium (see **Figure 4.1-A**).

So, the first change was the cleaning of eye cups after extra-ocular muscles removal (see **Table 4-1 – Condition 1**), with the aim to destroy the microbial load before opening the eye cups. Eyes were placed into three PBS solutions containing 1% P/S/F, 10% povidone iodine and PBS only respectively. Each step lasted 2 minutes. Still, contamination was visible at day 6 (see **Figure 4.1-B**).

So, the next change was a cleaning of IPE cell suspensions prior to the cell seeding (see **Table 4-1– Condition 2**). IPE suspensions were incubated for 10-15 min in a PBS 1% P/S/F

solution in a 15 ml Falcon© tube with movements to maximise microbe destruction and prevent cell suspensions to form a pellet with microbes inside. Tubes were then centrifuged, pellets resuspended and cell seeded. Once more, contamination was visible at day 3 and no growth was observed (see **Figure 4.1-B**).

So, antibiotic concentration was increased. Eye cups were cleaned in a PBS 2% P/S/F solution prior to the PBS 10% povidone iodine solution and the PBS cleaning, and IPE cell suspensions were incubated in PBS 2% P/S/F prior to cell seeding (see **Table 4-1– Condition 3**). Still, contamination was visible and cell attachment did not occur for most IPE samples processed (see **Figure 4.1-B**).

Thus, it was accepted that the microbial load would remain over the cell process. On the top of all previous changes, the antibiotic concentration in media was increased to 2% over the entire cell process (see **Table 4-1– Condition 4**). No more contaminations were observed in IPE culture but cell number counted at day 8 reduced instead (see **Figure *4.1*-B & -C**).

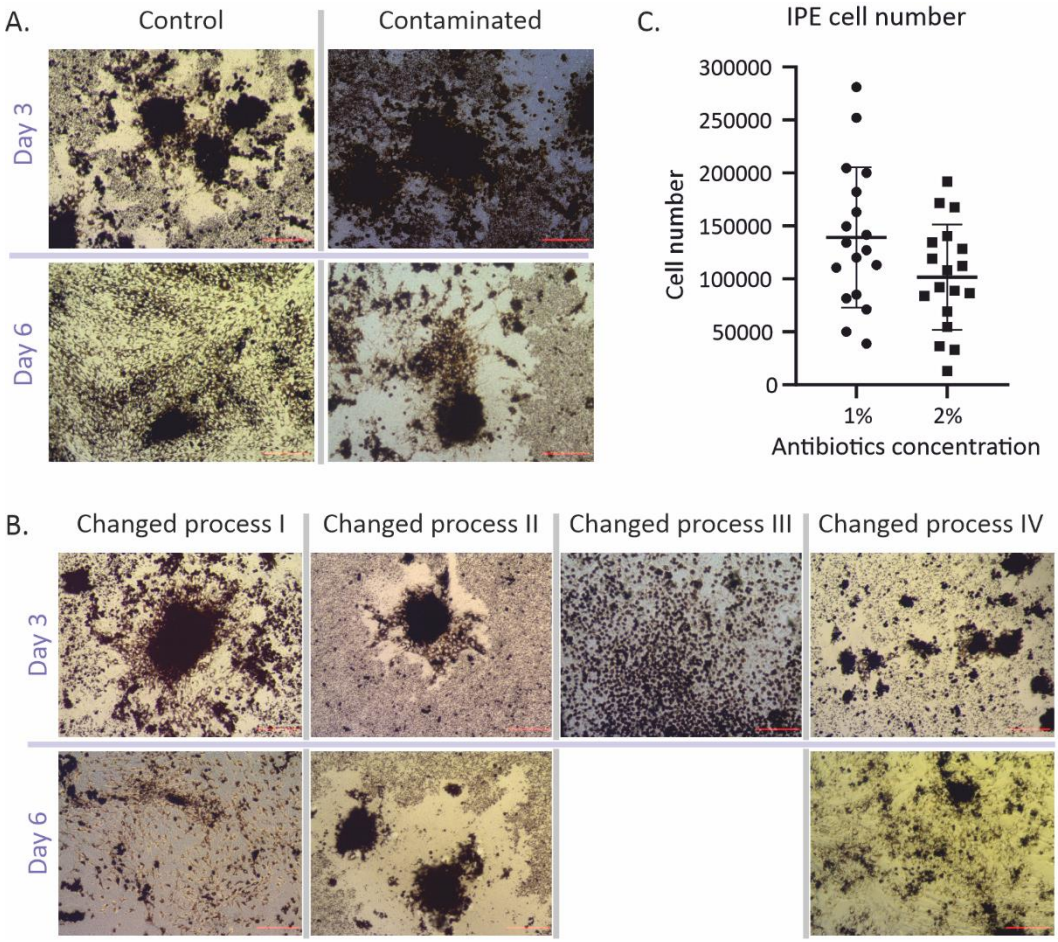

Figure 4.1: Representative images of primary porcine IPE cells in culture after extraction. **A.** IPE cultures grown by the original process prior to the contamination (= control) and

after it (= contaminated). Pictures show IPE cells 3 and 6 days after their extractions. Scale bars = 100 µm. **B.** IPE cells grown by the conditions exposed in **table 18**. Pictures show IPE cells 3 and 6 days after their extractions. Scale bars = 100 µm. **C.** Cell number measured at day 8. 18 porcine IPE culture were grown with antibiotics at 1% and 18 with antibiotics at 2%. Statistical analysis used an unpaired T-test with Welch's corrections. No significant differences were observed at P value <0.05.

4.3.2 IPE-derived aggregates formed and remained suspended only on Nunclon sphere plates

To compensate the lack of low adhesive Nunclon Sphera plates, two alternative plates were assessed: **1**. Greiner suspension plates with a hydrophobic surface expected to keep cells in suspension; **2**. Facellilate Bioflat plates with an U-shape and a repellent coating for cells.

The comparison revealed the Nunclon sphera plates to be the most efficient to generate and maintain the spheres in suspension. In Facellitate Bioflat plates, no spheres were observed over the process. Cells were supposedly forced to aggregate due to the well U-shape and the chemical compound supposed to repel the cells from the plastic. Instead, IPE cells were gathering in the bottom forming a layer (see **Figure 4.2-B**). Over time, the layer increased in density. When the layer was pipetted to observe potential spheres, it was disrupted. So, neither cells adhered to the well, nor they formed spheres.

The Greiner suspension 24 wells plates were used for some time as a replacement solution thanks to a gift from Prof. Heather Allison. As expected, spheres were quickly observed after 2 days of culture in suspended conditions (see **Figure 4.2-C**). However, it also quickly appeared that a consequent number of them attached to the bottom with cells spreading out of the sphere. Over one week of culture, most of the spheres generated had adhered (see **Figure 4.2-G**).

So, the Nunclon Sphera plates were not only better at generating aggregates (see **Figure 4.2-E**), they were also the only one able to maintain them in suspension. It was commonly observed that some spheres formed by a slow aggregation process, initial cells binding to each other before aggregating to other cell spheres. That resulted in a low number but tall cell spheres over 8 days of culture (see **Figure 4.2-D & -F**). Several small spheres were also present in the end of the process.

Thus, despite the shortage, it was clear that further investigations would require Nunclon Sphera 24 wells plates. The issues with adhesion to Greiner suspension 24 wells plates

was not remedied despite extensive pipetting of the cell “suspension”, not sufficient. Perhaps the use of a rolling machine in the incubator could have prevented attachment but it was not possible to implement it due to the lab settings. As no IPE spheres were observed on all Facellitate Bioflat 96 wells plates used, those ones were not used in further investigations.

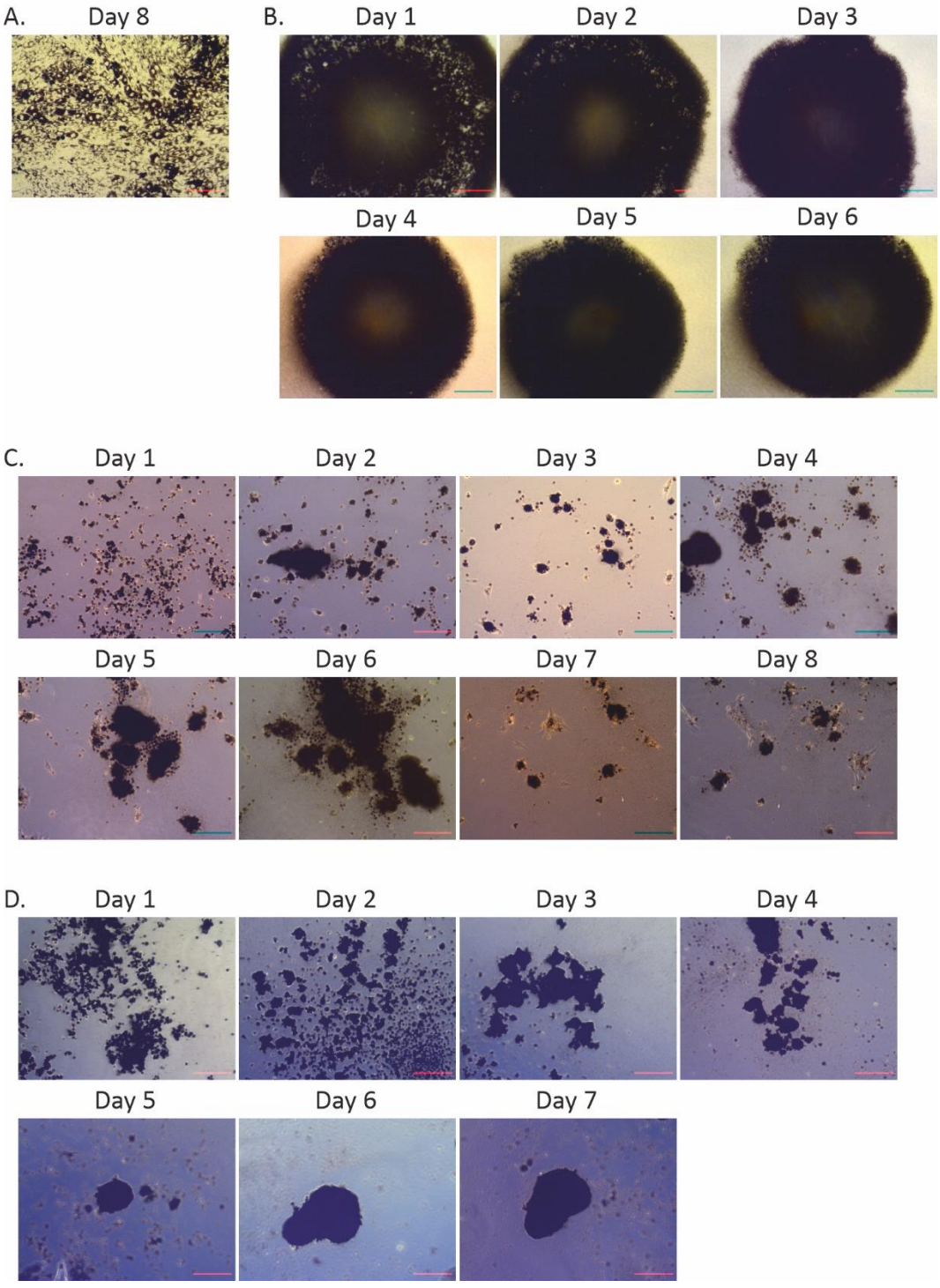

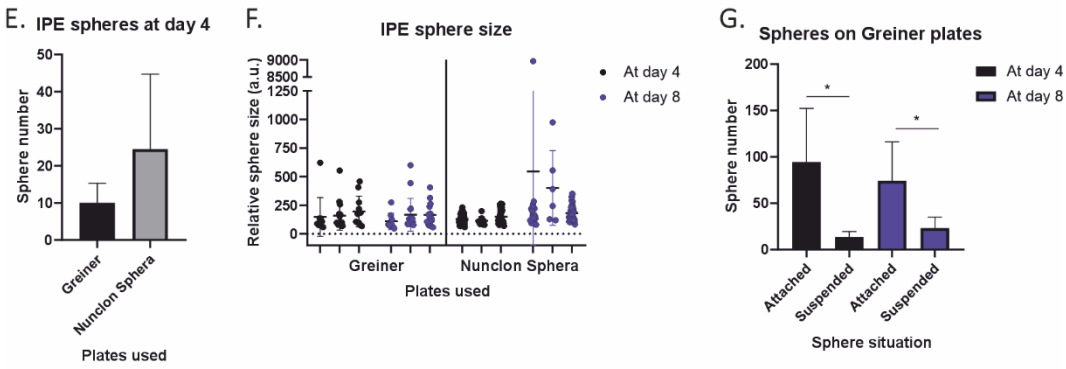

Figure 4.2: Plates efficiencies to generate aggregates from porcine IPE cells. A. IPE cells on adherent plates at day 8. Scale bars = 100 µm. **B.** IPE cells on Facellitate Bioflat plate over 6 days of culture. Scale bars = 100 µm. **C.** IPE aggregates on Greiner suspension plates over 8 days of culture. Scale bars = 100 µm. **D.** IPE aggregates on Nunclon Sphera plates over 8 days of culture. Scale bars = 100 µm. **E.** IPE aggregates numbers at day 4. Statistics were done by an unpaired T-test with Welch's corrections. No significant differences were observed. **F.** IPE aggregate size at day 4 and day 8 on Greiner and Nunclon Sphera plates. Statistical analysis was performed using a one-way ANOVA-based Kruskal Wallis test. No significant differences between the medians were observed (P-value <0.05). **G.** IPE aggregates suspended or attached to the Greiner plates at day 4 and day 8. Statistics were done using a one-way ANOVA-based Kruskal-Wallis test. Significant differences were observed at P-value <0.0001.

4.4 IPE spheres result from the aggregation of original cells

The lack of specific IPE stem cell markers prevented cell selection upstream of the culture process. Moreover, previous investigations on plate selection showed that spheres passed from the state of a single cell-based element to a massive sphere over 8 days. So, CFSE and DiD-DiI spread were investigated in IPE spheres. These dies allow to distinguish between a cell aggregate and a sphere generated from cell proliferation (see **Figure 4.3**).

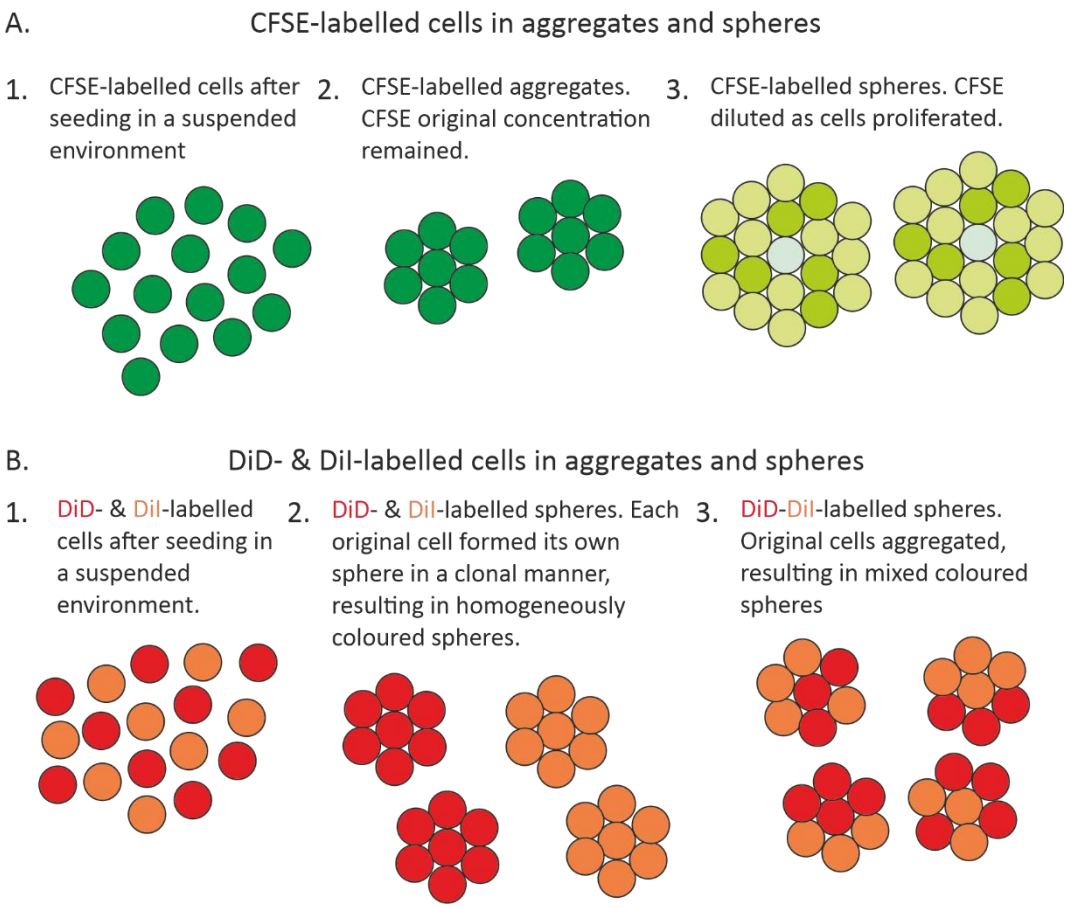

Figure 4.3: Representative scheme of CFSE and Di-dies used. A. CFSE-labelled cells could form aggregates. By doing so, they retain the initial CFSE in their cytoplasm[190]. Or they could proliferate and subsequently diluted the original CFSE between the different new generated cells[311]. **B.** DiD- & DiI-labelled cells could either proliferate in a clonal manner. By doing so, they would be coloured by a single dye[312]. Or they would result from aggregation, at least partly. Subsequently, they would be coloured by both DiD and DiI dyes.

4.4.1 CFSE-labelled spheres demonstrated heterogeneous cell proliferation over eight days

On images, CFSE is present over sections with various distributions (see **Figure 4.4-A**). The CFSE intensity suggested that IPE cells proliferated, but probably not all of them. Intense fluorescence areas were indeed observed in core and periphery regions, while lower fluorescence areas were present in intermediate regions. In parallel, DAPI labelled more cells at the periphery than in the center. So, these results suggest that: **1**. proliferation occurred in IPE aggregates in a similar fashion between the different sections assessed; **2**. the CFSE intensities being low in intermediate region, proliferation could have run at its

highest rate in that region. To note, some holes were also present where no DAPI or CFSE were observed, probably resulting from the cryosectioning.

Statistical analysis of green pixel numbers per green intensity (see from **Figure 4.4-B to -G**) supports the previous analysis. Few regions only demonstrated a high CFSE intensity, so those cells conserved a high CFSE content and probably did not proliferate, or slowly compared to their counterpart. Oppositely, the large number of green pixels with low green intensity suggests that a significant number of cell proliferated.

It is possible that the proliferation activity for each cells was intrinsically low with on the other side a major proportion of cells having proliferated. The opposite reaction would have indeed generated aggregates with mostly a low CFSE content, meaning a low green intensity. Plus dense DAPI regions.

In an attempt to assess if cells proliferated in specific areas only, FICC for Ki67 and PCNA were run (see **Figure 4.5**). The S phase marker PCNA was present through the section with various densities. Some regions demonstrated a high content of labelled nuclei while other remained unlabelled. Ki67 mitosis marker confirmed that observation, with marks spread in regions where PCNA was detected. Where PCNA was not observed, Ki67 was absent as well.

Taking together, these results suggest that IPE cells were able to proliferate, probably at a low rate. Some cells in the core probably did not proliferated as demonstrated by their high CFSE content and the absence of PCNA and Ki67. In total, these results underlined that spheres were not generated from homogeneous clonal proliferation but, in line with previous observations, from progressive cell aggregation.

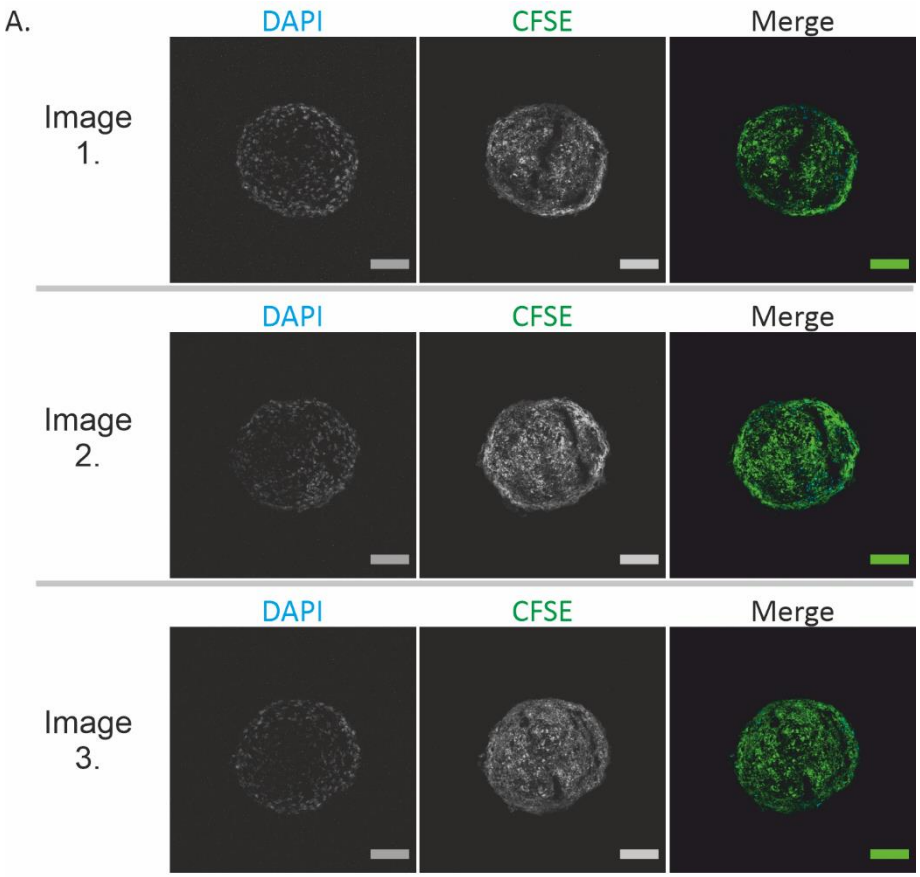
A.
DAPI
CFSE
Merge
Image 1.
Image 2.
Image 3.

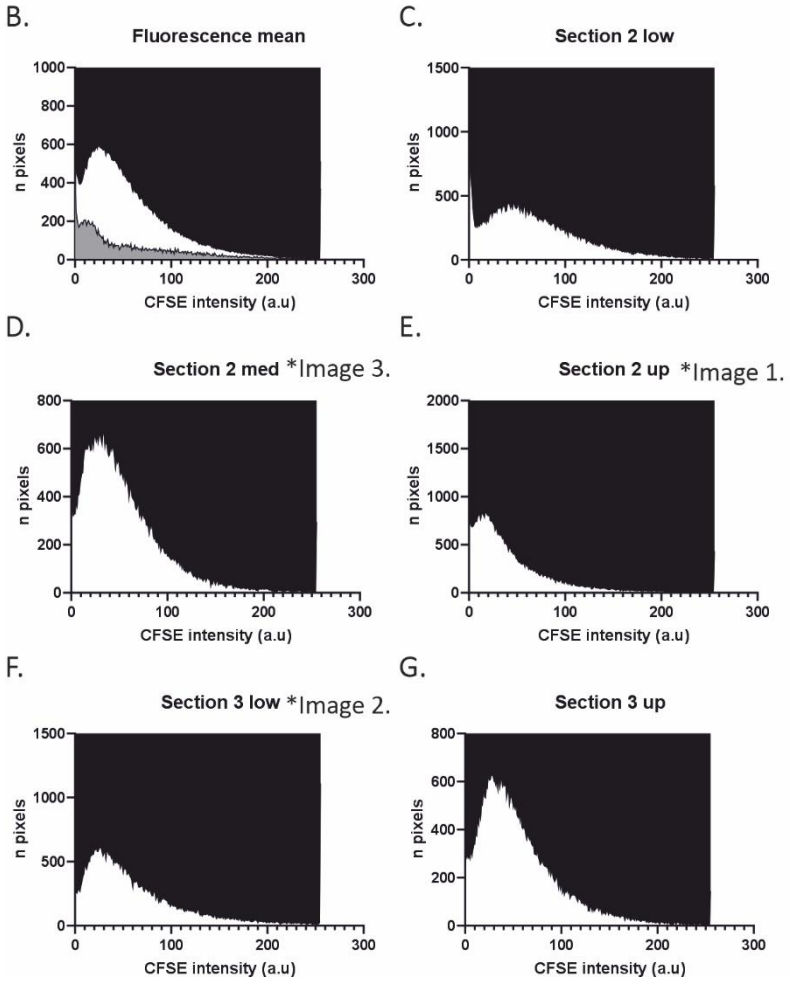
B.
Fluorescence mean
n pixels
CFSE intensity (a.u)
C.
Section 2 low
D.
Section 2 med *Image 3.
E.
Section 2 up *Image 1.
F.
Section 3 low *Image 2.
G.
Section 3 up

Figure 4.4: Representative images of CFSE-labelled porcine IPE spheres grown for eight days. CFSE intensity is heterogeneous depending the aggregate area: high in some cores areas and in periphery; low in between. **A.** Fluorescent pictures of three CFSE-labelled IPE spheres. Sections were counterstained for DAPI. DAPI is in blue, CFSE in green. Scale bars = 100 µm. **B-G.** Fluorescence intensity measured on five CFSE-labelled sections. Means and standard deviations per pixel value were obtained from the five sections investigated. Images showed in **A.** are labelled on top of the graphs.

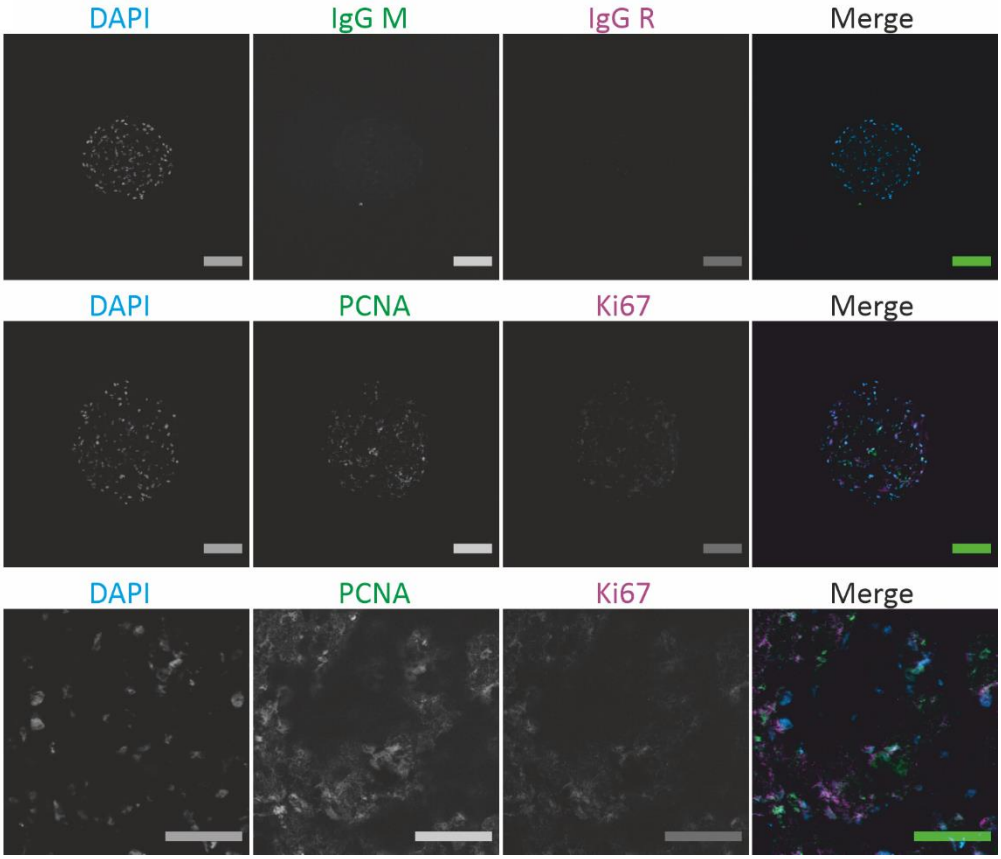

Figure 4.5: Fluorescent images of IPE aggregates labelled with anti-PCNA and anti-Ki67 antibodies. PCNA and Ki67 were found in similar locations. DAPI is in blue, PCNA in green and Ki67 in purple. Small SB = 100 µm, tall Scale bars = 50 µm.

4.4.2 DiD and DiI were mixed in spheres demonstrating an aggregation process rather than a proliferation one

Over the seven sections investigated for both dyes, controls not included, all of them demonstrated presence of DiD and DiI (see **Figure 4.6-B**). Dyes were mixed over all the sections. No area distinguished itself by the presence of a single colour. Some areas distinguished themselves by a lower die-based fluorescence intensity coupled with a higher one in DAPI. Cell density marked in these regions was higher as well, pointing that

proliferation diluted the dyes. So, aggregate cores demonstrating brighter fluorescence for both dyes did not proliferate, or at a lower rate than their counterparts.

Thus, in line with the data from the previous section (see section **4.4.1)**, aggregation was detected instead of clonal proliferation.

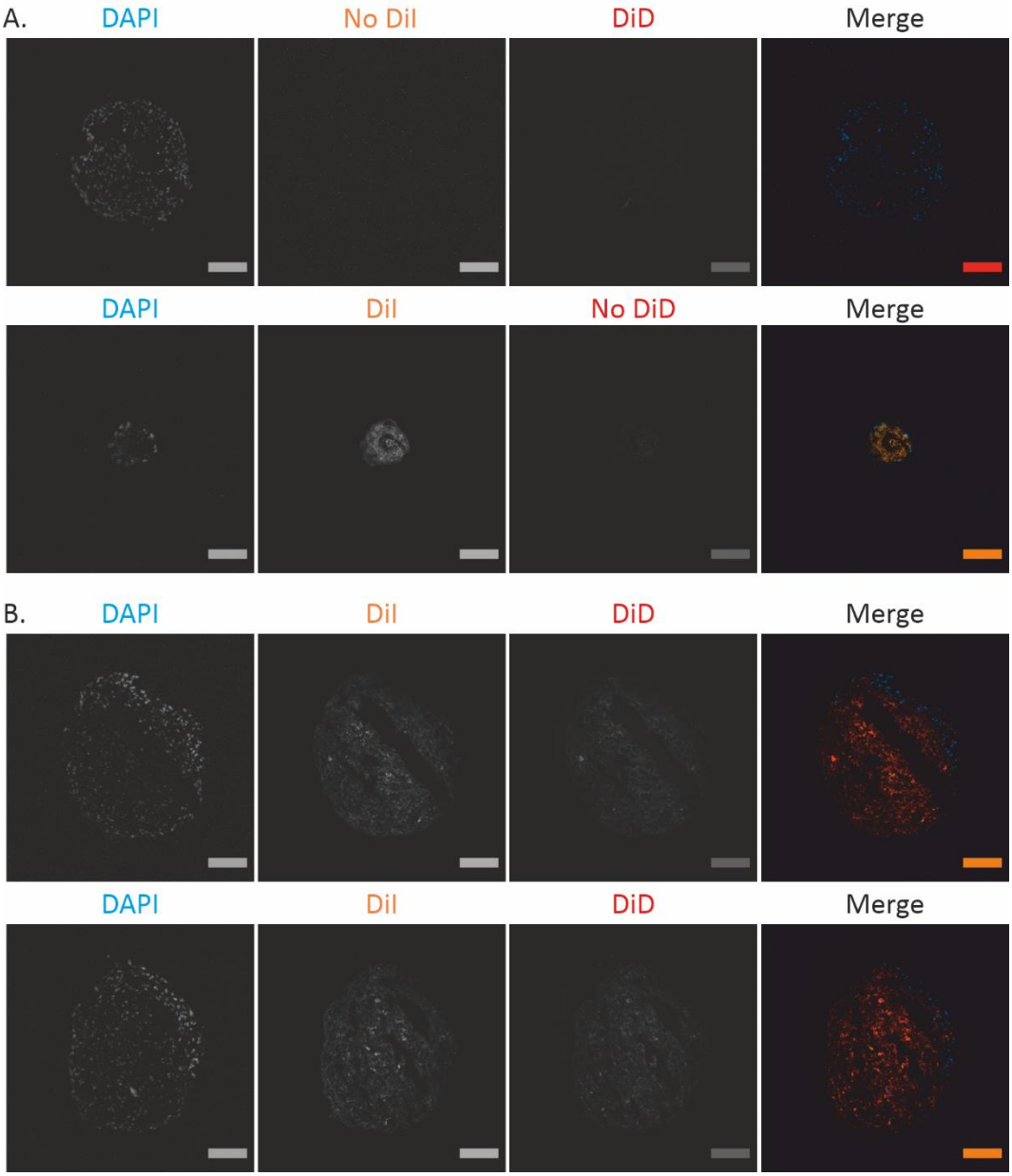

Figure 4.6: Representative images of DiD- and DiI-labelled porcine IPE spheres grown for 8 days. A. Fluorescent pictures of control aggregates labelled with DiD or DiI only. Sections were counter-stained for DAPI. DAPI is in blue, DiI in orange and DiD in red. Scale bars = 100 µm. **B.** Fluorescent pictures of sections labelled for both dies. Both dies were found spread over the aggregates. Sections were counter-stained for DAPI. DAPI is in blue, DiI in orange and DiD in red. Scale bars = 100 µm.

4.5 Epithelial and muscular features found in the tissue are conserved in the spheres

4.5.1 A-smooth actin is ubiquitously expressed by adherent cells and remained at the aggregate surface

In the tissue, α-SMA was detected in the IPE anterior part where it enters in contact with the posterior side of the iris stroma. A-SMA was present over the length of the tissue, from the ciliary bodies to the pupil (see **Figure 3.12**). So, a large cell population could be expected to produce α-smooth actin *in vitro*.

First, aRPE19 cells were used here as a negative control for mesenchymal proteins (see **Figure 4.7-A**). Despite the short culture time, some cells produced α-SMA and so underwent epithelial-mesenchymal transition. This phenomenon was already observed in aRPE-19 cell line[313, 314]. So, its use as a negative control for mesenchymal-based assessment would be reconsidered in later investigations.

In IPE adherent cells, α-SMA was strongly labelled over most of cells observed (see **Figure 4.7-B**). A-SMA-based stress fibres could be distinguished clearly in all cells. Cell morphology had the features of mesenchymal cells. No region without α-SMA were observed.

In IPE aggregates, α-SMA was detected at the sphere surface where the strongest fluorescence could be observed (see **Figure 4.7-C**). The core demonstrated positive staining as well with a lower intensity. It is possible that a part of that fluorescence there was due to the background. The IgG control demonstrated indeed a low but persistent background on the green channel in the core. Thus, α-SMA was properly labelled in both adherent IPE cells and in aggregates.

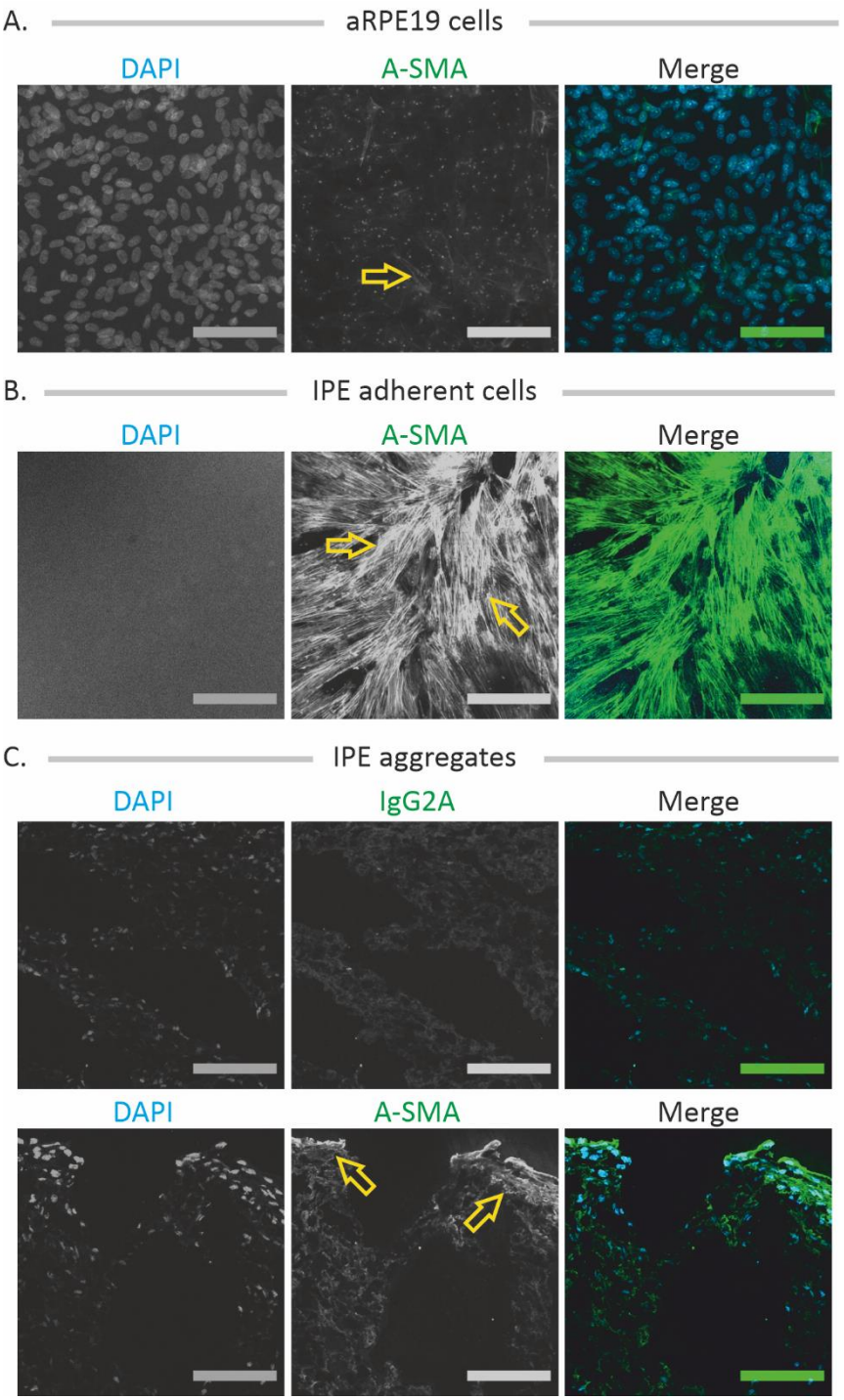

Figure 4.7: Representative images of α-smooth actin-labelled aRPE-19 cells, adherent IPE cells and IPE aggregates. A-SMA (= **yellow arrows**) was found in aRPE19 cells, IPE adherent cells and IPE aggregates. **A.** ARPE-19 cells negative control. **B.** IPE adherent cells. **C.** IPE aggregates. A-SMA is in green, DAPI in blue. Scale bars = 50 µm.

4.5.2 Desmin was observed in both adherent cells and spheres at a lower rate

In the porcine iris, desmin works for the dilator muscle. Its distribution arises from the ciliary body – IPE junction and finishes before the pupil (see **Figure 3.2**). In this investigation, it was hypothesised that desmin would diminish in adherent culture and would be absent in the suspended one. Firstly, the lack of muscle activity may favour a reduction of its expression. Secondly, myoblasts and desmin-expressing cells require specific media to produce desmin[315, 316] that were not used in this study.

ARPE-19 cells were found to not produce desmin as expected (see **Figure 4.8-A**). ARPE-19 derived indeed from a 19 years old human retinal pigmented epithelial cell extraction[204], and so never experienced muscles activities. IPE adherent cells showed few cases only of desmin-positive staining (see **Figure 4.8-B**). The labelled proteins were sparse and no fibres could be observed, the opposite of what was observed in the tissue. It is possible that the proteins observed there could be remnants of the tissue. Finally, IPE aggregates demonstrated desmin-positive staining at their surface, in the same manner than DAPI (see **Figure 4.8-C**). No background was observed on the IgG control. Thus, desmin was present in both stage of the cell process and as expected, the detected content was low.

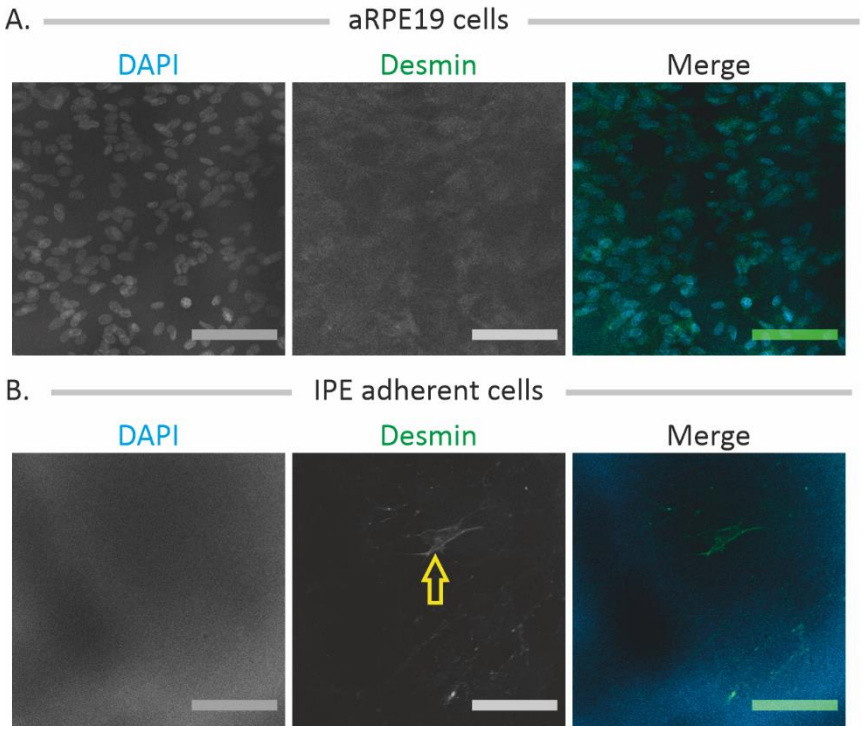

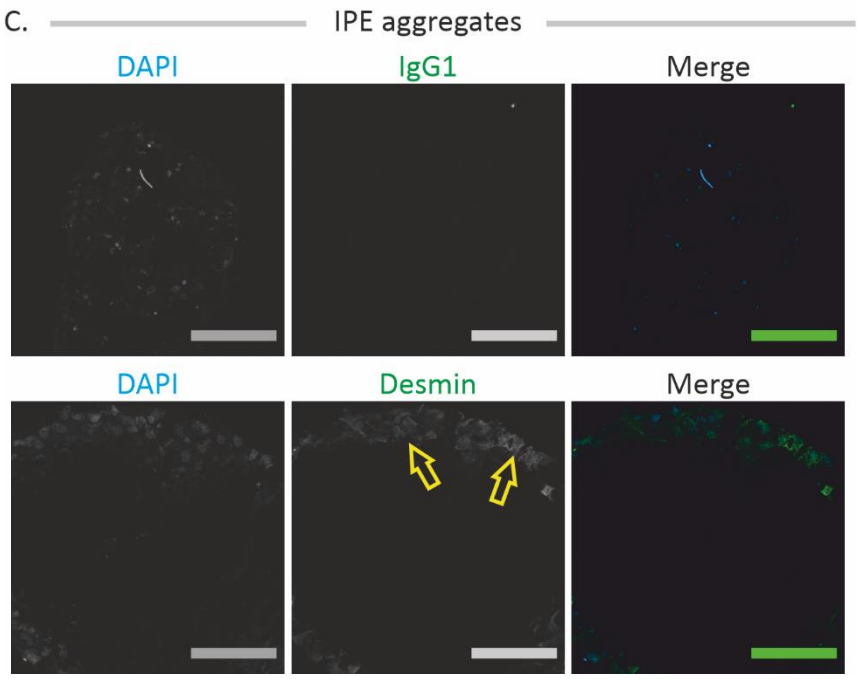

Figure 4.8: Representative images of desmin in aRPE19 cells, adherent IPE ones and IPE aggregates. Desmin (= **yellow arrows**) was found in some IPE adherent cells and in IPE aggregates in its periphery. **A.** ARPE-19 cells. **B.** IPE adherent cells. **C.** IPE aggregates. Desmin is in green, DAPI in blue. Scale bars = 50 µm.

4.5.3 Vimentin and nestin are major cytoskeletal proteins in both IPE adherent cells and IPE aggregates

In the previous chapter, vimentin was detected only by WB, despite several attempts to label it by FIHC (see **Figure 3.6** & **Figure 3.7**). So, its distribution remained unknown. On the human positive control used, vimentin was present through the IPE length from the ciliary bodies to the pupil. So, it is probable that vimentin distributed also in all porcine IPE cells. Thus, vimentin was expected to be found in IPE adherent cells and aggregates.

Oppositely, nestin was found only in rare places near the ciliary bodies – IPE junction (see **Figure 3.11**). So, nestin content from IPE cells *in vitro* was expected to be similarly low or even absent.

As a result, vimentin was expressed by all IPE cells observed after 8 days in culture (see **Figure 4.9-A**). The pattern of vimentin distribution was characteristic of mesenchymal cells. Vimentin was found through the whole body of IPE aggregate as well (see **Figure 4.9-B**). These data confirmed vimentin as a major cytoskeletal element of porcine IPE cells.

Oppositely, the presence of nestin over all IPE cells was unexpected (see **Figure 4.9-A**). In accordance with its natural heavy weight, preventing it to form filaments by its own[214], nestin was found colocalising with vimentin. Nestin was also highly present in IPE aggregates (see **Figure 4.9-B**). Repeated investigations revealed that nestin commonly appeared in adherent IPE cells and in IPE aggregates. Thus, nestin could be intrinsically linked to the IPE on the side of vimentin.

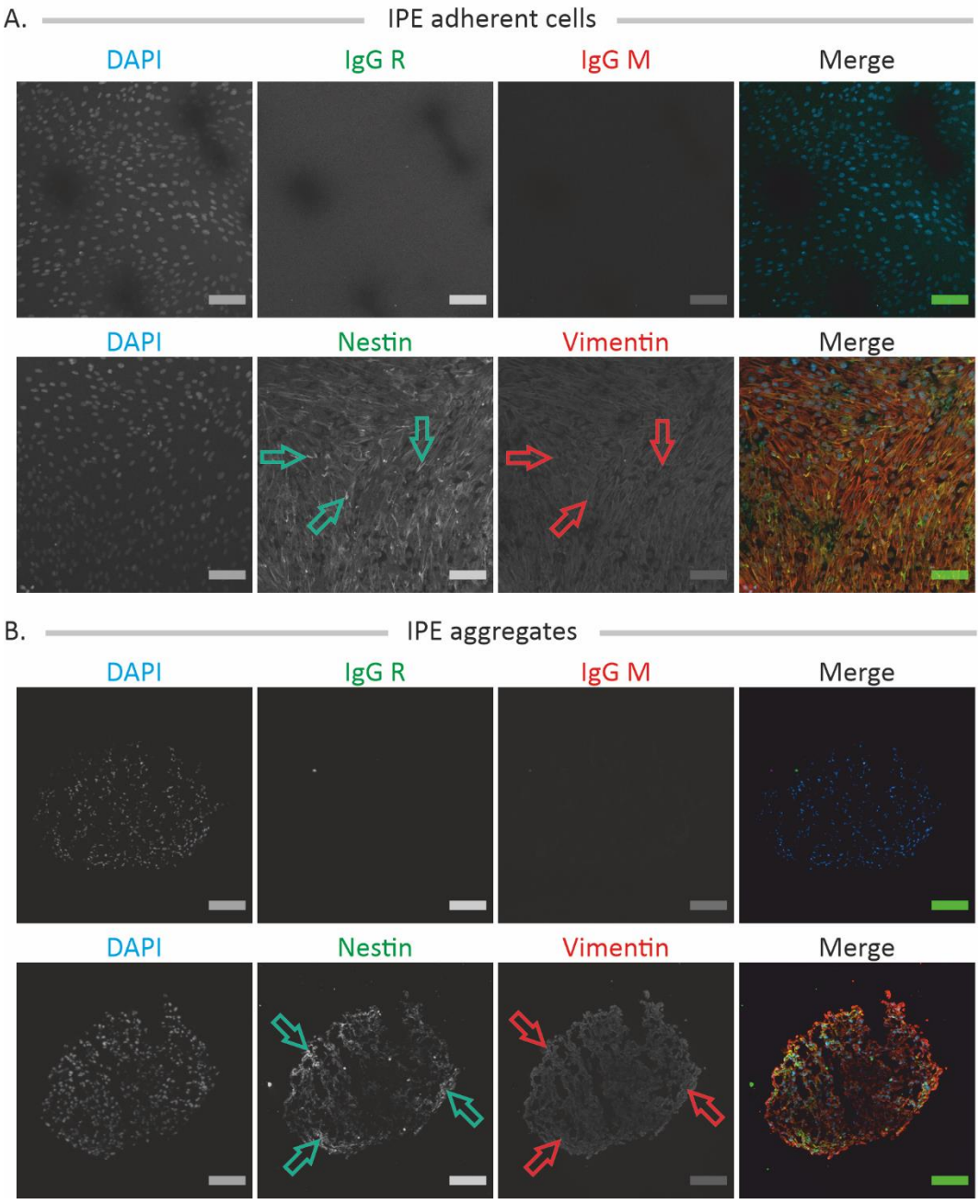

Figure 4.9: Representative images of nestin & vimentin-labelled IPE cells and IPE aggregates. Nestin (= **green arrows**) and vimentin (= **red arrows**) were found in all sample types. Green and red arrows are also placed in locations where both proteins were closely

labelled, giving a yellowish colour when plans were merged. **A.** IPE adherent cells. **B.** IPE aggregates. Nestin is in green, Vimentin in red, DAPI in blue. Scale bars = 100 µm.

4.6 Do IPE spheres revert their phenotype in culture?

To evaluate the cell behaviour requires quantitative techniques demonstrating increases, decreases and absence of the markers. WB have already been processed on porcine IPE samples (see **Figure 3.7-B**). However, proteins amounts are important for the sake of consistent results. Manufacturers recommend to load a minimal protein amount of 20 µg per well prior to perform the electrophoresis. However, IPE aggregates-based protein extracts showed really low protein contents (see **Table 4-2**), which made the loading technically challenging: right amount impossible to load; limited samples; inability to repeat the experiment. It would have generated tremendous cost and time in cell culture and materials to solve these issues. It was therefore decided to evaluate cell behaviour by retro-transcription quantitative PCR (RT-qPCR). All transcripts proved to work on one or more porcine sample are summarised in the **Table 2-6**.

Table 4-2: Summary of IPE spheres-based protein samples

IPE sample	IPE spheres sample VIII	IPE spheres sample IX
Total cell number prior to seeding	1,394,100	492,000
Time point	Day 8	Day 8
Protein amount (in µg/ml)	107.6	132
Final volume (in µl)	100	100

4.6.1 IPE aggregates reduced over time the expression of the transcripts of interest

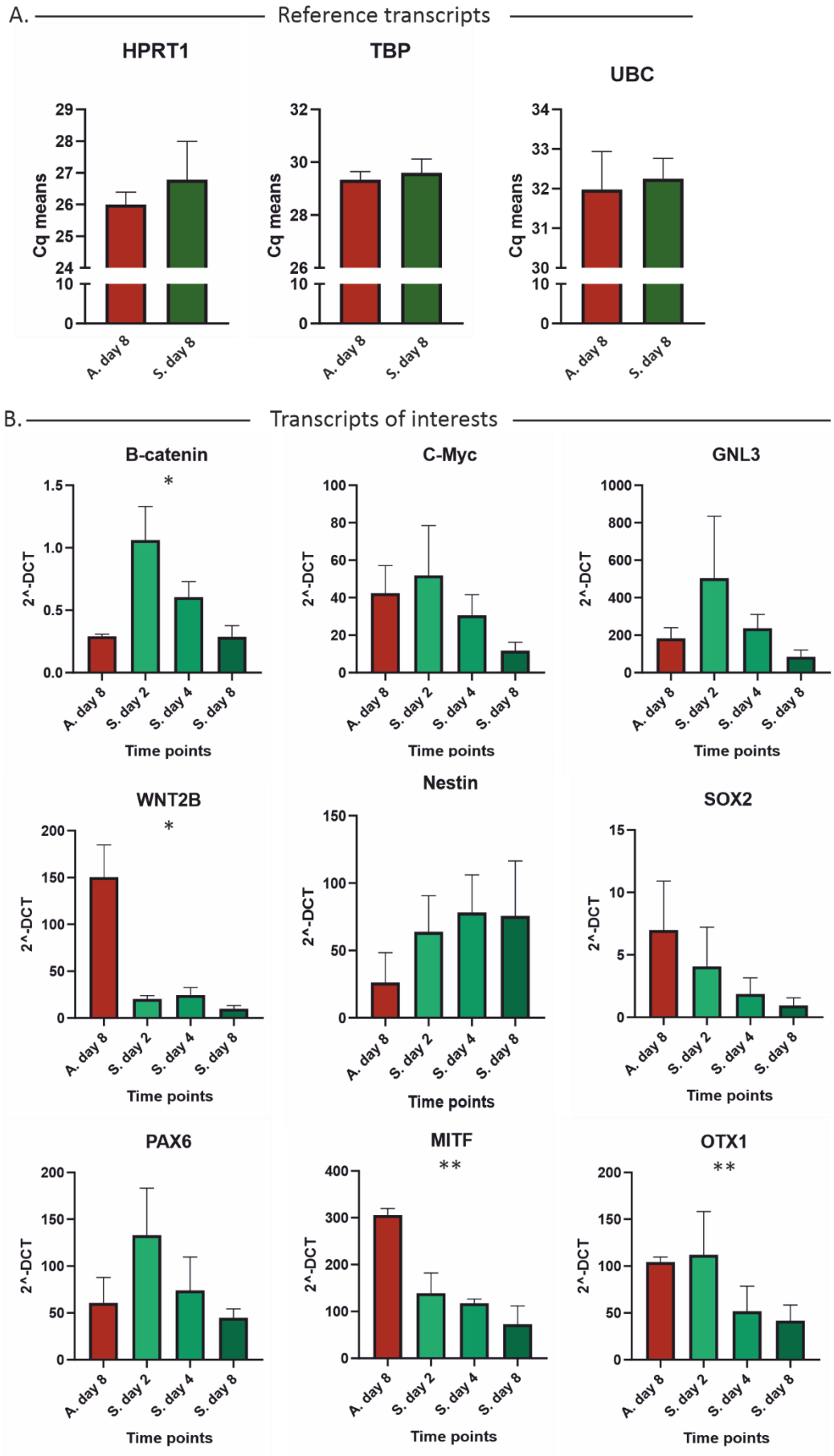
A.
Reference transcripts
HPRT1
TBP
UBC
Cq means
A. day 8
S. day 8
B.
Transcripts of interests
B-catenin
C-Myc
GNL3
WNT2B
Nestin
SOX2
PAX6
MITF
OTX1
2^-DCT
Time points
A. day 8
S. day 2
S. day 4
S. day 8

C.

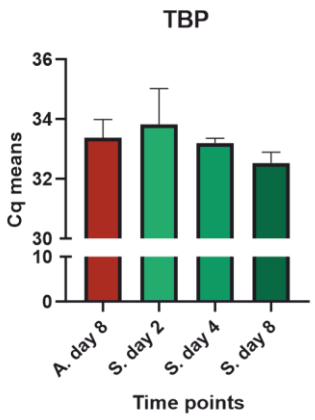

Figure 4.10: qPCR analysis of the various transcripts of interest in IPE cells and spheres. A. Reference transcripts were compared for their Cq values between adherent cells (A. day 8) and IPE aggregates (S. day 8). Four samples per conditions with three replicate per sample were used and plotted together. No significant differences were observed between conditions for each reference transcript ($p < 0.05$). **B.** Genes expression of adherent cells (A. day 8) and aggregates (S. day 2, day 4 and day 8). Three samples were used for the first and second time points, 4 for the two last ones. Cq mean was obtained from 3 replicates from each sample and plotted against TBP. Y-axis represent the subsequent $2^{-\Delta Ct}$, X-axis represent the time points at which RNA was extracted. Statistics were done with a Welch's ANOVA test ($p < 0.05$). **C.** TBP expression over the four times points described in **B.** Cq mean was obtained from 3 replicates from each sample. Y-axis represent Cq means. No significant differences were observed between the time points ($p < 0.05$).

4.6.1.1 TBP expression is the most stable of the reference transcripts

Once transcripts were validated, optimised when required (see **Table 2-6**), second assessment analysed the reference transcript varying the less between adherent and suspended cultures. So, HPRT1, TBP and UBC were assessed for two time points: after 8 days of adherent culture and after 8 days of suspended culture. As a result, the TBP transcripts demonstrated the closest Cq values between the two cultures (see **Figure 4.10-A**). HPRT1 demonstrated the lowest Cq values but increased variabilities in samples from suspended cultures. UBC demonstrated close Cq values higher than TBP and a larger variability. Thus, TBP was selected for being closely expressed by IPE cells in adherent culture and in suspended one plus for its low variability between the different samples.

To evaluate IPE behaviour over the culture, four time points were set up: **1**. adherent culture day 8; **2**. suspended culture day 2; **3**. suspended culture day 4; **4**. suspended culture day 8. To note, Cq values of the TBP reference transcript measured over these four time points were close enough to allow such measurements (see **Figure 4.10-C**).

4.6.1.2 WNT2B expression decreases while β-catenin increases, then decreases

B-catenin and WNT2B were measured due to previous investigations associating IPE cell transformation with the WNT/β-catenin canonical pathway[317]. Moreover, both markers

participate to the regulation of MITF, OTX1 and OTX2, crucial players in the RPE maturation-pigmentation[318, 319]. So, it was expected to observe an increased expression of these markers with a potential stabilisation in the end of the process. The reading of such result would be that aggregates participate to a reconversion/transformation toward a potential RPE-IPE progenitor phenotype.

An increase expression of β-catenin was indeed observed at day 2, followed by a large reduction (see **Figure 4.10-B**). In the end of the two cultures used, β-catenin expression was similar. Surprisingly, WNT2B expression dropped off significantly after the adherent culture, instead of increasing as originally hypothesised. Following expressions detected remained very low over for the rest of the process. These results suggest that these genes were used in different manners in IPE cells in suspension. The high expression of WNT2B asks the question of its uses by adherent IPE cells.

4.6.1.3 C-Myc and GNL3 followed β-catenin

To assess potential cell transformations, C-Myc and GNL3/nucleostemin were selected (see **Figure 4.10-B**). Their evolution followed the same trend as β-catenin, with their expressions increasing early and decreasing for the rest of the process. Their expressions in spheres at day 8 were lower than the ones observed in adherent cells. These results suggest that IPE cells in suspension could have transformed over a really short time, or have adapted to their environment quickly, and so these factors were not required anymore.

4.6.1.4 Nestin increased, SOX2 decreased

Nestin and SOX2 were investigated in regards of their potential neurogenic facilities[320]. Found in neuronal stem cells, they were investigated here to assess a potential transformation toward a neuronal phenotype.

Nestin was already found in adherent IPE cells and in IPE aggregates colocalising with vimentin on a broad scale (see **Figure 3.10-B**). So, the evolution of its expression in suspended culture was observed on the side of SOX2, expected to increase to support the reconversion of a subpopulation with neuronal facilities as already found in past investigations[201].

What resulted was an increased expression of nestin in early suspended culture followed by a stabilisation (see **Figure 4.10-B**). A longer culture time could have revealed some changes still in regard of the higher variability observed in the end of the culture. SOX2 on the other side demonstrated a continuous decrease over the process. To note, it was expressed in adherent cells. These results taken together suggest that nestin could have been needed more to adapt cytoskeletons to suspended culture than to assist a transformation toward a neuronal phenotype due to SOX2 decreasing.

4.6.1.5 PAX6 rises then falls, MITF drops off, OTX1 stabilises then falls

PAX6 was expected to play a part in the cell processes that occurred over the suspended culture. Similar to WNT2B and β-catenin, an increased expression could suggest that cells underdo transformation toward a RPE-IPE progenitor phenotype.

During development, MITF and OTX1 activate tyrosinase, TYRP-1 and TYRP-2 in the RPE after that both retina and RPE have differentiated from each other[321]. So, it was expected that IPE aggregates stably express or decrease MITF – OTX1 expression. In line with the idea that cells would transform into a RPE-IPE progenitor cell, such results would demonstrate such dedifferentiation. On the opposite, increased expression of MITF – OTX1 would rather suggest that cells differentiate, maybe into "*In vitro* IPE cells".

So, IPE aggregates demonstrated reduced expression of MITF and OTX1 in early and mid-culture time respectively (see **Figure 4.10-B**). PAX6 expression on the other hand increased then decreased continuously passed the day 2 time point, in a similar manner with β-catenin, C-Myc and GNL3.

These results show first that MITF - OTX1 were present in IPE adherent cells rising the possibility that IPE cells could also produce melanin *in vitro*. By extrapolation, they were not dedifferentiated. Second, MITF reduction in aggregates demonstrated that changes happened after the transfer, confirmed by the later decrease of OTX1. Third, PAX6 increased. So, potential reconversion toward other phenotypes associated with PAX6 could be activated. The following decrease suggests that either a certain pool of PAX6 was reached in IPE aggregates, or that another process took over control of cell fate decisions.

4.6.2 IPE cells and aggregates demonstrated presence of developmental markers and neural-associated ones

The impact of the cell transfer from an adherent culture to a suspended one demonstrated important changes in IPE expression. It is possible that cell transformation has occurred regarding the important expression of GNL3 and C-Myc. The reduction of SOX2 would suggest that if such a transformation has started, the neurogenic fate might not be prioritised. Moreover, the reduction of MITF and OTX1 might suggest that IPE aggregates have not differentiated more into pigmented epithelial cells. In an attempt to complete the "IPE aggregates picture" with the actors present in the IPE aggregates, FICC were run.

To assess if neuronal development occurred in cells and aggregates, Nestin, SOX2 and βIII-tubulin were investigated. To assess the opposite epithelial development, PAX6 was used. GNL3 was used to mark a potential transformation.

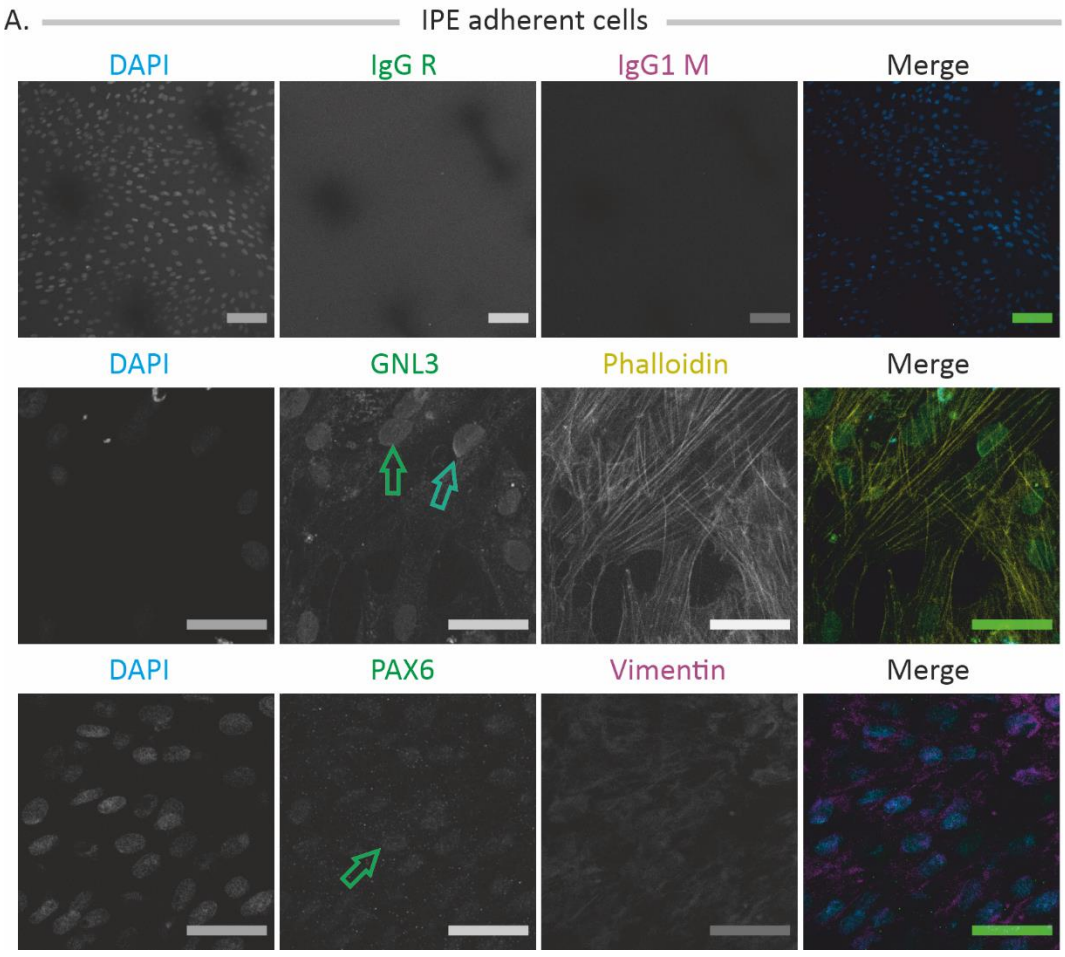

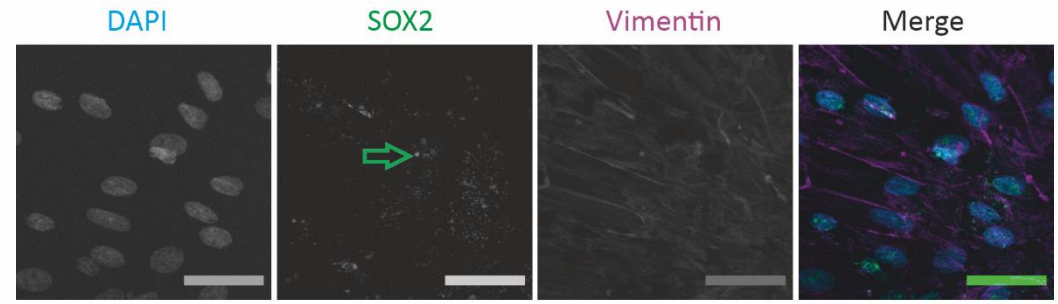

B. IPE aggregates

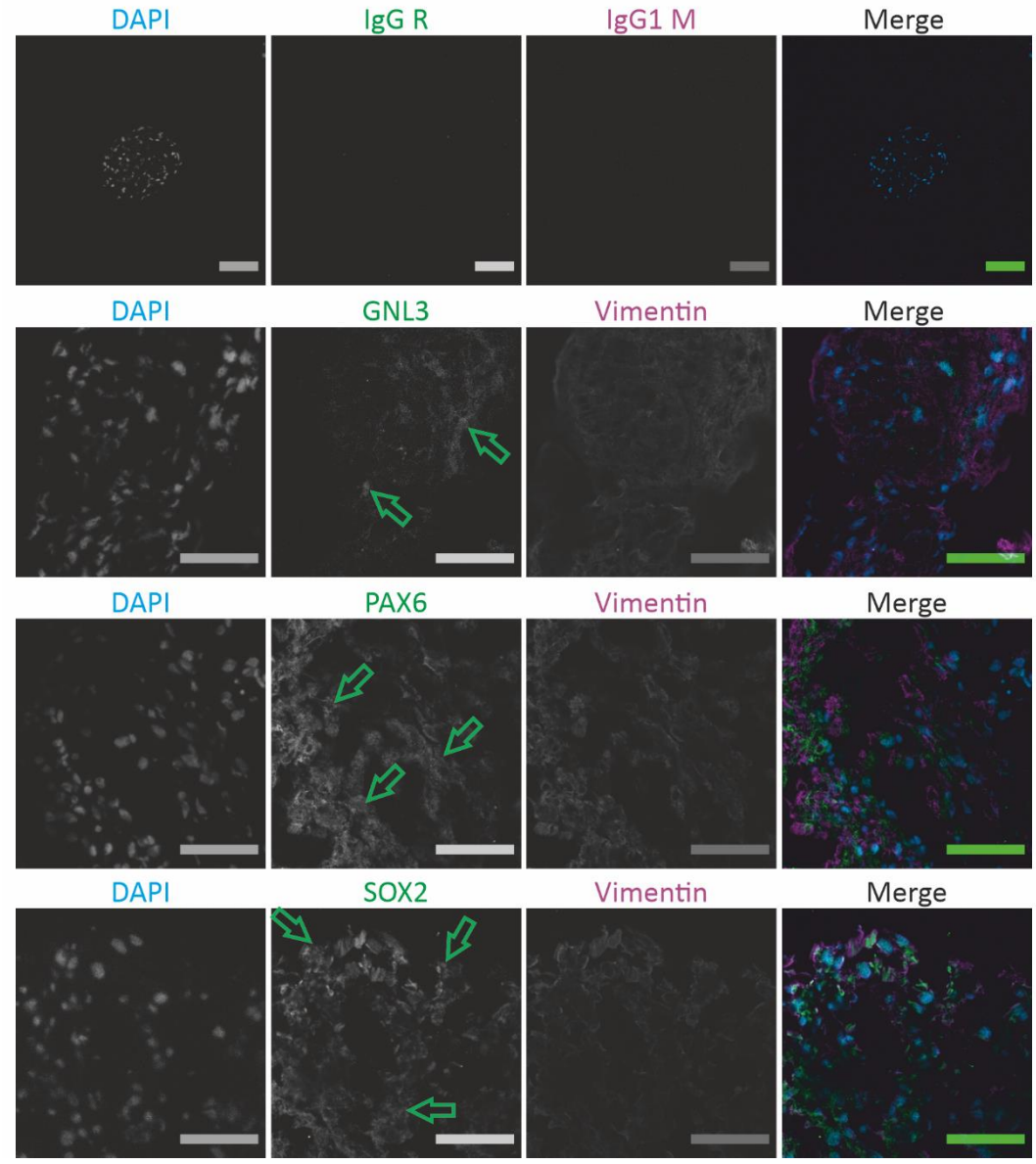

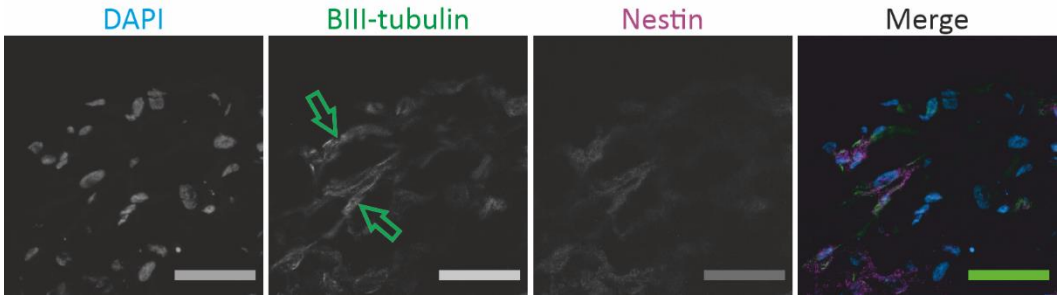

Figure 4.11: Representative images of IPE adherent cells and aggregates labelled for GNL3, PAX6, SOX2, vimentin, βIII-tubulin & nestin. A. Adherent IPE cells. Cells were labelled for the following combinations: GNL3 – phalloidin; PAX6 – vimentin; SOX2 – vimentin. **Green arrows** indicate structures labelled for GNL3, PAX6 and SOX2.Cells were counter-stained for DAPI. DAPI is in blue, IgG R, GNL3, PAX & SOX2 are in green, phalloidin in yellow, and IgG 1 M and vimentin in purple. Small scale bars = 100 µm, tall scale bars = 50 µm. **B.** IPE aggregates. Sections were labelled for the following combinations: GNL3 – vimentin; PAX6 – vimentin; SOX2 – vimentin; BIII-tubulin – nestin. **Green arrows** indicate structures labelled for GNL3, PAX6, SOX2 and βIII-tubulin. Sections were counterstained with DAPI. IgG R, GNL3, PAX6, SOX2 and βIII-tubulin are in green, IgG 1 M, vimentin and nestin are in purple. Small scale bars = 100 µm, tall scale bars = 50 µm.

4.6.2.1 GNL3 present in both adherent cells and aggregates, in both cytoplasms and nuclei

Adherent cells contained GNL3, which localised mainly into nuclei (see **Figure 4.11-A**) and perhaps in the cytoplasm, a low background being persistent in both the IgG control and the GNL3 samples investigated. GNL3 was also present in aggregates. Some nuclei demonstrated an important content in the periphery and several proteins were also labelled in cytoplasm (see **Figure 4.11-B**).

4.6.2.2 PAX6 demonstrated a similar distribution to GNL3

PAX6 was present in adherent cells (see **Figure 4.11-A**). The fluorescence demonstrated presence in nuclei and took a dot form in cytoplasms. Oppositely, IPE aggregates demonstrated an important fluorescence, probably in and around nuclei (see **Figure 4.11-B**). To note, all pictures of PAX6-labelled aggregates showed desynchronization between the channels. Despite different approaches, it was not possible to fix that issue, which affected other images as well.

It was important at that point to assess a technical issue specific of FICC on aggregates. Indeed, spheres and aggregates subjected to FICC are known to show a fluorescence halo

in their periphery during imaging, and that independently of the antibodies. So, some sections were subjected to pan-cytokeratin-based labelling known to be negative on IPE cells (see **Figure 7.6**). Results demonstrated that no halo was observed in aggregates but a background instead at low intensity as also observed in IPE adherent cells.

4.6.2.3 SOX2 was labelled, in adherent cells and in spheres

As the qPCR revealed a continuous decrease of SOX2 in suspended culture, it was expected to observe it in adherent cells and maybe label a small number of cells in aggregates.

Quite the opposite happened. Firstly, IPE adherent cells demonstrated SOX2 in most of IPE cells observed (see **Figure 4.11-A**). The observed proteins localised in both nuclei and cytoplasm taking either a dot shape either an aggregate-like one. Secondly, aggregates demonstrated a bright and condensed SOX2 content (see **Figure 4.11-B**). SOX2 was labelled in both nuclei and cytoplasm and demonstrated a large spread over the aggregates. It is possible that cells conserved a pool of SOX2 from the adherent culture and potentially increased that pool early in suspension.

4.6.2.4 BIII-tubulin appeared in spheres

The increased SOX2 also raised a hypothetic neuronal transformation to assess. To analyse that, βIII-tubulin was assessed on IPE aggregates with nestin (see **Figure 4.11-B**).

BIII-tubulin was found in a limited number of cells on the contrary of nestin. However, when βIII-tubulin was present, both proteins colocalised and surrounded nuclei. Whether these two proteins interacted between themselves was not investigated. So, it is possible that some cells in IPE aggregates had completed early neuronal transformation. Reproduction of that investigation confirmed the presence of βIII-tubulin from IPE aggregates more than once but not necessarily from whole aggregates. To note, these specific regions were low in melanin.

Thus, these results demonstrate that one group of cells in the porcine IPE has also neurogenic transformation potentials.

4.6.3 IPE aggregates conserve markers in suspension found in adherent ones

To complete observations from aggregates, N-cadherin, Tyrosinase and SNAIL/SLUG were assessed on both adherent cells and spheres.

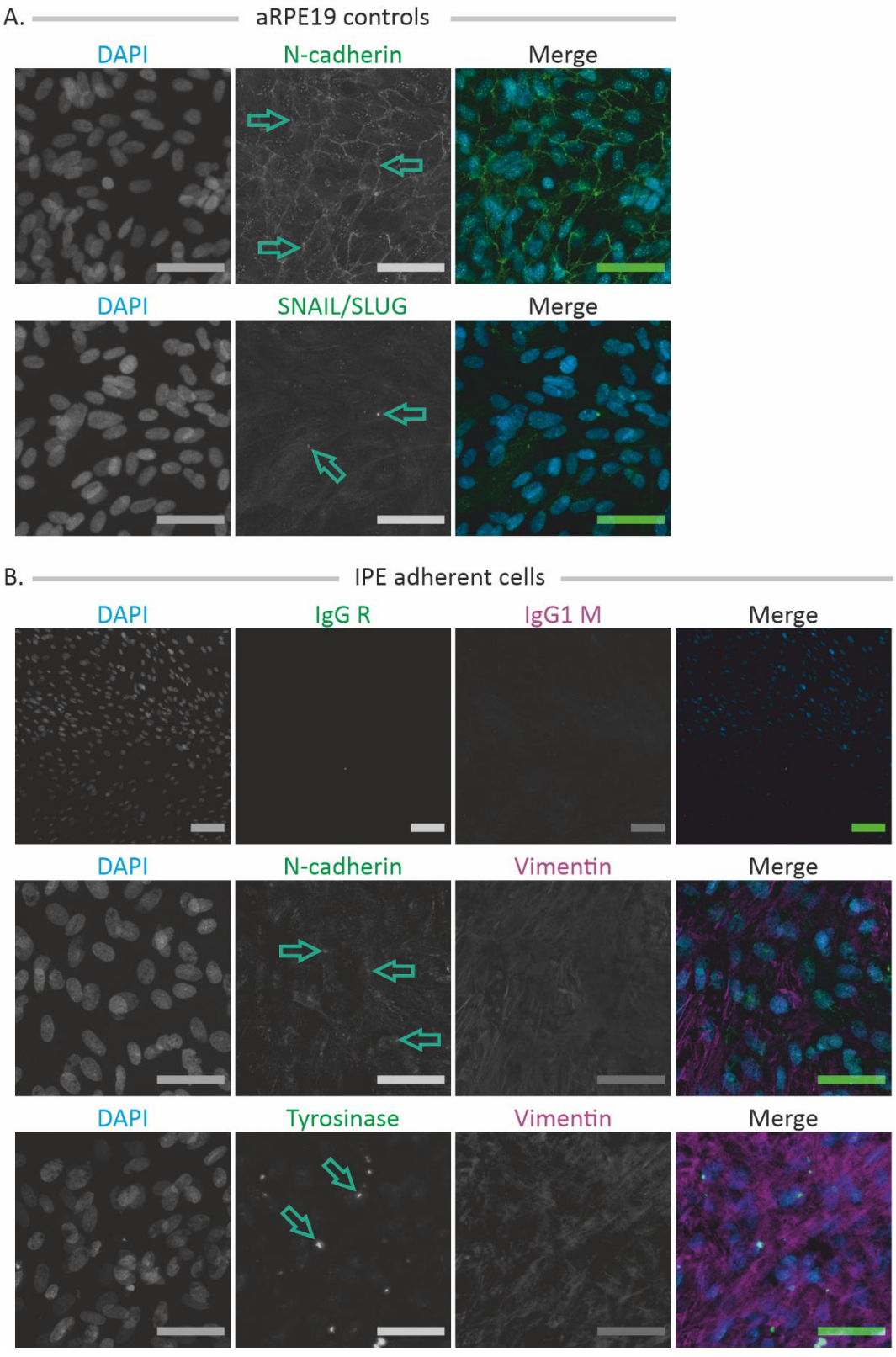

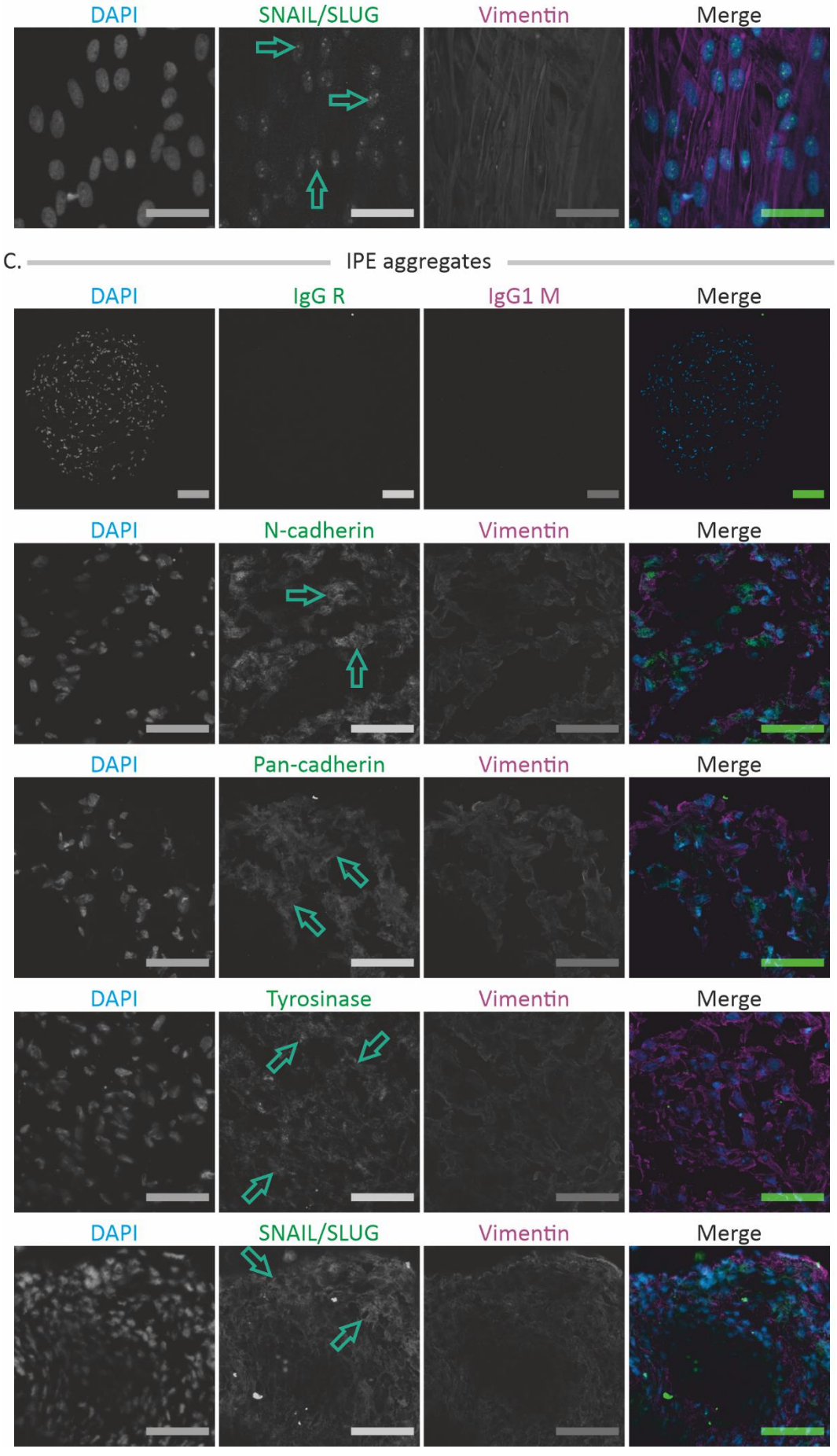
DAPI
SNAIL/SLUG
Vimentin
Merge
C.
IPE aggregates
DAPI
IgG R
IgG1 M
Merge
DAPI
N-cadherin
Vimentin
Merge
DAPI
Pan-cadherin
Vimentin
Merge
DAPI
Tyrosinase
Vimentin
Merge
DAPI
SNAIL/SLUG
Vimentin
Merge

Figure 4.12: Representative images of IPE adherent cells and aggregates labelled for N-cadherin, tyrosinase, SNAIL/Slug and vimentin. A. ARPE 19 cells used as positive controls for N-cadherin and SNAIL. **B.** IPE adherent cells. Cells were labelled for the following combinations: N-cadherin – vimentin; tyrosinase – vimentin; SNAIL/SLUG –vimentin. **Green arrows** indicate N-cadherin, tyrosinase or SNAIL/SLUG.Sections were counterstained for DAPI. Small scale bars = 100 µm, tall scale bars = 50 µm. **C.** IPE aggregates. Cells were labelled for the following combinations: N-cadherin – vimentin; tyrosinase – vimentin; SNAIL/SLUG –vimentin. **Green arrows** indicate N-cadherin, tyrosinase or SNAIL/SLUG. Sections were counterstained for DAPI. Small scale bars = 100 µm, tall scale bars = 50 µm.

4.6.3.1 N-cadherin was used by adherent cells and aggregates

N-cadherin was already found in the IPE tissue (see **Figure 3.17**) in both layers on pigmented sections. So, its presence was expected in adherent cells plus aggregates.

So, adherent cells were labelled (see **Figure 4.12-B**). The stained pattern did not resemble that expected of epithelial cells as observed in the ARPE19 control (see **Figure 4.12-A**). Instead, staining was dispersed, going along some vimentin fibres or where cells overlapped each other. Some were also observed colocalising with cell nuclei in both aRPE19 and adherent cells. Either it represents hemi-desmosomes below nuclei for aRPE19 cells, and hemi-desmosomes/desmosomes for IPE adherent ones. Or, N-cadherin was translocated into nuclei, as observed in aggregates (see **Figure 4.12-C**). Pattern observed there took a dot-like form in cytoplasms and in nuclei where it seemed to concentrate in.

Thus, N-cadherin distribution in adherent cells and aggregates was unexpected and could demonstrate a function from N-cadherin not anticipated in that investigation

4.6.3.2 Tyrosinase clustered in adherent cells and distributed everywhere in aggregates

MITF activates tyrosinase expression over ocular pigmented epithelium development to synthetize melanin[318]. So, the question of melanin synthesis over the culture was asked. Tyrosinase was expected to be absent or low in suspended culture compared with the adherent cells in regard of the PCR results.

Adherent cells demonstrated tyrosinase staining, in the form of clusters, not far away from the nuclei (see **Figure 4.12-B**). The observed distribution seemed to be low in

quantity. On aggregates, tyrosinase was homogenously distributed in all cells (see **Figure 4.12-C**). In a different fashion than the adherent cells, tyrosinase did not formed clusters there.

So, tyrosinase alone is not enough to state about the melanin production. However, its presence suggests that it was for IPE cells to synthetise melanin.

4.6.3.3 SNAIL and SLUG were present in all cultures

SNAIL/SLUG play important functions during EMT, favour mesenchymal phenotypes by repressing epithelial functions and markers, and associate with vimentin[322]. So, presence of SNAIL/SLUG in both adherent IPE and IPE aggregates was expected due to vimentin systematic presence and potential transformations induced by the suspended culture.

As a result, SNAIL/SLUG were present in adherent cells with clusters detected in several nuclei and dots distributed over cytoplasms (see **Figure 4.12-B**). In aggregates, SNAIL/SLUG were observed through their whole bodies (see **Figure 4.12-C**). In the same way than the adherent cells, clusters were observed in nuclei, while multiple dots were observed in cytoplasm.

Thus, the large presence of SNAIL/SLUG over aggregates confirmed that cells conserved EMT-associated transformation factors in neurogenic suspended culture.

4.7 Discussion

The aim of that chapter was to investigate the behaviour of IPE cells placed in generic neurospheres conditions.

The objectives were:

- To investigate protocols and materials able to generate spheres or aggregates;
- To investigate the way IPE spheres or aggregates form;
- To investigate the epithelial and muscular markers initially found in chapter I;
- To investigate potential cell transformations.

4.7.1 The origin of the contamination remained unknown

Systematic fungal contamination was resolved by increasing the antibiotics and amphotericin B to 2% in cell media (see **Figure 4.1**). Consequently, a lower cell number was observed. That was in accordance with previous investigations stating that antibiotics could impact cell proliferation, metabolism, DNA synthesis, cell differentiation, etc[321, 323, 324]. Other potential effects on IPE cells were not investigated.

Following these efforts, a try to reduce the antibiotic concentration from 2 to 1% resulted negatively. No clues indicated if the contamination came from the safety cabinet, the pipet and pipetboy, the sterilised tips, the plates or was already present in the cell culture upstream. Thus, despite the potential negative effects described in the previous paragraph, all subsequent cell processes included a cell medium with antibiotics at 2%.

4.7.2 IPE cells in suspension generated aggregates

CFSE investigations demonstrated that various proliferation activities were generated over the process. As explained earlier (see **Figure 4.3**), a homogenous CFSE distribution among aggregates would have demonstrated a clonal proliferation. Mother cells would have proliferated at similar rates and distributed similar levels of CFSE in daughter cells[325].

What happened instead was various distributions of CFSE (see **Figure 4.4-A to -F**). Some regions demonstrated high CFSE content, other intermediate content and some low content. So, the first analysis was that cell proliferation occurred at different rates among aggregates. It is indeed known that aggregates are not homogenous structures composed of a single type of cells but rather a heterogeneous one with a couple of cell subtypes and potentially multiple proliferation facilities[190, 326]. Moreover, considering the CFSE distribution, the number of aggregates and their size per cell seeded, it is also probable that generic proliferation did not run at a high rate neither

To complete these observations, PCNA and Ki67 were investigated on porcine IPE aggregate cryosections (see **Figure 4.5**). Their distributions varied drawing regions with both PCNA and Ki67 present in the same cells, while other regions demonstrated a complete absence. Both proteins being present in the same cells was originally non-intuitive, PCNA marking the S-phase while Ki67 doing so for the mitosis[327, 328, 329, 330]. However, some studies determined that these markers had dynamic kinetics over the cell

cycle and that it was more the quantity detected which could be associated with each cell cycle phase[284, 331].

So, the lack of these markers in some regions suggests that those cells were either quiescent or in G1 phase at the time point. In complement, the lack of CFSE in these sections suggest that a probably large proliferation activity has occurred prior to the time point. It is conceivable that cells of these regions completed a cell cycle a short time prior to the time point.

Moreover, Vybrant dies used demonstrated that spheres were all resulting from cell aggregation. With both dies present in all spheres assessed, the hypothesis of a clonal proliferation coming from a potential stem cell had lived.

Thus, IPE aggregates were the results of progressive cell aggregation with various proliferation activities inside, suggesting a heterogeneous cell population inside it.

4.7.3 IPE aggregates conserve their original cytoskeleton, plus nestin

In continuity with results from Chapter **3**, IPE cells kept **vimentin** and **α-SMA** as cytoskeletal proteins (see **Figure 4.7** & **Figure 4.9**). As interesting was the fact that **desmin** was barely found in adherent cells and in the aggregate periphery, while it was found over the major part of the IPE anterior layer (see **Figure 3.2**).

Oppositely to initial expectations, **nestin** presence was distributed over large portions of IPE cells in both adherent and suspended cultures. In the tissue, nestin was found only at the ciliary bodies – IPE junctions (see **Figure 3.11**). So, it is possible to state that:

- a change occurred favouring nestin production and desmin reduction concomitantly, the decrease of the latter being expected;
- that change was not specific to a small subset of IPE cells as most of them demonstrated nestin presence and desmin absence.

In the past, investigators observed nestin increasing in primary cell cultures from various origins. First example, vascular smooth muscle cells from the rat exhibited nestin synthesis and used it under serum conditions. The authors noted that the serum favoured the nestin production, and that nestin by itself favoured proliferation[332]. That assumption was not investigated there. Indeed, IPE cultures were already selected based on cell proliferation demonstrated over 8 days after extraction. Selection was done by

microscope observations and cell count. Samples with poor proliferation activities were not used for further investigation.

A second example comes from skeletal muscle cells cultivated over three weeks. There, a subpopulation of satellite cells giving rise to myocytes and myoblasts was generated. These satellite cells specifically demonstrated nestin synthesis plus the absence of myogenic differentiation markers[333]. Moreover:

- nestin has been found in different neuromuscular injuries where its presence is associated with morphologically dynamic cells, proliferation and migration[334];
- during development, nestin first appears in the skeletal muscle system and is then replaced by desmin[335].

Similar events have been observed in epithelial cells. For example, murine alveolar epithelial cells underwent EMT after extraction and synthetised nestin soon after[336]. During the investigations, the authors noted that cells produced nestin in response to TGF-β1, the later being secreted in an autocrine/paracrine manner. Another investigation using murine oral mucosal keratinocytes demonstrated that cells produced nestin in reaction to TGF-β1 in the medium[337].

Finally, nestin is often found as a marker of aggressive cancers. In breast cancer, the nestin content correlates with tumour aggressiveness, the more nestin in a breast cancer stem cell, the easier the formation of solid tumours[338]. In pancreatic ductal adenocarcinoma, which has a high mortality rate due to rapid metastasis, nestin suppression blocked cell migration, invasion and metastasis formation by preventing EMT[339, 340].

So, nestin is often involved in various processes where cells are either in a transformation stage, or in a phenotypically plastic state. The transformation stage is in line with pathological or non-physiological conditions, the phenotypically plastic state is in line with several reports using nestin as a neural stem cell marker[341] or indicating a stem multipotent facility[342]. Thus, nestin presence in IPE cells could be a simple reaction where cells adapt to *in vitro* culture.

On top of that, nestin is also an essential player in eye development. Nestin is found in the developing zebrafish eye where its presence is essential to NPC survival, the right development and specifications of different ocular tissues[343]. Closer to the pig, the developing murine eye demonstrated presence of nestin in the lens, the retina, the optic stalk, the CMZ and some developing extra-ocular muscle[344]. New-born rat IPE tissue

demonstrated presence of nestin[201]. Finally, investigations on the embryonic human eye demonstrated nestin presence as well in the lens, the optic stalk, the neuroepithelial layers and the corneal stroma[345, 346]. To the knowledge of the writer, no investigations on the presence of nestin in the developing iris have been done. What is known is that α-SMA appears at 28th week of gestation, desmin at the 37th and vimentin at 13th minimum[192]. Interestingly, the authors of that investigation also noted the presence of cytokeratins type 8 and 18 until 28th week of gestation.

Concomitantly with these observations, the decreased desmin suggests that IPE cells from the anterior layer transformed after their extraction. In opposition to nestin, which can be present in several cell types, desmin is commonly found *in vitro* in cells undergoing muscular differentiation[347]. Moreover, *in vitro* observations revealed that the muscle satellite cells remain desmin-free until they proliferate, expressing on the side MyoD and MiF-5[348]. These cells differentiating more will stop proliferation, express myogenin, form myofibers, and start myosin production. So, desmin is found *in vitro* in cells on a differentiation path, which requires specific factors and conditions to occur, or in cells already differentiated[349, 350].

Thus, the reason for nestin to rise in IPE cells and ensure their adaptation *in vitro* is nearly sure. The use of nestin as a developmental reconversion is possible. Both reasons could explain why so many cells produced nestin on the side of vimentin. Finally, the desmin decrease suggest that IPE cells lost their specific muscular features over the process.

4.7.4 In IPE aggregates, a neurogenic transformation occurred on the side of a potential epithelial one

4.7.4.1 The main use of B-catenin could be the reformation of AJs

B-catenin was investigated for its involvement in the RPE development[148, 318, 321, 351] (see **Figure 4.10**). In complement, β-catenin is involved in smooth muscle contraction. Its armadillo core binds to the N-cadherin and its N-terminal to α-catenin. The latter finally binds the complex to actin filaments[352, 353, 354]. As a reminder, N-cadherin was found in the IPE tissue along dilator fibres in the anterior layer (see **Figure 3.17**). So, β-catenin likely plays a part in the iris mydriasis *in vivo*.

Once extracted from the iris, IPE cells no longer perform muscular activities related to the dilator muscle. The loss of desmin in both adherent and suspended culture reflect that. So, N-cadherin distribution in both adherent cells and aggregates spreads from the plasma membrane to the nuclei as observed in FICC (see **Figure 4.12**). It is therefore possible that N-cadherin appears on images "behind" a nucleus or is indeed into nuclei.

N-cadherin intracellular observations happens under the influence of chondroitin sulfate E, a highly sulphated polysaccharide[355, 356]. Once the cell is exposed to it, the N-cadherin/β-catenin complex disrupts from the actin filaments. The complex is then endocytosed by cells with the N-cadherin C-terminus being cleaved by MMP9. From there, β-catenin is released and free to either be degraded by the destruction complex, or translocates into the nucleus to bind the transcription complex TCF-LEF, and activate gene transcription[357, 358].

So, it is possible to explain the qPCR-observed β-catenin increase as followed. Firstly, adherent cell exposure to TryplE during subculture denatured N-cadherin, its extracellular domains being cleaved by disruption of lysine and arginine amino acids. As a result, no more functional N-cadherins were present in the early suspension culture. Secondly, taking into account that cells regroup quickly and aggregated, new AJs were required and the pool of N-cadherin refilled. Thirdly, the β-catenin pool being either deleted or insufficient, the synthesis of new β-catenin was also necessary. Thus, these results could demonstrate a typical cell reaction after transfer from adherent to suspended culture where cells reform their AJs and associated complexes. Investigations to quantify gene expression involved in AJs and TJs could support or not that view.

To note, the total amount of β-catenin transcripts detected over the cultures was low compared to other transcripts. So, either β-catenin had a really strong potency[358], or it was needed for one particular reason, which could be the AJs reform. Moreover, the lack of AJs concerned ideally all cells transferred. As aggregation got along, the number of cells in need of N-cadherin and β-catenin lowered. So, the number of cells lacking both protein to reform their AJs could also reduce, explaining the important difference noticed by PCR.

Finally, it is possible that some β-catenins were released after TryplE incubation under chrondroitin sulfate E influence or by a different mechanism. The released β-catenin then translocated into nuclei as explained earlier. And among the various target of the Wnt-β-catenin pathway lies the C-Myc-related pathways, involved in cell transformations and proliferation[359].

4.7.4.2 C-Myc and GNL3 played with chromatin

Over the experiment, both C-Myc and GNL3 demonstrated evolution of their expression similar to the β-catenin. A significant increase was observed early after transfer, followed by a progressive decrease. Interestingly, GNL3 is one of the main targets of C-Myc, a relationship that is found in various cell lines, cancers and primary cells[360]. So, GNL3 evolution depended probably from C-Myc own evolution. With prospective, both C-Myc and GNL3 presence have been associated with various functions among which self-renewal, regulation of cell cycle, metabolism, protein folding, apoptosis, chromatin remodelling or interaction with nuclear β-catenin[361, 362, 363, 364, 365]. GNL3 has been found in human retinal progenitor cells[366] and generally, its presence suggests a certain plasticity from cells producing it[367, 368].

The increase in both C-Myc and GNL3 suggests that cells adapted to their environment by playing on multiple processes, potentially helped by the release of β-catenin from N-cadherin cleavage. The presence of GNL3 in aggregates demonstrated that an important pool specifically remained in nuclei and around, suggesting cells were still remodelling chromatin. By extrapolation, the presence of C-Myc there is possible. Thus, the evolution of these factors could be interpreted as:

- an adaptation to the suspension culture;
- in complement, a reconversion toward either a different phenotype, or a transient and plastic stage;
- a protein pool constituted and activated.

4.7.4.3 WNT2B, MITF and OTX1 were the last priority

In complete opposition to the markers discussed above, WNT2B and MITF demonstrated a strong decrease.

During mammalian eye development, WNT2B, among other WNT ligands, is associated with the development of the pigmented epithelia running from the RPE to the IPE[286]. Its paracrine actions allow regulation on a short range of cells, which is crucial when RPE and retina differentiate from each other. Indeed, over the time prior to the iris formation, both retinal and RPE cells can switch their phenotype and transform into the opposite cell. So, the presence of a short-range factor specifying cells in one cell type is logical to not

disrupt the tissue homeostasis. In that delicate environment, WNT2B supresses neurogenic genes and favours the expression of epithelial ones[318, 319, 369, 370, 371]. In line with that, WNT2B has not been found in mammalian presumptive or defined retinas.

Prior to the lens formation, MITF is first induced by PAX6 in the presumptive neuroepithelium[372]. While the lens forms, the inner layer gets thicker while the outer gets pigmented. It is in that outer layer, the presumptive RPE, that MITF associates with OTX1 and OTX2, to express enzymes involved in melanin synthesis: TYR, TYRP-1 and TYRP-2. Another function is to associate with TFEC to favour the epithelial proliferation[286]. A set of transcripts targeting TFEC was designed for this study but results in the validation step were poor and this gene was removed from the investigation. Another interesting point is that D- and H-MITF contains TCF-LEF binding sites in their promoters[318], and both participate to the RPE specification in the same time than WNT/β-catenin signalling. So, presence of D- and H-MITF in IPE aggregates could result by the activation or an increased activity of the Wnt-β-catenin pathway, finishing by the IPE aggregates specification into an ocular pigmented epithelial phenotype closely related to the RPE.

So, the quick decrease of WNT2B, MITF and OTX1 suggest a cell transformation toward a phenotype different than a mature and pigmented RPE. Both the rise of nestin expression plus the presence of GNL3 and C-Myc support that hypothesis. Moreover, the presence of βIII-tubulin in some spheres demonstrated that transformation toward neuronal phenotype already occurred for some cells with few pigments, as observed in MITF-depleted murine RPE[371]. The presence of bFGF in the medium could be at the origin of, or at least participates in, that process[373].

However, spheres which were βIII-tubulin-negative were strongly pigmented. Indeed, tyrosinase was present in all spheres assessed and well distributed on the contrary of tyrosinase-labelled adherent cells. So, it is possible that melanin synthesis also occurred. For technical reasons, assessment of Tyrp1 and Tyrp2 could not be done. So, further investigations including them would give another piece of the puzzle.

Thus, the process used there seemed to have potentially generated pigmented epithelial cells in reconversion and potentially depigmenting themselves. It is conceivable that neuronal progenitor cells could be generated as well, as suggested in previous investigations[201].

4.7.4.4 PAX6 and SOX2 demonstrated opposite evolutions

PAX6 is considered as one of the key regulators of eye development. It is essential for the specification of ocular tissues, the generation of retinal cells, the differentiation of pigmented epithelia, the development of the iris and ciliary bodies, and so on[3, 374]. Specifically, once the bilayered neuroepithelium has started its differentiation into RPE and retina, PAX6 participates to the specification of the RPE one. It activates in association with the WNT/β-catenin pathway genes involved in RPE differentiation and blocks the expression of retinogenic ones. At the top of activated genes are MITF and TFEC[286, 320].

Another crucial player for the retina is SOX2. It participates to the development of the neural system, the specification of the ocular inner layer toward a retinal fate, its subsequent differentiation and proliferation[375, 376, 377]. Its presence counterbalances PAX6 there to favour a neuronal fate rather than an epithelial one. In its absence, WNT signalling increases in the retina and supports thereafter the expression of RPE-associated genes. So, it has become obvious over different studies that an intrinsic part of the tissue specification during development relies on a balance between PAX6 and its subjacent targets, and SOX2[301, 303].

Both PAX6 and SOX2 were observed in adherent cells and aggregates. It is possible that a balanced expression similar to what happens over the eye development have occurred over the process. The ability of mammalian new-born and adult IPE to transform in neuronal or epithelial cells supports that assumption[177, 201, 378]. However, it was not possible to investigate both PAX6 and SOX2 on the same sample due to antibodies incompatible uses.

Still, it is possible that these proteins were both present at the same time in nuclei. The reduction of MITF and OTX1 could suggest that SOX2 potency was stronger than PAX6 in the suspended environment and inversely in the adherent one. The evolution of expression over the suspended culture was surprising. Both were expressed in adherent cells, but with transfer in suspended conditions, it was PAX6 transcription which increased while SOX2 decreased. The evolution of PAX6 then mimics those of β-catenin, C-Myc and GNL3. So, it is possible that aggregates were indeed reconverting/transforming, but not toward a neuronal phenotype. The original IPE phenotype there could have balanced the reconversion toward an epithelial progenitor phenotype instead. More markers specific of both presumptive retina and RPE would be necessary to affine toward which phenotypes cells are transforming to and by which processes they use to do so.

4.8 In conclusion

The transfer from adherent to suspended culture had deep impacts on cells. Cells having lost all contacts between them reactivated signalling pathways to adapt and survive. The finding of several markers associated with development and largely distributed demonstrated as well a certain immaturity from the cells. The finding of GNL3, plus βIII-tubulin-positive spheres demonstrated that. To note, it is possible that in the tissue, such cells already exist but are prevented to differentiate toward a neurogenic phenotype by the other cells.

The evolution of β-catenin and PAX6 are troubling as well. If it is possible that β-catenin was released by the dysfunctional N-cadherins after transfer, its potency on other genes was strong. The evolution of epithelial markers involved in epithelial specification could then result from the associated activity of C-Myc and GNL3, stimulated by the released β-catenin.

So, the next investigations would be to know which phenotypical state IPE aggregates reached following the transfer. Did they reconvert toward a pre-IPE stage? Have they transformed into CMZ cells? The lack of specific markers and developmental controls prevented to assess these questions. Longer cultures and different media would be necessary to push forward the early reconversion processes observed. To finish, the IPE cells seem quit reactive and plastic enough as they mostly survived in suspension culture. Thus, the use of more stringent conditions seem also a requirement to distinguish the potential progenitors or stem cells from the others.

5 Chapter 5: Identifying IPE-based neuronal progenitor cells

5.1 Background

Investigations on aggregates have demonstrated the presence of the neuronal marker βIII-tubulin and so, were in line with investigations on other animal models[201, 379, 380]. These cells were probably not numerous in the initial adherent cell culture but their early transformation into neuronal-like cells was possible as soon as the conditions were optimal.

One of these conditions could have been the exposure to the correct supplement/factor in the culture medium. This final investigation aimed to determine the conditions that favoured that cell transformation. These cultures would be used to assess some markers already studied in the previous chapter and linked with neuronal phenotypes. The hypothesis was that if these cells transform into neurons, all other cells would then be potential targets to reconvert into RPE cells.

5.2 Aim & objectives of the chapter

The aim of this chapter was to expose IPE cells to neuronal supplements and observe their subsequent behaviours.

The objectives were:

- To grow IPE cells on adherent plates and in medium supplemented with:
    - 10% FBS;
    - 1X B27;
    - 2X B27;
- To assess the morphology, the metabolism, the gene expression and the protein content and distribution IPE cells developed in these conditions.

5.3 Result

5.3.1 Diverse cells in a single IPE were observed in both FBS and B27 conditions

In previous cultures, EGF, bFGF and B27 were used to generate and cultivate IPE spheres. The aim of this chapter was to compare spontaneous neuronal transformations from primary IPE culture grown and supplemented with B27 or FBS. Culture with B27 containing media would expose cells to a cocktail of nutrients and factors adapted to neuronal cells cultures[381]. The overall time of culture was set up to 14 days without passage to avoid any form of stress and give cells the time to develop the changes (see **Figure 5.1**). Additionally, that process was thought to have the following advantages: B27 would spread over all cells for the integrity of the process; a long-term culture could favour the specification of one to several IPE subtypes[382, 383].

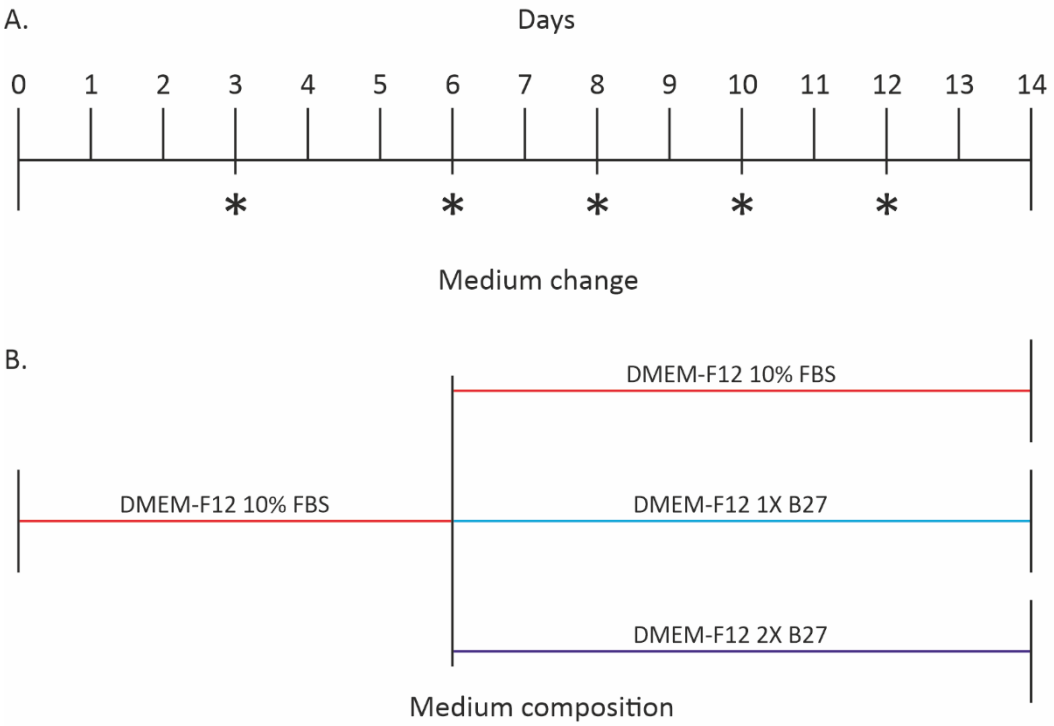

Figure 5.1: Schematic representation of the cell culture process undertaken in the chapter 4. A. Time frame with medium changes are represented with numbers and asterisks respectively. **B.** Media used are represented by specific colours: red for DMEM-F12 with 10% FBS 2% P/S/F, clear blue for DMEM-F12 with 1X B27 and 2% P/S/F, and dark blue for DMEM-F12 with 2X B27 and 2% P/S/F.

Over time in culture (see **Figure 5.2**), IPE cells demonstrated various morphologies. Initially in DMEM-F12 10% FBS, the first cells arose from cell clumps with processes extending outside these clumps (see **Figure 5.2-A day 3**). Some cells were also already outside cell clumps with a fibroblastic-like shape. At day 6, different shapes were present (see **Figure 5.2-A day 6**). Fibroblasts-like and epithelial-like cells were present in centre where cell density was the highest (see **Figure 5.2-A yellow arrows**). Some neuronal-like cells (see **Figure 5.2-A orange arrows**) were observed on the top of other epithelial-like cells/fibroblasts-like. These neuronal-like cells were also strongly pigmented and were barely observed at the end of the culture. Further from the centre, groups of strongly pigmented cells were observed (see **Figure 5.2-A magenta arrows**). These cells were only observed alone or in small group, always far from the fibroblasts-like and epithelial-like cells. They demonstrated a strong pigmentation and a size taller than the other cells, plus shaped in filiform-manner. The largest observed cell contents were the fibroblasts-like and the epithelial-like cells

In IPE cells grown in DMEM-F12 1X B27 (see **Figure 5.2-B**), the majority of cells formed regular epithelial-like carpets (see **Figure 5.2-B yellow arrows**). Fibroblasts-like were barely observed. Neuronal-like cells were well observed in areas with limited cell density (see **Figure 5.2-C orange arrows**). The last cell group was also observed but their number seemed lower (see **Figure 5.2-B magenta arrows**). The total cell number from the 1X B27 condition seemed lower than the FBS one.

In IPE cells grown in DMEM-F12 2X B27 (see **Figure 5.2-C**), new epithelial-like cell carpets appeared with a higher cell density than those observed in other conditions (see **Figure 5.2-C yellow arrows**). These cells were smaller and pigment content especially low compared with previous conditions. These carpets were surrounded by fibroblasts-like cells and some bigger epithelial-like cells were observed as well. Neuronal-like cells were present at a density higher in this condition (see **Figure 5.2-C orange arrows**). Finally, the last group of cells was observed, with a pigment content lower than usual (see **Figure 5.2-C magenta arrows**). The global cell content in this condition was the lowest from all conditions investigated.

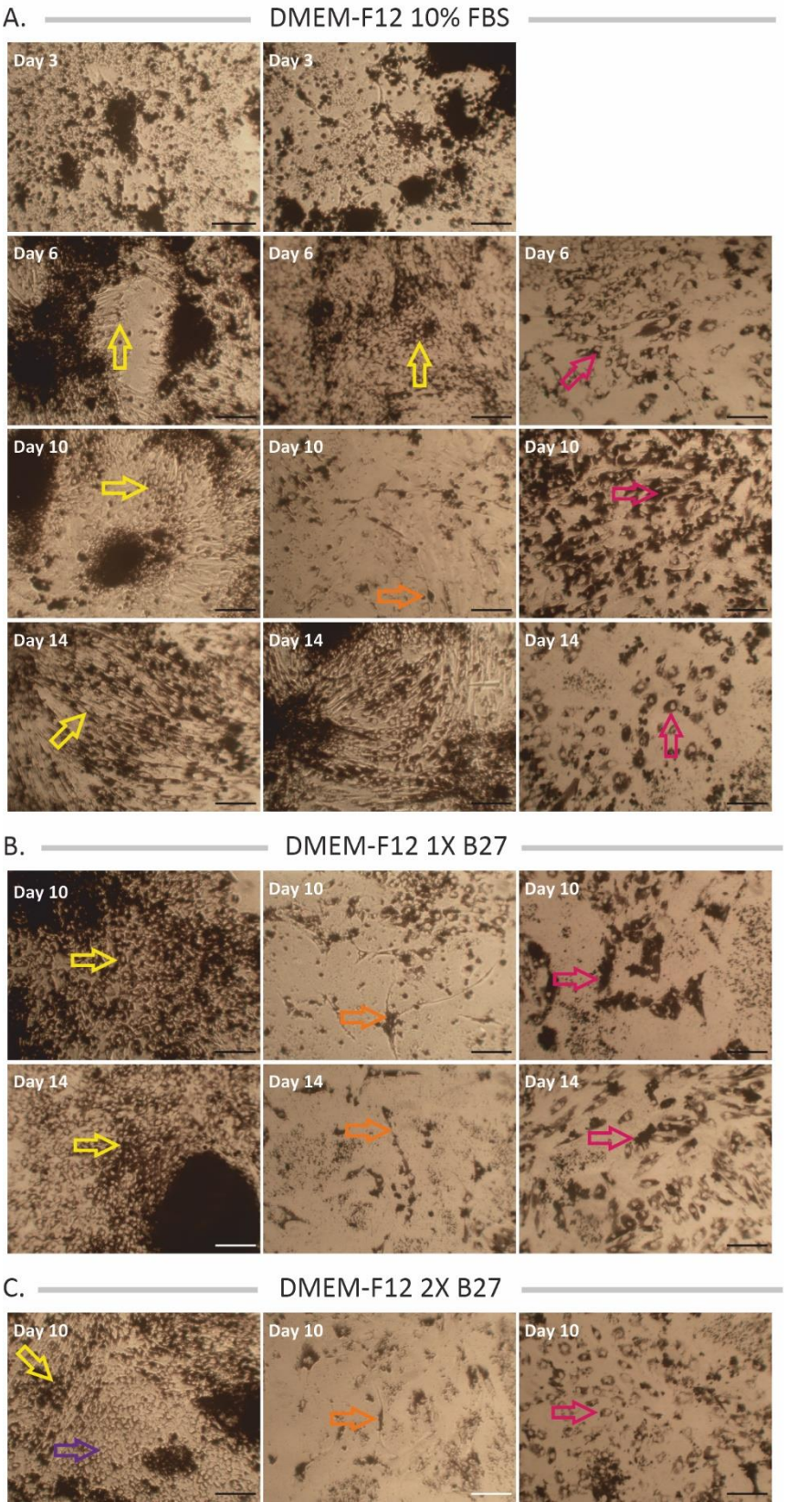
A.
DMEM-F12 10% FBS
Day 3
Day 3
Day 6
Day 6
Day 6
Day 10
Day 10
Day 10
Day 14
Day 14
Day 14
B.
DMEM-F12 1X B27
Day 10
Day 10
Day 10
Day 14
Day 14
Day 14
C.
DMEM-F12 2X B27
Day 10
Day 10
Day 10

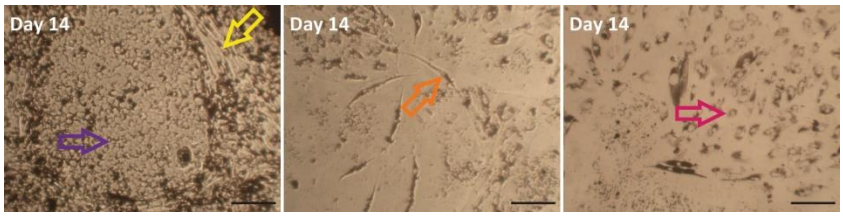

Figure 5.2: Representative pictures of IPE cells grown FBS and B27 conditions over 14 days. Epithelial-like and fibroblasts-like cells (= **yellow arrows**), neuronal-like cells (= **orange arrows**) and a third cell group (= **magenta arrows**) were observed. A last group of small epithelial-like cells (= **purple arrows**) was observed specifically in DMEM-F12 2X B27. **A.** Cells cultivated in FBS from day 0 to day 14. Pictures were taken prior to medium change. **B.** Cells grown in DMEM-F12 10% FBS from day 0 to day 6, then in DMEM-F12 1X B27 until day 14. Pictures were taken prior to medium change. **C.** Cells grown in DMEM-F12 10% FBS from day 0 to day 6, then in DMEM-F12 1X B27 until day 14. Pictures were taken prior to medium change. Scale bars = 100 µm.

5.3.2 B27 reduced metabolic activity compared to FBS in IPE cells

To assess metabolic activity, resazurin was used. Once in cells, it reduces into resafurin in contact with cytosolic and mitochondrial NADH and NADPH dehydrogenases. That reduction transforms the initial blue colour toward a pink one from which absorbance at 567 nm can be measured. That gives the metabolic activity from the respiratory chain or the lipid synthesis[384, 385, 386].

As cells proliferate, the volume of metabolic activities grows. So, an increase of the metabolic activity in all cultures was expected. Cells in FBS cultures, the most numerous, were expected to demonstrate the highest metabolic activity. 1X B27 cultures were expected to mimick the FBS evolutions, potentially at a slightly lower level. Finally, 2X B27 cultures were expected to have the lowest metabolic activity.

As a result, the highest metabolic activity was the FBS one (see **Figure 5.3**). The metabolic curve changed when approaching the end of the process. It is possible that as cell number reached a certain extent, proliferation gradually slowed and reduced the metabolic activity. B27 conditions corresponded to initial expectations but their evolutions differed. The 1X B27-based cultures demonstrated at day 10 similar metabolisms with the FBS ones, to then deeply decrease. That evolution was common to all 1X cultures as demonstrated by the low variability between those samples. The 2X B27-based cultures demonstrated a stable evolution with an average metabolic activity drastically lower than the FBS one. To note, the average metabolism of cells exposed to 1X B27 finished to be

lower than the 2X one. So, it is probable that B27 impaired or brake the metabolism of the majority of IPE cells.

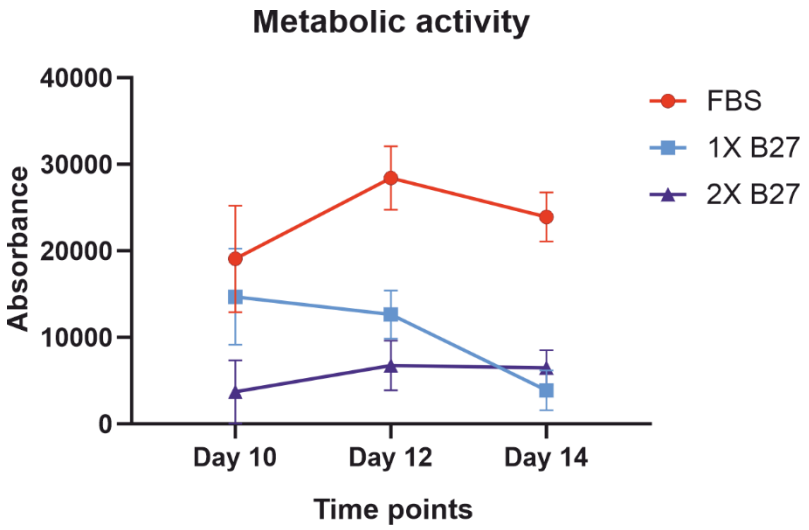

Figure 5.3: Resazurin-assessed metabolic activity of cells exposed to FBS or B27 measured from day 10 to day 14. Three samples per conditions were used over the three time points. Statistical analysis was performed by a 2-ways ANOVA, no significant differences were found.

5.3.3 B27 favoured more epithelial-associated genes transcription than the neuronal one

To observe the change in cell behaviour, genes belonging to developmental processes were assessed. In the previous chapter, GNL3 marked the chromatin modulation. Nestin was used as a mesenchymal / neuronal marker. SOX2 was specific to a neurogenic fate. WNT2B and PAX6 were associated with the development of early epithelia. MITF and OTX1 were associated with the specification of these epithelia toward an RPE-like fate.

FBS cultures were expected to demonstrate reduced expression of both neuronal and pigmented epithelial markers due to the increased proportion of fibroblasts-like and epithelial-like cells. Increased GNL3 content was expected to increase due to chromatin remodelling. 1X B27 cultures would demonstrate increased expression of WNT2B, MITF and OTX1 while the other markers would be down regulated. An increase in PAX6 could also be possible considering its association with these genes. GNL3 could be expressed in 1X B27 cultures at a similar level than in FBS cultures in the mid-time point. Finally, 2X B27 cultures were expected to demonstrate expressions of PAX6 higher than the other genes due to the presence of the epithelial-like carpets, expected to be less differentiated.

So, GNL3 expression was at its highest level at day 6, all conditions analysed (see **Figure 4.4**). In FBS cultures, following time points had a half-reduced but stable GNL3 expression. Nestin and SOX2 expressions deeply reduced. WNT2B and OTX1 expressions demonstrated variations between the two samples assessed. MITF evolution was unexpected considering the variation. However, the following technical investigations proved that result was real. Finally, PAX6 increased in the end of the process.

1X B27 cultures corresponded to original expectations. GNL3, despite variabilities, seemed to be expressed similarly to FBS at day 10 to then reduce by half. SOX2 and nestin decreased. Oppositely, WNT2B and OTX1 demonstrated higher expression than other conditions, while MITF slightly decreased. WNT2B expression was especially high at day 14. PAX6 remained stable. These results seemed to demonstrate that the epithelial genes were favoured over the neuronal ones in that condition.

Finally, 2X B27 cultures potentially mimicked 1X B27 cultures for GNL3 expression, both conditions demonstrating the same level at day 14. The same observations applied to SOX2. Nestin expression at day 10 was the lowest measured over all conditions, to then demonstrate different projections at day 14. So, one sample increased its nestin expression over the end of the culture. WNT2B expression remained stable, plus was higher than the average WNT2B expression in FBS condition. MITF only decreased, while OTX1 slightly increased in the end of the process. Finally, PAX6 expression also increased at day 14. Taken together, these results could suggest that epithelial genes specific RPE and RPE-like functions were not downregulated in that condition, while genes involved in the RPE development were upregulated.

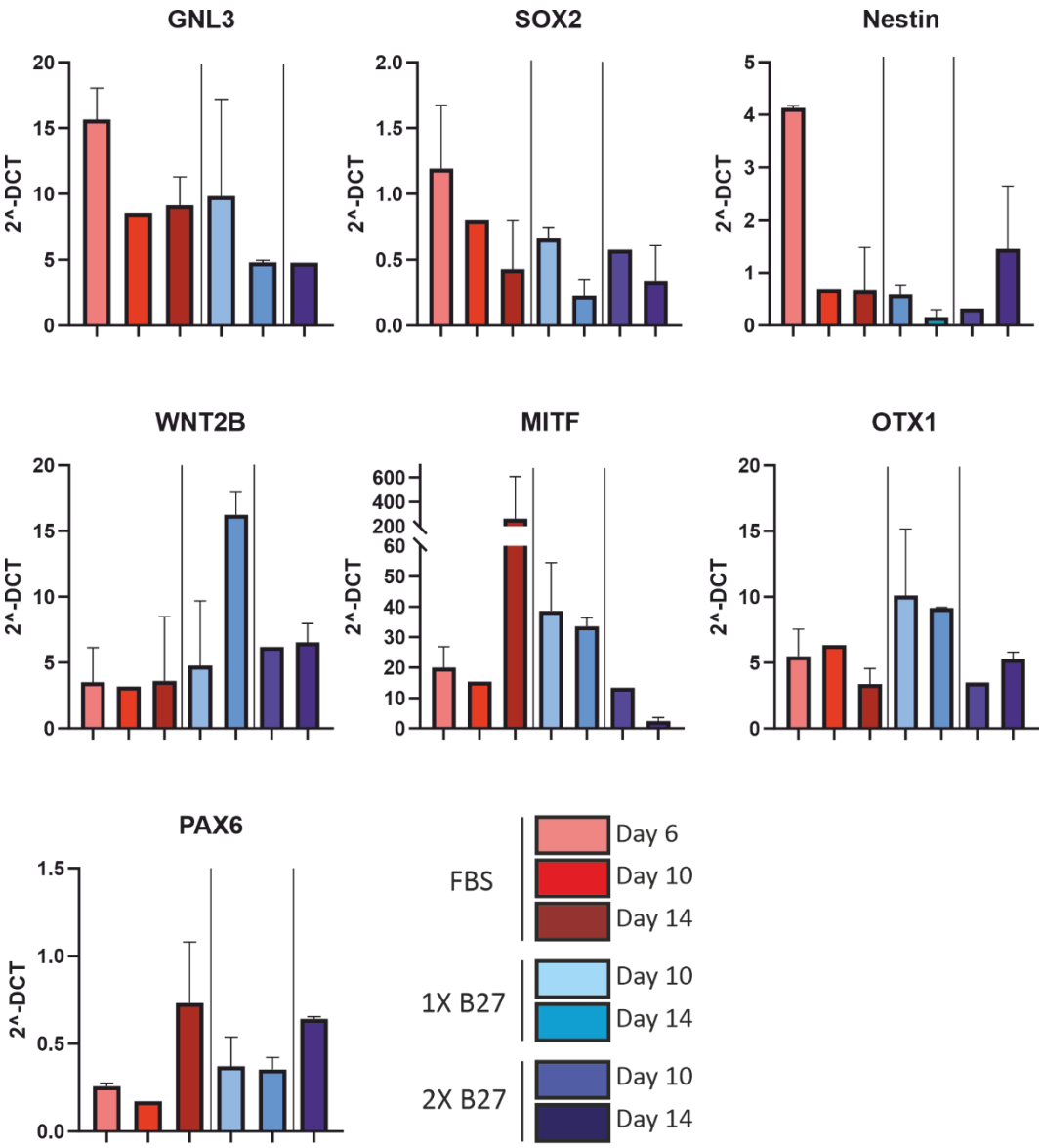

Figure 5.4: Gene expression and metabolic activities among IPE cells cultivated in FBS, B27 1X or 2X. QPCR demonstrating GNL3, Nestin, SOX2, WNT2B, OTX1, MITF and PAX6 expression in cells at day 6, day 10 and day 14. Specific supplements and time points are detailed in the legend on the right of the PAX6 graph. Two samples per condition for each time point were used. Genes were plotted against the Tata-Box binding protein housekeeper gene. Non-parametric Kruskal-Wallis tests were run, so significant differences were observed. To note, some results were technically unusable. So, the following data are missing: one sample from the FBS condition at day 10, two samples from the 2X B27 conditions at day 10 for for GNL3 and PAX6 investigations.

5.3.4 FICC demonstrated the absence of proper neuronal- and epithelial-like cells

B27 cultures were submitted to FICC at day 14. Nestin was used as a mesenchymal/neuronal marker. SOX2 and PAX6 were investigated to obverse potential

cell carpets in which both proteins could be balanced versus the other one. Specifically, SOX2 would be associated with the neurogenic fate, while PAX6 would be associated with the epithelial one. Finally, Tyrosinase was expected to mark cells which could potentially synthetize melanin. If so, these cells would be considered as "differentiated" compared to the epithelial cell carpets. To note, two samples per condition were investigated for each antibody.

In this investigation, the IgG control demonstrated signals on same locations over both the green and the blue channels (see **Figure 5.5-A**). Such signals were not observed in previous investigations but their number and distribution seemed kind of specific. Either these signals were due to autofluorescence, or a technical issue emerged and gave rise to these signals. Thus, the following results shall be reproduced to confirm following observations.

As nestin was already found in the previous chapter, the following analysis was to determine if B27 exposure over a long time would impact its distribution. As a result, both B27 cultures demonstrated similar distributions (see **Figure 5.5-B**). Some regions demonstrated a higher content, which could be related to the local higher cell density. Nestin labelled cells with elongated morphology for the most part.

SOX2 was investigated for the same prospect than nestin and so, results were contrasted (see **Figure 5.5-C**). Firstly, in regards of the IgG control, it is possible that signals were non-specific. Secondly, numerous cells in the 1X B27 demonstrated SOX2 in both cytoplasms and nuclei, with the cytoplasmic content seeming equivalent to the nucleic one. The 2X B27 culture demonstrated a close distribution to the 1X cultures. The higher cell density on the 2X picture made the fluorescence brighter. Some nuclei shapes were drawn by the antibody. So, the specificity of these signals being doubtful, the investigation shall be reproduced.

PAX6 also showed different distributions depending the B27 concentration. Cells from the 1X B27 culture were barely labelled (see **Figure 5.5-D**). In opposition, multiple nuclei were labelled in 2X B27 cultures. However, the fluorescence intensity being low, it is possible the PAX6 content was also low. Observations on the second sample demonstrated exactly the same things. Another reproduction would be beneficial here as well.

In regard of the melanin content which seemed to lower as cell proliferation ran (see **Figure 5.2**), and the media supposed to favour neurogenic fates, tyrosinase was expected to be minimal if not absent. That was more or less the results (see **Figure 5.5-E**).

Tyrosinase distributions were rarely observed in both B27 cultures. Distribution took a fibre-like shape or colocalised as clusters with nuclei (see **Figure 5.5**). So, it is probable that tyrosinase marked melanosomes distributing in certain areas of cells[387]. It is also possible that melanin synthesis still occurred but the absence of antibodies specific of the other proteins involved in melanogenesis prevented further investigations.

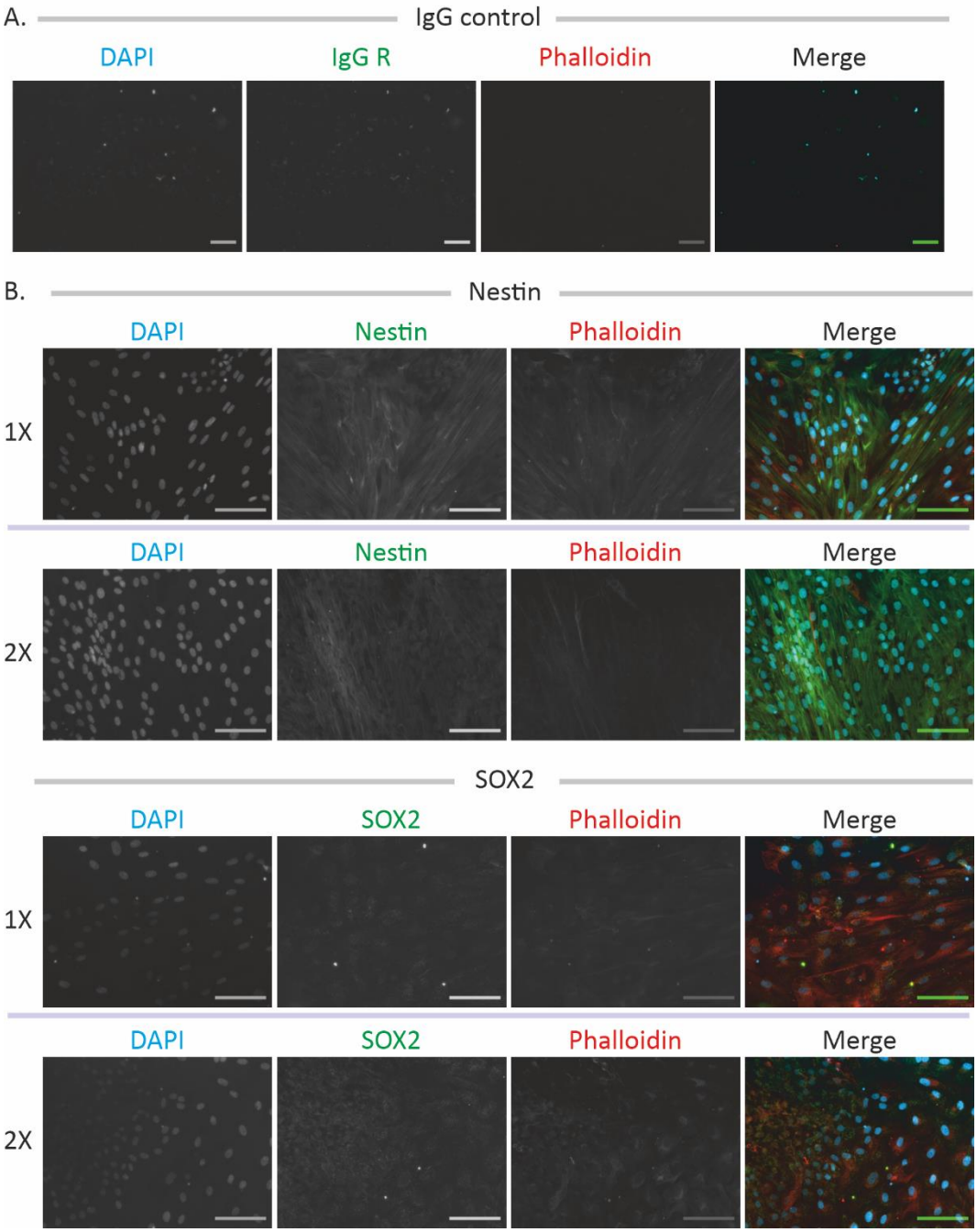

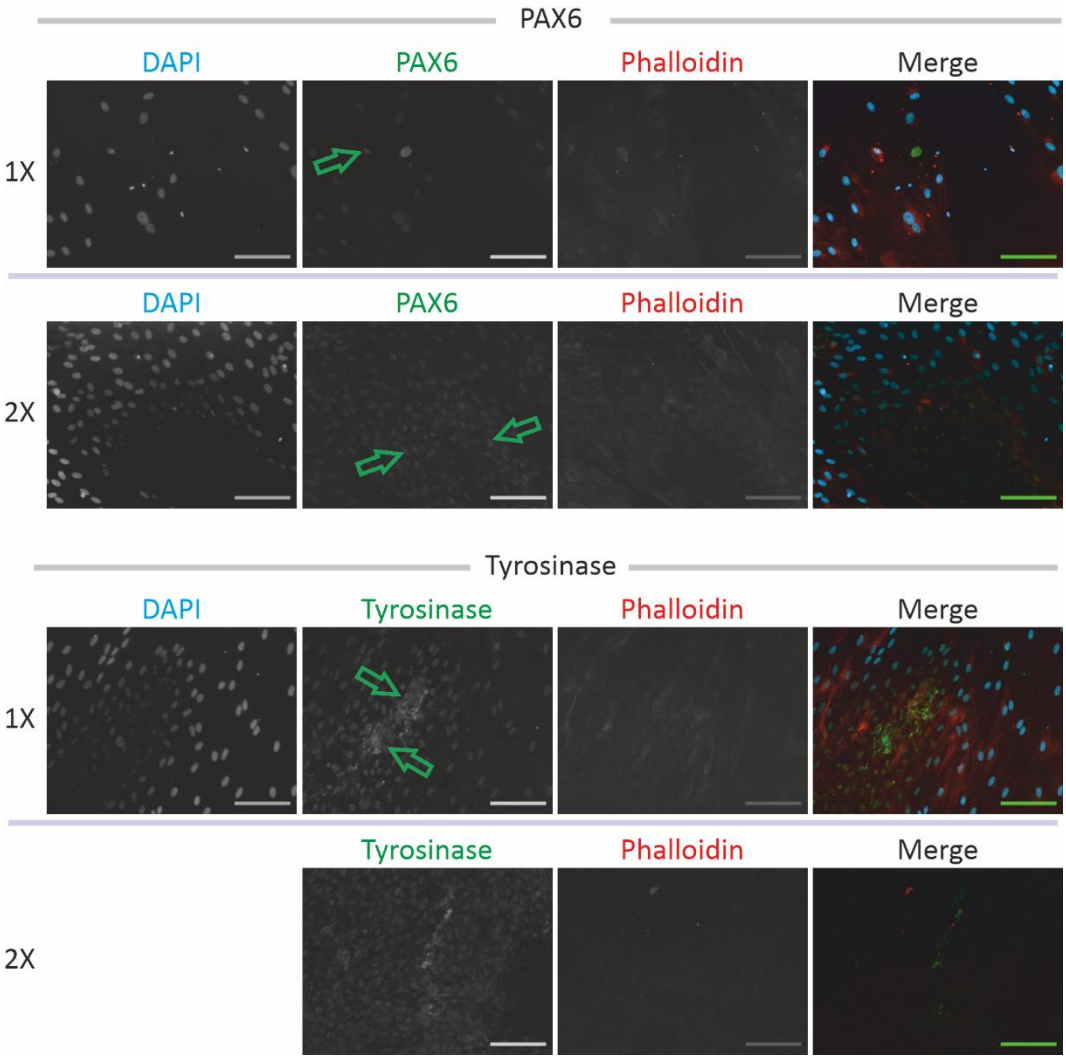

Figure 5.5: Representative pictures of IPE adherent cells labelled for Nestin, SOX2, PAX6 and tyrosinase. A. Rabbit IgG control. **B.** IPE cells labelled for Nestin. **C.** IPE cells labelled for SOX2. **D.** IPE cells labelled for PAX6. **E.** IPE cells labelled for tyrosinase. **Green arrows** indicate PAX6 and tyrosinase. Phalloidin-AF 594 conjugated and DAPI were used as counterstaining. Rabbit IgG, nestin, SOX2, PAX6 and tyrosinase are in green, phalloidin in red and DAPI in blue. 1X and 2X B27 are indicated on the left side. Scale bars = 100 µm.

5.3.5 WB demonstrated mostly no protein content

WB was used to assess potential protein changes over the process. A range of different samples was prepared, following the same spirit than the qPCR assessment. Controls depended of the target and are indicated in **Table 5-1**.

Table 5-1: Controls from porcine tissues used

Protein targeted	Positive control	Negative control
SOX2	Retinal protein extract	Iris extract
SNAIL/SLUG	Iris extract	Corneal epithelium
PAX6	Iris extract	Corneal epithelium

As a result (see **Figure 5.6 line 1**), SOX2 was labelled in samples from FBS conditions, with the strongest content detected at day 6. Following time points demonstrated a lower content in the FBS condition and nearly null content in the B27 ones. On column 3 and 4 corresponding to 1X and 2X B27 conditions respectively, it is possible that 1X B27 demonstrated a brighter contrast than the 2X. The use of retinal extract resulted from the lack of confirmed sources of SOX2 tissues in the porcine eye. Still, SOX2 was especially high in the initial phase of the culture to then decrease in FBS and being potentially absent in B27 conditions.

Next antibody was SNAIL/SLUG (see **Figure 5.6 line 2**). The iris protein extract was used as a positive control, the corneal epithelial one in column 5 as a negative one. If the iris extract demonstrated a tiny band, all other columns demonstrated samples nearly empty from SNAIL/SLUG at all time points.

Finally, PAX6 was expected to be present in the early process to then reduce once cells would be exposed to B27. Similar to the previous results (see **Figure 5.6 line 3**), poor bands were observed except in the iris extract.

As GAPDH was well labelled, the protein concentration was not a problem. On a technical note, one thing was observed: antibodies specifically designed for WB always worked much better than those designed for WB, FICC, IHC, etc. In that regard, a reproduction of that WB with specific WB-based antibodies could bring different and more valuable results.

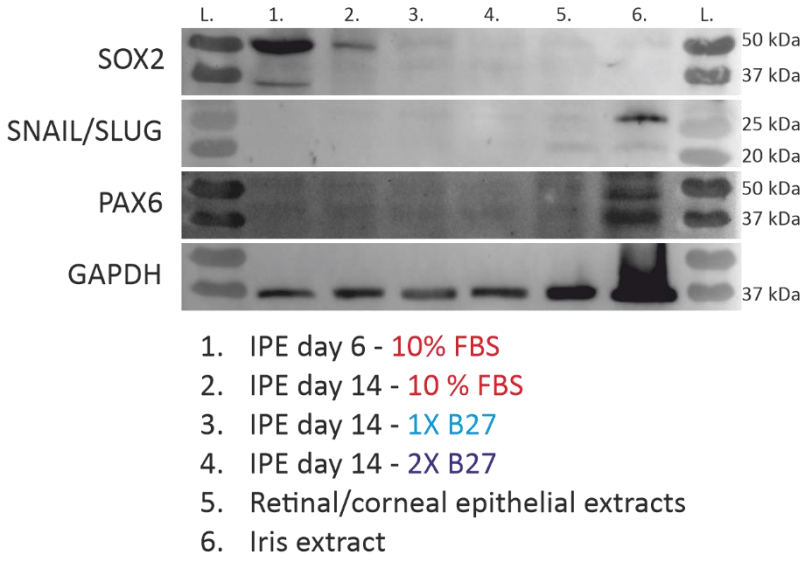

Figure 5.6: WB analysis on IPE samples and ocular tissues assessed for SOX2, SNAIL/SLUG and PAX6. Names on the left indicate the target, numbers at the top indicate the samples described below pictures. Protein weights are indicated on the right. 10 µg of proteins were loaded per well. GADPH was used at a loading control.

5.4 Discussion

The aim of this chapter was to expose IPE cells to neuronal supplements and observe their subsequent behaviours.

The objectives were:

- To grow IPE cells on adherent plates and in medium supplemented with:
  - 10% FBS;
  - 1X B27;
  - 2X B27;
- To assess the morphology, the metabolism, the gene expression and the protein content and distribution IPE cells developed in these conditions.

5.4.1 B27 favoured the epithelial-like cell and the neuronal-like one over the others

In this investigation, three main types of cells were observed: the fibroblasts like/epithelial-like cells, the neuronal-like cells and a third group not defined so far (see

Figure 5.2). All were present in the three conditions with cell number varying depending the supplement used.

FBS favoured cell proliferation from the fibroblasts-like/epithelial-like cells, especially the fibroblasts-like. The 1X B27 condition demonstrated a similar evolution with the epithelial-like cells representing the highest proportion of cells. In opposition, 2X B27 demonstrated the highest content of neuronal-like cells but the total cell number was the lowest of all conditions. The fourth cell type was observed in 2X B27 and formed carpets not observed in other conditions. Cell density in these carpets was high, cells were smaller and their pigment content was low.

So, as expected, supplements impacted, initiated or inhibited cell proliferation, metabolism and transformation as observed in other cells[388, 389, 390, 391]. In this investigation, FBS was used over the first six days to favour cell adaptation to the *in vitro* environment after initial isolation and to initiate proliferation. Then, B27 was used to favour the development of a cell population capable of transforming into neuronal-like cells. The rational to use B27 came from its use in neuronal long term cultures[392, 393, 394]. To increase the likelihood that such a transformation would happen and bypass a potential dose-dependent gradient, the supplement was used at 1X and 2X.

With three cell types being present in all conditions, transformations into fibroblasts-like/epithelial-like cells, neuronal-like ones and into the unclassified group probably occurred over the initial exposure to FBS. Then, the supplement would have simply favoured one cell type over the others. Subsequently, cell proliferation varied depending the intrinsic abilities of each type to do so, plus the exposure to the supplement[395, 396]. To note, a limitation of that experiment was the absence of cultures exposed at day 0 to B27 instead of FBS.

The metabolic activity was clearly impacted by the supplement type and its concentration (see **Figure 5.3**). FBS exposure correlated with the highest metabolic activity, growing until day 12. It would be of interest to passage cells at that point and push the culture for a longer term (see **Section 6.2**).

In B27 conditions, either metabolic activity mimicked initially the FBS condition to then be drastically reduced, or it remained stably low and increased slowly over time. In the end of the process, both conditions tend to a similar metabolic activity (see **Figure 5.3**). So, it is probable that 1X B27 exposure impacted cells on a progressive manner, while the 2X condition had drastic and deeper effects. That parallels with lower cell numbers observed

in each B27 conditions compared with FBS one. Thus, FBS replacement by B27 changed cell behaviours with deep effects.

5.4.2 B27 composition was optimised for neuronal cell long-term metabolism, not their proliferation

To get a complete picture, it was interesting to know the components of supplements used.

Concerning FBS, manufacturers have found more than 1000 elements in, including: growth and attachment factors, fatty acids, hormones, nutrients, carriers or antioxidant agents[397]. There is variation between lots as FBS is a by-product from the meat industry. That said, FBS composition ensures the presence of a large array of biological elements in the medium, supporting fast proliferation of various cells in a non-selective manner. So, it must be carefully assessed if its use in medium aims to select and/or transform a specific cell type.

On the contrary, B27 composition has been developed to favour survival of neurons and support their long-term culture. The composition of the commercial solution is not available, therefore the following list is based on initial publications, which developed the B27 supplement (see **Table 5-2**).

Table 5-2: Composition of B27 supplement[398]

Biotin	D(+)-galactose	Progesterone	Triodo-thyronine	Catalase
L-carnitine	Glutathione	Putrescine	DL-α-tocopherol	Insulin
Corticosterone	Linoleic acid	Retinyl acetate	DL-α-tocopherol acetate	Superoxide dismutase
Ethanolamine	Linolenic acid	Selenium	Albumin	Transferrin

1. Biotin: not synthesised in mammals, it acts as a cofactor to transfer carboxyl groups on proteins associated with the Krebs cycle, the amino acid leucine synthesis or the fatty acid synthesis. It locates in cytosolic, mitochondrial and nuclear compartments, where it helps to histone modifications[399].

2. L-carnitine: it is synthetized from leucine and methionine in the liver and the kidney to be then transported to skeletal muscle cells. There, it transports activated long chain fatty acids from the cytosol to the mitochondria, where β-oxidation degrades fatty acids toward energy production[400, 401]. In B27 original investigations, the addition of L-carnitine was demonstrated to slightly lower the formation of lipid droplets, responsible for metabolic disturbances *in vitro*[393].

3. Corticosterone: this hormone is involved in the rapid stress response once the hypothalamic-pituitary-adrenal axis is activated. It acts on brain cells and gene expression to support cell adaptation to the context. Among other targets, corticosterone acts on genes associated with energy metabolism, neuronal structure, vesicle dynamics, neurotransmitter catabolisms, cell adhesion and regulators of glucocorticoid-signalling[402, 403].

4. Ethanolamine: this component of the glycosylphosphatidylinositol-anchored proteins comes from external sources as mammals do not synthetize it. It stimulates cell growth by supporting phosphoethanolamine and phosphatidylcholine synthesis and protects cells *in vitro* from low-serum induced apoptosis. To note, both ethanolamine and phosphoethanolamine have been show to inhibit aerobic respiration in a dose-dependant manner[393, 404, 405].

5. D-galactose: this sugar is present in bacteria, plants and animals where it binds oligosaccharides, polysaccharides, glycoproteins and glycolipids. High concentrations are maintained in the brain where it associates with plasma membranes of neurons, astrocytes and oligodendrocytes. It is also used for amino acid synthesis and myelin glycosylation. Other observations demonstrated that D-galactose was increasingly present in development and could participate to oxidative stress in aging tissues[393, 406, 407, 408].

6. Glutathione: it is the most important low molecular weight antioxidant agent synthesized in cells. It results from the addition of cysteine then glycine to glutamate. It is mostly present in the cytosol where it regulates apoptosis and necrosis, and in fluids exposed to gas exchange such as the lung epithelial barrier [393, 409, 410].

7. Linoleic acid – linolenic acid: these molecules are poly-unsaturated fatty acids with a carbon double bond for the former and a triple for the latter. That difference induces antagonist functions. For example, linoleic acid has pro-inflammatory functions while linolenic acid has anti-inflammatory ones[411]. Depending on the dose and the cell type, these fatty acids inhibit or increase cell proliferation[412, 413]. In neurons, multiple roles have been described from the growth of axons[414], neuron protection against caspase-3/-9-based apoptosis[415] or excitotoxicity[416]. Several other effects have been described including antimutagenic, anticarcinogenic and antidiabetic[417, 418]. Finally, they serve as precursors of arachidonic acid, leading to prostaglandins synthesis among others[419, 420].

8. Progesterone: this hormone originates primarily from ovary, testes and adrenal cortex. Various protective roles in experimental models have been described in the literature. Among them are the attenuation of oxidative and excitatory injuries, the increase in brain-derived neurotrophic factor supporting cell survival and synaptic plasticity[421, 422]. Various benefit effects have also been observed in pathological models including the Alzheimer's disease in which neurons *in vitro* increased their glucose metabolism[423].

9. Putrescine: it belongs to the polyamine group containing also spermine and spermidine[424]. When present in neuronal culture, it favours neuronal network formation and neuron differentiation[425]. However, recent investigations tend to show that putrescine induces more deleterious effects than beneficial ones[426].

10. Retinyl acetate: it is used as a potent neuronal differentiation agent, acting as a precursor of retinoic acid and favouring an endogenous production of retinoic acid[427, 428].

11. Selenium: it favours neuronal growth and improves neurologic outcomes in traumatic brain injuries[429]. Specifically, its most known form is its association with the amino acid cysteine in the glutathione peroxidase degrading hydrogen peroxide. Its inactivation is known to exacerbate neuronal damage in cerebral ischemia or upon application of neurotoxins[430].

12. Triodo-L-thyronine: this hormone belongs to the thyroid hormonal family, critical in multiple developmental and growth processes from the brain to the skeleton[431, 432]. Its concentration increases rapidly after birth in both blood and cerebrospinal fluid with 10% being free and active. It participates to the neuronal development by increasing the secretion of neuronal growth factors. When assessed on rat occipitus foetus, neuronal and glial outgrowth were stimulated. However, higher concentrations generated lipids droplets and cell debris completed with the degeneration of large neurons[393].

13. DL-α-tocopherol & DL-α-tocopherol acetate: also called vitamin E, no specific functions have been determined so far. Experimental deficiency demonstrated sterility, muscle degeneration and axonal dystrophy among other issues. Still, biochemically, vitamin E is known to have strong anti-oxidant properties. It incorporates into both mitochondrial and plasma membranes where it protects poly-unsaturated fatty acids from peroxidation by free radicals[460]. To note, vitamin E inhibits retinal pigmented epithelium cell proliferation *in vitro* without exerting cytotoxic effects. That phenomenon was also observed in smooth muscle cells[433, 434]. Finally, in human RPE cultures, increasing age parallels reduced proliferation and increased α-tocopherol content[435, 436].

14. Albumin: it is a major protein in biological fluids and in lab solutions. It serves as a colloid osmotic pressure agent, maintaining the pH and serving as a carrier for hormones, fatty acids, electrically charged compounds, etc. It removes toxic ionic compounds and oxidant agents from fluids. To note, the albumin concentration decreases in the brain as it is filtered by the cerebrospinal barrier[393, 437].

15. Catalase: this protein is a scavenger of the aerobic metabolism. So, it protects cells and tissues from oxidants and catalyses by degrading hydrogen peroxide into oxygen and water. To note, NADPH can bind to it and so, decreases its susceptibility/inactivates it in low hydrogen peroxide environments. Reversely, catalase can release $NADP^+$ with the induction of glycolysis for example[438, 439].

16. Insulin: it is indispensable in the organism to regulate glucose amount through the body. It is also known to stimulate cell growth, especially during foetal development, by facilitating the use of glucose, protein and fatty acid synthesis.

In vitro, it helps to absorb the low molecular weight nutrients[393]. In astrocytes for example, exposure to insulin favours cell proliferation and glycogenesis[440]. Depending on their original location, insulin protects neurons from death in case of hypoglycaemia to various degrees[441].

17. Superoxide dismutase: mammalian superoxide dismutases are composed of three proteins: copper-zinc superoxide dismutase, manganese superoxide dismutase and extracellular superoxide dismutase. They elicit similar functions but are distributed in different locations. They are specialised in eliminating superoxide anion radicals in extracellular environments, cytosol and in mitochondria, balancing the ROS concentration[393, 442].

18. Transferrin: this β-glycoprotein is a major protein involved in iron transfer in blood. Each molecule can bind 2 atoms of Fe^{3+} and remove them by a reduction into Fe^{2+}, by vitamin C *in vivo*. The iron binding activity *in vitro* is indispensable for neuronal cell survival. In the absence of glial cells in the culture, it is the only way for cells to absorb iron. In opposition, transferrin seems dispensable in retinal cell culture[393, 443].

So, if the recipe remained unchanged, B27 supplement contained a few growth factors, some anti-apoptotic factors, multiple proteins and agents conducting anti-oxidative stress activities, and some metabolites. Originally, the inventors of the B27 cocktail defined its anti-oxidant properties as a key feature; neuronal degeneration *in vivo* and *in vitro* being partly associated with oxidative stress[444, 445]. So, such a combination reduced significantly the formation of free radicals arising from cell metabolism[393]. Thus, IPE cells grown in B27 media suffered less from oxidative stress.

The lower proliferative activities observed in B27 conditions, especially the 2X one, directly resulted from this cocktail. The presence of anti-apoptotic factors in the medium has probably contributed in preventing cell degeneration. As cell proliferation was not favoured and apoptosis blocked, it is possible that IPE cells would have survived for a longer term in culture than the period tested here. So, the four different populations described would probably have developed deeper changes as well, supporting that it is

require to select carefully the medium and the supplements to further characterise these cells.

5.4.3 Small pro-epithelial cells in 2X B27 with iPSC-like morphology

The most interesting observation was the epithelial-like cells in 2X B27, which formed layers not observed elsewhere. As described in the Section **5.3.1**, those layers were dense, contained small cells with a large nucleus surrounded by a small content of melanosomes. These characteristics are similar to those seen in iPSC. So, it is possible that this specific phenotype related to dedifferentiated cells[446, 447].

However, except the observations at the optic microscope (see **Figure 5.2**), few data were obtained. Indeed, FICC (see **Figure 5.5**) did not allow to distinguish those layers despite extensive observations. WB did not clarify the situation and would require a reproduction (see **Figure 5.6**). Only qPCR demonstrated that Nestin, WNT2B, OTX1 and PAX6 expressions increased in the end of the process (see **Figure 5.4**) without direct links to these cells.

Thus, further investigations shall focus on the growth of these cells, potentially by increasing the time frame of that process. Further characterisations could focus on the downstream targets of the pathways involved in the RPE specification, the GNL3-related cell transformation and other markers associated with the development of the neuro-epithelium at the origin of the RPE and the retina. Inspiration for the process running in these IPE cells could also come from dedifferentiation observed from other mammal cells, white adipocytes being the most described cells able to do so[448, 449].

5.5 In conclusion

The use of the B27 supplement over long term favoured the emergence of four IPE cell types after 14 days. No characterisation could be conducted due to the lab time constraint but the identification of each type seems essential in first instance. Each of them could indeed have a specific ability to transform or not in other cells such as RPE ones or neuronal ones. So, in this prospect, a medium-to-long term adherent cell culture combined with a B27 supplemented medium seems to be a reasonable initial approach in a characterisation process.

6 Chapter 5: General discussion & conclusion

6.1 IPE stem cell existence remains to be proved, potentially by cultivating them in medium supplemented with B27

To run its functions, a tissue requires effectors. However, due to their activity, their genetic background or/and their exposure to the environment, the effectors can degenerate[450, 451]. Two strategies have been developed by cells to maintain the integrity of their tissues: either the tissue forms one, or more[452], dedicated structures to maintain a reserve, meaning some cells in a non-functional state or a proliferative state, while, at the other end of the process, it regulates apoptosis[278, 279] or, in a less common strategy, the tissue maintains the same cell pool through the ontogenesis of the organism[138, 139].

Here, it was hypothesised that the IPE maintains its homeostasis by using the first strategy. The identification of Ki-67-positive proliferating cells near the ciliary body–IPE junction demonstrated that the process was localised in a peripheral region. The relevant cells potentially benefit there from minimal iris movements and a mechanically more stable basal lamina, both essential to the regulation of cell proliferation[453, 454].

The number of Ki67-labelled cells suggests that several cells were undergoing cellular division simultaneously[455]. So, in contrast to the RPE, the IPE would benefit from a pool of ready-to-use cells. On the other side of the homeostatic balance, and near the pupil in the tissue, some observations analysed the presence of melanosomes in iris stromal cells as evidences of IPE cell apoptosis[3]. Thus, the IPE could maintain its homeostasis by having a ready-to-use cell reserve in its periphery. These cells could progressively move toward the pupil, where they could physiologically die and desquamate as does the corneal epithelial cells.

In stem cell niches, cells which proliferate are generated from stem cells, which reside in the innermost part of the tissue to preserve them from external stress[456]. Maintenance of stem cell potency (see **Table 1-4**) requires specific cells, dedicated proteins from the basal lamina and specific cell-signalling[5, 134, 276, 279, 280, 452]. So, the investigation of the IPE basal lamina was run to identify and localise the ECM proteins. As mentioned in Section **3.5.2.2**, the laminin-α4 was present over the majority of the IPE portion, except at the ciliary body-IPE junction (see **Figure 3.15**). The lack of specific antibodies to laminin chains associated with stem cell niches[221, 222] prevented further investigations.

Two other markers, at the edge of stemness and development, were also investigated with the expectation that they would localise in specific cells. In its study on the rat IPE, Asami *et al* suggested that nestin and Pax6 could balance IPE cell faculties to transform into retinal progenitor cells or neuronal progenitor ones[201]. Based on their observations of IPE transformation *in vitro* toward these cell types, the authors also suggested that IPE cells could maintain a developmental memory, susceptible to reactivate other patterns linked to the original neuro-ectoderm (see Section **1.2.2**).

Here, the presence of PAX6 in the pig and the human IPE was broader than expected. It could suggest that IPE cells need it not only through development, but also through ontogenesis[457]. Its importance as a central regulatory transcription factor has been underlined in several studies regarding several pathways associated with development[457]. Being highly involved into the specification of the lens, the cornea, the RPE, the CB, the IPE and to a lower degree other ocular tissues, it is possible that some interactions between these tissues in adulthood involve PAX6, which would then controls the subsequent signalings. In addition, the distribution could also be related to the IPE localisation in the eye. Indeed, the IPE localises at the front of both anterior and posterior chambers, nearly in contact with the lens and the aqueous humour. In a more specific manner, the IPE anterior layer is polarised into its anterior myogenic part and its posterior pigmented epithelial one. The balance between these two parts and their respective regulations could mimic the one between PAX6 and some BMP factors, at the origin of the iris smooth muscles[458]. Thus, the exposure to various factors, which could generate antagonist processes, requires safeguarding mechanisms and thin regulations in which PAX6 could be a keystone.

Nestin was labelled in the porcine tissue in an opposite manner to what was observed in rats by Asami *et al*[201]. Nestin in the new-born rats was observed over most of the IPE posterior layer. In opposition, the porcine section demonstrated nestin limited to the ciliary body-IPE junction (see Section **3.4.1.3**). In an analogous situation, skeletal muscles demonstrated between their basal lamina and plasma membranes nestin-positive satellite cells, running as the local myogenic stem cells[333, 459]. Another analogous location is the hair follicles, with the bulge area containing nestin-positive keratin-negative cells able to generate *in vitro* glial cells, neurons, keratinocytes, smooth muscle cells and melanocytes[460, 461]. Despite their different origins[3], these tissues demonstrated nestin-positive cells in locations isolated from the main activity of the tissue. So, it is tempting to see the nestin-positive IPE cells as local potential stem cells.

Indeed, the nestin gene sequence demonstrated enhancer elements in its first intron driving its selective expression in endothelial and muscular lineage cells[462, 463], other in its second intron driving its selective expression in neuronal cells[464]. As further described by Josephson *et al*[465], the second intron into the rat nestin gene contains a 257 basepair enhancer targeted by the POU family, a large family of transcription factors involved in the development of the CNS and in its maintenance in adulthood[465, 466, 467]. To note, a previous study demonstrated that the rat and the human sequence of this specific enhancer were identic at 78%[468]. Over their study, Mignone *et al* demonstrated in the developing mouse that nestin was specifically associated with multipotent neuronal cells[213]. They confirmed these results *in vitro* by observing a significant increase in neurospheres generated from nestin-positive cells, plus the ability to generate cells from neurogenic and astrocytic lineages.

The IPE originates from the neurectoderm and run smooth muscular functions in adulthood. In this perspective, the specific use of nestin either to maintain the homeostasis of the smooth muscle cells or to run a different function related to neurogenic functions, is yet to be elucidated. It is possible that a thin process specific to the IPE balances between pigmented epithelial functions, the partial transformation toward smooth muscular activity and its maintenance[3, 4], and the neuroectoderm origin. It could explain that in the generic neurogenic conditions used in Chapter **4**, βIII-tubulin, associated with committed neuroblasts and neurons[213, 464], was found in several but not all aggregates as a result of differences in the balance of these two processes. Thus, as Mignone *et al* did for development of the CNS, the development of neuronal-nestin positive IPE cells and their muscular-nestin positive counterparts could be tracked *in vivo* and *in vitro* with appropriate genetic tags, selectively characterised, and potentially identified as multipotent cells.

Related to this, the use of DMEM-F12 supplemented with either FBS or B27 proved that stringent media could led to surprising observations (see Chapter **5**). It was known that the medium contributes to the emergence of cell phenotypes *in vitro*[469]. As demonstrated in the discussion of the Chapter 5 (see Section **5.4)**, these two media induce different processes: cell proliferation and high metabolic activity for FBS[397]; cell survival and anti-oxidative metabolic processes for B27[398]. In that prospect, the B27 supplement is more relevant regarding the stem cell needs compared with FBS (see **Table 5-2**). Indeed, Ng *et al* suggested that understanding stem cells metabolic needs *in vivo* and *in vitro* would help to control their fates[471]. A suggestion based on works such as the one from Takashima *et*

al[472], who demonstrated that resetting human pluripotent stem cells into naïve embryonic stem cells, which are relatively more stable and more homogeneous[473], is accompanied by a consistent mitochondrial activation plus epigenetic readjustments toward hypo-methylation. Some proteins directly involved in the mitochondrial respiratory chain, LIF-induced Stat3[474], Esrrb[475], have been proposed as pluripotency factors as they participate to maintain in activity the dioxygenases removing DNA methylations, so regulating the chromatin state and favouring the expression of pluripotent factors. Ng *et al* also remembered that metabolic activities deeply impact the protein activities, their processes, the associated productivities, and their impact on the epigenetic state[471]. So, in the IPE cultures, B27 impacted not only the metabolic pathways cells were using but also probably the epigenetic state of all IPE cells.

In adult organisms, neural stem cells, skeletal muscle satellite cells or hematopoietic stem cells remain mostly quiescent to preserve their self-renewal capacities[471]. As a correlate, their metabolic activity is lower than the average from their differentiated cell counterparts. So, if they start to proliferate, metabolic processes change and the oxygen consumption increases[471, 476]. This means that quiescent stem cells experience mainly hypoxic environments *in vivo*. *In vitro*, such hypoxic environment was not implemented. However, on the other side of the spectrum, an anti-oxidant was generated by the DMEM-F12 2X B27. There, the metabolic activity was lower (see Section **5.3.2**) as the cell number (see Section **5.3.1**). The emergence of the small epithelial-like cells, morphologically close from the iPSC[156, 157] was unique to that medium only. As cell proliferation was not favoured due to the quick change from FBS to B27 (see **Figure 5.2**), it is possible that these small epithelial-like cells have been preserved from the FBS-induced proliferation. As time advances, the 2X B27 supplement favoured a quiescence-like *in vitro*, suitable for the survival of these cells. Lab-time constraints made further analysis not possible. Given the fact that such IPE cells have never been observed *in vitro*, further characterisations are indicated in the following section (see section **6.2.1**).

In summary, the data gained about the porcine IPE tissue demonstrated that cell proliferation occurred in periphery of the iris, near and in the ciliary-body IPE junction. Conversely, PAX6 was distributed over a vast portion of the IPE, supporting that it maintains or balances some functions essential to the IPE. No laminin specifically involved in stem cell maintenance *in vivo* was found. However, nestin-positive cells were detected in that region, a protein known to be *in vivo* representative of muscular and neuronal multipotent cells. As Chapters **4** & **5** further demonstrated, porcine IPE cells have the

abilities to give rise to neuronal cells, pigmented ones and small non-pigmented, epithelial-like ones. The diversity of cells observed is intrinsic to the IPE but the *in vitro* environments used made them visible under specific conditions only.

6.2 Future plans

Chapter 5 demonstrated that at least 4 different cell types were generated *in vitro*: the fibroblasts-like/epithelial-like cells; the neuronal-like cells; the small epithelial-like cells; a fourth group to define. To the knowledge of the writer, these four cell types arising from porcine IPE cell clumps have not been described in the literature so far.

6.2.1 Short term plan: small epithelial-like cell characterisation & cell culture developments

So, in works to follow this PhD, the first main objective would be to observe processes susceptible to demonstrate distinct behaviours. These distinct behaviours could then be linked to one or more IPE subtypes. The following points describe a potential process suitable to select and characterise potential stem cells in the IPE cell as this was the subject of this thesis, with a focus on the small epithelial-like cells.

As explained in section **5.3.1**, these cells demonstrated morphological features that are found in iPSC *in vitro*[446, 447]. In absence of further elements demonstrating that this cell subpopulation was pluripotent, the scope of following investigations shall be placed on their growth and characterisation. Pluripotent stem cells constitute a cell population able: **1**. to differentiate into a variety of lineages and tissues; **2**. to self-renew themselves without committing in a lineage if appropriately grown[446, 447, 477]. So, an initial and simple investigation would be to grow porcine IPE cells by the method used in Chapter **5** over a longer period. In 2007, Yamanaka et al. observed flat colonies of human iPSC after 25 days of culture for example[157]. The authors also noted that the initial proportion of cells that reprogrammed into iPSC was very low[157, 478]. As explained in section **5.4.2**, DMEM-F12 – 2X B27 did not favour cell proliferation from the other cell subtypes. Moreover, continuous adherent culture system allows pluripotent stem cell continuous growth, with potential pigmented loci emerging[479]. So, despite a potentially initial small subpopulation,

it is possible that in DMEM-F12 – 2X B27, the small epithelial-like cells would be the only ones to grow and constitute in the end-term the main subpopulation.

The following investigation shall search for proteins specifically associated with pluripotency and cell plasticity. Some proteins investigated in this PhD would be relevant:

- Nestin: present in progenitors and undifferentiated neuronal/muscular cells[252, 253, 254, 255, 335, 341, 402], its presence would suggest that the small epithelial-like cells are in an undifferentiated state or a low-differentiated one;
- GNL3: preserving the genome and telomers integrity in stem cells[366, 367, 368], its presence in IPE small epithelial-like cells would also suggest that the small epithelial-like cells are in an undifferentiated state or a low-differentiated one;
- PAX6: master regulator of the ocular development[285, 286, 287, 288, 289, 290, 298, 391], its assessment in the small epithelial-like cells would state if these cells maintain a generic neuro-epithelial phenotype;
- MITF: one of the main RPE markers appearing firstly in the neuroepithelium before the specification of the later into RPE and retina, its expression is then restricted to the presumptive RPE[45, 372, 480].

Other markers involved in ocular tissue development from the original neuroectoderm would strengthen this assessment. The following ones are proposed for this purpose as their roles in the eye morphogenesis are essential. **LHX2** and its obligatory co-factors **LDB1** and **LDB2** maintain neuroectodermal phenotype at the optic pit by suppressing alternative fates and maintaining the optic cup one through the following developmental processes[481, 482, 483]. Later during the optic vesicle formation, LHX2 initiate the expression of MITF and VSX2, both participating respectively to the RPE and retina specifications[482, 484]. Once the retina and the RPE form distinct layers, LHX2 remains active in the first one by maintaining the balance between neurogenesis and gliogenesis[485]. **SIX3** runs as an upstream regulator at different stages during the eye development[482]. It participates to the formation of presumptive eye tissue[483, 486]; it regulates PAX6 and SOX2 during the lens formation[487]; it represses Wnt signalling in the prospective retina to the specification of the retina versus the RPE[488]. **SIX6**, another member of the Sine Oculis subfamily of vertebrate homeobox genes (SIX)[482], has been shown to co-localise with SIX3[489]. Despite having less potent actions than SIX3, SIX6 – SIX3 association is essential for the right development of the eye as it participates to maintain multipotent neuroretinal progenitors[490]. **RX** is another eye field transcription factor essential for the optic pit

specification and following developments[484], with evidences demonstrating that it specifies neuroectodermal cells toward neuroepithelial cells, then neuroretinal ones[491].

The sum of these investigations could provide enough data in its end to establish generic molecular identity elements characteristic of these small epithelial-like cells. With this part completed, the following one shall focus on the potency of these cells to grade their differentiation abilities. A gold standard in such investigation is the teratoma formation using a nude mouse, meaning an adaptive immune system-free mouse[492]. This model allows biologist to graft tissues or cells in subcutaneous region(s) and observe how the graft evolves. In the stem cell field, the grafts of presumed stem cells in nude mice provide these cells with a "no limit" environment suitable for them to grow and differentiate while forming "physiological" tissues. This result by the formation of various tissues related to one germ layer or more depending their original potency to differentiate[132, 156, 157, 194, 493,]. Would the small epithelial-like stem cells form an optic cup-like structure or some at least some structures related to the eye if they were grafted in a nude mouse?

Complementary axis requiring investigations are: **1**. the definition of a collection of cell-surface markers that can be found over multiple samples; **2**. the development and optimisation of the environment to grow cells. Indeed, to evaluate the therapeutical potential of a primary stem cell population, scientist must rely on a highly homogeneous cell population, meaning that most if not all cells must have the same differentiation degree. So, this requires that selected cells present specific cell surface markers over a specific time that can be identified by cytometry or by other methods[132, 494]. This would permit investigators to compare both results and methods used to grow cells[494]. The second requirement is to develop and optimise the appropriate environment for stem cells depending their stage of differentiation and the objectives of the investigation[160, 477, 495]. This would be to favour the original stem cell emergence from primary tissue, then to grow these stem cells in a homogeneous manner while maintaining them into an undifferentiated state.

At this stage of investigation, small epithelial-like cells have emerged only when grown in DMEM-F12 2X B27. So, if these small epithelial-like cells are proved to be stem cells, DMEM-F12 2X B27 shall be considered for further developments.

6.2.2 Long-term plan: RPE differentiation & AMD treatment

Increased fundamental and technical knowledges on the IPE stem cell identity and culture methods bring the question of IPE stem cell differentiation into a tissue. As the idea behind this thesis was to find IPE stem cells to then graft them into the RPE of AMD-affected patients, the following development focus on IPE stem cell differentiation into RPE only, taking inspiration from what is known in the current literature. This is also based on the hypothesis that the small epithelial-like cells are indeed stem cells.

As explained in Chapter **1** section **1.3.4**, ESC and iPSC have been used to generate RPE cells by different approaches. The first report demonstrating ESC-derived RPE cells used PA6 cells, a stromal cell line derived from the skull bone marrow[496], as a feeder layer on which were seeded mouse ESC[497]. The main body of cells differentiated into neurons but a small part was positive for PAX6 while demonstrating early pigmentation and RPE cobblestone morphologies. In 2004, Klimanskaya *et al* successfully scraped the ESC-derived pigmented cells with a glass capillary[498]. After the following passages grown on gelatin-coated plates, the authors observed transcriptomic profiles similar to the foetal RPE cells. Spontaneous differentiation from iPSC into RPE cells was also observed, the iPSC-derived RPE cells being functionally equivalent to foetal RPE cells and ESC-derived RPE cells[499]. The spontaneous differentiation of ESC remained until recently a method of choice as it limits the use of xeno-elements during the process and so fulfil clinical requirements[153, 500].

Other investigations, especially in the last decade, took inspiration from the RPE development to mimick it *in vitro*[479, 501]. The importance of **Wnt** and **Nodal** signals to increase the yield of RPE differentiation was demonstrated by Osakada *et al* in 2008[502]. The use of **nicotinamide** and **activin A** was then proved to increase the RPE specification markers in the early steps of the ESC differentiation[151]. Later investigation led by Buchholz *et al* supported that nicotinamide speeds up the early eye field specification in early stage and that activin A combined with the FGFR1 inhibitor **SU5402** decreased Rx expression in late stage[150]. As a result, Buchholz *et al* obtained pigmented RPE cells in 14 days. The authors explained that such speed was attributed to the VIP, known to promote cell differentiation[503].

To assess the differentiation means that RPE specific markers shall be investigated and functional assessments of the derived cells be run. The following list of markers is not

exclusive but includes reliable RPE markers: **MITF** for its role in RPE specification; tyrosinase for its role in melanin synthesis; **PMEL17**, a melanosome-based protein upon which melanin sets[150]; PEDF for its neuroprotective properties[504]; **VEGF** for its angiogenic properties[505]; **RPE65** specific to the RPE, this retinol isomerase is essential in the visual cycle[506]; **CRALBP**, another protein associated with the visual cycle, it process all-trans-retinaldehyde into 11-cis-retinaldehyde[507]; **MERKT**, a tyrosine kinase receptor involved in POS phagocytosis[508]; **Bestrophin**, a calcium-dependant anion channel localising on the RPE basolateral membrane[509]; **ZO1** for the formation of tight junctions if cells get confluent[163]. Functional assessments on their side shall include: 1. photoreceptor outer segment phagocytosis assays; 2. polarised factor secretion; 3. Trans-epithelial barrier resistance; 4. Pigmentation[163].

In the last decade, sophisticated protocols and tests were published aiming to improve the RPE differentiation efficiency from iPSC as these cells tend to be less efficient than the ESC[479]. Still, similarities in protocols are important. Therefore, inspiration shall be taken from both. The spontaneous differentiation seems to be the simplest protocol and so, could serve to prove that IPE stem cells can differentiate into RPE cells. Then, more advanced protocols shall be used to improve in quality, quantity and consistency the IPE-derived RPE cells.

Finally, the safety shall be considered. In allogeneic graft therapies, HLA incompatibility between a donor and a patient is major barrier which caused host antibody-based and complement-associated acute and chronic rejection of the organ[510]. These rejections require to treat grafted patients with immunosuppressive therapies aiming to remove circulating donor-specific anti-HLA antibodies from the organ to graft prior to the surgery. Once the organ is grafted, therapies include plasma exchange or glucocorticoid injection[510]. Stem cells therapies aiming to replace the RPE in AMD-affected patients face such issue as well as grafted cells are not recognised by the host immune system in absence of immune suppressive drugs[511, 512]. In what could be IPE stem cells therapies however, this issue could be resolved by the use of autologous sources as it is done with autologous iPSC-derived RPE grafts[513].

Another concern would be the teratoma formation after the surgery or the risk of differentiation toward an unwanted phenotype. To avoid these issues, good manufacturing practices in RPE differentiation protocols have been developed to establish cell purity based on functions and proteins associated with a mature RPE while

proving the absence of any immature RPE marker[514]. In addition, cells must be grown in serum-free media and supplements[514]. If original stem cells are grown on inactivated MEFs, the FDA would consider the graft as a xenotransplantation product with specific guidelines in charge of the patient monitoring and product processing, testing and archiving[154].

So far, no adverse effects originating from the pluripotent-derived RPE cells in clinical investigations has led to serious adverse effects[91, 153, 154, 166, 513, 515], proving that appropriate protocols following strict guidelines can potentially lead to long-term benefits for the patients. If IPE stem cells are clearly and deeply characterised, grown in appropriate environments, differentiated into RPE by state-of-the-arts protocols and rigorously checked at every stage of the process, then they could also bring some benefits to many patients affected by the AMD.

6.3 General conclusion

Thus, in the light of this work, no stem cells have been identified in the porcine iris pigmented epithelium. This tissue runs two processes aiming to control the light intensity in the posterior chamber. The first is a smooth muscle skirting the iris on its posterior side. That participates to open the pupil by contracting the iris. The second is devolved to the absorption of light passing through the iris. This prevents light from saturing and/or disrupting the photoreceptor system. It also requires a process to depigment it for histological purposes. Further investigations on the tissue could still bring evidence to support the hypothesis that some stem cells reside in the IPE.

Indeed, this work also demonstrated evidence that some IPE cells could be multipotent. Cell transformations toward different phenotypes were observed in the different conditions experimented *in vitro*. This supports that further in-depth molecular tracking of some crucial keystone proteins, in cells exposed to stringent non-proliferative conditions, seem essential. Indeed, four IPE cell types were observed. So, either for a fundamental prospect, or for the aim to replace deficient RPE cells in AMD, it is essential to identify these different IPE cell types. It is as important to understand their behaviours *in vitro*, how can they be distinguished according to their differentiation stage and to their epigenetic state, and how can this knowledge be linked to the IPE *in vivo*.

6.4 Summary of findings

- Melanin can be removed from porcine iris pigmented epithelium sections by the exposure to H_2O_2 (3%) for 20 min at 60^{o}C

- Porcine IPE uses smooth muscular and muscular-associated proteins in its anterior layer; its basal laminal surrounds it on its anterior and posterior faces

- Proliferation occurs in and near the ciliary bodies – IPE junction; this region potentially contains multipotent cells

- IPE aggregates grown in generic neurogenic conditions developed neuronal specific protein content

- RT-qPCR run from these aggregates established other potential transformations involving the Wnt/β-catenin canonical pathway, associated with the RPE development

- *In vitro*, four types of IPE cells were observed: the neuronal-like cells, the epithelial-like cells/fibroblasts-like, the small epithelial-like cells and a fourth group remaining to define; the small epithelial-like cells were observed only in anti-oxidant medium.

7 Appendices

7.1 Appendix 1: adjustement of the H_2O_2 depigmentation

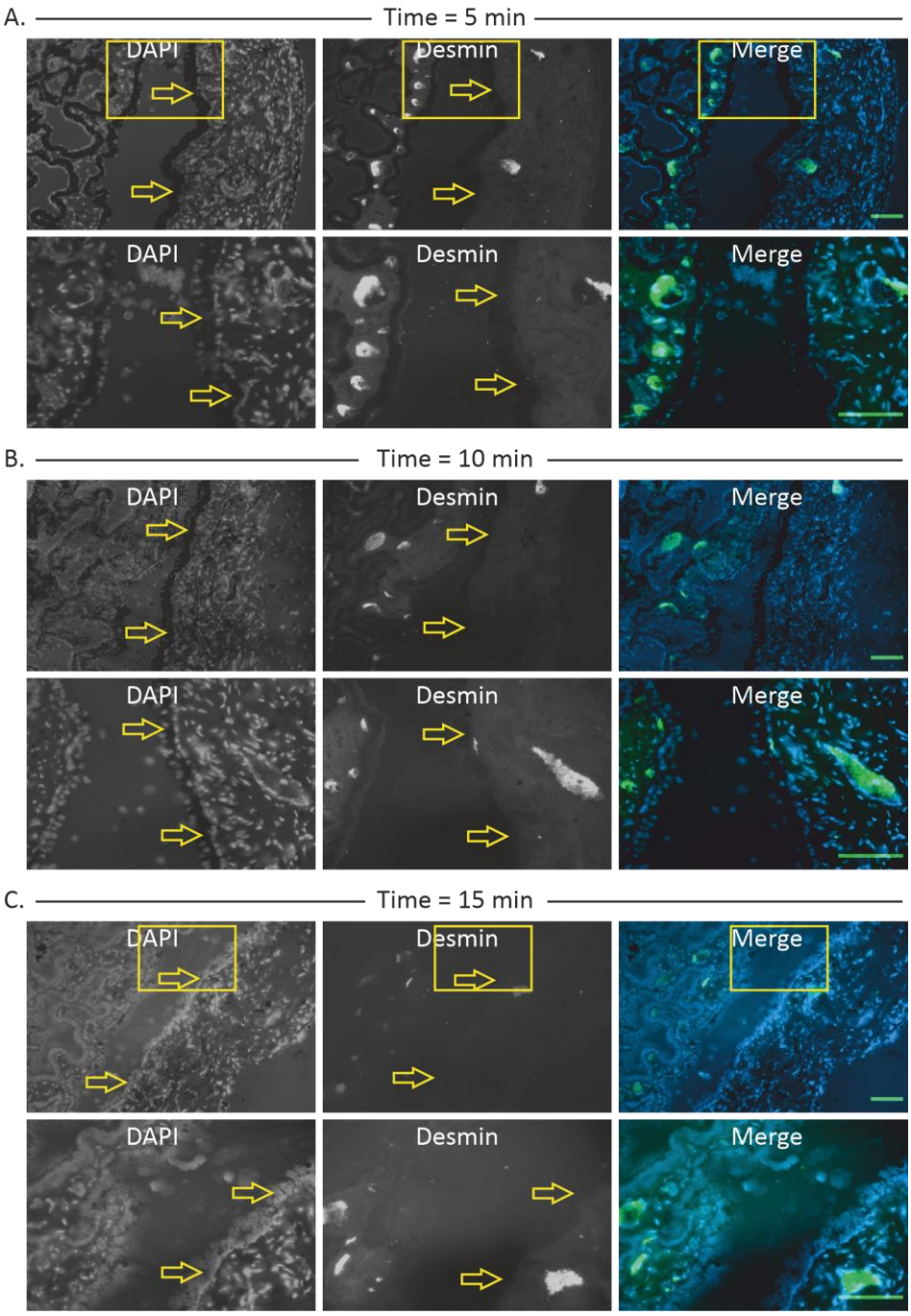

Figure 7.1: Representative pictures of porcine tissue sections depigmented in 10% H_2O_2 at 60°C. A. Sections were incubated into H2O2 for 5 min. **B.** Incubation lasted 10 min. **C.** Incubation lasted 15 min. Arrows indicate the IPE. Arrowheads indicate desmin. Yellow boxes indicate higher magnifications below. DAPI is in blue, desmin in green. Small SB = 100 µm, tall SB = 50 µm.

7.2 Appendix 2: Adjustement of the H2O2 solution

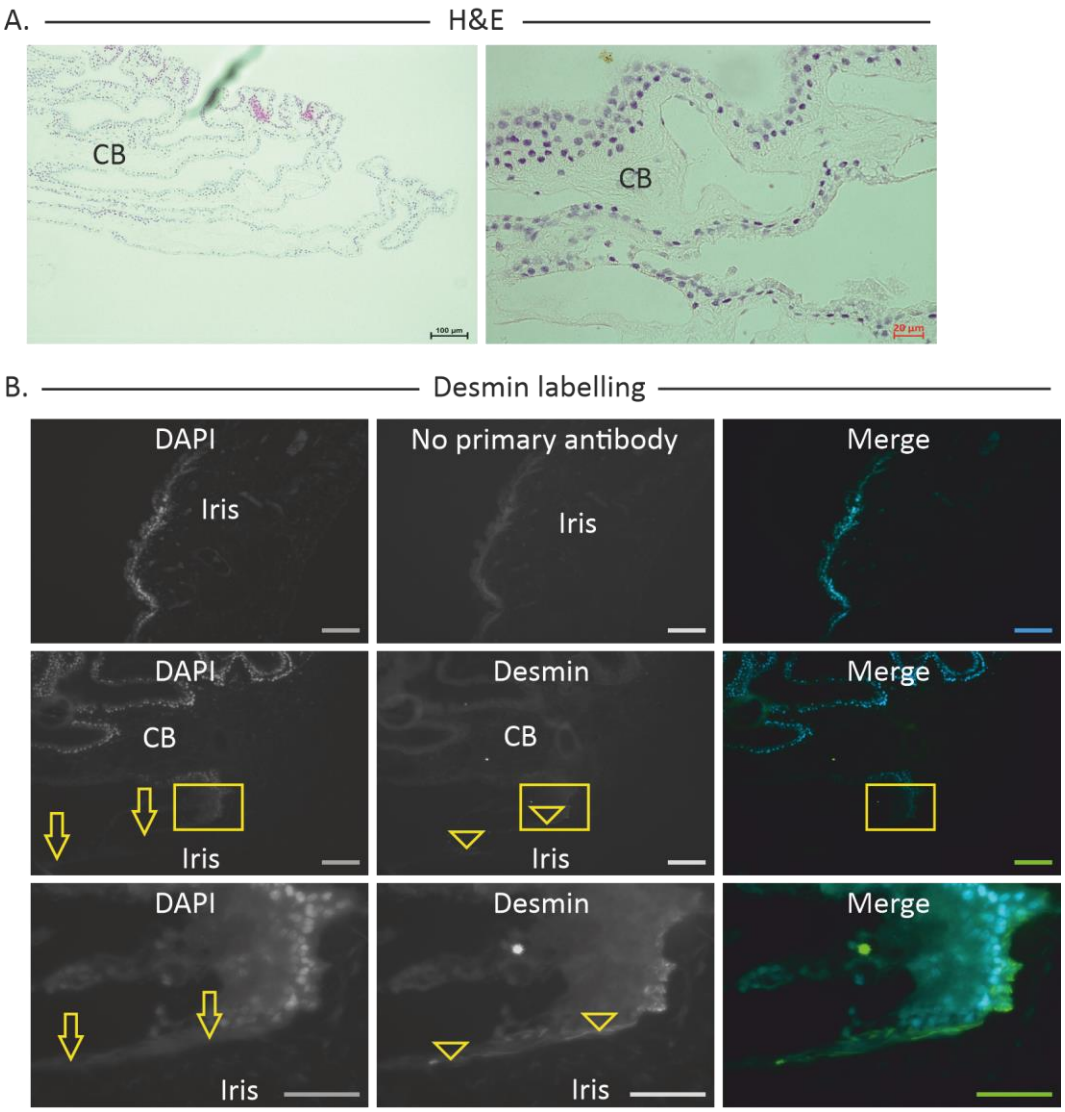

Figure 7.2: Representative pictures of porcine section depigmented in 10% H_2O_2 1% Na_2. **A.** H&E of depigmented sections. Left SB = 100 µm, right SB = 20 µm. **B.** Desmin labelling of depigmented sections. Arrows indicate the IPE, arrowheads indicate desmin. Yellow boxes indicate higher magnifications below. Small SB = 100 µm, tall SB = 50 µm.

7.3 Appendix 3: Laminin β1 and β2 in the human IPE

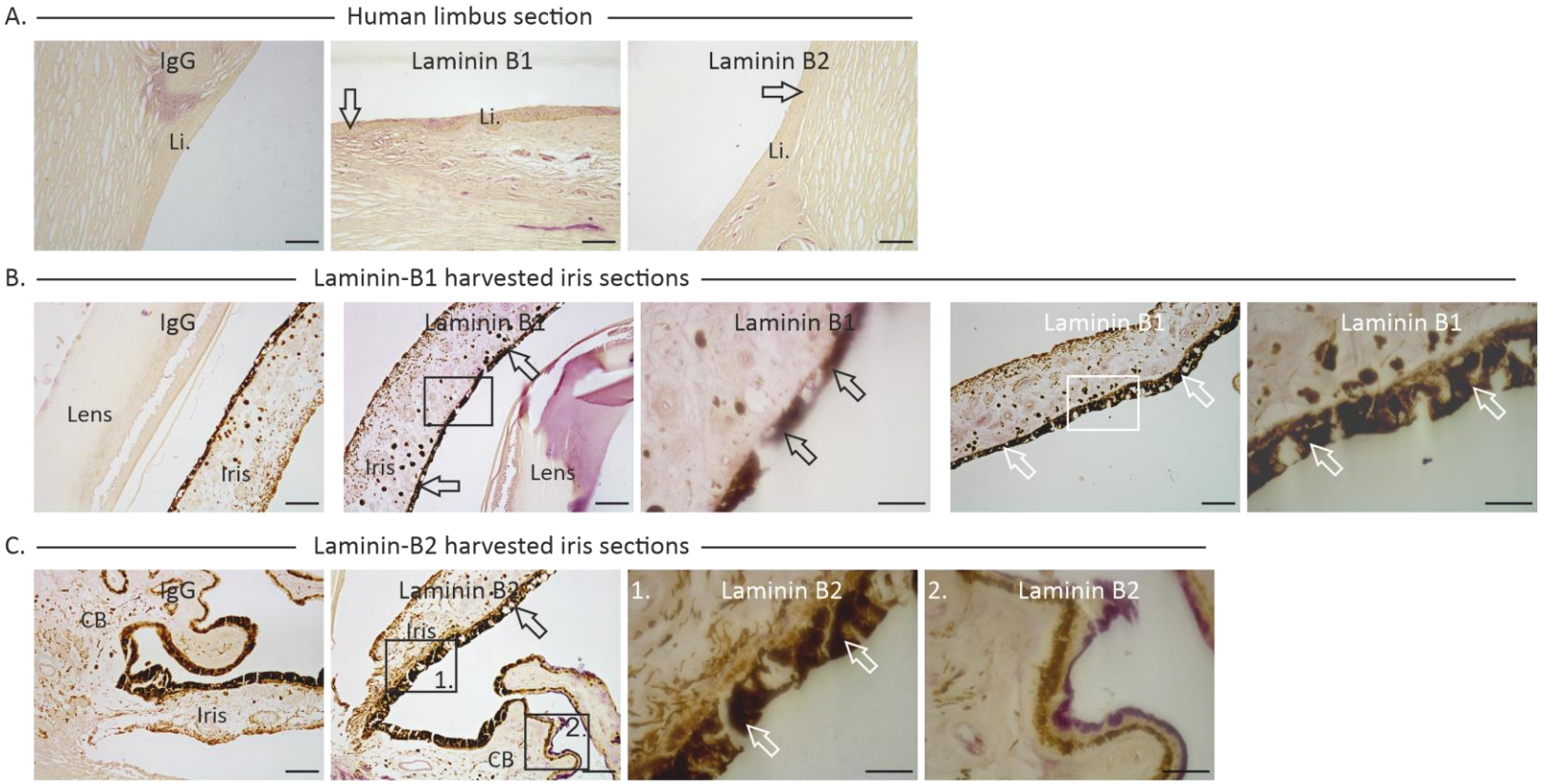

Figure 7.3: Representative pictures of Laminin B1 and laminin B2 in the human eye. A. Positive control limbus sections. Arrows indicate the corneal epithelium. **B.** Laminin B1 in iris sections. Arrows indicate the IPE, boxes indicate higher magnifications on the right. Small SB = 100 µm, tall SB = 50 µm. **C.** Laminin B2 in iris sections. Arrows indicate the IPE. Boxes indicate higher magnifications on the left. Small SB = 100 µm, tall SB = 50 µm. Li. = Limbus; CB = Ciliary body.

7.4 Appendix 4: positive control for ΔN-p63.

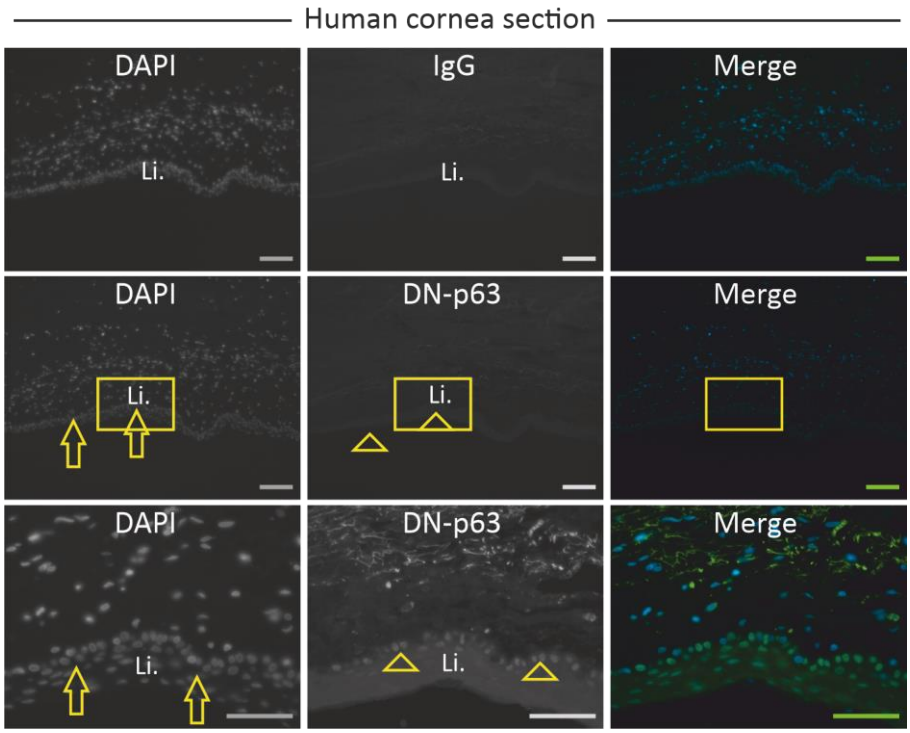

Figure 7.4: Representative pictures of human corneal sections labelled for DN-p63. Arrows indicate the corneal epithelium, arrowheads indicate ΔN-p63. Yellow boxes indicate higher magnifications below. Small SB = 100 µm, tall SB = 50 µm. Li. = Limbus.

7.5 Appendix 5: SOX2 in porcine cornea and iris sections

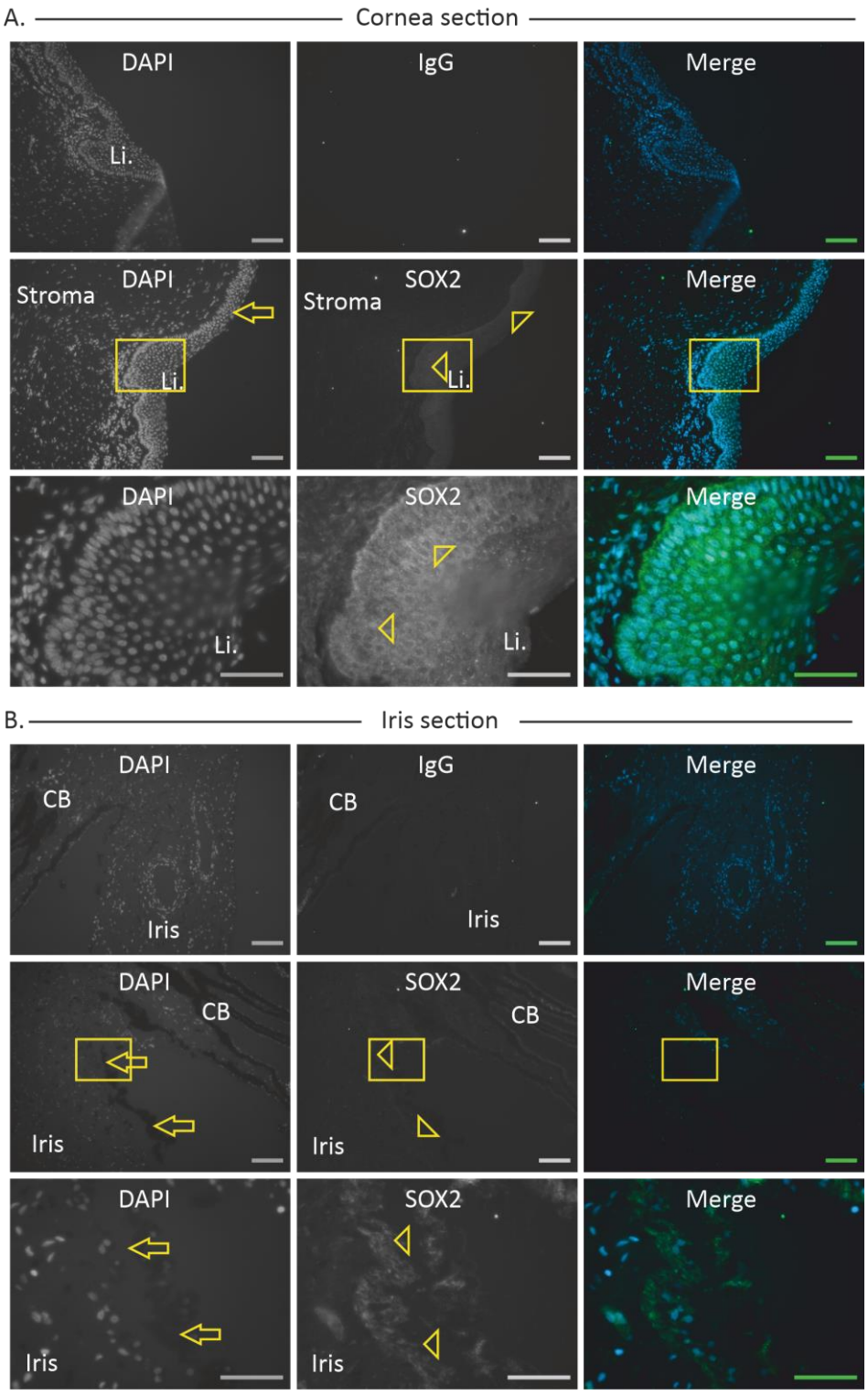

Figure 7.5: Representative pictures of SOX2-labelled cornea and iris sections. A. Cornea sections. Arrows indicate the corneal epithelium, arrowheads indicate SOX2. **B.** Iris sections. Arrows indicate the IPE, arrowheads indicate SOX2. Yellow boxes indicate higher magnifications below. Li. = limbus; CB = Ciliary body

7.6 Appendix 6: Cytokeratins in IPE cells and aggregates

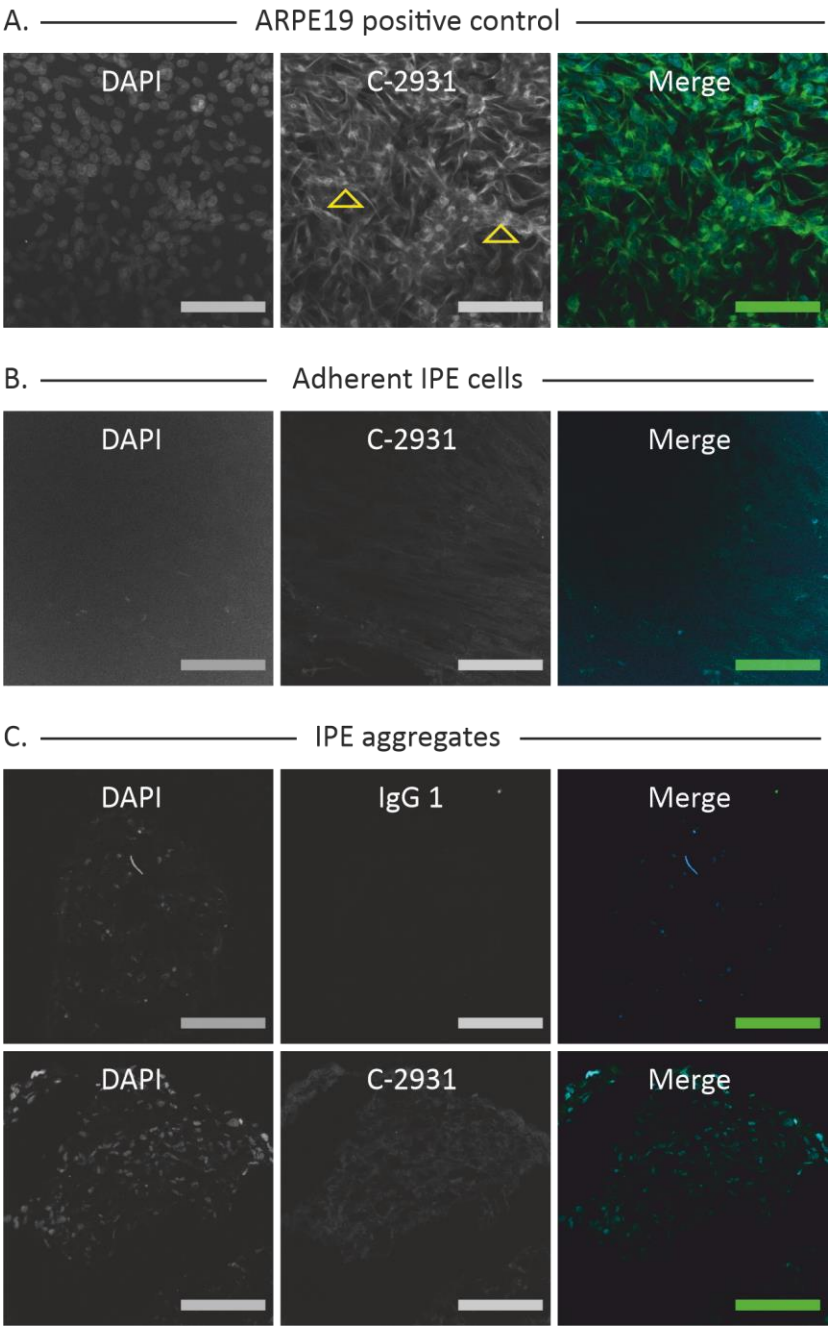

Figure 7.6: Representative pictures of aPRE19 cells, IPE cells and IPE aggregates labelled with a C-2931 pan-cytokeratin antibody. A. ARPE19 cells. Arrowheads indicate cytokeratins. **B.** IPE adherent cells. **C.** IPE aggregates. SB = 50 µm.

References

1. Wong WL, Su X, Li X, Cheung CM, Klein R, Cheng CY, Wong TY. Global prevalence of age-related macular degeneration and disease burden projection for 2020 and 2040: a systematic review and meta-analysis. Lancet Glob Health. 2014 Feb;2(2):e106-16
2. Institut national de la statistique et des études économiques. Population par âge. [Internet]. C2023 [cited 2023 Aug 11]. Available from https://www.insee.fr/fr/statistiques/4277619?sommaire=4318291
3. Oyster CW. The Human eye. 1 st ed. Sunderland: Sinauer; 1999
4. Marieb EN, Hoehn K. Anatomie et physiologie humaines. 8 th ed. Paris: Pearson Education; Pearson. 2010
5. Amin S, Jalilian E, Katz E, Frank C, Yazdanpanah G, Guaiquil VH et al. The limbal niche and regenerative strategies. Vision (Basel). 2021 Sep 22; 5(4): 43-60
6. Liu J, Li Z. Resident innate immune cells in the cornea. Front Immunol. 2021 Feb 26; 12:620284
7. Ethier CR, Johnson M, Ruberti J. Ocular biomechanics and biotransport. Annu Rev biomed Eng. 2004 Aug 15; 6: 249-73
8. Buffault J, Labbe A, Hamard P, Brignole-Baudouin F, Baudouin C. The trabecular meshwork : structure, function and clinical implications. A review of the literature. J Fr ophtalmol. 2020 Sep; 43(7): 217-230
9. Nucci C, Martucci A, Giannini C, Morrone LA, Bagetta G, Mancino R. Neuroprotective agents in the management of glaucoma. Eye (Lond). 2018 May ; 32 (5) : 938 – 45
10. Dorgaleleh S, Naghipoor K, Barahouie A, Dastaviz, Oladnabi M. Molecular and biochemical mechanisms of human iris color: a comprehensive review. J Cell Physiol. 2020 Dec; 235(12): 8972-82
11. Sturm RA, Larsson M. Genetics of human iris colour and patterns. Pigment cell melanoma res. 2009 Oct; 22(5):544-62
12. Kiel JW, Hollingsworth M, Rao R, Chen M, Reitsamer HA. Ciliary blood flow and aqueous humor production. Prog Retin Eye Res. 2011 Jan;30(1):1-17. doi: 10.1016/j.preteyeres.2010.08.001. Epub 2010 Aug 27
13. Behar-Cohen F, Gelizé E, Jonet L, Lassiaz P. Anatomie de la rétine [Anatomy of the retina]. Med Sci (Paris). 2020 Jun-Jul;36(6-7):594-599. [French]
14. Gupta MP, Herzlich AA, Sauer T, Chan CC. Retinal Anatomy and Pathology. Dev Ophthalmol. 2016;55:7-17. doi: 10.1159/000431128. Epub 2015 Oct 26
15. Milston R, Madigan MC, Sebag J. Vitreous floaters : Etiology, diagnostic, and management. Surv Ophthalmol. 2016 Mar-Apr ; 61(2) : 211-27
16. 9 Laboratoire national de Metrologie et d'Essais. Le Candela. [Internet]. c2022 [cited 2022 Nov 08]. Available from https://www.lne.fr/fr/comprendre/systeme-international%20unites/candela
17. Hawking S. Une breve histoire du temps. Du big bang aux trous noirs. 1 st ed. New York: Flammarion; 1987 [French]
18. Laboratoire national de Metrologie et d'Essais. Le Metre. [Internet]. c2022 [cited 2022 Nov 08]. Available from https://www.lne.fr/fr/comprendre/systeme-international-unites/metre
19. Leszczynski B, Sojka-Leszczynska P, Wojtysiak D, Wrobel A, Pedrys R. Visualisation of porcine eye anatomy by X-ray microtomography. Exp Eye Res. 2018 Feb; 167:51-55
20. McMenamin PG, Steptoe RJ. Normal anatomy of the aqueous humour outflow system in the domestic pig eye. J Anat. 1991 Oct; 178:65-77
21. Olsen TW, Sanderson S, Feng X, Hubbard WC. Porcine sclera: thickness and surface area. Invest Ophthalmol Vis Sci. 2002 Aug; 43(8); 2529-32

22. Sanchez I, Martin R, Ussa F, Fernandez-Bueno I. The parameters of the porcine eyeball. Graefes Arch Clin Exp Ophthalmol. 2011 Apr ; 249(4) : 475-82
23. Augusteyn RC, Mohammed A. Biometry of the human cornea and globe : an evaluation by age, gender and population. Exp Eye Res. 2022 Mar ; 216
24. Menduni F, Davies LN, Madrid-Costa D, Fratini A, Wolffsohn JS. Characterisation of the porcine eyeball as an in vitro model for dry eye. Cont Lens Anterior Eye. 2018 Feb; 41(1): 13-17
25. Leung CK, Li H, Weinreb RN, Liu J, Cheung CY, Lai RY, Pang CP, Lam DS. Anterior chamber angle measurement with anterior segment optical coherence tomography : a comparison between slit lamp OCT. Invest Ophthalmol Vis Sci. 2008 Aug ; 49(8) : 3469-74
26. Asejczyk-Widlicka M, Schachar RA, Pierscionek BK. Optical coherence tomography measurements of the fresh porcine eye and response of the outer coats of the eye to volume increase. J Biomed Opt. 2008 Mar-Apr; 13(2): 024002
27. Whitcomb JE, Amini R, Simha NK, Barocas VH. Anterior-posterior asymmetry in iris mechanics measured by indentation. Exp Eye Res. 2011 Oct; 93(4): 475-81
28. Santaella RM, Destafeno JJ, Stinnet SS, Proia AD, Chang DF, Kim T. The effect of alpha1-adrenergic receptor antagonist tamsulosin (Flomax) on iris dilator smooth muscle anatomy. Ophthalmology. 2010 Sep; 117(9): 1743-49
29. Diehl DL, Robin AL, Wand M. The influence of iris pigmentation on the miotic effect of thymoxamine. Am J ophthalmol. 1991 Mar 15; 111(3); 351-51
30. Mohamed A, Nandyala S, Ho A, Manns F, Parel JA, Augusteyn RC. Relationship of the cornea and globe dimensions to the changes in adult human crystalline lens diameter, thickness and power with age. Exp eye Res. 2021 Aug; 209: 108653
31. Miesfeld JB, Brown NL. Eye organogenesis: a hierarchical view of ocular development. Curr Top Dev Biol. 2019; 132: 351-393
32. Freddo TF. Ultrastructure of the iris. Microsc Res Tech. 1996 Apr 1; 33(5): 369-89
33. Freddo TF. Intercellular junctions of the iris epithelia in Macaca mulatta. Inest Ophthalmol Vis Sci. 1984 Sep; 25(9): 1094-104
34. Cunha-Vaz J. The blood-ocular barriers. Surv Ophthalmol. 1979 Mar-Apr ; 23 (5) : 279-96
35. Embryologie humaine. Embryogénèse. [Internet]. c2023 [cited 2023 Aug]. Available from https://embryology.ch/fr/embryogenese/disque-embryonnaire/
36. Gerri C, Menchero S, Mahadevaiah SK, Turner JMA, Niakan KK. Human embryogenesis : a comparative perspective. Annu Rev Cell Dev Biol. 2020 Oct 6 ; 36 : 411-40
37. Augusteyn RC. On the growth and internal structure of the human lens. Exp Eye Res. 2010 Jun; 90(6): 643-54
38. Graw J. Eye development. Curr Top Dev Biol. 2010; 90: 343-86
39. Lutty GA, McLeod DS. Development of the hyaloid, choroidal and retinal vasculatures in the fetal human eye. Prog Retin Eye Res. 2018 Jan; 62: 58-76
40. Centanin L, Wittbrodt J. Retinal neurogenesis. Development. 2014 Jan; 141(2): 241-44
41. Aldiri I, Xu B, Wang L, Chen X, Hiler D, Griffiths L et al; St. Jude Children's Research Hospital – Washington university Pediatric Cancer Genome Project. The dynamic epigenetic landscape of the retina during development, reprogramming and tumorigenesis. Neuron. 2017 May 3; 94(3): 550-68
42. Hoshino A, Ratnapriya R, Brooks MJ, Chaitankar V, Wilken MS, Zhang C et al. Molecular anatomy of the developing human retina. Dev Cell. 2017 Dec 18; 43(6): 763-79
43. Bumsted KM, Barnstable CJ. Dorsal retinal pigment epithelium differentiates as neural retina in the microphthalmia (mi/mi) mouse. Invest Ophthalmol Vis Sci. 2000 Mar; 41(3): 903-08
44. Rowan S, Chen CM, Young TL, Fisher DE, Cepko CL. Transdifferentiation of the retina into pigmented cells in ocular retardation mice defines a new function of the homeodomain gene Chx10. Development. 2004 Oct; 131(20): 5139-52
45. Nguyen M, Arnheiter H. Signaling and transcriptional regulation in early mammalian eye development: a link between FGF and MITF. Development. 2000 Aug; 127(16): 3581-91

46. Bharti K, Nguyen MT, Skuntz S, Bertuzzi S, Arnheiter H. The other pigment cell: specification and development of the pigmented epithelium of the vertebrate eye. Pigment cell res. 2006 Oct; 19(5): 380-94
47. Peces-Pena MD, de la Cuandra-Blanco C, Vicente A, Merida-Velasco JR. Development of the ciliary body: morphological changes in the distal portion of the optic cup in the human. Cells Tissues Organs. 2013; 198(2): 149-59
48. .Cvekl A, Tamm ER. Anterior eye development and ocular mesenchyme: new insights from mouse models and human diseases. Bioessays. 2004 Apr; 26(4): 374-86
49. Uusitalo M, Kivela T. Development of cytoskeleton in neuroectodermally derived epithelial and muscle cells of the human eye. Invest Ophthalmol Vis sci. 1995 Dec; 36(13): 2584-91
50. The multi-dimensional human embryo. Cargenie stage. [Internet]. c2023 [cited 2023 Aug]. Available from https://embryo.stamps.umich.edu/carnStages/carnStages.html
51. Strauss O. The retinal pigment epithelium in visual function. Physiol Rev. 2005 Jul; 85(3): 845-81
52. Whitmore SS, Sohn EH, Chirco KR, Drack AV, Stone EM, Tucker BA et al. Complement activation and choriocapillaris loss in early AMD: implications for pathophysiology and therapy. Prog Retin Eye Res. 2015 Mar; 45: 1-29
53. Chowers G, Cohen M, Marks-Ohana D, Stika S, Eijzenberg A, Banin E et al. Course of sodium iodate-induced retinal degeneration in albino and pigmented mice. Invest Ophthalmol Vis Sci. 2017 Apr 1; 58(4); 2239-49
54. Coleman HR, Chan CC, Ferris FL 3rd, Chew EY. Age-related macular degeneration. Lancet. 2008 Nov 22; 372(9652): 1835-45
55. Ramanoel S, Chokron S, Hera R, Kauffman L, Chiquet C, Krainik A et al. Age-related macular degeneration changes the processing of visual scenes in the brain. Vis Neurosci. 2018 Jan; 35: E006
56. Nowak JZ. Age-related macular degeneration: pathogenesis and therapy. Pharmacol rep. 2006 May-Jun; 58(3): 353-63
57. Homayouni M. Vascular endothelial growth factors and their inhibitors in ocular neovascular disorders. J Ophthalmic Vis res. 2009 Apr; 4(2): 105-14
58. Thomas CJ, Mirza RG, Gill MK. Age-related macular degeneration. Med Clin North Am. 2021 May; 105(3): 473-91
59. Murali A, Krishnakumar S, Subramanian A, Parameswaran S. Bruch's membrane pathology: a mechanistic perspective. Eur J Ophthalmol. 2020 Nov; 30(6): 1195-1206
60. Armento A, Ueffing M, Clark SJ. The complement system in age-related macular degeneration. Cell Mol Life Sci. 2021 May; 78(10): 4487-505
61. Sparrow JR, Boulton M. RPE lipofuscin and its role in retinal pathobiology. Exp Eye Res. 2005 May;80(5):595-606.
62. Bergen AA, Arya S, Koster C, Pilgrim MG, Wiatrek-Moumoulidis D, van der Spek PJ, Hauck SM, Boon CJF, Emri E, Stewart AJ, Lengyel I. On the origin of proteins in human drusen: The meet, greet and stick hypothesis. Prog Retin Eye Res. 2019 May;70:55-84.
63. Crabb JW. The proteomics of drusen. Cold Spring Harb Perspect Med. 2014 May 5;4(7)
64. Viedma-Poyatos Á, González-Jiménez P, Langlois O, Company-Marín I, Spickett CM, Pérez-Sala D. Protein Lipoxidation: Basic Concepts and Emerging Roles. Antioxidants (Basel). 2021 Feb 16;10(2):295.
65. Gillery P. Produits avancés de glycation (AGE), radicaux libres et diabète [Advanced glycation end products (AGEs), free radicals and diabetes]. J Soc Biol. 2001;195(4):387-90. [French]
66. Tarau IS, Berlin A, Curcio CA, Ach T. The Cytoskeleton of the Retinal Pigment Epithelium: from Normal Aging to Age-Related Macular Degeneration. Int J Mol Sci. 2019 Jul 22;20(14):3578
67. Shen JK, Dong A, Hackett SF, Bell WR, Green WR, Campochiaro PA. Oxidative damage in age-related macular degeneration. Histol Histopathol. 2007 Dec;22(12):1301-8

68. 42 Klein RJ, Zeiss C, Chew EY, Tsai JY, Sackler RS, Haynes C et al. Complement factor H polymorphism in age-related macular degeneration. Science. 2005 Apr 15; 308(5720): 385-89
69. Rodríguez de Córdoba S, Esparza-Gordillo J, Goicoechea de Jorge E, Lopez-Trascasa M, Sánchez-Corral P. The human complement factor H: functional roles, genetic variations and disease associations. Mol Immunol. 2004 Jun;41(4):355-67.
70. Toomey CB, Johnson LV, Bowes Rickman C. Complement factor H in AMD: Bridging genetic associations and pathobiology. Prog Retin Eye Res. 2018 Jan;62:38-57
71. Fleckenstein M, Mitchell P, Freund KB, Sadda S, Holz FG, Brittain C et al. The progression of geographic atrophy secondary to age-related macular degeneration. Ophthalmology. 2018 Mar; 125(3): 369-90
72. Mazzoni F, Safa H, Finnemann SC. Understanding photoreceptor outer segment phagocytosis: use and utility of RPE cells in culture. Exp Eye Res. 2014 Sep;126:51-60
73. Masland RH. The neuronal organization of the retina. Neuron. 2012 Oct 18;76(2):266-80
74. Al-Zamil WM, Yassin SA. Recent developments in age-related macular degeneration: a review. Clin Interv Aging. 2017 Aug 22; 12: 1313-30
75. Fleckenstein M, Keenan TDL, Guymer RH, Chakravarthy U, Schmitz-Valckenberg S, Klaver CC et al. Age-related macular degeneration. Nat Rev Dis Primers. 2021 May 6; 7(1): 31
76. Rudnicka AR, Kapetanakis VV, Jarrar Z, Wathern AK, Wormald R, Fletcher AE et al. Incidence of late-stage age-related macular degeneration in American whites: systematic review and meta-analysis. Am J Ophthalmol. 2015 Jul; 160(1): 85-93
77. Rudnika AR, Jarrar Z, Wormald R, Cook DG, Fletcher A, Owen CG. Age and gender variations in age-related macular degeneration in populations of European ancestry: a meta-analysis. Ophthalmology. 2012 Mar; 119(3); 571-80
78. Sobrin L, Seddon JM. Nature and nurture- genes and environment- predict onset and progression of macular degeneration. Prog Retin Eye Res. 2014 May; 40: 1-15
79. Myers CE, Klein BE, Gangnon R, Sivakumaran TA, Lyengar SK, Klein R. Cigarette smoking and the natural history of age-related macular degeneration: the Beaver Dam eye study. Ophthalmology. 2014 Oct; 121(10): 1949-55
80. Wang JJ, Klein R, Smith W, Klein BE, Tomany S, Mitchell P. Cataract surgery and the 5-year incidence of late-stage age-related maculopathy: pooled findings from the Beaver dam and blue mountains eye studies. Ophthalmology. 2003 Oct; 100(10); 1960-67
81. Van der Schaft TL, Mooy CM, de Brujin WC, Mulder PG, Pameyer JH, de Jong PT. Increased prevalence of disciform macular degeneration after cataract extraction with implantation of an intraocular lens. Br J Ophthalmol. 1994 Jun; 78(6): 441-45
82. Seddon JM, Cote J, Page WF, Aggen SH, Neale MC. The US twin study of age-related macular degeneration: relative roles of genetic and environmental influences. Arch Ophthalmol. 2005 Ma; 123(3): 321-27
83. Klein RJ, Zeiss C, Chew EY, Tsai JY, Sackler RS, Haynes C et al. Complement factor H polymorphism in age-related macular degeneration. Science. 2005 Apr 15; 308(5720): 385-89
84. Rivera A, Fisher SA, Fritsche LG, Keilhauer CN, Lichtner P, Meitinger T et al. Hypothetical LOC387715 is a second major susceptibility gene for age-related macular degeneration contributing independently of complement factor H to disease risk. Hum Mol genet. 2005 Nov 1; 14(21): 3227-36
85. Adams MK, Simpson JA, Aung KZ, Makeyeva GA, Giles GG, English DR et al. Abdominal obesity and age-related macular degeneration. Am J Epidemiol. 2011 Jun 1; 173(11): 1246-55
86. Schaumberg DA, Christen WG, Hankinson SE, Glynn RJ. Body mass index and the incidence of visually significant age-related maculopathy in men. Arch Ophthalmol. 2001 Sep; 119(9): 1259-65

87. Rastogi N, Smith RT. Association of age-related macular degeneration and reticular macular disease with cardiovascular disease. Surv Ophthalmol. 2016 Jul-Aug; 61(4): 422-33
88. Wang T, Xia J, Yuan M, Wu X, Zhu Y, Chen C et al. Hypertension affects the treatment of wet age-related macular degeneration. Acta Ophthalmol. 2021 Dec; 99(8): 871-76
89. Klein R, Cruickshanks KJ, Myers CE, Sivakumaran TA, Iyengar SK, Meuer SM et al. The relationship of artherosclerosis to the 10-year cumulative incidence of age-related macular degeneration: the Beaver Dam studies. Ophthalmology. 2013 May; 120(5): 1012-19
90. Zhang W, Liu H, Al-Shabrawey M, Cardwell RW, Caldwell RB. Inflammation and diabetic retinal microvascular complications. J Cardiovasc Dis Res. 2011 Apr; 2(2): 96-103
91. Heersterbeek TJ, Lores-Motta L, Hoyng CB, Lechanteur YTE, den Hollander AI. Risk factors for progression of age-related macular degeneration. Ophthalmic Physiol Opt. 2020 Mar; 40(2): 140-70
92. Khan JC, Shadid H, Thurlby DA, Bradley M, Clayton DG, Moore AT et al. Age-related macular degeneration and sun exposure, iris colour, and skin sensitivity to sunlight. Br J Ophthalmol. 2006 Jan; 90(1): 29-32
93. Mitchell P, Liew G, Gopinath B, Wong TY. Age-related macular degeneration. Lancet. 2018 Sep 29; 392(10153): 1147-59
94. Ferris FL 3rd, Wilkinson CP, Bird A, Chakravarthy U, Chew E, Csaky K et al. Clinical classification of age-related macular degeneration. Ophthalmology. 2013 Apr; 120(4): 844-51
95. Bord AC, Bressler NM, Bressler SB, Chisholm IH, Coscas G, Davis MD et al. An international classification and grading system for age-related maculopathy and age-related macular degeneration. The international ARM epidemiological study group. Surv Ophthalmol. 1995 Mar-Apr; 39(5): 367-74
96. Macular Society. Diagnosing macular disease. [Internet]. c2023 [cited 2023 Aug]. Available from https://www.macularsociety.org/diagnosis-treatment/how/
97. Taylor C. Digital ophthalmoscopy ; through a non-specialist lens. Future Healthc J. 2021 Mar ; 8 (1)
98. Bouma BE, de Boer JF, Huang D, Jang IK, Yonestu T, Leggett CL, Leitgeb R, Sampson DD, Suter M, Vakoc B, Villiger M, Wojtkowski M. Optical coherence tomography. Nat Rev Methods Primers. 2022 ; 2 : 79
99. Cavallerano AA. Ophthalmic fluorescein angiography. Optom Clin. 1996 ; 5(1) : 1-23
100. Campochiaro PA, Nguyen QD, Shah SM, Klein ML, Holz E, Frank RN et al. Adenoviral vectordelivered pigment epithelium-derived factor for neovascular age-related macular degeneration: results of a phase I clinical trial. Hum Gene Ther. 2006. feb; 17(2): 167-76
101. Vessey KA, Ho T, Jobling Al, Mills SA, Tran MX, Brandli A et al. Nanosecond laser treatment for age-related macular degeneration does not induce focal vision loss or new vessel growth in the retina. Invest Ophthalmol Vis Sci. 2018 Feb 1; 59(2): 731-45
102. Parodi MB, Virgili G, Evans JR. Laser treatment of drusen to prevent progression to advanced age-related macular degeneration. Cochrane Database Syst Rev. 2009 Jul 8; (3): CD006537
103. Dorin G. Evolution of retinal laser therapy: minimum intensity photocoagulation (MIP). Can the laser heal the retina without harming it? Semin Ophthalmol. 2004 Mar-Jun; 19(1-2): 62-68
104. Wood JP, Shibeeb O, Plunkett M, Casson RJ, Chidlow G. Retinal damage profiles and neuronal effects of laser treatment: comparison of a conventional photocoagulator and a novel 3-nanosecond pulse laser. Invest Ophthalmol Vis Sci. 2013 mar 28; 54(3): 2305-18
105. Zhang JJ, Sun Y, Hussain AA, Marshall J. Laser-mediated activation of human retinal pigment epithelial cells and concomitant release of matrix metalloproteinases. Invest Ophthalmol Vis Sci. 2012 17; 53(6): 2928-37

106. Wong D, Lois N. Foveal relocation by redistribution of the neurosensory retina. Br J Ophthalmol. 2000 Apr; 84(4): 352-57
107. Stanga P, Hiscott P, Li K, Wong D. Macular relocation after photodynamic therapy for recurrent choroidal neovascular membrane: visual results and histopathological findings. Br J Ophthalmol. 2003 Aug; 87(8): 975-76
108. Wong D, Stanga P, Briggs M, Lenfestey P, Lancaster E, Li KK et al. Case selection in macular relocation surgery for age-related macular degeneration. Br J ophthalmol. 2004 feb: 88(2): 186-90
109. Lien S, Lowman HB. Therapeutic anti-VEGF antibodies. Handb Exp Pharmacol. 2008; (181): 131-50
110. Parravano M, Costanzo E, Scondotto G, Trifiro G, Virgili G. Anti-VEGF and other novel therapies for neovascular age-related macular degeneration: an update. BioDrugs. 2021 Nov; 35(6): 673-92
111. Sarao V, Veritti D, Boscia F, Lanzetta P. Intravitral steroids for the treatment of retinal diseases. Scientific World Journal. 2014 Jan 8; 2014: 989501
112. Mozetic V, Pacheco RL, Latorraca COC. Lee FCYO, Gomes JVB, Riera R. What do Cochrane systematic reviews say about interventions for age-related macular degeneration? Sao Paulo Med J. 2019 Nov-Dec; 137(6): 530-42
113. Ammar MJ, Hsu J, Chiang A, Ho AC, Regillo CD. Age-related macular degeneration therapy: a review. Curr Opin Ophthalmol. 2020 May; 31(3): 215-21
114. Khanani AM, Thomas MJ, Aziz AA, Weng C'Y, Danzig CJ, Yiu G et al. reviez of gene therapies for age-related macular degeneration. Eye (Long). 2022 Feb; 36(2): 303-11
115. Rizzolo LJ, Nasonkin IO, Adelman RA. Retinal Cell Transplantation, Biomaterials, and In Vitro Models for Developing Next-generation Therapies of Age-related Macular Degeneration. Stem Cells Transl Med. 2022 Mar 31;11(3):269-281
116. Gragoudas ES, Adamis AP, Cunningham ET Jr, Feinsod M, Guyer DR; VEGF inhibition study in Ocular neovascularisation clinical trial group. Pegaptanib for neovascular age-related macular degeneration. N Engl J Med. 2004 Dec 30; 351(27): 2805-16
117. Tadayoni R, Sararols L, Weissgerber G, Verma R, Clemens A, Holz FG. Brolucizumab: a newly developed anti-VEGF molecule for the treatment of neovascular age-related macular degeneration. Ophthalmologica. 2021; 244(2): 93-101
118. Nicolo M, Ferro Desideri L, Vagge A, Traverso CE. Faricimab: an investigational agent targeting the Tie-2/angiopoietin pathway and VEGF-A for the treatment of retinal diseases. Expert opin Investig Drugs. 2021 Mar; 30(3): 193-200
119. Shirley M. Faricimab: first approval. Drugs. 2022 May; 82(7): 825-30
120. Flood MT, Gouras P, Kjeldbye H. Growth characteristics and ultrastructure of human retinal pigment epithelium in vitro. Invest Ophthalmol Vis Sci. 1980 Nov; 19(11): 1309-20
121. Boulton ME, Marshall J, Mellerio J. Human retinal pigment epithelial cells in tissue culture: a means of studying inherited retinal diseases. Birth Defects Orig Artic Ser. 1982 18(6): 101-18
122. He S, Wang HM, Ogden TE, Ryan SJ. Transplantation of cultured human retinal pigment epithelium into rabbit subretina. Graefes Arch Clin Exp ophthalmol. 1993 Dec; 231(12): 737-42
123. Castillo BV Jr, del Cerro M, White RM, Cox C, Wyatt J, Nadiga G et al. Efficacy of nonfatal human RPE for photoreceptor rescue: a study in dystrophic RCS rats. Exp neurol. 1997 jul; 146(1): 1-9
124. da Cruz L, Chen FK, Ahmado A, Greenwood J, Coffey P. RPE transplantation and its role in retinal disease. Prog Retin Eye Res. 2007 Nov; 26(6): 598-635
125. Lund RD, Adamson P, Sauve Y, Keegan DJ, Girman SV, Wang S et al. Subretinal transplantation of genetically modified human cell lines attenuates loss of visual function in dystrophic rats. Proc Acad Sci USA. 2001 Aug 14; 98(17): 9942-47
126. Gaillard D, Sauve Y. Cell-based therapy for retinal degeneration: the promise of a cure. Vision Res. 2007 Oct; 47(22): 2815-24

127. Bruce Alberts, Alexander Johnson, Julian Lewis, Martin Raff, Keith Roberts & Peter Walter. Biologie moleculaire de la cellule. 5 th ed. Paris: Medecine Sciences Publication; 2011
128. Chatzeli L, Simons BD. Tracing the dynamics of stem cell fate. Cold Spring harb Perspect Biol. 2020 Jun 1; 12(6): a036202
129. Donati G, Watt FM. Stem cell heterogeneity and plasticity in epithelia. Cell Stem Cell. 2015 May 7; 16(5): 465-76
130. Date S, Sato T. Mini-gut organoids: reconstitution of the stem cell niche. Annu Rev Cell Dev Biol. 2015; 31: 269-89
131. Leeb C, Jurga M, McGuckin C, Forraz N, Thallinger C, Moriggl R, Kenner L. New perspectives in stem cell research: beyond embryonic stem cells. Cell Prolif. 2011 Apr;44 Suppl 1(Suppl 1):9-14
132. Zakrzewski W, Dobrzyński M, Szymonowicz M, Rybak Z. Stem cells: past, present, and future. Stem Cell Res Ther. 2019 Feb 26;10(1):68
133. Perry AR, Linch DC. The history of bone-marrow transplantation. Blood Rev. 1996 Dec;10(4):215-9
134. Gehart H, Clevers H. Tales from the crypt: new insights into intestinal stem cells. Nat Rev Gastroenterol Hepatol. 2019 Jan; 16(1): 19-34
135. Gonzales KAU, Fuchs E. Skin and Its Regenerative Powers: An Alliance between Stem Cells and Their Niche. Dev Cell. 2017 Nov 20;43(4):387-401
136. Bremond-Gignac D, Copin H, Benkhalifa M. Corneal epithelial stem cells for corneal injury. Expert Opin Biol Ther. 2018 Sep;18(9):997-1003
137. Boulton M, Dayhaw-Barker P. The role of the retinal pigment epithelium: topographical variation and ageing changes. Eye (Lond). 2001 Jun;15(Pt 3):384-9
138. Fuhrmann S, Zou C, Levine EM. Retinal pigment epithelium development, plasticity, and tissue homeostasis. Exp Eye Res. 2014 Jun; 123: 141-50
139. Boulton M.E Ageing of the retina and retinal pigment epithelium. In Holz F, Pauleikhoff D, Spaide R, Bird A. Age-related macular degeneration. 2 nd ed. Heidelberg: Springer Berlin; 2013
140. Salero E, Blenkinsop TA, Corneo B, Harris A, Rabin D, Stern JH, Temple S. Adult human RPE can be activated into a multipotent stem cell that produces mesenchymal derivatives. Cell Stem Cell. 2012 Jan 6;10(1):88-95
141. Chen F, Liu X, Chen Y, Liu JY, Lu H, Wang W, Lu X, Dean KC, Gao L, Kaplan HJ, Dean DC, Peng X, Liu Y. Sphere-induced reprogramming of RPE cells into dual-potential RPE stem-like cells. EBioMedicine. 2020 Feb;52:102618
142. Bertolotti E, Neri A, Camparini M, Macaluso C, Marigo V. Stem cells as source for retinal pigment epithelium transplantation. Prog Retin Eye Res. 2014 Sep;42:130-44
143. Pera MF, Reubinoff B, Trouson A. Human embryonic stem cells. J Cell Sci. 2000 jan; 113 (pt 1): 5-10.
144. Biswas A, Hutchins R. Embryonic stem cells. Stem cells dev. 2007 Apr; 16(2): 213-22
145. Vazin T, Freed WJ. Human embryonic stem cells: derivation, culture and differentiation; a review. Restor Neurol Neurosci. 2010; 28(4): 589-603
146. Haruta M, Sasai Y, Kawasaki H, Amemiya K, Ooto S, Kitada M et al. In vitro and in vivo characterisation of pigment epithelial cells differentiated from primate embryonic stem cells. Invest Ophthalmol Vis Sci. 2004 Mar; 45(3): 1020-5
147. Aoki H, Hara A, Nakagawa S, Motohashi T, Hirano M, Takahashi Y et al. Embryonic stem cells that differentiate into RPE cell precursors in vitro develop into RPE cell monolayers in vivo. Exp Eye Res. 2006 Feb; 82(2): 265-74
148. Leach LL, Buchholz DE, Nadar VP, Lowenstain SE, Clegg DO. Canonical/β-catenin Wnt pathway activation improves retinal pigmented epithelium derivation from human embryonic stem cells. Invest Ophthamol Vis Sci. 2015 Jan 20; 56(2): 1002-13
149. Eiraku M, Takata N, Ishibashi H, Kawada M, Sakakura E, Okuda S et al. Self-organising optic-cup morphogenesis in three-dimensional culture. Nature. 2011 Apr 7; 472(7341): 51-56

150. Buchholz DE, Pennington BO, Croze RH, Hinman CR, Coffey PJ, Clegg DO. Rapid and efficient directed differentiation of human pluripotent stem cells into retinal pigmented epithelium. Stem Cells Transl Med. 2013 May; 2(5): 384-93
151. Idelson M, Alper R, Obolensky A, Ben-Shushen E, Hemo I, Yachimovivh-Cohen N et al. Directed differentiation of human embryonic stem cells into functional retinal pigment epithelium cells. Cell Stem Cell. 2009 Oct 2; 5(4): 396-408
152. Schwartz SD, Regillo CD, Lam BL, Eliott D, Rosenfled PJ, Gregori NZ et al. Human embryonic stem cell-derived retinal pigment epithelium in patients with age-related macular degeneration and Stargardt's macular dystrophy: follow-up of two open-label phase ½ studies. Lancet. 2015 Feb 7; 385(9967): 509-16
153. da Cruz L, Fynes K, Georgiadis O, Kerby J, Luo YH, Ahmado A et al. Phase 1 clinical study of an embryonic stem cell-derived retinal pigment epithelium patch in age-related macular degeneration. Nat Biotechnol. 2018 Apr; 36(4): 328-37
154. Kashani AH, Lebkowski JS, Rahhal FM, Avery RL, Salehi-had H, Dang W et al. A bioengineered retinal pigment epithelial monolayer for advanced, dry age-related macular degeneration. Sci Transl Med. 2018 Apr; 36(4): 328-37
155. Dehghan S, Mirshahi R, Shoae-Hassani A, Naseripour M. Human-induced pluripotent stem cells-derived retinal pigmented epithelium, a new horizon for cells-based therapies for age-related macular degeneration. Stem Cell Res Ther 2022 May 26; 13(1): 217
156. Takahashi K, Yamanaka S. Induction of pluripotent stem cells from mouse embryonic and adult fibroblast cultures by defined factors. Cell. 2006 Aug 25; 126(4): 663-76
157. Takahashi K, Tanabe K, Ohnuki M, Narita M, Ichisaka T, Tomoda K et al. Induction of pluripotent stem cells from adult human fibroblasts by defined factors. Cell. 2007 Nov 30; 131(5): 861-72
158. Lister R, Pelizzola M, Kida YS, Hawkins RD, Nery JR, Hon G et al. Hotspots of aberrant epigenomic reprogramming in human induced pluripotent stem cells. Nature. 2011 Mar 3; 471(7336): 68-73
159. Ohi Y, Qin H, Hong C, Blouin L, Polo JM, Guo T et al. Incomplete DNA methylation underlies a transcriptional memory of somatic cells in human iPS cells. Nat Cell Biol. 2011 may; 13(5): 541-49
160. Yamanaka S. Induced pluripotent stem cells: past, present, and future. Cell Stem Cell. 2012 Jun 14; 10(6): 678-84
161. Newman AM, Cooper JB. Lab-specific gene expression signatures in pluripotent stem cells. Cell Stem Cell. 2010 Aug 6; 7(2): 258-62
162. Buchholz DE, Hikita ST, Rowland TJ, Friedrich AM, Hinman CR, Johnson LV et al. Derivation of functional retinal pigmented epithelium from induced pluripotent stem cells. Stem Cells. 2009 Oct; 27(10): 2427-34
163. Kamao H, Mandai M, Okamoto S, Sakai N, Suga A, Sugita S et al. Characterisation of human-induced pluripotent stem cell-derived retinal pigment epithelium cell sheets aiming for clinical application. Stem Cell Reports. 2014 jan 23; 2(2): 205-18
164. Kuroda T, Ando S, Takeno Y, Kishino A, Kimura T. Robust induction of retinal pigment epithelium cells from human induced pluripotent stem cells by inhibiting FGF/MAPK signaling. Stem Cell Res. 2019 Aug; 39: 101514
165. Makuloluwa AK, Hamill KJ, Rauz S, Bosworth L, Haneed A, Romano V et al. Biological tissues and components, and synthetic substrates for conjunctival cell transplantation. Ocul Surf. 2021 Oct; 22: 15-26
166. Mandai M, Watanabe A, Kurimoto Y, Hirami Y, Morinaga C, Daimon T et al. Autologous induced stem cell-derived retinal cells for macular degeneration. N Engl J Med. 2017 Mar 16; 376(11): 1038-46
167. Eguchi G, Shingai R. Cellular analysis on localisation of lens forming potency in the newt iris epithelium. Dev growth differ. 1971 dec; 13(4): 337-49

168. Sousounis K, Bhavsar R, Looso M, Kruger M, Beebe J, Braun T et al. Molecular signatures that correlate with induction of lens regeneration in newts: lessons from proteomic analysis. Hum genomics. 2014 Dec 11; 8(1): 22
169. Rezai KA, Kohen L, Wiedemann P, Heimann K. Iris pigment epithelium transplantation. Graefes Arch Clin Ophthalmol. 1997 Sep; 235(9): 558-62
170. Schraermer U, Kociok N, Heimann K. Rescue effects of IPE transplants in RCS rats: short-term results. Invest Ophthalmol vis sci. 1999 Jun; 40(7): 1545-56
171. Schraermeyer U, Enzmann V, Kohen L, Addicks K, Wiedemann P, Heimann K. Porcine iris pigment epithelial cells can take up retinal outer segments. Exp eye res. 1997 Aug; 65(2): 277-87
172. Thumann G, Bartz-Schmidt KU, El Bakri H, Schraermeyer U, Spee C, Cui JZ et al. Transplantation of autologous iris pigment epithelium to the subretinal space in rabbits. Transplantation. 1999 Jul 27; 68(2): 195-201
173. Crafoord S, Geng L, Seregard S, Algvere PV. Photoreceptor survival in transplantation of autologous iris pigment epithelial cells to the subretinal space. Acta Ophthalmol Scand. 2002 Aug; 80(4): 387-94
174. Abe T, Tomita H, Yoshida M, Ohashi T, Nakamura Y, Nishikawa S et al. Autologous iris pigment epithelial cell transplantation in monkey subretinal region. Curr eye res. 2000 Apr; 20(4): 268-75
175. Schraermeyer U, Kayatz P, Thumann G, Luther TT, Szurman P, Kociok N et al. Transplantation of iris pigment epithelium into the choroid slows down the degeneration of photoreceptors in the RCS rat. Graefes Arch Clin Exp Ophthalmol. 2000 Dec ; 238(12): 979-84
176. Arnhold S, Semkova I, Andressen C, Lenartz D, Meisser G, Sturm V et al. Iris pigment epithelial cells: a possible cell source for the future treatment of neurodegenerative diseases. Exp neurol. 2004 Jun; 187(2): 410-17
177. Thumann G. Development and cellular functions of the iris pigment epithelium. Surv ophthalmol. 2001 Jan-Feb; 45(4): 345-54
178. Bennis A, Ten Brink JB, Moerland PD, Heine VM, Bergen AA. Comparative gene expression study and pathway analysis of the human iris and the retinal pigment epithelium. PLoS One. 2017 Aug 21; 12(8): e182983
179. Abe T, Yoshida M, Tomita H, Kano T, Nakagawa Y, Sato M et al. Functional analysis after auto iris pigment epithelial cell transplantation in patients with age-related macular degeneration. Tohoku J exp med. 1999 Dec; 189(4): 295-305
180. Abe T, Yoshida M, Tomita H, Kano T, Sato M, Wada Y et al. Auto iris pigment epithelial cell transplantation in patients with age-related macular degeneration: short-term results. Tohoku J exp med. 2000 May; 191(1): 7-20
181. Lappas A, Weinberger AW, Foerster AM, Kube T, Rezai KA, Kirchhof B. Iris pigment epithelial cell translocation in exudative age-related macular degeneration. A pilot study in patients. Graefes arch clin exp ophthalmol. 2000 Aug; 238(8): 631-41
182. Lappas A, Foerster AM, Weinberger AW, Coburger S, Schrage NF, Kirchhof B. Translocation of iris pigment epithelium in patients with exudative age-related macular degeneration: long-term results. Graefes arch clin exp ophthalmol. 2004 Aug; 242(8): 638-47
183. Aisenbrey S, Lafaut BA, Szurman P, Hilgers RD, Esser P, Walter P et al. Iris pigment epithelial translocation in the treatment of exudative macular degeneration: a three-year follow-up. Arch ophthalmol. 2006 Feb; 124(2): 183-88
184. Kriegstein A, Alvarez-Buylla A. The glial nature of embryonic and adult neural stem cells. Annu Rev Neurosci. 2009; 32: 149-84
185. Li H, Ghazanfari R, Zacharaki D, Lim HC, Scheding S. Isolation and characterisation of primary bone marrow mesenchymal stromal cells. Ann N Y Acad Sci. 2016 Apr; 1370(1): 109-18
186. Duval K, Grover H, Han LH, Mou Y, Pegoraro AF, Fredberg J, Chen Z. Modeling Physiological Events in 2D vs. 3D Cell Culture. Physiology (Bethesda). 2017 Jul;32(4):266-277

187. Edmondson R, Broglie JJ, Adcock AF, Yang L. Three-dimensional cell culture systems and their applications in drug discovery and cell-based biosensors. Assay Drug Dev Technol. 2014 May; 12(4): 207-18
188. Chen W, Villa-Diaz LG, Sun Y, Weng S, Kim JK, Lam RH, Han L, Fan R, Krebsbach PH, Fu J. Nanotopography influences adhesion, spreading, and self-renewal of human embryonic stem cells. ACS Nano. 2012 May 22;6(5):4094-103.
189. Tibbitt MW, Anseth KS. Hydrogels as extracellular matrix mimics for 3D cell culture. Biotechnol Bioeng. 2009 Jul 1; 103(4): 655-63
190. Pastrana E, Silva-Vargas V, Doetsch F. eyes wide open: a critical review of sphereformation as an assay for stem cells. Cell Stem cell. 2011 May 6; 8(5): 486-98
191. Edmondson R, Broglie JJ, Adcock AF, Yang L. Three-dimensional cell culture systems and their applications in drug discovery and cell-based biosensors. Assay Drug Dev Technol. 2014 May;12(4):207-18
192. Taddei ML, Giannoni E, Fiaschi T, Chiarugi P. Anoikis: an emerging hallmark in health and diseases. J Pathol. 2012 Jan;226(2):380-93.
193. Rookmaaker MB, Schutgens F, Verhaar MC, Clevers H. Development and application of human stem or progenitor cell organoids. Nat Rev Nephrol. 2015 Sep; 11(9): 546-54
194. Chen H, Fu H, Wu X, Duan Y, Zhang S, Hu H et al. Regeneration of pulpo-dentinal-like complex by a group of unique multipotent CD24a+ stem cells. Sci Adv. 2020 Apr 8; 6(15): eaay1514
195. Jung P, Sato T, Merlos-Suarez A, Barriga FM, Iglesias M, Rossell D et al. Isolation and in vitro expansion of human colonic stem cells. Nat Med. 2011 Sep 4; 17(10): 1225-27
196. Nunes MC, Roy NS, Keyoung HM, Goodman RR, McKhann G, Jiang L et al. Identification and isolation of multipotential neural progenitor cells from the subcortical white matter of the adult human brain. Nat Med. 2003 Apr; 9(4): 439-47
197. Solis-Castro OO, Boissonade FM, Rivolta MN. Establishment and neural differentiation of neural crest-derived stem cells from human dental pulp in serum-free conditions. Stem Cells Transl Med. 2020 Nov; 9(11): 1462-76
198. Shaw FL, Harrison H, Spence K, Ablett MP, Simoes BM, Farnie G et al. A detailed mammosphere assay protocol for the quantification of breast stem cell activity. J Mammary Gland Biol Neoplasia. 2012 Jun; 17(2): 111-17
199. Ishiguro T, Ohata H, Sato A, Yamawaki K, Enomoto T, Okamoto K. Tumor-derived spheroids: relevance to cancer stem cells and clinical applications. Cancer Sci. 2017 Mar; 108(3): 283-89
200. Hirschhaeuser F, Menne H, Dittfeld C, West J, Mueller-Klieser W, Kunz-Schughart LA. Multicellular tumor spheroids: an underestimated tool is catching up again. J Biotechnol. 2010 Jul 1; 148(1): 3-15
201. Asami M, Sun G, Yamaguchi M, Kosaka M. Multipotent cells from mammalian iris pigment epithelium. Dev Biol. 2007 Apr 1; 304(1): 433-46
202. Sun G, Asami M, Ohta H, Kosaka J, Kosaka M. Retinal stem/progenitor properties of iris pigment epithelial cells. Dev biol. 2006 Jan 1; 289(1): 243-52
203. Hoffmann A, Nakamura K, Tsonis PA. Intrinsic lens forming potential of mouse lens epithelial versus newt iris pigment epithelial cells in three-dimensional culture. Tissue Eng Part C Methods. 2014 Feb; 20(2): 91-103
204. Dunn KC, Aotaki-Keen AE, Putkey FR, Hjelmeland LM. ARPE-19, a human retinal pigment epithelial cell line with differentiated properties. Exp Eye Res. 1996 Feb;62(2):155-69
205. Manicam C, Pitz S, Brochhausen C, Grus FH, Pfeiffer N, Gericke A. Effective melanin depigmentation of human and murine ocular tissues: an improved method for paraffin and frozen sections. PLoS One. 2014 Jul 15; 9(7): e102512
206. Kivela T, Uusitalo M. Structure, development and function of cytoskeletal elements in non-neuronal cells of the human eye. Prog Retin Eye Res. 1998 Jul; 17(3): 385-428

207. Kivela T, Fuchs U, Tarkkanen A. Cytoskeleton in neuroectodermally-derived epithelial and muscle cells of the human iris and ciliary body. J Histochem Cytochem. 1992 Oct; 40(10): 1517-26
208. Shi SR, Imam SA, Young L, Cote RJ, Taylor CR. Antigen retrieval immunohistochemistry under the influence of pH using monoclonal antibodies. J Histochem Cytochem. 1995 feb; 43(2): 193-201
209. Franke WW, Schmid E, Osborn M, Weber K. Different intermediate-sized filaments distinguished by immunofluorescence microscopy. Proc Natl Acad Sci USA. 1978 Oct; 75(10): 5034-38
210. Danielsson F, Peterson MK, Caldeira Araujo H, Lautenschlager F, Gad AKB. Vimentin diversity in health and disease. Cells. 2018 Sep 21; 7(10): 147
211. Eliasmaziah Alice. Report for advance material for tissue engineering project. Internal unpublished report. 2017
212. Takahashi H, Tajima K, Hattori T, Yamanaka N, Ito N, Goto H. Novel primary epithelial cell toxicity assay using porcine corneal explants. Cornea. 2015 May; 34(5): 597-75
213. Mignone JL, Kukekov V, Chiang AS, Steindler D, Enikolopov G. Neural Stem and progenitor cells in nestin-GFP transgenic mice. J Comp Neurol. 2004 Feb 9; 469(3): 311-24
214. Steinert PM, Chou YH, Prahlad V, Parry DA, Marekov LN, Wu KC et al. A high molecular weigth intermediate filament-associated protein in BHK-21 cells is nestin, a type VI intermediate filament protein. Limited co-assembly in vitro to form heteropolymers with type III vimentin and type IV alpha-internexin. J Biol Chem. 1999 Apr 2; 274(14): 9881-90
215. Herrman H, Aebi U. Intermediate filaments and their associates: multi-talented structural elements specifying cytoarchitecture and cytodynamics. Curr Opin Cell Biol. 2000 Feb; 12(1): 79-90
216. Velle KB, Fritz-Laylin LK. Diversity and evolution of actin-dependant phenotypes. Curr Opin Genet Dev. 2019 Oct; 58-59: 40-48
217. Ricard-Blum S. The collagen family. Cold Spring Harb Perspect Biol. 2011 Jan 1; 3(1): a004978
218. Yurchenco PD, Patton BL. Developmental and pathogenic mechanisms of basement membrane assembly. Curr Pharm Des. 2009; 15(12): 1277-94
219. Aumailley M. The laminin family. Cell Adh Migr. 2013 Jan-Feb; 7(1): 48-55
220. Ichikawa-Tomikawa N, Ogawa J, Douet V, Xu Z, Kamikubo Y, Sakurai T et al. Laminin-α1 is essential for mouse cerebellar development. Matrix Biol. 2012 Jan; 31(1): 17-28
221. Polisetti N, Sorikin L, Okumura N, Koizumi N, Kinoshita S, Kruse FE et al. Laminin-511 and -521-based matrices for efficient ex vivo-expansion of human limbal epithelial progenitor cells. Sci Rep. 2017 Jul 11; 7(1): 5152
222. Iriyama S, Yasuda M, Nishikawa S, Takai E, Hosoi J, Amano S. Decrease of laminin-511 in the basement membrane due to photoaging reduces epidermal stem/progenitor cells. Sci Rep. 2020 Jul 28; 10(1): 12592
223. Scarpellini C, Ramos Llorca A, Lanthier C, Klejborowska G, Augustyns K. The potential role of regulated cell death in dry eye diseases and ocular surface dysfunction. Int J Mol Sci. 2023 Jan 1; 24(1): 731
224. Hayashi R, Yamato M, Sugiyama H, Sumide T, Yang J, Okano T et al. N-cadherin is expressed by putative stem/progenitor cells and melanocytes in the human limbal epithelial stem cell niche. Stem Cells. 2007 Feb; 25(2): 289-96
225. Zihni C, Mills C, Matter K, Balda MS. Tight junctions: from simple barriers to multifunctional molecular gates. Nat Rev Mol Cell Biol. 2016 Sep; 17(9): 564-80
226. Di Girolamo N. Moving epithelia: tracking the fate of mammalian limbal epithelial stem cells. Prog Retin Eye res. 2015 Sep; 48: 203-25
227. Yeung AM, Tint NL, Kulkarni BB, Mohammed I, Suleman H, Hopkinson A et al. Infant limbus: an immunohistochemistry study. Exp Eye Res. 2009 Jun; 88(6): 1161-64
228. Pellegrini G, Dellambra E, Golisoni O, Martinelli E, Fantozzi I, Bondanza S et al. P63 identifies keratinocyte stem cells. Proc Natl Acad Sci USA. 2001 Mar 13; 98(6): 3516-61

229. Bhattacharya S, Serror L, Nir E, Dhiraj D, Altshuler A, Khreish M et al. SOX2 regulates P63 and stem/progenitor cell state in the corneal epithelium. Stem Cells. 2019 Mar; 37(3): 417-29
230. Riley PA. Melanin. Int J Biochem Cell Biol. 1997 Nov; 29(11): 1235-39
231. Brenner M, Hearing VJ. The protective role of melanin against UV damage in human skin. Photochem Photobiol. 2008 May-Jun; 84(3): 539-49
232. Meredith P, Sarna T. The physical and chemical properties of eumelanin. Pigment Cell Res. 2006 Dec; 19(6): 572-94
233. Larson K, Ho HH, Anumolu PL, Chen TM. Hematoxylin and eosin tissue stain in Mohs micrographic surgery: a review. Dermatol Surg. 2011 Aug; 37(8): 1089-99
234. Chan JK. The wonderful colors of the hematoxylin-eosin stain in diagnostic surgical pathology. Int J Surg Pathol. 2014 Feb; 22(1): 12-32
235. Liu CH, Lin CH, Tsai MJ, Chen WT, Chai CY, Huang YC et al. Melanin bleaching with dilute hydrogen peroxide: a simple and rapid method. Appl Immunohistochem Mol Morphol. 2013 May; 21(3): 275-9
236. Werner M, Chott A, Fabiano A, Battifora H. Effect of formalin tissue fixation and processing on immunohistochemistry. Am J Surg Pathol. 2000 jul; 24(7): 1016-19
237. Wickert U, Mucke N, Wedig T, Muller SA, Aebi U, Herrmann H. Characterisation of the intermediate filament proteins vimentin and desmin: mixed polymers at all stages of assembly. Eur J Cell Biol. 2005 Mar; 84(2-3): 379-91
238. Hnia K, Ramspacher C, Vermot J, Laporte J. Desmin in muscle and associated diseases: beyond the structural function. Cell Tissue Res. 2015 Jun; 360(3): 591-608
239. Ramos-Vara JA, Miller MA. When tissue antigens and antibodies get along: revisiting the technical aspects of immunohistochemistry - the red, brown and blue technique. Vet Pathol. 2014 Jan; 51(1): 42-87
240. Koomen BM, van der Starre-Gaal J, Vonk JM, von der Thusen JH, van der Meij JJC, Monkhorst K et al. Formalin fixation for optimal concordance of programmed deathligand 1 immunostaining between cytologic and histologic specimens from patients with non-small cell lung cancer. cancer Cytopathol. 2021 Apr; 129(4): 304-17
241. Macura S, Mishra PK, Gamez JD, Pirko I. MR microscopy of formalin fixed paraffin embedded histology specimens. Magn Reson Med. 2014 Jun; 71(6): 1989-94
242. Musial A, Gryglewski RW, Kielczewski S, Loukas M, Wadja J. Formalin use in anatomical and histological science in the 19th and 20th centuries. Folia Med Cracov. 2016; 56(3): 31-40
243. Katayama H, Hama H, Nagasawa K, Kurokawa H, Sugiyama M, Ando R et al. Visualizing and modulating mitophagy for therapeutic and studies of neurodegeneration. Cell. 2020 May 28; 181(5): 1176-87
244. Orchard GE. Use of heat provides a fast and efficient way to undertake melanin bleaching with dilute hydrogen peroxide. Br J Biomed Sci. 2007; 64(2): 89-91
245. .Ohsie SJ, Sarantopoulos GP, Cochran AJ, Binder SW. Immunohistochemical characteristics of melanoma. J Cutan Pathol. 2008 May; 35(5): 433-44
246. Korytowski W, Sarna T. Bleaching of melanin pigments. The Journal of Biological Chemistry. 1990 Jul 25; 265(21): 12410-6
247. Chung JY, Choi J, Sears JD, Ylaya K, Perry C, Choi CH et al. A melanin-bleaching methodology for molecular and histopathological analysis of formalin-fixed paraffinembedded tissue. Lab Invest. 2016 Oct; 96(10): 1116-27
248. Wang J, Zohar R, McCulloch CA. Multiple roles of alpha-smooth muscle actin in mechanotransduction. Exp Cell Res. 2006 Feb 1; 312(3): 205-14
249. Arora PD, McCulloch CA. Dependence of collagen remodelling on α-smooth muscle actin expression by fibroblast. J Cell Physiol. 1994 Apr; 159(1): 161-75
250. Steinert PM, Chou YH, Prahlad V, Parry DA, Marekov LN, Wu KC et al. A high molecular weight intermediate filament-associated protein in BHK-21 cells is nestin, a type VI intermediate filament protein. J Biol Chem. 1999 Apr 2; 274(14): 9881-90

251. Yamagishi A, Susaki M, Takano Y, Mizusawa M, Mishima M, Iijima M et al. The structural function of nestin in cell body softening is correlated with cancer cell metastasis. Int J Biol Sci. 2019 Jun 2; 15(7): 1546-56
252. Means AL, Meszoely IM, Suzuki K, Miyamoto Y, Rustgi AK, Coffey RJ Jr et al. Pancreatic epithelial plasticity mediated by acinar cell transdifferentiation and generation of nestin positive intermediates. Development. 2005 Aug; 132(16): 3767-76
253. Zhang Y, Shen W, Sun B, Lv C, Dou Z. Plasticity of marrow mesenchymal stem cells from human first-trimester fetus: from single-cell clone to neuronal differentiation. Cell Reprogram. 2011 Feb; 13(1): 57-64
254. Parlakian A, Paulin D, Izmiryan A, Xue Z, Li Z. Intermediate filaments in peripheral nervous system: their expression, dysfunction and diseases. Rev Neurol (Paris). 2016 Oct; 172(10): 607-13
255. Carlsson L, Li Z, Paulin D, Thornell LE. Nestin is expressed during development and in myotendinous and neuromuscular junctions in wild type and desmin knock-out mice. Exp Cell Res. 1999 Aug 25; 251(1): 213-23
256. Mak KM, Mei R. Basement membrane type IV collagen and laminin: an overview of their biology and value as fibrosis biomarkers of liver disease. Anat Rec (Hoboken). 2017 Aug; 300(8): 1371-90
257. Rousselle P, Montmasson M, Garnier C. Extracellular matrix contribution to skin wound re-epithelialisation. Matrix Biol. 2019 jan; 75-76: 12-26
258. Wilson SE, Torricelli AAM, Marino GK. Corneal epithelial basement membrane: structure, function and regeneration. Exp Eye Res. 2020 May; 194: 108002
259. Fidler AL, Darris CE, Chetyrkin SV, Pedchenko VK, boudko SP, Brown KL et al. Collagen IV and basement membrane at the evolutionary dawn of metazoan tissues. Elife. 2017 Apr 18; 6: e24176
260. Khoshnoodi J, Pedchenko V, Hudson BG. Mammalian collagen type IV. Microsc Res Tech. 2008 May; 71(5): 357-70
261. Murata Y, Kaidoh T, Inoue T. Ultrastructural changes of the myoepithelium of the dilator pupillae during miosis and mydriasis in the rat iris. Arch histol Cytol. 1998. PMID: 9557965
262. Kortesmaa J, Yurchenco P, Tryggvason K. Recombinant laminin-8 α4 β1 γ1. Production, purification and interactions with integrins. J Biol Chem. 2000 May 19; 275(20): 14853-59
263. Livanainen A, Sainio K, Sariola H, Tryggvason K. Primary structure and expression of a novel human laminin α4 chain. FEBS Lett. 1995 May 29; 365(2-3): 183-88
264. Radice GL. N-cadherin-mediated adhesion and signaling from development to disease: lessons from mice. Prog Mol Biol Transl Sci. 2013; 113: 263-89
265. Logan CM, Rajakaruna S, Bowen S, Radice GL, Robinson ML, Menko AS. N-cadherin regulates signaling mechanisms required for lens fiber cell elongation and lens morphogenesis. Dev Biol. 2017 Aug 1; 428(1): 118-34
266. El Sayegh TY, Kapus A, McCulloch CA. Beyond the epithelium: cadherin function in fibrous connective tissues. FEBS Lett. 2007 Jan 23; 581(2): 167-74
267. Miyamoto Y, Sakane F, Hashimoto K. N-cadherin-based adherens junction regulates the maintenance, proliferation, and differentiation of neural progenitor cells during development. Cell Adh Migr. 2015; 9(3): 183-92
268. Sun Z, Parrish AR, Hill MA, Meininger GA. N-cadherin, a vascular smooth muscle cell-cell signalling for vasomotor control. Microcirculation. 2014 Apr; 21(3): 208-18
269. Su W, van Wijk SW, Brundel BJJM. Desmin variants: trigger for cardiac arrhythmias? Front Cell Dev Biol. 2022 Sep 9; 10: 986718
270. Sobieszek IJ, Sobieszek A. Myosin assembly of smooth muscle: from ribbons and side polarity to a row polar helical model. J Muscle res Cell Motil. 2022 Sep; 43(3): 113-33
271. Agnetti G, Herrmann H, Cohen S. new roles for desmin in the maintenance of muscle homeostasis. FEBS J. 2022 May; 289(10): 2755-70
272. Svitkina T. The actin cytoskeleton and actin-based motility. Cold Spring Harb Perspect Biol. 2018 Jan 2; 10(1): a018267

273. Chaponnier C, Goethals M, Janmey PA, Gabbiani F, Gabbiani G, Vandekerckhove J. The specific NH2-terminal sequence Ac-EEED of alpha-smooth muscle tin plays a role in polymerisation in vitro and in vivo. J Cell Biol. 1995 Aug; 130(4): 887-95
274. Khaitlina SY. Functional specificity of actin isoforms. Int Rev Cytol. 2001; 202: 35-98
275. Chen J, Li H, Sundar Raj N, Wang JH. Alpha-smooth muscle actin expression enhances cell traction force. Cell Motil Cytoskeleton. 2007 Apr; 64(4): 248-57
276. Sun X, Joost S, Kasper M. Plasticity of epithelial cells during skin wound healing. Cold Spring Harb Perspect Biol. 2022 Nov 14; a041232
277. Hallmann R, Horn N, Selg M, Wendler O, Pausch F, Sorokin LM. Expression and function of laminins in the embryonic and mature vasculature. Physiol Rev. 2005 Jul; 85(3): 979- 1000
278. Yazdanpanah G, Jabbehdari S, Djalilian AR. Limbal and corneal epithelial homeostasis. Curr opin Ophthalmol. 2017 Jul; 28(4): 348-54
279. .Jensen UB, Lowell S, Watt FM. The spatial relationship between stem cells and their progeny in the basal layer of human epidermis: a new view based on whole-mount labelling and lineage analysis. Development. 1999 Jun; 126(11): 2409-18
280. Wallaeys C, Garcia-Gonzalez N, Livert C. Paneth cells as the cornerstones of intestinal and organismal health: a primer. EMBO Mol Med. 2022 Dec 27; e16427
281. Ramadan R, Wouters VM, van Neerven SM, de Groot NE, Garcia TM, Muncan V et al. The extracellular matrix controls stem cell specification and crypt morphology in the developing and adult mouse gut. Biol Open. 2022 Dec 15; 11(12): bio059544
282. Pentinmikko N, Lozano R, Scharaw S, Andersson S, Englund JI, Castillo-Azofeifa D et al. Cellular shape reinforces niche to stem cell signaling in the small intestine. Sci Adv. 2022 Oct 14; 8(41): eabm1847
283. Brunet A, Goodell MA, Rando TA. Ageing and rejuvenation of tissue stem cells and their niches. Nat Rev Mol Cell Biol. 2023 Jan; 24(1): 45-62
284. Miller I, Min M, yang C, Tian C, Gookin S, Carter D et al. Ki67 is a graded rather than a binary marker of proliferation versus quiescence. Cell Rep. 2018 Jul 31; 24(5): 1105-12. e5
285. Simpson TI, Price DJ. PAX6; a pleiotropic player in development. Bioessays. 2002 Nov; 24(11): 1041-51.
286. Bharti K, Gasper M, Ou J, Brucato M, Clore-Gronenborn K, Pickel J et al. A regulatory loop involving PAX6, MITF, and WNT signaling controls retinal pigment epithelium development. PLoS Genet. 2012 Jul; 8(7): e1002757
287. Hingorani M, Hanson I, van Heyningen V. Aniridia. Eur J Hum Genet. 2012 Oct; 20(10): 1011-17
288. Van Heyningen V, Williamson KA. PAX6 in sensory development. Hum Mol Genet. 2002 May 15; 11(10): 1161-67
289. Aksan I, Goding CR. Targeting the microphthalmia basic helix-loop-helix-leucine zipper transcription factor to a subset of E-box elements in vitro and in vivo. Mol Cell Biol. 1998 Dec; 18(12): 6930-38
290. Ashery-Padan R, Marquardt T, Zhou X, Gruss P. PAX6 activity in the lens primordium is required for lens formation and for correct placement of a single retina in the eye. Genes Dev. 2000 Nov 1; 14(21): 2701-11
291. Georgala PA, Carr CB, Price DJ. The role of PAX6 in forebrain development. Dev Neurobiol. 2011 Aug; 71(8): 690-709
292. Kleinjan DA, Seawright A, Mella S, Carr CB, Tyas DA, Simpson TI, Mason JO, Price DJ, van Heyningen V. Long-range downstream enhancers are essential for PAX6 expression. Dev Biol. 2006 Nov 15; 299(2): 563-81
293. Lima Cunha D, Arno G, Corton M. Moosajee M. The spectrum of PAX6 mutations and genotype-phenotype correlations in the eye. Genes (Basel). 2019 Dec 17; 10(12): 1050
294. Davis-Silberman N, Kalich T, Oronkarni V, Marquardt T, Kroeber M, Tamm ER et al. Genetic dissection of PAX6 dosage requirements in the developing mouse eye. Hum Mol Genet. 2005 Aug 1; 14(15): 2265-76

295. Grant MK, Bobilev AM, Branch A, Lauderdale JD. Structural and functional consequences of PAX6 mutations in brain: implications for aniridia. Brain Res. 2021 Apr 1; 1756: 147283
296. Wang X, Shan X, Gregory-Evans CY. A mouse model of aniridia reveals the in vivo downstream targets of PAX6 driving iris and ciliary body development in the eye. Biochim Biophys Acta Mol Basis Dis. 2017 Jan; 1863(1): 60-67
297. Zhao S, Chen Q, Hung FC, Overbeek PA. BMP signaling is required for development of the ciliary body. Development. 2002 Oct; 129(19): 4435-42
298. Cvekl A, Callaerts P. PAX6: 25th anniversary and more to learn. Exp Eye Res. 2017 Mar; 156: 10-21
299. Dash S, Brastrom LK, Patel SD, Scott CA, Slusarski DC, Lachke SA. The master transcription factor SOX2, mutated in anophthalmia/microphthalmia, is post-transcriptionally regulated by the conserved RNA-binding protein RBM24 in vertebrate eye development. Hum Mol Genet 2020 Mar 13; 29(4): 591-604
300. Hever AM, Williamson KA, van Heyningen V. Developmental malformations of the eye: the role of PAX6, SOX2 and OTX2. Clin Genet. 2006 Jun; 69(6): 459-70
301. Li Y, Shen Y, Cai D, Shen Y. SOX2 knockdown in the neonatal retina causes cell fate to switch from amacrine to bipolar. Brain Res. 2021 Feb 1; 1752: 147265
302. Kautzman AG, Keeley PW, Nahmou MM, Luna G, Fisher SK, Reese BE. SOX2 regulates astrocytic and vascular development in the retina. Glia. 2018 Mar; 66(3): 623-36
303. Matsushima D, Heavner W, Pevny LH. Combinatorial regulation of optic cup progenitor cell fate by SOX2 and PAX6. Development. 2011 Feb; 138(3): 443-54
304. Wang X, Xiong K, Lu L, Gu D, Wang S, Chen J et al. Developmental origin of the posterior pigmented epithelium of iris. Cell Biochem Biophys. 2015 Mar; 71(2): 1067-76
305. Ma W, Yan RT, Li X, Wang SZ. Reprogramming retinal pigment epithelium to differentiate toward retinal neurons with SOX2. Stem Cells. 2009 Jun; 27(6): 1376-87
306. Liu YR, Laghari ZA, Novoa CA, Hughes J, Webster JR, Goodwin PE et al. SOX2 acts as a transcriptional repressor in neural stem cells. BMC Neurosci. 2014 Aug 8; 15: 95
307. Liu K, Lin B, Zhao M, Yang X, Chen M, Gao A et al. The multiple roles for SOX2 in stem cell maintenance and tumorigenesis. Cell Signal. 2013 May; 25(5): 1264-71
308. Rizzino A, Wuebben EL. SOX2/OCT4: a delicately balanced partnership in pluripotent stem cells and embryogenesis. Biochim Biophys Acta. 2016 Jun; 1859(6): 780-91
309. Baltus GA, Kowalski MP, Zhai H, Tutter AV, Quinn D, Wall D et al. Acetylation of SOX2 induces its nuclear export in embryonic stem cells. Stem Cells. 2009 Sep; 27(9): 2175-84
310. MacNail A, Pearson RA, Maclaren RE, Smith AJ, Sowden JC, Ali RR. Comparative analysis of progenitor cells isolated from the iris, pars plana, and ciliary body of the adult porcine eye. Stem Cells. 2007 oct; 25(10): 2430-38
311. Chojnacki A, Weiss S. Production of neurons astrocytes and oligodendrocytes from mammalian CNS stem cells. Nat Protoc. 2008; 3(6): 935-40
312. Wang YJ, Bailey JM, Rovira M, Leach SD. Sphere-forming assays for assessment of benign and malignant pancreatic stem cells. Methods Mol Biol. 2013; 980: 281-90
313. Li H, Wang H, Wang F, Gu Q, Xu X. Snail involves in the transforming growth factor β1-mediated epithelial-mesenchymal transition of retinal pigment epithelial cells. PLoS One. 2011; 6(8): e23322
314. Zhou L, Shi DP, Chu WJ, Yang LL, Xu HF. LGR1 promotes epithelial-mesenchymal transition of retinal pigment epithelium cells by activating NOX4. Int J Opthalmol. 2021 Mar 18; 14(3): 349-55
315. Botha CJ, Venter EA, Ferreira GCH, Phaswane RM, Clift SJ. Geigerin-induced disorganization of desmin, an intermediate filament of the cytoskeleton, in a murine myoblast cell line (C2C12). Toxicon. 2019 Sep; 167: 162-67
316. Balci-Hayta B, Bekircan-Kurt CE, Aksu E, Dayangac-Erden D, Tan E, Erdem-Ozdamar S. Establishment of primary myoblast cell cultures from cryopreserved skeletal muscle biopsies to serve as a tool in related research & development studies. J Neurol Sci. 2018 Oct 15; 393: 100-104

317. Hayashi T, Mizuno N, Kondoh H. Determinative roles of FGF and Wnt signals in iris-derived lens regeneration in newt eye. Dev Growth Differ. 2008; 50(4): 279-87
318. Fujimura N, Taketo MM, Mori M, Korinek V, Kozmik Z. Spatial and temporal regulation of Wnt/β-catenin signalling is essential for development of the retinal pigment epithelium. Dev Biol. 2009 Oct 1; 334(1): 31-45
319. Westenskow P, Piccolo S, Fuhrmann S. B-catenin controls differentiation of the retinal pigment epithelium in the mouse optic cup by regulating Mitf and Otx2 expression. Development. 2009 Aug; 136(15): 2505-10
320. Fujimura N, Klimova L, Antosova B, Smolikova J, Machon O, Kozmik Z. Genetic interaction between PAX6 and β-catenin in the developing retinal pigment epithelium. Dev Genes Evol. 2015 Apr; 225(2): 121-28
321. .Kallala R, Graham SM, Nikkhad D, Kyrhos M, Heliotis M, Mantalaris A et al. In vitro and in vivo effects of antibiotics on bone cell metabolism and fracture healing. Expert Opin Drug Saf. 2012 Jan; 11(1): 15-32
322. Serrano-Gomez SJ, maziveyi M, Alahari SK. Regulation of epithelial-mesenchymal transition through epigenetic and post-translational modifications. Mol Cancer. 2016 Feb 24; 15: 18
323. Llobet L, Montoya J, Lopez-Gallardo E, Ruiz-Pesini E. Side effects of culture media antibiotics on cell differentiation. Tissue Eng Part C Methods. 2015 Nov; 21(11): 1143-47
324. Cohen S, Samadikuchaksaraei A, Polak JM, Bishop AE. Antibiotics reduce the growth rate and differentiation of embryonic stem cell cultures. Tissue Eng. 2006 Jul; 12(7): 2025-30
325. Bocharov G, Luzyanina T, Cupovic J, ludewig B. Asymmetry of cell division in CFSE-based lymphocyte proliferation analysis. Front immunol. 2013 Sep 2; 4: 264
326. Gil-Perotin S, Duran-Moreno M, Cebrian-Silla A, Ramirez M, Garcia-Belda P, Garcia Verdugo JM. Adult neural stem cells from the subventricular zone: a review of the neurosphere assay. Anat rec. 2013 Sep; 296(9): 1435-52
327. Schonenberger F, Deutzmann A, Ferrando-May E, Merhof D. Discrimination of cell cycle phases in PCNA-immunolabelled cells. BMC Bioinformatics. 2015 May 29; 16: 180
328. Ulrich HD, Takahashi T. Readers of PCNA modifications. Chromosoma. 2013 Aug; 122(4): 259-74
329. Sobecki M, Mrouj K, Colinge J, Gerbe F, Jay P, Krasinska L et al. Cell-cycle regulation accounts for variability in Ki67 expression levels. Cancer Res. 2017 May 15; 77(10): 2722-34
330. Sobecki M, Mrouj K, Camasses A, Parisis N, Nicolas E, Lleres D et al. The cell proliferation antigen Ki67 organises heterochromatin. Elife. 2016 Mar 7; 5: e13722
331. Zerjatke T, Gak IA, Kirova D, Fuhrmann M, Daniel K, Gonciarz M et al. Quantitative cell cycle analysis based on an endogenous all-in-one reporter for cell tracking and classification. Cell rep. 2017 May 30; 19(9): 1953-66
332. Oikawa H, Hayashi K, Maesawa C, Masuda T, Sobue K. Expression profiles of nestin in vascular smooth muscle cells in vivo and in vitro. Exp Cell Res. 2010 Apr 1; 316(6): 940-50
333. Day K, Shefer G, Richardson JB, Enikolopov G, Yablonka-Reuveni Z. Nestin-GFP reporter expression defines the quiescent state of skeletal muscle satellite cells. Dev Biol. 2007 Apr1; 304(1): 246-59
334. Sahlgren CM, Mikhailov A, Vaittinen S, Pallari HM, Kalimo H, Pant HC et al. Cdk5 regulates the organisation of nestin and its association with p35. Mol Cell Biol. 2003 Jul; 23(14): 5090-106
335. Sejerson T, Lendahl U. Transient expression of the intermediate filament nestin during skeletal muscle development. J Cell Sci. 1993 dec; 106 (Pt 4): 1291-300
336. Chabot A, Hertig V, Boscher E, Nguyen QT, Boivin B, Chebli J et al. Endothelial and epithelial cell transition to a mesenchymal phenotype was delineated by nestin expression. J cell Physiol. 2016 Jul; 231(7): 1601-10

337. Bazina F, Brouxhon SM, Kyrkanides S. Reprogramming oral epithelial keratinocytes into a pluripotent phenotype for tissue regeneration. Clin Exp Dent Res. 2021 Dec; 7(6): 1112-21
338. Zhao Z, Lu P, Zhang H, Xu H, Gao N, Li M et al. Nestin positively regulates the Wnt/β-catenin pathway and the proliferation, survival and invasiveness of breast cancer stem cells. Breast Cancer Res. 2014 Jul 24; 16(4): 408
339. Hagio M, Matsuda Y, Suzuki T, Ishiwata T. Nestin regulates epithelial-mesenchymal transition marker expression in pancreatic ductal adenocarcinoma cell lines. Mol Clin Oncol. 2013 Jan; 1(1): 83-87
340. Matsuda Y, Naito Z, Kawahara K, Nakazawa N, Korc M, Ishiwata T. Nestin is a novel target for suppressing pancreatic cancer cell migration, invasion and metastasis. Cancer Biol Ther. 2011 Mar 1; 11(5): 512-23
341. Lagace DC, Whitman MC, Noonan MA, Ables JL, deCarolis NA, Arguello AA et al. Dynamic contribution of nestin-expressing stem cells to adult neurogenesis. J Neurosci. 2007 Nov 14; 27(46): 12623-29
342. Wiese C, Rolletschek A, Kania G, Blyszczuk P, Tarasov KV, Tarasova Y et al. Nestin expression – a property of multi-lineage progenitor cells? Cell Mol life Sci. 2004 Oct; 61(19-20): 2510-22
343. Chen HL, Yuh CH, Wu KK. Nestin is essential for zebrafish brain and eye development through control of progenitor cell apoptosis. PLoS One. 2010 Feb 19; 5(2): e9318
344. Yang J, Bian W, Gao X, Chen L, Jing N. Nestin expression during mouse eye and lens development. Mech Dev. 2000 Jun; 94(1-2): 287-91
345. Matas A, Filipovic N, Znaor L, Mardesic S, Saraga-Babic M, Vukojepic K. Interplay of proliferation and differentiation factors is revealed in the early human eye development. Graefes Arch Clin Exp Ophthalmol. 2015 Dec; 253(12): 2187-201
346. Bozanic D, Bocina I, Saraga-Babic M. Involvement of cytoskeletal proteins and growth factor receptors during development of the human eye. Anat Embryol. 2006 Oct; 211(5): 367-77
347. Kumar BM, Maeng GH, Lee YM, Kim TH, Lee JH, Jeong BG et al. Neurogenic and cardiomyogenic differentiation of mesenchymal stem cells isolated from minipig bone marrow. Res Vet Sci. 2012 Oct; 93(2): 749-57
348. Musaro A, Carosio S. Isolation and culture of satellite cells from mouse skeletal muscle. Methods Mol Biol. 2017; 1553: 155-67
349. Eberli D, Sojer S, Atala A, Yoo JJ. Optimisation of human skeletal muscle precursor cell culture and myofiber formation in vitro. Methods. 2009 Feb; 47(2): 98-103
350. Wang T, Xu Z, Jiang W, Ma A. Cell-to-cell contact induces mesenchyma stem cell to differentiate into cardiomyocyte and smooth muscle cell. int J Cardiol. 2006 Apr 28; 109(1): 74-81
351. Hagglund AC, Berghard A, Carlsson L. Canonical Wnt/β-catenin signalling is essential for optic cup formation. PLoS One. 2013 Dec 4; 8(12): e81158
352. Gul IS, Hulpiau P, Saeys Y, van Roy F. Evolution and diversity of cadherins and catenins. Exp Cell res. 2017 Sep 1; 358(1): 3-9
353. Van der Wal T, Van Amerongen R. Walking the tight wire between cell adhesion and WNT signalling: a balancing act for β-catenin. Open Biol. 2020 Dec; 10(12): 200267
354. Wang T, Wang R, Clearly RA, Gannon OJ, Tang DD. Recruitment of β-catenin to N-cadherin is necessary for smooth muscle contraction. J Biol Chem. 2015 Apr 3; 290(14): 8913-24
355. Nadanaka S, Kinouchi H, Kitagawa H. Chondroitin sulfate-mediated N-cadherin/β-catenin signaling is associated with basal-like breast cancer cell invasion. J Biol Chem. 2018 Jan 12; 293(2): 444-65
356. Yang S, Zhang H, Liu Q, Sun S, Lei P, Zhao Z et al. The synthesis and biological evaluation of chondroitin sulfate E glycodendrimers. Future Med Chem. 2019 Jun; 11(12): 1403-15
357. Stamos JL, Weis WI. The β-catenin destruction complex. Cold Spring Harb Perspect Biol. 2013 Jan 1; 5(1): a007898

358. Anthony CC, Robbins DJ, Ahmed Y, Lee E. Nuclear regulation of Wnt/β-catenin signalling: it's a complex situation. Genes (Basel). 2020 Aug 4; 11(8): 886
359. He TC, Sparks AB, Rago C, Hermeking H, Zawel L, da Costa LT et al. Identification of C-Myc as a target of the APC pathway. Science. 1998 Sep 4; 281(5382): 1509-12
360. Zwolinska AK, Heagle Whiting A, Beekman C, Sedivy JM, Marine JC. Suppression of Myc oncogenic activity by nucleostemin haploinsufficiency. Oncogene. 2012 Jul; 31(28): 3311-21
361. Dang CV, O'Donnel KA, Zeller KI, Nguyen T, Osthus RC, Li F. The C-Myc target gene network. Semin Cancer Biol. 2006 Aug; 16(4): 253-64
362. Bretones G, Delgado MD, Leon J. Myc and cell cycle control. Biochim Biophys Acta. 2015 May; 1849(5): 506-16
363. .Eilers M, Eisenman RN. Myc's broad reac. Genes Dev. 2008 Oct 15; 22(20): 2755-66
364. Myant K, Sansom OJ. Wnt/Myc interactions in intestinal cancer: partners in crime. Exp Cell Res. 2011 Nov 15; 317(19): 2725-31
365. Bisso A, Filipuzzi M, Gamarra Figueroa GP, Brumana G, Biagioni F, Dino M et al. Cooperation between Myc and β-catenin in liver tumorigenesis requires Yap/Taz. Hepatology. 2020 Oct; 72(4): 1430-43
366. Schmitt S, Aftafb U, Jiang C, Redenti S, Klassen H, Miljan E et al. Molecular characterisation of human retinal progenitor cells. Invest Ophthalmol Vis sci. 2009 Dec; 50(12): 5901-08
367. .Tsai RY, McKay RD. A nucleolar mechanism controlling cell proliferation in stem cells and cancer cells. Genes Dev. 2002 Dec 1; 16(23): 2991-3003
368. Tsai RY. Turning a new page on nucleostemin and self-renewal. J Cell Sci. 2014 Sep 15; 127 (Pt 18): 3885-91
369. Kitamoto J, Hyer J. The expression of Wnt2b in the optic cup lip requires a border between the pigmented and nonpigmented epithelium. Mol Vis. 2010 Dec 14; 16: 2701-17
370. Kubo F, Takeichi M, Nakagama S. WNT2b controls retinal cell differentiation at the ciliary marginal zone. Development. 2003 feb; 130(3): 587-98
371. Martinez-Morales JR, Rodrigo I, Bovolenta P. Eye development: a view from the retina pigmented epithelium. Bioessays. 2004 Jul; 26(7): 766-77
372. Baumer N, Marquardt T, Stoykova A, Spieler D, Treichel D, Ashery-Padan R et al. Retinal pigmented epithelium determination requires the redundant activities of PAX2 and PAX6. Development. 2003 Jul; 130(13): 2903-15
373. Hicks D, Courtois Y. Fibroblast growth factor stimulates photoreceptor differentiation in vitro. J Neurosci. 1992 Jun; 12(6): 2022-33
374. Klimova L, Kozmik Z. Stage-dependant requirements of neuroretinal Pax6 for lens and retina development. Development. 2014 Mar; 141(6): 1292-302
375. Wood HB, Episkopou V. Comparative expression of the mouse SOX1, SOX2 and SOX3 genes from pre-gastrulation to early somite stages. Mech Dev. 1999 Aug; 86(1-2): 197-201
376. Bachleda AR, Pvny LH, Weiss ER. Sox2-deficient muller glia disrupt the structural and functional maturation of the mammalian retina. Invest Ophthalmol Vis Sci. 2016 Mar; 57(3): 1488-99
377. Taranova OV, Magness ST, Fagan BM, Wu Y, Surzenko N, Hutton SR et al. SOX2 is a dose-dependant regulator of retinal neural progenitor competence. Genes Dev. 2006 May 1; 20(9): 1187-202
378. Froen RC, Johnson EO, Petrovski G, Berenyi E, Facsko A, Berta A et al. Pigment epithelial cells isolated from human peripheral iridectomies have limited properties of retinal stem cells. Acta Ophthalmol. 2011 Dec; 89(8): e635-44
379. Venters SJ, Cuenca PD, Hyer J. Retinal and anterior eye compartments derive from a common progenitor pool in the avian optic cup. Mol Vis. 2011; 17: 3347-63
380. Seko Y, Azuma N, Kaneda M, Nakatani K, Miyagawa Y, Noshiro Y et al. Derivation of human differential photoreceptor-like cells from the iris by defined combinations of CRX, RX, and NEUROD. PLoS One. 2012; 7(4): e35611

381. ThermoFisher Scientific. Neurobiology protocol handbook. [Internet]. c2022 [cited 2022 Jan]. Available from https://assets.thermofisher.com/TFS-assets/BID/Handbooks/gibco-neurobiology%20protocol-handbook.pdf
382. D'Aiuto L, Zhi Y, Kumar Das D, Wilcox MR, Johnson JW, McClain L et al. Large-scale generation of human iPSC-derived neural stem cells/early neural progenitor cells and their neuronal differentiation. Organogenesis. 2014; 10(4): 365-77
383. Dhara SK, Stice SL. Neural differentiation of human embryonic stem cells. J Cell Biochem. 2008 Oct 15; 105(3): 633-40
384. Anoopkumar-Dukie S, Carey JB, Conere T, O'sullivan E, van Pelt FN, Allshire A. Resazurin assay of radiation response in cultured cells. Br J Radiol. 2005 Oct; 78(934): 945- 7
385. Pesch KL, Simmert U. Combined assays for lactose and galactose by enzymatic reactions. Milchw Forsch. 1929
386. Aleshin VA, Artiukhov AV, Oppermann H, Kazantsev AV, Lukashev NV, Bunik VI. Mitochondrial impairment may increase cellular NAD(P)H: resazurin oxidoreductase activity, perturbing the NAD(P)H-based viability assays. Cells. 2015 Aug 21; 4(3): 427-51
387. Nishizawa A, Maruta Y, Fukuda M. Rab32/38-dependant and –independent transport of tyrosinase to melanosomes in B16-F1 melanoma cells. Int J Mol Sci. 2022 Nov 16; 23(22): 14144
388. Bardy C, van den Hurk M, Eames T, Marchand C, Hernandez RV, Kellogg M et al. Neuronal medium that supports basic synaptic functions and activity of human neurons in vitro. Proc Natl Acad Sci USA. 2015 May 19; 112(20): E2725-34
389. Gordon J, Amini S. General overview of neuronal cell culture. Methods Mol Biol. 2021; 2311: 1-8
390. Ribeiro-Filho AC, Levy D, Ruiz JLM, Mantovani MDC, Bydlowski SP. Traditional and advanced cell cultures in hematopoietic stem cell studies. Cells. 2019 Dec 12; 8(12): 1628
391. Ferrin I, Beloqui I, Zabaleta L, Salcedo JM, Trigueros C, Martin AG. Isolation, culture and expansion of mesenchymal stem cells. Methods Mol Biol. 2017; 1590: 177-90
392. Brewer GJ, Torricelli JR, Evege EK, Price PJ. Optimized survival of hippocampal neurons in B27-supplemented neurobasal, a new serum-free medium combination. J Neurosci Res. 1993 Aug 1; 35(5): 567-76
393. Romjin HJ, van Huizen F, Wolters PS. Towards an improved serum-free, chemically defined medium for long-term culturing of cerebral cortex tissue. Neurosci Biobehav Rev. 1984 Fall; 8(3): 301-34
394. Chouaib B, Collart-Dutilleul PY, Blanc-Sylvestre N, Younes R, Gergely C, Raoul C et al. Identification of secreted factors in dental pulp cell-conditioned medium optimised for neuronal growth. Neurochem int. 2021 Mar; 144: 104961
395. Cornwall S, Cull G, Joske D, Ghassemifar R. Green tea polyphenol "epigallocatechin-3-gallate", differentially induces apoptosis in CLL B- and T-cells but not in healthy B- and Tcells in a dose dependant manner. Leuk Res. 2016 Dec; 51: 56-61
396. Borreli V, Sterpetti AV, Coluccia P, Randone B, Cavallaro A, Santoro D'Angelo L et al. Bimodal concentration-dependant effect of thrombin on endothelial cell proliferation and growth factor release in culture. J Surg Res. 2001 Oct; 100(2): 154-60
397. ThermoFisher. [Internet]. c2022 [cited 2022 Jan]. Available from https://www.thermofisher.com/fr/fr/home/references/gibco-cell%20culture-basics/cell-culture-environment/culture-media/fbs-basics/what-does-fetal%20bovine-serum-do.htm
398. Brewer GJ, Torricelli JR, Evege EK, Price PJ. Optimised survival of hippocampal neurons in B27-supplemented neurobasalTM, a new serum-free medium combination. J Neurosci res. 1993 Aug 1; 35(5): 567-76
399. Said HM. Biotin: biochemical, physiological and clinical aspects. Subcell Biochem. 2012; 56: 1-19

400. Pekala J, Patkowska-Sokola B, Bodkowski R, Jamroz D, Nowakowski P, Lochynski S et al. L-carnitine metabolic functions and meaning in humans life. Curr Drug Metab. 2011 Sep; 12(7): 667-78
401. Houten SM, Violante S, Ventura FV, Wanders RJ. The biochemistry and physiology of mitochondrial fatty acid β-oxidation and its genetic disorders. Annu Rev Physiol. 2016; 78: 23-44
402. Kinlein SA, Phillips DJ, Keller CR, Karatsoreos IN. Role of corticosterone in altered neurobehavioral responses to acute stress in a model of compromised hypothalamicpituitary-adrenal axis function. Psychoneuroendocrinology. 2019 Apr; 102: 248-55
403. Datson NA, Morskink MC, Meijer OC, de Kloet ER. Central corticosteroid actions: search for gene targets. Eur J Pharmacol. 2008 Apr 7; 583(2-3): 272-89
404. Patel D, Witt SN. Ethanolamine and phosphatidylethanolamine: partners in health and disease. Oxid Med Cell Longev. 2017; 2017: 4829180
405. Modica-Napolitano JS, Renshaw PF. Ethanolamine and phosphoethanolamine inhibit mitochondrial function in vitro: implications for mitochondrial dysfunction hypothesis in depression and bipolar disorder. Biol Psychiatry. 2004 Feb 1; 55(3): 273-7
406. Melisi D, Curcio A, Luongo E, Morelli E, Rimoli MG. D-galactose as a vector for prodrug design. Curr Top Med Chem. 2011; 11(18): 2288-98
407. Azman KF, Zakaria R. D-galactose-induced accelerated aging model: an overview. Biogerontology. 2019 Dec; 20(6): 763-82
408. Coelho AI, Berry GT, Rubio-Gozalbo ME. Galactose metabolism and health. Curr opin Clin Nutr Metab Care. 2015 Jul; 18(4): 422-7
409. Forman HJ, Zhang H, Rinna A. Glutathione: overview of its protective roles, measurement, and biosynthesis. Mol Aspects Med. 2009 Feb-Apr; 30(1-2): 1-12
410. Cantin AM, North SL, Hubbard RC, Crystal RG. Normal alveolar epithelial lining fluid contains high levels of glutathione. J Appl Physiol. 1987 Jul; 63(1): 152-7
411. Jandacek RJ. Linoleic Acid: a nutritional quandary. Healthcare. 2017 May 20; 5(2): 25
412. Belal SA, Sivakumar AS, Kang DR, Chose S, Choe HS, Shim KS. Modulatory effect of linoleic and oleic acid on cell proliferation and lipid metabolism gene expressions in primary bovine satellite cells. Anim Cells Syste. 2018 Sep 9; 22(5): 324-33
413. Maurin AC, Chavassieux PM, Vericel E, Meunier PJ. Role of polyunsaturated fatty acids in the inhibitory effect of human adipocytes on osteoblastic proliferation. Bone. 2002 Jul; 31(1): 260-6
414. Hennebelle M, Morgan RK, Sethi S, Zhang Z, Chen H, Grodzki AC et al. Lineoleic acidderived metabolites constitute the majority of oxylipins in the rat pup brain and stimulate axonal growth in primary rat cortical neuron-glia co-cultures in a sex-dependant manner. J Neurochem 2020 Jan; 152(2): 195-207
415. Yaguchi T, Fujikawa H, Nishizati T. Linoleic acid derivate DCP-LA protects neurons from oxidative stress-induced apoptosis by inhibiting caspase-3/-9 activation. Neurochem Res. 2010 May; 35(5): 712-7
416. Hunt WT, Kamboj A, Anderson HD, Anderson CM. Protection of cortical neurons from excitotoxicity by conjugated linoleic acid. J Neurochem. 2010 Oct; 115(1): 123-30
417. Koba K, Yanagita T. Health benefits of conjugated linoleic acid. Obes Res Clin Pract. 2014 Nov-Dec; 8(6): e525-32
418. Clarke SD, Gasperikova D, Nelson C, Lapillonne A, Heird WC. Fatty acid regulation of gene expression: a genomic explanation for the benefits of the Mediterranean diet. Ann N Y Acad Sci. 2002 Jun; 967: 283-98
419. Whelan J, Fritsche K. Linoleic acid. Adv in Nutrition. 2013 May 1; 4(3): 311-2
420. Wlodawer P, Samuelsson B. On the organisation and mechanism of prostaglandin synthetase. The Journal of Biological chemistry. 1973 Aug 25; 248(16): 5673-8
421. Singh M, Su C. Progesterone and neuroprotection. Horm Behav. 2013 Feb; 63(2): 284-90

422. Singh M, Su C. Progesterone, brain-derived neurotrophic factor and neuroprotection. Neuroscience. 2013 Jun 3; 239: 84-91
423. Wu H, Wu ZG, Shi WJ, Gao H, Wu HH, Bian F et al. Effects of progesterone on glucose uptake in neurons of Alzheimer's disease animals and cell models. Life Sci. 2019 Dec 1; 238: 116979
424. Sagar NA, Tarafdar S, Agarwal S, Tarafdar A, Sharma S. Polyamines: functions, metabolism and role in human disease management. Med Sci. 2021 Jun 9; 9(2): 44
425. Seiler N, Sarhan S, Roth-Schechter BF. Polyamines and the development of isolated neurons in cell culture. Neurochem res. 1984 Jul; 9(7): 871-86
426. De Vera N, Martinez E, Sanfeliu C. Spermine induces cell death in cultured human embryonic cerebral cortical neurons trough N-methyl-D-aspartate receptor activation. J Neurosci Res. 2008 Mar; 86(4): 861-72
427. Brewer GJ, Torricelli JR. Isolation and culture of adult neurons and neurospheres. Nat Protoc. 2007; 2(6): 1490-98
428. Orsolits B, Borsy A, Madarasz E, Meszaros Z, Kohidi T, Marko K et al. Retinoid machinery in distinct neural stem cell populations with different retinoid responsiveness. Stem cells Dev. 2013 Oct 15; 22(20): 2777-93
429. Branca JJV, Pacini S, Morucci G, Bocchi L, Cosentino A, Boni E et al. Effects of ultrasound and selenium on human neurons in vitro. Arch ital. Biol. 2018 dec 31; 156(4): 153-63
430. Roth S, Zhang S, Chiu J, Wirth EK, Schweizer U. Development of a serum-free supplement for primary neuron culture reveals the interplay of selenium and vitamin E in neuronal survival. J trace Elem Med Biol. 2010 Apr; 24(2): 130-7
431. Chatonnet F, Fauquier T, Picou F, Guyot R, Flament F. [Thyroid hormone and cerebellum development: direct and indirect effects?] Ann Endocrinol. 2011 Apr; 72(2): 99-102. [French]
432. Combs CE, Nicholls JJ, Duncan Bassett JH, Williams GR. Thyroid hormones and bone development. Minerva Endocrinal. 2011 Mar; 36(1): 71-85
433. Mojon D, Boscoboinik D, Haas A, Bohnke M, Azzi A. Vitamin E inhibits retinal pigment epithelium cell proliferation in vitro. Ophthalmic res. 1994; 26(5): 304-9
434. Azzi A, Boscoboinik D, Bartoli GM, Chatelain E. A-tocopherol inhibits smooth muscle cell proliferation and protects against arteriosclerosis. From Adenine nucleotides in cellular energy transfer and signal transduction. 1992
435. Flood MT, Gouras P, Kjeldbye H. Growth characteristics and ultra-structure of human retinal pigment epithelium in vitro. Invest Ophthalmol Vis Sci. 1980
436. Organisciak DT, Bermann ER, Wang HM, Feeney-Burns L. Vitamin E in human neural retina and retinal pigment epithelium: effect of age. Curr Eye Res. 1987 Aug; 6(8): 1051-5
437. Rozga J, Piatek T, Malkowski P. Human albumin: old, new and emerging applications. Ann Transplant. 2013 May 10; 18: 205-17
438. Goyal MM, Basak A. Human catalase: looking for complete identity. Protein Cell. 2010 Oct; 1(10): 888-97
439. Glorieux C, Calderon PB. Catalase, a remarkable enzyme: targeting the oldest antioxidant enzyme to find a new cancer treatment approach. Biol Chem. 2017 Sep 26; 398(10): 1095-108
440. Chow HM, Shi M, Cheng A, Gao Y, Chen G, Song X et al. Age-related hyperinsulinemia leads to insulin resistance in neurons and cell-cycle-induced senescence. Nat neurosci. 2019 Nov; 22(11): 1806-19
441. Tanaka Y, Takata T, Satomi T, Sakurai T, Yonoko K. The double-edged effect of insulin on the neuronal cell death associated with hypoglycaemia on the hippocampal slice culture. Kobe J Med Sci. 2008 Jul 18; 54(2): E97-107
442. Miao L, St Clair DK. Regulation of superoxide dismutase genes: implications in disease. Free Radic Biol Med. 2009 Aug 15; 47(4): 344-56
443. Bruinink A, Sidler C, Birchler F. Neurotrophic effects of transferrin on embryonic chick brain and neural retinal cell cultures. Int J Dev Neurosci. 1996 Oct; 14(6): 785-95

444. Yoshikawa A, Kamide T, Hashida K, Ta HM, Inahata Y, Takarada-Iemata M et al. Deletion of Atf6α impairs astroglial activation and enhances neuronal death following brain ischemia in mice. J Neurochem. 2015 Feb; 132(3): 342-53
445. Ghouili I, Bahdoudi S, Morin F, Amri F, Hamdi Y, Coly PM et al. Endogenous expression of ODN-related peptides in astrocytes contributes to cell proliferation against oxidative stress: astrocyte-neuron crosstalk relevance for neuronal survival. Mol Neurobiol. 2018 Jun; 55(6): 4596-611
446. Rivea T, Zhao Y, Ni Y, Wang J. Human-induced pluripotent stem cell culture methods under cGMP conditions. Curr Protoc Stem Cell Biol. 2020 Sep; 54(1): e117
447. Baghbaderani BA, Tian X, Neo BH, Burkall A, Dimezzo T, Sierra G, Zeng X, Warren K, Kovarcik DP, Fellner T, Rao MS. cGMP-manufactured human induced pluripotent stem cells are available for pre-clinical and clinical applications. Stem Cell Reports. 2015 Oct 13; 5(4): 647-59.
448. Jumabay M, Abdmaulen R, Ly A, Cubberly MR, Shahmirian LJ, Heydarkhan-Hagvall S et al. Pluripotent stem cells derived from mouse and human white mature adipocytes. Stem Cells Transl Med. 2014 Feb; 3(2): 161-71
449. Jopling C, Boue S, Izpisua Belmonte JC. Dedifferentiation, transdifferentiation and reprogramming: three routes to regeneration. Nat Rev Mol Cell Biol. 2011 Feb; 12(2): 79-89
450. Collier JJ, Olahova M, McWilliams TG, Taylor RW. Mitochondrial signalling and homeostasis: from cell biology to neurological disease. Trends Neurosci. 2023 Feb; 46(2): 137-52
451. Scarpellini C, Ramos Llorca A, Lanthier C, Klejborowska G, Augustyns K. The potential role of regulated cell death in dry eye diseases and ocular surface dysfunction. Int J Mol Sci. 2023 Jan 1; 24(1): 731
452. Crane GM, Jeffery E, Morrison SJ. Adult haematopoitic stem cell niches. Nat Rev Immunol. 2017 Sep; 17(9): 573-90
453. Hecht S, Perez-Mockus G, Schienstock D, Recasens-Alvarez C, Merino-Aceituno S, Smith M et al. Mechanical constraints to cell-cycle progression in a pseudostratified epithelium. Curr Biol. 2022 May 9; 32(9): 2076-83
454. Biswas R, Banerjee A, Lembo S, Zhao Z, Lakshmanan V, Lim R et al. Mechanical instability of adherens junctions overrides intrinsic quiescence of hair follicle stem cells. Dev Cell. 2021 Mar 22; 56(6): 761-80. e7
455. Scholzen T, Gerdes J. The Ki-67 protein: from the known and the unknown. J Cell Physiol. 2000 Mar; 182(3): 311-22
456. Aihara M, Sugawara K, Torii S, Hosaka M, Kurihara H, Saito N et al. Angiogenic endothelium-specific nestin expression is enhanced by the first intron of the nestin gene. Lab Invest. 2004 Dec; 84(12): 1581-92
457. Daruich A, Duncan M, Robert MP, Lagali N, Semina EV, Aberdam D et al. Congenital aniridia beyond black eyes: from phenotype and novel genetic mechanisms to innovative therapeutic approaches. Prog Retin Eye Res. 2022 Oct 21; 101133
458. Jensen AM. Potential roles for BMP and Pax genes in the development of iris smooth muscle. Dev Dyn. 2005 Feb; 232(2): 385-92
459. Collins CA, Olsen I, Zammit PS, Heslop L, Petrie A, Partridge TA et al. Stem cell function, self-renewal, and behavioural heterogeneity of cells from the adult muscle satellite cell niche. Cell. 2005 Jul 29; 122(2): 289-301
460. Li L, Mignone J, Yang M, Matic M, Penman S, Enikolopov G et al. Nestin expression in hair follicle sheath progenitor cells. Proc Natl Acad Sci USA. 2003 Aug 19; 100(17): 9958-61
461. Amoh Y, Li L, Katsuoka K, Penman S, Haffman RM. Multipotent nestin-positive, keratin-negative hair-follicle bulge stem cells can form neurons. Proc Natl Acad Sci USA. 2005 Apr; 102(15): 5530-4

462. Aihara M, Sugawara K, Torii S, Hosaka M, Kurihara H, Saito N et al. Angiogenic endothelium-specific nestin expression is enhanced by the first intron of the nestin gene. Lab Invest. 2004 Dec; 84(12): 1581-92
463. Zimmerman L, Parr B, Lendahl U, Cunningham M, McKay R, Gavin B et al. Independent regulatory elements in the nestin gene direct transgene expression to neural stem cells or muscle precursors. Neuron. 1994 Jan; 12(1): 11-24
464. Fanarraga ML, Avila J, Zabala JC. Expression of unphosphorylated class III β-tubulin isotype in neuroepithelial cells demonstrates neuroblast commitment and differentiation. Eur J Neuro. 1999 Feb; 11(2): 517-27
465. Jospehson R, Muller T, Pickel J, Okabe S, Reynolds K, Turner PA et al. POU transcription factors control expression of CNS stem cell specific genes. Development. 1998 Aug; 125(16): 3087-100
466. Latchman DS. POU family transcription factors in the nervous system. J Cell Physiol. 1999 May; 179(2): 126-33
467. Ryan AK, Rosenfeld MG. POU domain family values: flexibility, partnerships, and developmental codes. Genes Dev. 1997 May 15; 11(10): 1207-25
468. Lothian C, Lendahl U. An evolutionarily conserved region in the second intron of the human nestin gene directs gene expression to CNS progenitor cells and to early neural crest cells. Eur J Neurosci. 1997 Mar; 9(3): 452-62
469. Allen SL, Elliott BT, Carson BP, Breen L. Improving physiological relevance of cell culture: the possibilities, considerations and future directions of the ex vivo co-culture model. Am J Physiol Cell Physiol. 2023 Feb 1; 324(2): C420- C427
470. Shyh-Chang N, Ng HH. The metabolic programming of stem cells. Genes Dev. 2017 Feb 15; 31(4): 336-46
471. Shyh-Chang N, Ng HH. The metabolic programming of stem cells. Genes Dev. 2017 Feb 15; 31(4): 336-46
472. Takashima Y, Guo G, Loos R, Nichols J, Ficz G, Krueger F et al. Resetting transcription factor control circuitry toward ground-state pluripotency in human. Cell. 2014 Sep 11; 158(6): 1254-69
473. Wray J, Kalkan T, Smith AG. The ground state of pluripotency. Biochem Soc Trans. 2010 Aug; 38(4): 1027-32
474. Carbognin E, Betto RM, Soriano ME, Smith AG, Martello G. Stat3 promotes mitochondrial transcription and oxidative respiration during maintenance and induction of naïve pluripotency. EMBO J. 2016 Mar 15; 35(6): 618-34
475. Zhou W, Choi M, Margineantu D, Margaretha L, Hesson J, Cavanaugh C et al. HIF1α induced switch from bivalent to exclusively glycolytic metabolism during ESC-to-EpiSC/hESC transition. EMBO J. 2012 May 2; 31(9): 2103-16
476. Suda T, Takubo K, Semenza GL. Metabolic regulation of hematopoietic stem cells in the hypoxic niche. Cell Stem Cell. 2011 Oct 4; 9(4): 298-310
477. Rehman J. Empowering self-renewal and differentiation: the role of mitochondria in stem cells. J Mol Med (Berl). 2010 Oct;88(10):981-6
478. Wilmut I. The first direct reprogramming of adult human fibroblasts. Cell Stem Cell. 2007 Dec 13;1(6):593-4
479. Leach LL, Clegg DO. Concise Review: Making Stem Cells Retinal: Methods for Deriving Retinal Pigment Epithelium and Implications for Patients With Ocular Disease. Stem Cells. 2015 Aug;33(8):2363-73
480. Bora N, Conway SJ, Liang H, Smith SB. Transient overexpression of the Microphthalmia gene in the eyes of Microphthalmia vitiligo mutant mice. Dev Dyn. 1998 Nov;213(3):283-92
481. Roy A, de Melo J, Chaturvedi D, Thein T, Cabrera-Socorro A, Houart C, Meyer G, Blackshaw S, Tole S. LHX2 is necessary for the maintenance of optic identity and for the progression of optic morphogenesis. J Neurosci. 2013 Apr 17;33(16):6877-84

482. Diacou R, Nandigrami P, Fiser A, Liu W, Ashery-Padan R, Cvekl A. Cell fate decisions, transcription factors and signaling during early retinal development. Prog Retin Eye Res. 2022 Nov;91:101093.
483. Lagutin O, Zhu CC, Furuta Y, Rowitch DH, McMahon AP, Oliver G. Six3 promotes the formation of ectopic optic vesicle-like structures in mouse embryos. Dev Dyn. 2001 Jul;221(3):342-9
484. Yun S, Saijoh Y, Hirokawa KE, Kopinke D, Murtaugh LC, Monuki ES, Levine EM. Lhx2 links the intrinsic and extrinsic factors that control optic cup formation. Development. 2009 Dec;136(23):3895-906
485. de Melo J, Clark BS, Venkataraman A, Shiau F, Zibetti C, Blackshaw S. Ldb1- and Rnf12-dependent regulation of Lhx2 controls the relative balance between neurogenesis and gliogenesis in the retina. Development. 2018 Apr 30;145(9):dev159970
486. Lagutin OV, Zhu CC, Kobayashi D, Topczewski J, Shimamura K, Puelles L, Russell HR, McKinnon PJ, Solnica-Krezel L, Oliver G. Six3 repression of Wnt signaling in the anterior neuroectoderm is essential for vertebrate forebrain development. Genes Dev. 2003 Feb 1;17(3):368-79
487. Liu W, Lagutin OV, Mende M, Streit A, Oliver G. Six3 activation of Pax6 expression is essential for mammalian lens induction and specification. EMBO J. 2006 Nov 15;25(22):5383-95
488. Liu W, Lagutin O, Swindell E, Jamrich M, Oliver G. Neuroretina specification in mouse embryos requires Six3-mediated suppression of Wnt8b in the anterior neural plate. J Clin Invest. 2010 Oct;120(10):3568-77.
489. Liu W, Cvekl A. Six3 in a small population of progenitors at E8.5 is required for neuroretinal specification via regulating cell signaling and survival in mice. Dev Biol. 2017 Aug 1;428(1):164-175
490. Diacou R, Zhao Y, Zheng D, Cvekl A, Liu W. Six3 and Six6 Are Jointly Required for the Maintenance of Multipotent Retinal Progenitors through Both Positive and Negative Regulation. Cell Rep. 2018 Nov 27;25(9):2510-2523.
491. Medina-Martinez O, Amaya-Manzanares F, Liu C, Mendoza M, Shah R, Zhang L, Behringer RR, Mahon KA, Jamrich M. Cell-autonomous requirement for rx function in the mammalian retina and posterior pituitary. PLoS One. 2009;4(2):e4513
492. Chen J, Liao S, Xiao Z, Pan Q, Wang X, Shen K, Wang S, Yang L, Guo F, Liu HF, Pan Q. The development and improvement of immunodeficient mice and humanized immune system mouse models. Front Immunol. 2022 Oct 19;13:1007579
493. Cao F, van der Bogt KE, Sadrzadeh A, Xie X, Sheikh AY, Wang H, Connolly AJ, Robbins RC, Wu JC. Spatial and temporal kinetics of teratoma formation from murine embryonic stem cell transplantation. Stem Cells Dev. 2007 Dec;16(6):883-91
494. Trusler O, Huang Z, Goodwin J, Laslett AL. Cell surface markers for the identification and study of human naive pluripotent stem cells. Stem Cell Res. 2018 Jan;26:36-43
495. Hu C, Fan L, Cen P, Chen E, Jiang Z, Li L. Energy Metabolism Plays a Critical Role in Stem Cell Maintenance and Differentiation. Int J Mol Sci. 2016 Feb 18;17(2):253
496. Kawasaki H, Mizuseki K, Nishikawa S, Kaneko S, Kuwana Y, Nakanishi S, Nishikawa SI, Sasai Y. Induction of midbrain dopaminergic neurons from ES cells by stromal cell-derived inducing activity. Neuron. 2000 Oct;28(1):31-40
497. Kawasaki H, Suemori H, Mizuseki K, Watanabe K, Urano F, Ichinose H, Haruta M, Takahashi M, Yoshikawa K, Nishikawa S, Nakatsuji N, Sasai Y. Generation of dopaminergic neurons and pigmented epithelia from primate ES cells by stromal cell-derived inducing activity. Proc Natl Acad Sci U S A. 2002 Feb 5;99(3):1580-5
498. Klimanskaya I, Hipp J, Rezai KA, West M, Atala A, Lanza R. Derivation and comparative assessment of retinal pigment epithelium from human embryonic stem cells using transcriptomics. Cloning Stem Cells. 2004;6(3):217-45

499. Buchholz DE, Hikita ST, Rowland TJ, Friedrich AM, Hinman CR, Johnson LV, Clegg DO. Derivation of functional retinal pigmented epithelium from induced pluripotent stem cells. Stem Cells. 2009 Oct;27(10):2427-34
500. Thomas BB, Zhu D, Zhang L, Thomas PB, Hu Y, Nazari H, Stefanini F, Falabella P, Clegg DO, Hinton DR, Humayun MS. Survival and Functionality of hESC-Derived Retinal Pigment Epithelium Cells Cultured as a Monolayer on Polymer Substrates Transplanted in RCS Rats. Invest Ophthalmol Vis Sci. 2016 May 1;57(6):2877-84
501. Nair DSR, Thomas BB. Stem Cell-based Treatment Strategies for Degenerative Diseases of the Retina. Curr Stem Cell Res Ther. 2022;17(3):214-225
502. Osakada F, Ikeda H, Mandai M, Wataya T, Watanabe K, Yoshimura N, Akaike A, Sasai Y, Takahashi M. Toward the generation of rod and cone photoreceptors from mouse, monkey and human embryonic stem cells. Nat Biotechnol. 2008 Feb;26(2):215-24. doi: 10.1038/nbt1384. Epub 2008 Feb 3. Erratum in: Nat Biotechnol. 2008 Mar;26(3):352. Akaike, Akiori [corrected to Akaike, Akinori]
503. Koh SM. VIP enhances the differentiation of retinal pigment epithelium in culture: from cAMP and pp60(c-src) to melanogenesis and development of fluid transport capacity. Prog Retin Eye Res. 2000 Nov;19(6):669-88
504. Tombran-Tink J, Barnstable CJ. PEDF: a multifaceted neurotrophic factor. Nat Rev Neurosci. 2003 Aug;4(8):628-36
505. Ponnalagu M, Subramani M, Jayadev C, Shetty R, Das D. Retinal pigment epithelium-secretome: A diabetic retinopathy perspective. Cytokine. 2017 Jul;95:126-135
506. Redmond TM, Poliakov E, Yu S, Tsai JY, Lu Z, Gentleman S. Mutation of key residues of RPE65 abolishes its enzymatic role as isomerohydrolase in the visual cycle. Proc Natl Acad Sci U S A. 2005 Sep 20;102(38):13658-63
507. Maw MA, Kennedy B, Knight A, Bridges R, Roth KE, Mani EJ, Mukkadan JK, Nancarrow D, Crabb JW, Denton MJ. Mutation of the gene encoding cellular retinaldehyde-binding protein in autosomal recessive retinitis pigmentosa. Nat Genet. 1997 Oct;17(2):198-200
508. Gal A, Li Y, Thompson DA, Weir J, Orth U, Jacobson SG, Apfelstedt-Sylla E, Vollrath D. Mutations in MERTK, the human orthologue of the RCS rat retinal dystrophy gene, cause retinitis pigmentosa. Nat Genet. 2000 Nov;26(3):270-1
509. Cordes M, Bucichowski P, Alfaar AS, Tsang SH, Almedawar S, Reichhart N, Strauß O. Inhibition of Ca^{2+} channel surface expression by mutant bestrophin-1 in RPE cells. FASEB J. 2020 Mar;34(3):4055-4071
510. Loupy A, Lefaucheur C. Antibody-Mediated Rejection of Solid-Organ Allografts. N Engl J Med. 2018 Sep 20;379(12):1150-1160
511. McGill TJ, Stoddard J, Renner LM, Messaoudi I, Bharti K, Mitalipov S, Lauer A, Wilson DJ, Neuringer M. Allogeneic iPSC-Derived RPE Cell Graft Failure Following Transplantation Into the Subretinal Space in Nonhuman Primates. Invest Ophthalmol Vis Sci. 2018 Mar 1;59(3):1374-1383
512. Lu B, Malcuit C, Wang S, Girman S, Francis P, Lemieux L, Lanza R, Lund R. Long-term safety and function of RPE from human embryonic stem cells in preclinical models of macular degeneration. Stem Cells. 2009 Sep;27(9):2126-35
513. Takagi S, Mandai M, Gocho K, Hirami Y, Yamamoto M, Fujihara M, Sugita S, Kurimoto Y, Takahashi M. Evaluation of Transplanted Autologous Induced Pluripotent Stem Cell-Derived Retinal Pigment Epithelium in Exudative Age-Related Macular Degeneration. Ophthalmol Retina. 2019 Oct;3(10):850-859
514. Lojudice FH, Fernandes RAB, Innocenti F, Franciozi CE, Cristovam P, Maia M, Sogayar MC, Junior RB. In vitro differentiation of cGMP-grade retinal pigmented epithelium from human embryonic stem cells. Int J Retina Vitreous. 2019 Oct 21;5:45
515. Kashani AH, Lebkowski JS, Rahhal FM, Avery RL, Salehi-Had H, Dang W, Lin CM, Mitra D, Zhu D, Thomas BB, Hikita ST, Pennington BO, Johnson LV, Clegg DO, Hinton DR, Humayun MS. A bioengineered retinal pigment epithelial monolayer for advanced, dry age-related macular degeneration. Sci Transl Med. 2018 Apr 4;10(435):eaao4097